
Investigating Accuracy and Precision of Sonoacoustics for Range Determination of Ion Beams in Water

Sebastian Lehrack



München 2018

Investigating Accuracy and Precision of Sonoacoustics for Range Determination of Ion Beams in Water

Sebastian Lehrack

Dissertation
an der Fakultät für Physik
der Ludwig-Maximilians-Universität
München

vorgelegt von
Sebastian Lehrack
aus Merseburg an der Saale

München, den 11.6.2018

Erstgutachter: Prof. Dr. Katia Parodi
Zweitgutachter: Prof. Dr. Otmar Biebel
Tag der mündlichen Prüfung: 11.7.2018

Für das Leben, das Universum und den ganzen Rest.

Contents

List of Figures	xi
List of Tables	xiii
Abstract, Zusammenfassung	xv
1. Introduction	1
1.1. Motivation and State-of-the-Art	2
1.2. Ionoacoustics as a new Approach to in-vivo Range Verification . . .	11
1.3. Thesis Outline	15
2. Theoretical Concepts of Ionoacoustics	17
2.1. Deriving Ionoacoustics from Photoacoustics	18
2.1.1. General Acoustic Wave Equation	18
2.1.2. Spherical Wave Solution	19
2.1.3. Green's Function Approach	20
2.1.4. Initial Pressure Derivation	21
2.2. Influences on Ionoacoustical Signals	26
2.2.1. General Model of Signal Generation	27
2.2.2. Non-Delta Spike Excitations	30
2.2.3. Realistic Detector Surfaces	31
2.2.4. Influences of Realistic Detectors Electronics	31
2.2.5. Attenuation in Water	32
2.2.6. Dispersion	32
2.3. Simulation Studies	33
2.3.1. Direct Integration applied to the General Solution	33
2.3.2. Global Finite-Difference Method using k-Wave	34
2.3.3. Calculation of SIR using Field II	35
2.3.4. Simulation Examples	35
2.3.4.1. Disc Source Example	35
2.3.4.2. Pulse Width and Shape Dependency	38
2.3.4.3. Influence of a Realistic Spatial Impulse Response .	39
2.4. Conclusion	42

3. Experimental Tools and Methods	43
3.1. General Experimental Setup and Beam Properties	44
3.2. Accelerating Particles	45
3.2.1. Particle Accelerators investigated for Ionoacoustics	45
3.2.2. Typical Beam Properties for Medical Applications	48
3.3. Calculating Dose Depositions	50
3.3.1. Using Stopping Power Tables	50
3.3.2. Monte Carlo in SRIM and Geant4	51
3.4. Measuring Dose with established Methods	51
3.4.1. Radiochromic Films	52
3.4.2. Ionization chambers	52
3.5. Measuring Dynamic Pressure and Ultrasound	53
3.5.1. Piezoelectric Effect	53
3.5.2. Different Forms of Detectors	54
3.5.3. Calibration of PZT Transducers	55
3.6. Used Hydrophones and Transducers	55
3.6.1. PA Needle Hydrophone	55
3.6.2. Olympus PZT	55
3.6.3. Cetacean C305X	58
3.7. DAQ Software and Hardware	61
4. Evaluation Techniques	63
4.1. Signal Origin	64
4.1.1. Signal Elements following Albul et al	66
4.2. Relative Evaluation	68
4.3. Time-of-Flight Mode	69
4.4. Frequency Based Method or Autocorrelation Method	71
4.5. Retrieval of Polyenergetic Spectra	76
4.6. Conclusion on Evaluation Techniques	79
4.6.1. Comparison of the different methods	79
4.6.2. Closing	80
5. Experimental Studies	81
5.1. Proof of Principle Experiments with 20 MeV	82
5.1.1. Simulation of Experiments with 20 MeV Protons	83
5.1.2. Deriving the Speed of Sound in Water Experimentally	87
5.1.3. Calculating Ranges for 20 MeV protons	90
5.1.4. Absorption Wheel Measurements	93
5.1.5. Dose Determination using Quantitative Pressure Measure- ments	97
5.1.6. Coherent Ionoacoustics	99

5.2. Measurements at Medical Accelerators up to 230 MeV Protons . . .	103
5.2.1. From 20 MeV to 200 MeV	103
5.2.2. Measurements at UPENN	105
5.2.3. Measurements at the Synchrocyclotron at CAL	108
5.2.3.1. Scintillator triggered Ionoacoustics	110
5.2.3.2. Range Determination Results	112
5.3. Measurements at the High Energy Synchrotron SIS18 at GSI	117
5.3.1. Results from ^{124}Xe and ^{238}U Ion Beam Times	121
5.3.2. Results from ^{12}C Ion Beam Time	122
5.4. Demonstration with Laser Accelerated Particles at LEX	124
5.5. Conclusion on Experimental Studies	127
6. Discussion and Outlook	131
6.1. Summary on comparative Methods	132
6.1.1. Comparing Ionoacoustic Results to other experimental Meth- ods	132
6.1.2. Comparing Ionoacoustic in Simulations	135
6.2. Feasibility of medical Ionoacoustics	137
6.2.1. Technical Requirements	137
6.2.1.1. Pulse Widths	137
6.2.1.2. Beam Charge and Intensity	138
6.2.1.3. Angular and Patient-site Dependence	139
6.2.2. Heterogeneous Studies	141
6.3. Ionoacoustic as a general Ion Energy Monitor	144
Appendix A. GSI Results	149
Appendix B. Additional Data from 20 MeV proton beam	159
Appendix C. Relevant Publications by the Author	163
Bibliography	193
Danksagung, Acknowledgement	209

List of Figures

1.1.	Stopping power of protons in water.	5
1.2.	Comparison of dose profiles from photon and proton irradiation. . .	6
1.3.	Different irradiation options for a prostate cancer patient.	8
1.4.	Hepatic cancer irradiation with acoustic detection.	12
2.1.	Overview of theoretical parameters.	22
2.2.	Stress and thermal confinement in overview.	24
2.3.	Analytical simulation on simplified Bragg peak source.	29
2.4.	Overview for the disc source example.	36
2.5.	Simulation example demonstrating the detector distance relationship. .	37
2.6.	Influence of temporal profiles.	38
2.7.	Pulse width study.	39
2.8.	SIR influence of a 3.5 MHz spherical focus transducer.	40
2.9.	SIR study on z position dependency.	41
3.1.	Sketch of the general, experimental setup.	45
3.2.	Calculated pulse profile for GSI experiments.	49
3.3.	Sensitivity of the PA needle hydrophone.	56
3.4.	Olympus PZT constructions.	56
3.5.	Sensitivity and frequency bandwidth of 3.5 MHz PZT Olympus V382. .	57
3.6.	The CRT C305X inside out.	59
3.7.	Ultrasound measurement setup performed on the C305X.	60
3.8.	Frequency response and receiving pattern of the C305X.	61
3.9.	IonoDAQ software schematic.	62
4.1.	Example of ionoacoustic signal.	65
4.2.	Signal overview following Albul <i>et al.</i>	67
4.3.	Demonstration of a deconvolution of experimental data taken from Jones <i>et al.</i> (2016b).	71
4.4.	Demonstration of autocorrelation method.	73
4.5.	Results of autocorrelation analysis.	74
4.6.	Pulse width correction for autocorrelation method	76
4.7.	Flowchart of simulated annealing procedure.	77
4.8.	Polyenergetic retrieval work flow taken from Yang (2017).	78

5.1.	Comparison of measurement signal with simulations.	84
5.2.	Simulation of 20 MeV ionoacoustic pressure.	85
5.3.	Example and frequency analysis for thick Kapton entrance foil. . . .	86
5.4.	Deriving the speed of sound experimentally.	88
5.5.	Variation of simulation parameter.	92
5.6.	WER measurements on modulating wheel.	95
5.7.	Absolute pressure measurement.	98
5.8.	Beam foci with and without multi-slit collimator.	100
5.9.	Coherent ionoacoustics results.	101
5.10.	Simulation comparing 20 MeV and 200 MeV.	104
5.11.	Pressure traces taken at UPENN.	108
5.12.	Relative range shifts from ionoacoustic measurements at UPENN. .	109
5.13.	Precision of different trigger sources at MLL.	110
5.14.	Shot-by-Shot differences from PMT.	111
5.15.	Example of CAL Measurements with absolute pressure values. . . .	112
5.16.	Result of energy variation acquired at CAL.	113
5.17.	Dose dependence of CAL measurements.	116
5.18.	Demonstration of autocorrelation method on GSI data.	120
5.19.	Images of the LIONo-acoustic setup and detector.	125
5.20.	I-BEAT results.	126
5.21.	Summary of evaluated ranges and their precision.	129
6.1.	Systematic error in determining the Bragg peak distance, taken from Jones <i>et al.</i> (2016a).	140
6.2.	Reconstruction of initial pressure in heterogeneous medium.	143
A.1.	^{12}C ion depth dose profile.	152
A.2.	^{124}Xe ions depth dose profile.	153
A.3.	^{238}U ion depth dose profile.	153
A.4.	Ionoacoustic example of 300 MeV ^{124}Xe ion beam.	154
A.5.	Ionoacoustic example of 200 MeV ^{12}C ions.	154
A.6.	Exemplary measurement of ^{124}Xe ions with different PZT transducers.	155
A.7.	Autocorrelation analysis on k-Wave simulation data from single pulse ^{238}U ions.	156
A.8.	Autocorrelation analysis on k-Wave simulation data ^{238}U ions using the GSI pulse train as temporal profile.	157
B.1.	2D raster scan of 20 MeV protons with additional scattering.	160
B.2.	Pulse width study at the MLL tandem.	161
B.3.	Example of a lateral measurement with a 20 MeV proton beam stopped in water.	162

List of Tables

3.1.	Summary of particle accelerators used for ionoacoustic measurements.	48
3.2.	Relevant values for calculating the temporal pulse shape at the GSI synchrotron with fast extraction.	50
4.1.	Summary of 20 MeV proton beam time results.	79
5.1.	Stopping power values for different materials and 20 MeV proton beams.	83
5.2.	Coefficient for sound velocity fit from Marczak (1997).	89
5.3.	Temperature dependent density of water as used in Geant4 simulations.	91
5.4.	Variation of temperature and ionization potential.	92
5.5.	Constant values used for quantitative pressure measurements.	97
5.6.	Summary of all absolute range measurements at CAL.	114
5.7.	GSI Geant4 Data for ^{12}C , ^{124}Xe , and ^{238}U ions.	118
5.8.	Results from time and frequency based analysis of GSI data compared to Geant4.	119
5.9.	Comparision of ^{12}C ion range data.	123
A.1.	Results from ^{12}C ions at GSI, time based.	150
A.2.	Results from ^{12}C ions at GSI, frequency based.	150
A.3.	Difference in the resulting ranges in water for different beam energies for ^{12}C ions at GSI.	150
A.4.	Results from ^{238}U ions at GSI, time based.	151
A.5.	Results from ^{238}U ions at GSI, frequency based.	151
A.6.	Results from ^{124}Xe ions at GSI, time based.	151
A.7.	Results from ^{124}Xe ions at GSI, frequency based.	151
A.8.	GSI range uncertainty translated to energy uncertainty.	152

Zusammenfassung

Bei der externen Strahlentherapie wird Patienten Dosis mithilfe von hochenergetischen Photonen oder geladenen Teilchen, hauptsächlich Protonen zugeführt. Aufgrund der geringeren Kosten im Kauf und Unterhalt klinischer Photonenanlagen werden diese derzeit bevorzugt, obwohl die Dosisverteilung im Patienten weniger präzise ist als mit Protonenstrahlen. Der Grund dafür ist das exponentielle Abschwächungsverhalten energetischer Photonen in Materie, womit ein signifikanter Anteil an zusätzlicher Dosis in umliegendem, gesundem Gewebe in Kauf genommen werden muss. Protonen weisen ein Tiefendosisprofil in der Form der sog. Braggkurve mit einer scharf begrenzten, endlichen Reichweite auf, sodass in Einstrahlrichtung Risikoorgane vor unnötiger Dosis geschützt werden können. Aufgrund von Reichweitenungenauigkeiten, einem der größten, technischen Probleme moderner Strahlentherapie, werden Sicherheitssäume eingeplant und der Vorteil in der Dosisverteilung, der sich aus dem unterschiedlichen physikalischen Absorptionsverhalten von Photonen und Protonen ergibt, wird aufgegeben. Diese Ungenauigkeiten sind bedingt durch diverse praktische Begrenzungen während der Bestrahlung, wie zum Beispiel dem Atemzyklus des Patienten oder andere intrafraktionale Organbewegungen, oder durch Veränderungen zwischen den Behandlungstagen, wie Gewichtsverlust oder die innere Verschiebung der Organe von Tag zu Tag.

Einen möglichen Ansatz, diese Reichweitenungenauigkeit zu verringern, bietet hierbei die in-vivo Dosimetrie, eine Methode, die idealerweise in Echtzeit die zugeführte Dosis, oder zumindest die Reichweite, im Patienten messen, verifizieren und darstellen kann. Dafür ist in den letzten Jahrzehnten vor allen an zwei Abbildungsmethoden basierend auf der Detektion der durch Kernreaktionen induzierten Sekundärstrahlung geforscht worden: Messungen der Positronen-Emissionen ausgelöst durch die Bestrahlung und Prompt- γ -Monitoring. Auch wenn bereits erste Prototypen in klinischen Studien getestet werden, handelt es sich hierbei um anspruchsvolle nuklearphysikalische Experimente, für die bisher mitunter komplexe Rechnungen und Rekonstruktionen nötig waren, was im Gegensatz zu der Forderung nach einer Echtzeitmethode stand. Auch wenn z.B. mit der Entwicklung der Einzelschlitz-Prompt- γ Kamera ein großer Fortschritt in der Überwindung dieser Probleme erreicht wurde, möchte diese Arbeit eine alternative Methode der Reichweitenbestimmung erneut aufgreifen: Ionoakustik. Es soll in dieser Arbeit gezeigt werden, dass es sich dabei um eine kostengünstige Möglichkeit handelt, um quasi in Echtzeit Informationen über die tatsächliche Bragg Peak Position zu erhalten. Bei der Bestrahlung mit gepulsten Ionenstrahlen kann eine Ultraschallwelle gemessen werden, welche räumliche und zeitliche Information über den Ionenpuls und die auslösende adiabatische Erwärmung in sich trägt. Ionoakustik ist die Messung und Auswertung dieser Ultraschallwelle, um die Energie und Reichweite der geladenen Teilchen zu bestimmen. In dieser Arbeit wird die grundlegende Erzeugung

des Druckes erklärt, welche Einflüsse während der Messung auf das Signal auftreten, und wie die gemessenen Signale auszuwerten sind. Im Rahmen dieser Arbeit wurden verschiedene Experimente an unterschiedlichen Beschleunigern durchgeführt. Hierbei wurden zahlreiche Messungen mit ausreichendem Signal-zu-Rausch-Verhältnis gemacht und die dabei gemessenen Reichweiten werden präsentiert. Es konnten bei Protonen mit einer kinetischen Energie von 20 MeV Reichweiten im Wasser mit einer Genauigkeit und Präzision von weniger als 50 μm gemessen werden. An medizinischen Beschleunigern mit >200 MeV Protonen wurden Reichweiten im Wasser mit einer Genauigkeit und Präzision von weniger als 1 mm gemessen, bei anderen schweren Ionen war die Genauigkeit und Präzision weniger als 100 μm . Dabei steht die mögliche Übertragbarkeit in eine medizinische Anwendung besonders im Fokus der Diskussionen, da diese guten Ergebnisse die Verringerung der Sicherheitssäume in der Behandlungsplanung zur Folge haben könnten und damit eine Verbesserung der Bestrahlung mit geladenen Teilchen im Allgemeinen.

Die hier vorgestellten experimentellen Ergebnisse beinhalten Messungen von verschiedenen kinetischen Energien, unterschiedlichen Ionen und Intensitäten. In allen Fällen zeigten vergleichende Simulationsrechnungen gute Übereinstimmungen. Besonders in Messungen, in denen die experimentellen Parameter sehr detailliert bestimmt werden konnten, können diese Messung als Bestätigung von Simulationsparametern interpretiert werden, obwohl diese Parameter normalerweise zur Anpassung an Messwerte Variationen unterzogen werden. Das hier verwendete Ionisationspotential für Wasser mit einem Wert von 78 eV, die derzeit gültige Empfehlung der Internationalen Kommission für Strahlungseinheiten und Messung ICRU, zeigte in den hier durchgeführten Studien die beste Übereinstimmung mit den Messergebnissen. Die mögliche Einsetzbarkeit ist derzeit auf Regionen beschränkt, die mit klinischem Ultraschall abgebildet werden können. Die technische Machbarkeit und nötige nächste Schritte werden diskutiert und mit einem möglichen Behandlungsszenario abgeschlossen, welches akustische Messungen einbezieht. Hierbei ist die derzeitige größte Herausforderung die immer noch hohe Dosis, die benötigt wird, um hinreichende ionoakustische Signale zu erzeugen.

Abstract

In radiation therapy using external beams, delivery of dose is currently done with energetic photons or heavy charged particles, mainly protons. The treatment with photons is favoured as installation and maintenance costs are lower than with proton therapy, although the delivered dose distribution is less confined in space. This is due to the exponentially decaying depth dose distribution of photons in matter, adding a significant dose to tissue surrounding the tumour site. Protons, on the contrary, have a finite penetration depth in matter and a distinct maximum of deposited energy, the Bragg peak, both mainly depending on the initial kinetic energy of the incident heavy charged particle. This offers spatially confined dose distributions compared to the irradiation with photons, if the range of heavy charged particle in tissue is known precisely. However, due to several practical limitations, relatively large safety margins are added in the treatment planning in order to compensate for range uncertainties, e.g. limited knowledge on the tissue stopping power as well as changes in the patient anatomy during a single treatment, like breathing and other intra-fractional organ motions, and between several treatment days, like weight loss and large scale organ displacements. These range uncertainties are one of the biggest challenges in modern radiation therapy with heavy charged particles, thus hampering the potential superiority of this irradiation modality in terms of dose conformity

A practical approach which would allow a reduction of these safety margins would be in-vivo-dosimetry, an online method verifying and displaying the currently delivered dose, or at least the beam range, to the patient. To this end, methods based on secondary radiation induced by nuclear interactions have been studied over the last decades, and at least two promising approaches have reached the status of clinical trials. However, Positron-Emission-Tomography and prompt- γ monitoring require relatively bulky and expensive instrumentation as well as complex simulations and reconstructions. Although considerable progress has been made with the development of a single-slit prompt- γ device, in the past the previously mentioned problems were hindering these approaches to become truly online methods. In this thesis, Ionoacoustics is revisited as a range determination mechanism offering a cost-effective technology providing quasi real-time informations on the actual Bragg peak position.

Following irradiation with a pulsed ion beam, a pressure wave is measured, which contains spatial and temporal information on the initiating adiabatic heating. The evaluation of the pressure signal in order to extract energy, specifically range information, is called Ionoacoustics. In this framework, the basis of the pressure generation and detection is thoroughly studied together with different evaluation techniques. Several experiments at different accelerators have been conducted, which provided measurements with a good signal to noise ratio, and their results

are discussed. It can be shown that ranges of 20 MeV protons in water can be determined with a precision and accuracy better than 50 μm , the range of high energetic protons under clinical condition better than 1 mm, and other heavy ions better than 100 μm . It will be discussed, whether the translation of these precise results to clinical applications is feasible, as this would lower the currently used safety margins used in treatment planning.

The presented experiments cover a wide range of particle energies, ion types, and intensities. Simulation studies showed very good agreement to the collected experimental results. Especially for the studies at low-energies, where experimental parameters are defined precisely, simulation parameters can be confirmed. The ionization potential of water of 78 eV following the latest recommendation of the International Commission on Radiation Units and Measurements ICRU yielded results in best agreement to experimental data. The technical feasibility and next required steps will be discussed concluding with a possible scenario for treatment verification with acoustic measurements for a favourable anatomical indication of viable sonic accessibility. The currently biggest challenge in this step towards a clinical application is the still high dose that is required to generate ionoacoustic signals.

1. Introduction

Who are these men of lust, greed, and glory?
Rip off the mask and let's see!
But that's not right- oh no, what's the story?
There's you, and there's me. That can't be right.

SUPERTRAMP in *Crime of the Century*

1.1. Motivation and State-of-the-Art

Radiotherapy is, next to chemotherapy and surgery, one of the 3 pillars in today's cancer therapy. As cancer is the second leading cause of death (Stewart and Wild, 2014, Kaatsch, 2015), one of the major goals for modern medical physics is the improvement and transfer of technology into medicine in order to advance radiation therapy and medical imaging. The 3 pillars have a rather simple principle in common: destroy cancerous tissue and spare healthy one. In the case of radiation therapy, this is achieved by depositing *radiation energy* locally, which results in irreversible damage to the DNA double helix of a cell in a complex pattern, i.e. no correct repair of the DNA is possible and the cell can no longer reproduce itself. This local deposition of radiation energy normalized by the irradiated mass is the *dose*. In the interaction of high energy particles such as photons or ions, secondary electrons are produced, transferring energy from these primary particle beams to the cells (Barendsen *et al.*, 1960). One can distinguish between internal and external delivery methods. The first one is amongst others the so called *Brachytherapy*, where radioactive sources are implanted in or positioned close to the tumour site. In *Radionuclide therapy*, *Radiopharmaceuticals* can transport such a source close to the tumour site. For the course of this work, the focus will be on the two major external beam radiation treatments using protons and photons. Important differences between these two treatment modality root in the different physical behaviour of charged and uncharged particles in the interaction with matter. (Wilson, 1946, Attix, 1991, Newhauser and Zhang, 2015)

A photon is an uncharged massless particle. Its interaction with matter is dominated by collisions with electrons. The three major physical processes to describe the energy transfer in matter are the *Photoelectric effect*, *Compton scattering*, and *Pair production*. Their dominance is given by the photon kinetic energy and the atomic number Z of the absorbing material.

The Photoelectric effect is the absorption of an incident photon with energy $h\nu$ by an inner shell electron bounded by potential energy E_b . The electron leaves the atomic bound with remaining kinetic energy $h\nu - E_b$, and follow up processes as the emission of characteristic photons and Auger electrons due to the refilling of the ejected electron are possible. The photoelectric effect is dominant for low photon energies, that are higher than the binding energies of the electrons, and high Z of the absorbing material.

The Compton effect is the scattering of an incident photon at a quasi unbound stationary electron. The amount of energy transferred to the electron is depending on the initial photon energy and the scattering angle. For low- Z media (e.g. carbon, air, water, human tissue) the range of Compton effect dominance is very broad, extending from photon energies of 20 keV to 30 MeV.

Pair production is an absorption process near an atomic nucleus in which a photon

is converted to an electron and positron. This process is therefore in photon interactions only possible with photon energies above the rest mass of the resulting electron-positron pair, i.e. $h\nu = 1.022 \text{ MeV}$, and is more likely in high- Z material. As photons do not have an electric charge, they will lose their energy in matter in some of these events, while the later described charged particles, i.e. protons and electrons, will lose energy gradually and continuously due to the Coulomb interaction. The deposited energy (and resulting dose) by high energetic photons in matter can be in first order described as exponentially decreasing with the penetration depth. Considering the treatment of a typical deep seated tumour site, e.g. prostate or pancreas, the radiation dose delivered to tissue before and beyond the target needs to be considered. To this end, the photon beam is directed into the patient from different angles, overlapping at the tumour and thus improving the ratio of dose delivered to tumour compared to surrounding healthy tissue. Critical organs where the possible damage needs to be kept below a certain tolerance threshold are called *organs at risk* or OAR, which might be the heart or the bladder closely located to the lung and the prostate, respectively. The production of photons suitable for cancer treatment is, compared to the later described acceleration and guidance of protons or even heavier ions, straightforward via the usage of compact linear electron accelerators and Bremsstrahlung conversion. However, the selectivity in dose delivery is limited due to basic physical principles. Nevertheless, photon radiation is currently the widely practised irradiation modality for radiotherapeutic treatment. One of the reasons, besides the proven effectiveness in many cases, is the still lower costs in installation, maintenance, and operation. Protons, and also heavier ions, are positively charged massive particles. Therefore, the Coulomb interaction with electrons bounded in the target's atomic shells and the target nuclei are the dominant interaction mechanisms. Contrary to photons, charged particles undergo many more interactions due to the long range of the Coulomb interaction. Due to their higher mass compared to electrons radiative processes can be ignored for clinically relevant energies. The different events of Coulomb interactions are distinguished by the relative size of the classical *impact parameter* b in comparison to the atomic radius a . In order to avoid confusion, the incident particle will be simply called *ion* while *the atom* is the nucleus with its electronic shell of the absorbing material.

In a *soft collision*, the ion passes an atom at considerable distance ($b \gg a$). The influence of the ion affects the atom as a whole, thereby distorting it, exciting it to a higher energy level and sometimes ionizing it by ejecting a valence-shell electron. Because large values of b are more probable than nearby hits on individual atoms, *soft collisions* are by far the most numerous type of charge-particle interactions, accounting for roughly half the energy transfer to the absorbing medium.

In a *hard collision*, the incident ion is interacting directly with a single atomic

electron ($b \sim a$). This atomic electron is then ejected from the atom as a delta ray, undergoing additional Coulomb interactions on its own. Furthermore, the ejected electron provokes the emission of characteristic x-rays and Auger electrons from the depleted atom. Although hard collisions are few in number compared to soft collisions, the fractions of the ion's energy that are transferred by these two processes are generally comparable.

When the impact parameter b of the incident ion is much smaller than the atomic radius, the Coulomb-force interaction takes place mainly with the nucleus. In these interactions, 3 types are considered: *elastic Coulomb scattering*, *Non-elastic nuclear reactions*, and *Bremstrahlung*. As said before, for protons and ions, this latter radiative process can be ignored in the considered energy range. Second, the elastic scattering will lead to a change in the trajectory of the incident ion and recoil the target nucleus, thus degrading the lateral penumbral sharpness. Finally, an ion with sufficiently high kinetic energy and an impact parameter less than the nuclear radius may interact inelastically with the nucleus. When one or more individual nucleons are struck, they may be driven out of the nucleus in an *intranuclear cascade* process, collimated strongly in the forward direction. The highly excited nucleus decays from its excited state by emission of so-called *evaporation* particles and γ -rays. This process changes the spatial distribution of the absorbed energy, as some of these neutron and photon emissions are long ranged and carry energy, that would otherwise be deposited as local excitation and ionization, away from the interaction point. While the contribution of the long ranging neutral particles is typically neglected some of these evaporation particles are short ranged and thus contribute to the local dose. These inelastic nuclear processes will be important later in the context of PET and prompt- γ monitoring.

In order to describe the total energy loss of charged particles in matter by Coulomb interactions with the electronic shell of the atoms, the *electronic stopping power* is defined as the expectation value of the rate of energy loss per unit of path length x by a charged particle with kinetic energy E . The stopping power is usually tabulated in units of MeV/cm (ICRU, 2014b). The *mass stopping power* is the stopping power divided by the density ρ of the absorbing material in units of MeV cm²/g. This provides an approximately material-independent quantity, which can easily be adopted e.g. to various temperatures or densities of water.

A formula to calculate the electronic stopping power, i.e. all Coulomb interactions of the incident ion with the electronic shell, is the so-called *Bethe-Equation* (Bethe, 1930)(Attix, 1991, eqn. 8.10):

$$\frac{dE}{\rho dx} = \frac{4\pi n e^4 z_{eff}^2}{m_e c^2 \beta^2} \cdot \left[\ln \left(\frac{2m_e c^2 \beta^2}{I \cdot (1 - \beta^2)} \right) - \beta^2 \right]. \quad (1.1)$$

In eq. (1.1), e and m_e are the electron elemental charge and mass, n the electron density, z_{eff} the effective charge of the incident particle, $\beta = v/c_\gamma$ the speed of

the incident particle given as a fraction of the speed of light in vacuum c_γ , and I the mean excitation potential of the atoms in the absorbing medium. The speed of light is given here as c_γ in order to avoid confusion with the later more often used speed of sound c . Figure 1.1 is showing stopping power values of protons in water for clinically relevant energies.

Figure 1.2a shows a more sophisticated simulation result of such proton interac-

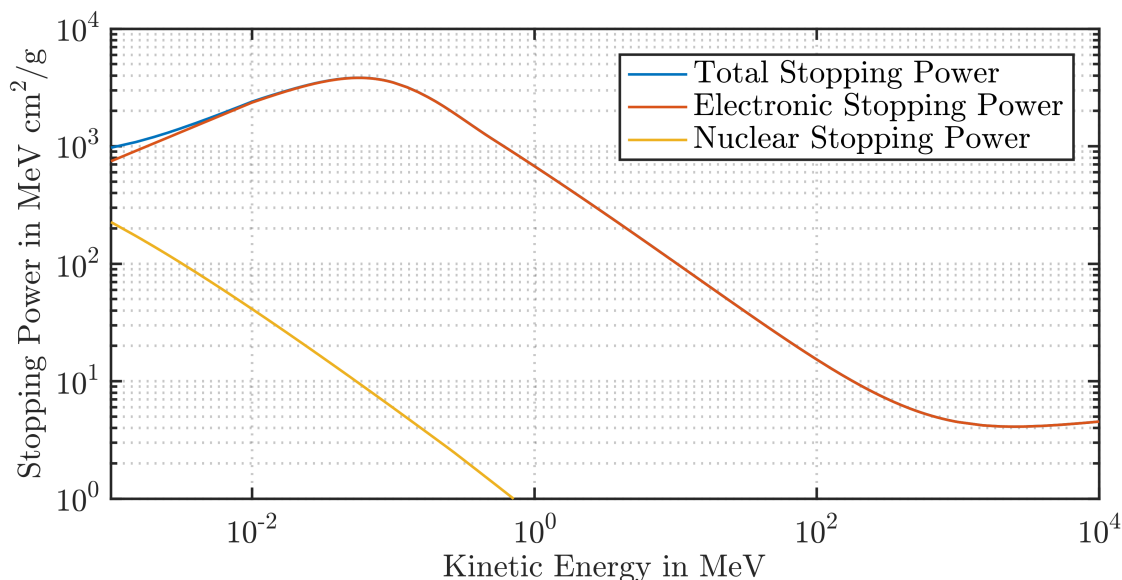


Figure 1.1.: Stopping power of protons in water. Data derived from the NIST PSTAR database (ICRU, 2014b).

tions, including not only the simple energy absorption in one dimension, but also realistic scattering and initial momentum spread of the beam. It shows here the two-dimensional energy distribution and demonstrates the potential superiority of charged particles compared to photons in fig. 1.2b. Compared to the exponentially decreasing depth dose profile of photons after an initial build-up maximum, fig. 1.2b shows the characteristic depth dose profile of protons in water, the so-called *Bragg curve* (Bragg and Kleeman, 1905). The position of highest dose, the *Bragg peak*, depends on the initial mean beam energy and the deviation in energy. Almost no further dose deposition occurs beyond this peak, and only up to one third of the total energy is deposited in the first part, which is called the *plateau region*.

The *range* can be introduced as a practical property of high energetic ion beams following Attix (1991, Chap. 8, sec. IV):

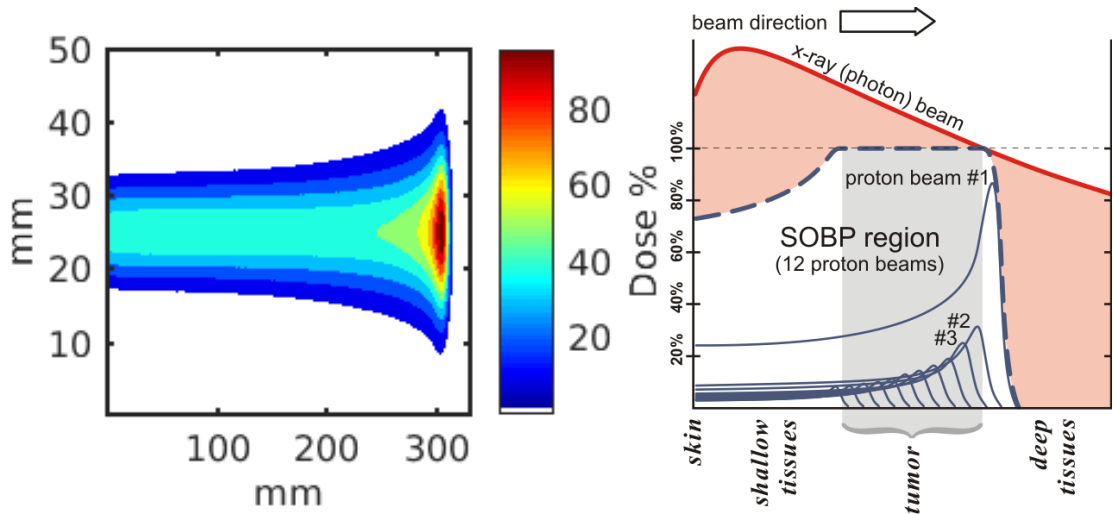
The range \mathfrak{R} of a charged particle of a given type and energy in a given medium is the expectation value of the path length p that [the particle] follows until it comes to rest (discounting thermal motion).

This definition can be written in the so called *continuous slowing down approximation* (CSDA), assuming that the rate of energy loss at every point along the track is equal to the total stopping power. With that assumption, a range can be calculated as:

$$\mathfrak{R}_{CSDA} \equiv \int_0^{E_0} \left(\frac{dE}{\rho dx} \right)^{-1} dE \quad (1.2)$$

This definition of the range would provide the longest distance a particle of a certain energy would pass in a medium given by the lower integration limit of zero in eq. (1.2). A more common use is the so-called R_{80} , where the distance to the point when the dose declined to 80% of the peak value is given. Instead of specifying the point of the maximum dose, the Bragg peak, this 80% falloff position is insensitive to the energy spread of the beam and therefore a better use in range measurements (Gottschalk, 2012). Both values can be extracted by reasonable fits to measured or calculated depth dose profiles and as shown later in section 4.1, our measurements are sensitive to the Bragg Peak.

When protons are used in radiation treatment, this Bragg curve is used to directly



(a) Single energy 2D dose distribution of 220 MeV protons in water.

(b) Comparison of dose profiles from photon and proton irradiation.

Figure 1.2.: Comparison of dose profiles from photon and proton irradiation. a) Simulation of a 200 MeV proton beam stopped in water. b) Several proton beam energies are combined in a *Spread-out Bragg peak SOBP* in order to cover the full tumour volume. In red, a typical depth dose profile of a photon irradiation is given in comparison. (Source for fig. 1.2b: MarkFilipak/WikiCommons, adaption of Fig. 1 in Levin *et al.* (2005).)

target tumours with a better ratio of dose to the tumour with respect to healthy tissue in comparison to photon therapy (Wilson, 1946). One obvious reason is the fact that tissue beyond the Bragg peak receives no dose. Combining several initial beam energies results in the superposition of the single beam energy doses, adding up to the so called *Spread-out Bragg Peak* SOBP (see fig. 1.2b). It is plausible that a better dose conformity than with photons can be achieved even without an improvement by using multiple irradiation angles. The ideal approach in treatment planning is an accurate calculation of necessary initial beam energies and thus ranges in order to deliver dose at the desired depths (Paganetti, 2012). This calculation is also considering the different stopping powers of the tissue relative to water in the beam path and can be optimized, similar to the multi-angle approach with photons described before, for a good ratio of dose in tumour and healthy tissue. However, this calculation of the required energies cannot be done with sufficient accuracy, which will be motivated in the next part.

In order to understand the difficulties in treatment planning one has to know the normal clinical routine, which is executed like this: A patient with tumour diagnosis is scanned with *computer tomography* (CT) and an oncologist contours tumorous regions on these CT images. These images are not only X-ray scans, but most often overlaid with additional informations from *Magnetic-Resonance-Tomography* (MRT) or *Positron-Emission-Tomography* (PET). The smallest visible volume on the image of the tumour is called the *gross target volume GTV*. The volume defined by the oncologist includes a margin additionally to that GTV defining the full volume that needs to be treated. This is called *clinical target volume CTV*. On the basis of this a treatment plan is calculated, which means that based on the required ranges the required energies and machine settings are calculated, taking into account also previously delineated organs at risk and clinical dose prescription. Therefore, the actual stopping power values of the patient's tissue relative to water need to be extracted from the CT images, which are based on Röntgen imaging. This conversion from an electron density measurement to stopping power values of charged particles is not linear and based on empirical values and classification (Durante and Paganetti, 2016). This approach might be improved by a direct measurement of the tissue stopping power ratio, e.g. relative to water with *proton tomography* (Koehler, 1968, Schneider and Pedroni, 1995), and is including the statistical nature of previously mentioned scattering effects blurring the Bragg peak in lateral and longitudinal direction. However, there are additional practical problems occurring on site, e.g. the inaccuracies in patient positioning and moving targets in the lung or the abdomen. Even with the best treatment planning, considerable errors can occur during actual dose delivery when the tissue that is traversed changes in the course of the treatment. This can easily happen due to the weight loss of patients or air cavities in the intestine. It can be seen here that

the Bragg peak becomes a double-edged sword when the highly locally confined dose is accidentally delivered to healthy tissue and missing the CTV. In order to prevent this situation, safety margins are added to the CTV by the treatment plan in the order of 1 mm plus 3% of the range (Paganetti, 2012), forming the *planned target volume PTV*. This margin should cover all errors but is trading the potentially good CTV coverage of charged particles as the PTV is intentionally including healthy tissue. This whole subject is discussed under the term of *range uncertainty* and is currently the biggest technical challenge in proton therapy.

To underline this problem, different possible treatment plans are displayed in fig. 1.3 for a prostate cancer patient taken from Tang *et al.* (2012). The prostate is in an extraordinary delicate position between bladder and rectum, both OAR where over dosage can lead to severe problem or patient's discomfort. The direct angle as shown in fig. 1.3b is not suitable. An erroneous dose delivery for any reasons resulting in an *overshoot*, i.e. the delivery of dose further than the intended position, would give a large dose to an OAR. Small errors induced by the daily changing size of the bladder will lead to incorrect dose deliveries. This becomes even more severe when considering that the largest range needs to apply the full dose. Lower energies will stack on the pedestal part of this highest energy contribution, as indicated in fig. 1.2b. Mistakes at this furthest position cannot

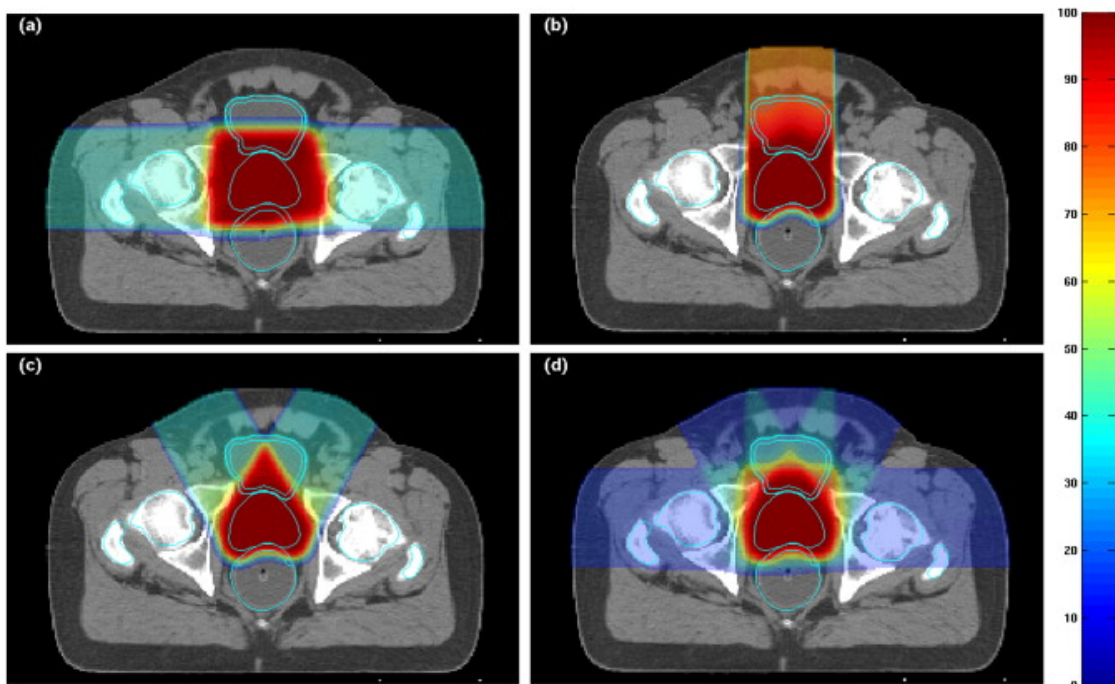


Figure 1.3.: Different irradiation options for a prostate cancer patient, taken from Tang *et al.* (2012).

be compensated by later contributions. Hence, the case shown in fig. 1.3a is the currently preferred case, irradiating lateral anterior through the hip bones. Here the decision has been made in favour of bladder and rectum, such that possible range error would overlap. However, the highly absorbing bones are suffering, and metallic hip replacements might even prohibit these configurations. The ideal case would be the one shown in fig. 1.3c and d, but are currently limited and therefore avoided due to the yet unsolved problem of range uncertainty.

The computation techniques applied in treatment planning are limited as challenges such as moving targets in the lower abdomen on a large scale cannot be perfectly anticipated by pre-calculations. Furthermore, the volume of the tumour shrinks during the treatment in a barely predictable manner. Hence, along with improved in-room morphological imaging, experimental online techniques are clearly needed to monitor the dose delivery during or after the irradiation (Knopf and Lomax, 2013, Mijnheer *et al.*, 2013). So far, the potential of highly confined dose delivery by charged particles, mainly protons, is not fully exploited due to the range uncertainties (Durante and Paganetti, 2016). At the current clinical practice no actual online verification method is available in order to ensure the correct delivery with sufficient, absolute certainty, which would be a correct determination of the range in tissue with an uncertainty of ± 1 mm, enabling to safely reduce the current margin in the PTV. One obvious problem is that in order to measure delivered dose, a part of the beam needs to somehow interact with a detector, e.g. a small solid state detector as in Hoesl *et al.* (2016). If the direct beam is used for such a measurement, the energy loss and possible distortion in such a detector needs to be considered or would need to be measured in the PTV, but this tissue needs to be irradiated, not the detector. Possible approaches therefore must rely on the measurement of *secondary radiation*, i.e. long range radiation induced by the high energetic primary beam. The field of *in-vivo range verification* is facing this challenge of measuring and evaluating this secondary radiation. There are two major techniques relying on nuclear reactions initiated by high energetic charged particles, *Positron-Emission-Tomography* (PET) (Bennett *et al.*, 1975) and *Prompt Gamma Monitoring* (PG) (Min *et al.*, 2006, Polf *et al.*, 2009a), which will be briefly presented here.

PET relies on the production of positron emitters, the anti-particle of the electron. These two annihilate after a collision producing at least two gamma ray photons. From the consideration of the conservation of energy, linear and angular momentum, in most of the cases two photons with the rest energy of an electron (0.511 MeV) are emitted in opposite directions. PET scanners are therefore gamma detectors typically positioned on a ring around the patient trying to detect coincidental photons (Parodi, 2016). With a reconstruction process using the *line of response* LOR between the two detectors detecting such a coincidental pho-

ton pair, it is possible to retrieve the location where the annihilation, and closely thereby the positron emission, occurred. Positron emitting radionuclides are also produced during radiation treatment in the interaction of the ions with the tissue (Durante and Paganetti, 2016). Typical positron emitters created in tissue are e.g. ^{15}O , or ^{11}C with half-lives of approximately 2-20 minutes (España Palomares *et al.*, 2011). Hence, a PET scan during or closely following radiation treatment will show the positron emission from the irradiated tissue, allowing to reconstruct a range in tissue (Bennett and Archambeau, 1977, Litzenberg *et al.*, 1999, Parodi *et al.*, 2007, Yamaya *et al.*, 2011, Tashima *et al.*, 2012).

Prompt- γ verification is a collective term for many different monitoring approaches relying on the measurement of prompt- γ radiation. The atomic nuclei of the target material are excited by the energetic particles through nuclear reactions and energy is emitted in the form of γ photons (Kozlovsky *et al.*, 2002). Measuring the energy of those prompt- γ photons will reveal the nuclear excitation levels of the target materials, but also spatial information can be retrieved and hence be used in in-vivo range verification (Min *et al.*, 2006, Polf *et al.*, 2009b, Moteabbed *et al.*, 2011, Verburg *et al.*, 2012). The most practical approach is a slit camera detector (Smeets *et al.*, 2012). Here, a massive tungsten slit is used to project the signal during irradiation onto a detector scintillator array, similar to a pin hole camera. This concept has been recently deployed in first clinical trials (Richter *et al.*, 2017, Xie *et al.*, 2017). Another approach to gain spatial information without mechanical collimation is the observation of an induced Compton scattering process. This *Compton camera* consists of a photon scatterer, sometimes combined with an electron tracker, and a photon detector behind it (Roellinghoff *et al.*, 2011, Thirolf *et al.*, 2014). By detecting the scattering angle and the remaining energy of the photon, the kinematics of the scattering process is used to reconstruct a *Compton cone* as a possible origin of the prompt- γ . Similar to the PET reconstruction, overlaying many processes results in a probable region of the irradiation (Draeger *et al.*, 2018).

These two nuclear imaging techniques have one disadvantage in common. As they rely on the production of the described particles, certain energy in the primary beam is needed to overcome the Coulomb barrier. This means that at the Bragg peak itself not enough energy is left in the primary beam in order to initiate the required nuclear reactions. This results in intensity profiles of the γ -emission which are not directly correlated to the dose profile and therefore need to be properly modelled via analytical calculations or more complex Monte Carlo simulations. Both methods rely on complicated nuclear physics measurements including many components for data acquisition and have high computational demands. This criticism is intended to motivate the following discussion of an alternative range verification method introduced in the next section. Although these two nuclear-based

monitoring methods have the described disadvantages, they offer the possibility to be used on any site of the patient and still offer the assessment of ranges with a resolution down to 1 mm, while using a reasonable amount of dose, which is still a critical point for the alternative method presented in the next section.

1.2. Ionoacoustics as a new Approach to in-vivo Range Verification

This thesis is dedicated to *ionoacoustics*¹, another in-vivo technique that relies on the detection of a pressure wave following the dose deposition process, which is correlated to the heating of the irradiated region. Ionoacoustics is derived from the more general phenomenon *Thermoacoustics*, but in this case the heat is obtained from the ion dose. To be noted is the active field of *Photo- or Optoacoustics*, where the heat is generated by a high intensity laser pulse and many basic concepts for this thesis are taken from there.

The first mentioning of the *photoacoustic effect* was given by Bell (1880), describing a *pure musical tone* of a modulated light beam in a gas volume. From there on, the generation of acoustics in gases or fluids has been studied in several fields (Askaryan, 1957). Ionoacoustics gained interest as a possible implementation of neutrino detection by installing wide-spread detector arrays in the ocean. First studies were made in 1979 with highly energetic proton beams stopped in the beam dump filled with water (Askaryan *et al.*, 1979, Sulak *et al.*, 1979) and were continued until now (De Bonis, 2008, Lahmann *et al.*, 2015).

As described in more details later in section 2.1, a pulsed proton beam stopped in matter produces a temperature increase. This stopping of protons can be considered as instantaneous compared to the progression of sound waves, which travel with roughly 1.5 mm/ μ s in water. This means that the temperature differences dissolve adiabatically in a pressure wave. Considering the proper experimental circumstances described in chapter 5, the location of energy depositions can then be reconstructed. The goal of this thesis is to provide a full understanding of the underlying process and a list of evaluation techniques and experimental results that will show the high potential of ionoacoustics. Compared to the known nuclear techniques, the detector is much cheaper and simpler. For optimal geometries, the range of protons can be read directly from an oscilloscope screen. Additionally, as ultrasound is an everyday technique in today's medicine, ionoacoustics can resort to decades of development and experiences in ultrasound imaging and detector

¹In Jones *et al.* (2014), the term *Protoacoustics* is introduced. In foresight of the measurements with heavy ions at GSI, see chapter 5, the more general term ionoacoustics is preferred in this work. Furthermore, in plasma physics the *ion acoustic wave* is a type of longitudinal oscillation of ions and electrons in a plasma mimicking the behaviour of an acoustic wave.

equipment involved.

First studies for particle treatment were done in the beginning of the 1990s in Japan. Here, the high occurrence of hepatic cancer and the re-use of an experimental synchrotron facility enabled the first measurement of ionoacoustic signals during treatment in a patient in Tsukuba (Tada *et al.*, 1991, Hayakawa *et al.*, 1995), which is shown in fig. 1.4. This field has then been intensively reviewed in simulations and measurements by Albul *et al.* (2004, 2005) and Terunuma *et al.* (2007), coining the description of different features of the signal used later on. At the treatment centre in Tsukuba, the beam delivered to patients was *passively scattered*, where a broad dose delivery is achieved by placing scattering and energy degrading material into the beam path. A patient specific collimator is ensuring the correct lateral irradiation of the tumour, while the axial dimension is typically covered by a *modulator wheel* and *compensator*. With such a wheel, the proton range is decreased with increasing absorbing material arranged by the angle on a disc or wheel, delivering a certain extension and distal position of a SOBP, which is then further conformed to the tumour distal shape with a patient-specific compensator. The dose distributions generated with passive scattering techniques are rather broad and hence not well suited for ionoacoustics. These passively scattering techniques are nowadays replaced by *active scattering*, commonly known as

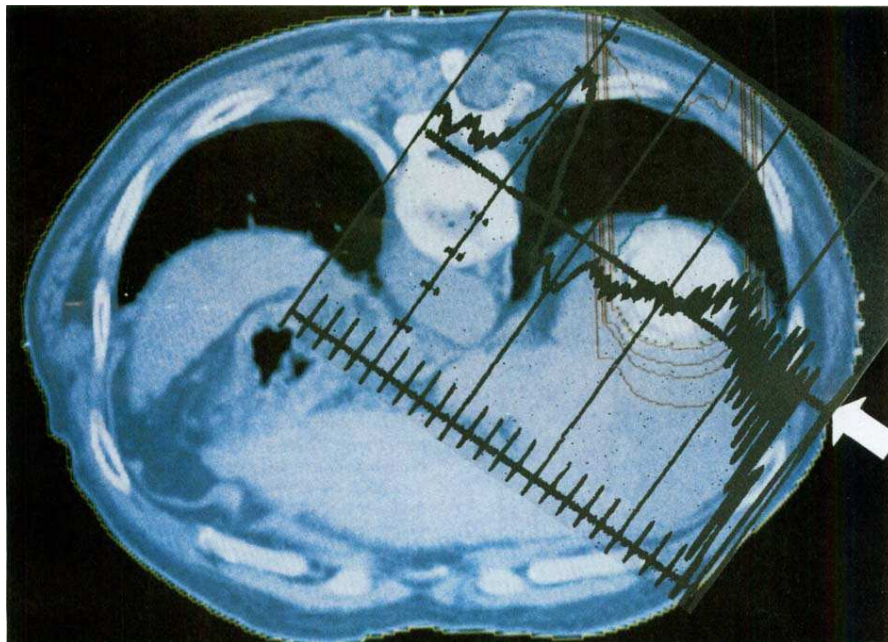


Figure 1.4.: Treatment plan of a hepatic cancer patient with superimposed acoustic pulse, taken from Hayakawa *et al.* (1995). The arrow is indicating the position of the used hydrophone.

pencil beam or *spot scanning*. Here, the beam is deflected with dipole magnets to cover the tumour in lateral directions, similar to old TV monitors, while the beam energy (hence Bragg peak depth) can be adjusted at the accelerator level or immediately after beam extraction. This spot scanning technique has several advantages, e.g. no patient specific scatterer has to be produced, which is time-consuming, while the passively scattered beam produces a considerable neutron background dose and the irradiated components are activated during treatment, which requires special disposal. Furthermore, with active scanning an online adaptation to moving targets or multiple irradiation angles and intensities in IMPT is possible. These advanced techniques in active scanning are considerably challenging, and passive scattering with compensatory smearing and gating of the particle beam are reasonably used possibilities for the treatment of moving targets today. However, the achieved spot sizes with active scanning are advantageous for ionoacoustics.

Despite the promising results reported in the 1990s by the mentioned Japanese group with passive beam delivery, by the mid of the 2000s, the interest in ionoacoustics vanished, since without spot scanning the generation of pressure was too low and unspecific. Although the temporal requirements were met at the synchrotron in Tsukuba, meaningful pressure amplitudes were not achieved with broad radiation fields. Also German studies conducted by Alexander Peiffer and co-workers at GSI, the *Gesellschaft für Schwerionenforschung* in Darmstadt, came to the rather pessimistic conclusion in 1998 that the current instrumentation at medical facilities are not sufficient, but the effect could be used for high intensity particle beam characterization (Peiffer *et al.*, 1995, Peiffer and Köhler, 1997, Peiffer, 1998). Here at GSI, the spot scanning was already implemented in the 90's (Haberer *et al.*, 1993), but only long pulses (slow extraction) were used in radiation treatment². So, contrary to the Japanese studies, this accelerator fulfilled the spatial requirements, but not the temporal needs. Notably, at CERN, the acoustic detections of high energetic protons hitting the beam line tube has been investigated (Redaelli *et al.*, 2005, Deboy *et al.*, 2011, 2013). This has been tried in order to prevent serious damage to the beam line, but had also been discontinued eventually.

To give a rule of thumb, in ideal conditions a dose of 1 Gy can produce an initial pressure of roughly 200 Pa. Ideal condition for a 200 MeV proton beam, that is about 30 cm range in water, would be a pulse width below 10 μ s delivering around 2 pC per pulse. These numbers will be explained in more detail in section 2.1. The currently most used types of proton accelerator in radiation treatment facili-

²In the work of Peiffer and co-workers, experiments were also done with the bunched, short pulses for demonstrating purposes, but as this beam modality was not considered for radiation treatment, the conclusion was drawn against a medical application.

ties are isochronous cyclotrons. Those types of particles accelerators are not able to fulfil the stated requirements without additional modifications, as described in chapter 3.

However, the simplicity of this method was intriguing. Newer simulation studies were published starting with Jones *et al.* (2014) and Alsanea *et al.* (2015). These theoretical studies were then followed by experimental studies at low energies with a linear electrostatic accelerator in Assmann *et al.* (2015), and at clinical energies with a specially adapted cyclotron in Jones *et al.* (2015), and most recently at a synchrocyclotron in Lehrack *et al.* (2017), demonstrating the potential of a very precise and accurate determination of the Bragg peak position. All those publications used the recent advancement of the sampling and remote control techniques, ultrasound equipment as well as sophisticated imaging modalities developed in the past decade. Furthermore, the development of medical proton accelerators over the last decade were in favour of ionoacoustics, which includes the clinical implementation of the pencil beam scanning technique and recently the installation of synchrocyclotrons offering inherently short and intense pulses. Currently 18 of these machines are sold and planned in medical facilities offering almost ideal conditions for ionoacoustics, hence interesting advancement can be expected in the near future. This progress has been reviewed in Parodi and Assmann (2015) in the context of medical applications.

This thesis is focused on the generation of ultrasound via charged particle, as the spatial advantage of the Bragg peak provides the production of ultrasound waves almost naturally. With high energetic photons, the exponentially decreasing depth dose profile is not expected to produce enough temperature increase in order to detect a measurable ultrasound signal. Nevertheless, by introducing specific markers or highly absorbing materials, ultrasound can also be generated by the absorption of x-rays in these markers, and can be detected and evaluated similar to the presented methods (Bowen *et al.*, 1991, Xiang *et al.*, 2013). However, the production of x-ray induced ultrasound has not been a part of this thesis and is not further discussed.

1.3. Thesis Outline

A detailed description of the underlying theory of ionoacoustics is given in chapter 2. This includes a derivation of the general acoustic wave equation and its solution for the corresponding detector response. Then a collection of useful simulations is concluding this chapter.

In chapter 3, the tools and methods developed and applied in this thesis are explained in detail. This includes the used hydrophones along with a summary of particle accelerators and their specific properties in the context of ionoacoustics. Evaluation techniques for ionoacoustic data are presented in chapter 4. Several methods have been developed in the framework of this thesis depending on explicit experimental situations. This chapter concludes with a comparison of the most promising evaluation techniques applied to several measured ionoacoustic data from multiple beam times at the *Maier-Leibnitz-Laboratorium* (MLL) Tandem accelerator in Garching.

After the general presentation of range measurements with ionoacoustics, sophisticated conducted measurements and results are presented in chapter 5, which are based on the ionoacoustic range determination with 20 MeV protons. High energy particle beam experiments with 230 MeV protons, 200 MeV/u ^{12}C , and 200 MeV/u ^{124}Xe and ^{238}U are then following, the later exploring the possibility of ionoacoustics as a possible mechanism for high energetic particle detection. Additionally, more experimental data is given in appendix A and appendix B.

The thesis is then concluded in chapter 6 with a discussion of general topics connecting the results presented in chapter 5, and an outlook.

2. Theoretical Concepts of Ionoacoustics

This time it was right, it would work, and no one would have to get nailed to anything.

Sadly, however, before she could get to a phone to tell anyone about it, a terrible stupid catastrophe occurred, and the idea was lost for ever.

This is not her story.

But it is the story of that terrible stupid catastrophe and some of its consequences.

DOUGLAS ADAMS in the prologue of
The Hitchhiker's Guide to the Galaxy

2.1. Deriving Ionoacoustics from Photoacoustics

The following derivation is based on Wang and Wu (2007), Treeby and Cox (2010), Cox *et al.* (2007), and Feynman *et al.* (1977, Chap. 47). Ionoacoustics is a special application of Thermoacoustics, where any kind of pulsed temperature gradient produces a pressure wave. Most of these concepts have been used in another specific application, Photoacoustics or Optoacoustics, where the temperature gradient is produced by a high-intensity, short pulsed laser excitation. To some extent, this is similar to the ionic excitation process.

For the following discussion, two streams of thoughts are brought together: *How is the initial pressure generated?* and *What is the dynamics of that pressure?*

An overview on the used theoretical parameters and their notation is given in fig. 2.1.

2.1.1. General Acoustic Wave Equation

When an acoustic wave passes through a compressible medium, the following first order partial differential equations can be used to describe momentum conservation (eq. (2.1)), mass conservation (eq. (2.2)) and the correlation of pressure and density (eq. (2.3)):

$$\partial_t \mathbf{u} = -\frac{1}{\rho_0} \nabla p, \quad (2.1)$$

$$\rho_0 \nabla \mathbf{u} = -\partial_t \rho, \quad (2.2)$$

$$p = c^2 \rho. \quad (2.3)$$

Here \mathbf{u} is the acoustic particle velocity, p is the acoustic pressure, ρ and ρ_0 the dynamic and ambient density, respectively, and c the speed of sound. Those equations can be coupled to a second order wave equation without a source term by calculating the spatial gradient of eq. (2.1) and the time derivative of eq. (2.2), interchanging spatial and temporal differentiation, and using eq. (2.3):

$$\nabla^2 p(\mathbf{r}, t) = \frac{1}{c^2} \frac{\partial^2}{\partial t^2} p(\mathbf{r}, t). \quad (2.4)$$

This describes only the propagation of acoustic waves, so source terms need to be included. Here, the expansion following a heat input is considered, i.e. additional energy is added. This can be implemented as a linear mass source to the equation for mass conservation eq. (2.2):

$$\partial_t \rho = -\rho_0 \nabla \mathbf{u} + \frac{\beta}{C_p} \mathcal{H}. \quad (2.5)$$

Here, β is the volume thermal expansion coefficient, C_p the constant pressure specific heat capacity, and \mathcal{H} the injection of heat per unit volume and time. This will lead to the general wave equation with heat source term:

$$\left(\nabla^2 - \frac{1}{c^2} \frac{\partial^2}{\partial t^2}\right) p(\mathbf{r}, t) = -\frac{\beta}{C_p} \partial_t \mathcal{H}. \quad (2.6)$$

A deeper analysis of the acoustic source term in the context of ionoacoustics is given in section 2.1.4.

2.1.2. Spherical Wave Solution

Before the Green function approach can be used in order to derive a general solution for a specific detector point, it needs to be verified that spherical waves in the form of:

$$p(\mathbf{r}, t) = \frac{A}{r} e^{i(\mathbf{k}\mathbf{r} \pm \omega t)}, \quad (2.7)$$

are a valid solution to eq. (2.4). Here, \mathbf{k} is the wave number and ω the angular frequency. For that, the Laplace operator in spherical coordinates is used:

$$\nabla^2 = \frac{1}{r^2} \partial_r (r^2 \partial_r) + \frac{1}{r^2} \nabla_{\phi\theta}^2, \quad (2.8)$$

$$\nabla_{\phi\theta}^2 = \frac{1}{\sin\theta} \partial_\theta (\sin\theta \partial_\theta) + \frac{1}{\sin^2\theta} \partial_\phi^2 \stackrel{!}{=} 0. \quad (2.9)$$

It can be assumed that the solution is spherical symmetric, hence the solution needs to satisfy:

$$\left(\frac{1}{r^2} \partial_r (r^2 \partial_r) - \frac{1}{c^2} \partial_t^2\right) p(r, t) \stackrel{!}{=} 0 \quad (2.10)$$

In the following, the spatial and temporal part is studied separately in eq. 2.11 and eq. 2.12, respectively. Inserting eq. (2.7) into eq. (2.10) yields:

$$\frac{1}{r^2} \partial_r (r^2 \partial_r) \frac{A}{r} e^{i(kr \pm \omega t)} = -k^2 \frac{A}{r} e^{i(kr \pm \omega t)} \quad (2.11)$$

$$\frac{1}{c^2} \partial_t^2 \frac{A}{r} e^{i(kr \pm \omega t)} = \frac{-A\omega^2}{rc^2} e^{i(kr \pm \omega t)} \quad (2.12)$$

$$\Rightarrow \frac{A}{r} e^{i(kr \pm \omega t)} \left(\frac{\omega^2}{c^2} - k^2\right) \stackrel{!}{=} 0, \quad (2.13)$$

bringing us down to the well known dispersion relation $\omega = kc$. It is to be noted that the pressure amplitude is a *field* or *root-power quantity*, as seen here with a $1/r$ dependency. This is notably different than the *acoustic intensity*, which is defined as the power carried by a sound wave per unit area in a direction perpendicular to that area, thus decreasing with $1/r^2$.

2.1.3. Green's Function Approach

The Green's function approach can be applied to eq. (2.6), where the right-hand source term is simplified to $q(\mathbf{r}', t')$. On the basis of the reciprocity relation, Green's function $G(\mathbf{r}, t; \mathbf{r}', t')$ satisfies the following equation:

$$\nabla'^2 G(\mathbf{r}, t; \mathbf{r}', t') - \frac{1}{c^2} \frac{\partial^2 G(\mathbf{r}, t; \mathbf{r}', t')}{\partial t'^2} = -\delta(\mathbf{r} - \mathbf{r}') \delta(t - t'). \quad (2.14)$$

Multiplying eq. (2.6) with G and eq. (2.14) with p , subtracting both, and calculating the volume integral over \mathbf{r}' in the volume of interest V' and also over t' from 0 to t^+ , the obtained solution is, rigorously simplified:

$$\begin{aligned} p = & \underbrace{\int_0^{t^+} dt \int_{V'} d\mathbf{r}' Gq}_{\text{I. source}} + \\ & \underbrace{\int_0^{t^+} dt \int_{V'} d\mathbf{r}' (G\nabla'^2 p - p\nabla'^2 G)}_{\text{II. boundary}} + \\ & \underbrace{\int_0^{t^+} dt \int_{V'} d\mathbf{r}' \frac{1}{c^2} (p\partial_t^2 G - G\partial_t^2 p)}_{\text{III. initial}}. \end{aligned} \quad (2.15)$$

Equation (2.15) can be separated in 3 parts depending on I. source, II. boundary, and III. initial or pre-existing conditions. It will be shown in the following that part II and III can be neglected.

Considering part II Green's theorem is used, providing a relationship for 2 functions L and M defined over a region including D which is bounded by ∂D :

$$\oint_{\partial D} Ldx + Mdy = \iint_D \partial_x M - \partial_y L dx dy, \quad (2.16)$$

to simplify part II in eq. (2.15) to:

$$\int_0^{t^+} dt \int_S d\mathbf{S} G\nabla p - p\nabla G. \quad (2.17)$$

Here, \mathbf{S} is the surface enclosing V' , corresponding to D and ∂D . This part is therefore dependent on the boundary conditions. Infinite space can be assumed later in order to neglect this part.

For part III in eq. (2.15), the time integral can be calculated, thus resulting in:

$$\frac{1}{c^2} \int_{V'} d\mathbf{r}' [p\partial_t G - G\partial_t p]_0^{t^+}. \quad (2.18)$$

t^+ can be chosen large, so that equilibrium conditions are reached, which means:

$$p(\mathbf{r}', t^+) = 0, \quad (2.19)$$

$$\partial_{t'} p(\mathbf{r}', t')|_{t'=t^+} = 0. \quad (2.20)$$

Part III in eq. (2.15) can then be written as:

$$\frac{1}{c^2} \int_{V'} d\mathbf{r}' p|_{t'=0} \partial_{t'} G|_{t'=0} - G|_{t'=0} \partial_{t'} p|_{t'=0}. \quad (2.21)$$

Equilibrium conditions can be chosen as initial condition, allowing to drop this part as well.

From eq. (2.14), the Green function is starting with (Wang and Wu, 2007, Example 12.5):

$$G(\mathbf{r}, t; \mathbf{r}', t') = \frac{\delta\left(t - t' - \frac{|\mathbf{r} - \mathbf{r}'|}{c}\right)}{4\pi |\mathbf{r} - \mathbf{r}'|}. \quad (2.22)$$

By substituting eq. (2.22) into eq. (2.15), infinite time and no boundaries are assumed as discussed above. The delta function in eq. (2.22) is used to evaluate the integral over t' and the pressure response at a specific detector point in space \mathbf{r} caused by an arbitrary source at \mathbf{r}' is received:

$$p(\mathbf{r}, t) = \frac{\beta}{4\pi C_p} \frac{\partial}{\partial t} \int d\mathbf{r}' \frac{1}{|\mathbf{r} - \mathbf{r}'|} \mathcal{H}\left(\mathbf{r}', t - \frac{|\mathbf{r} - \mathbf{r}'|}{c}\right). \quad (2.23)$$

Equation (2.23) can be simplified to the time derivative of the sum of all heat contribution located on a sphere expanding around the point of detection. Considering specific heat distributions later on in section 2.3.4, this sphere can be seen as a *scanning sphere*, as it scans through the heat contributions with increasing time. The sampling time will determine the *thickness* of the surface of this scanning sphere. For a large detector, different points have to be summed up, which naturally introduces a phase between these detection points and directivity, once several centres of scanning spheres are considered.

2.1.4. Initial Pressure Derivation

The start is a simple thermodynamic law:

$$\frac{dV}{V} = -\kappa \delta p + \beta \delta T, \quad (2.24)$$

with κ being the *isothermal compressibility coefficient* and β being the *volume expansion coefficient*. Equation (2.24) is a derivation of Boyle's law. For Thermoacoustics to work, the volume expansion needs to be negligible. For that the

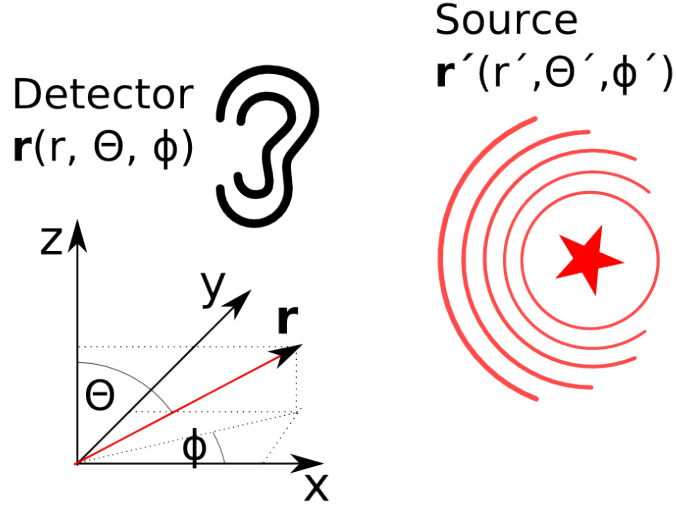


Figure 2.1.: Overview of theoretical parameters.

energy input is required to be instantaneous, so that any kind of thermal diffusion can be neglected. For that, the *thermal relaxation time* is considered to be:

$$\tau_{thermal} = \frac{d_c^2}{\alpha_{thermal}}, \quad (2.25)$$

where d_c is the *characteristic dimension*, i.e. the heated volume, and $\alpha_{thermal}$ the *thermal diffusivity*. The characteristic dimension is thereby the length observed by the detector in the field of view through the heated volume. For water at 25 °C, $\alpha_{thermal} = 0.15 \text{ mm}^2/\text{s}$. Any heating process which is faster than this time is called *thermally confined*. Here, only adiabatic processes are considered, hence eq. (2.24) becomes:

$$\delta p = \frac{\beta}{\kappa} \delta T. \quad (2.26)$$

Equation (2.26) can be written in terms of a change in energy with the help of the *specific heat capacity* C_V :

$$\delta p = \frac{\beta \eta}{\kappa C_V m} \delta E. \quad (2.27)$$

Here, η is the efficiency for the conversion of energy into heat. For ionoacoustic excitations, this is expected to be close to 1 and for simplicity, this is assumed for the rest of this thesis. It is also to be noted that here already the necessity of a pulsed beam for any kind of Thermoacoustics is visible, i.e. a change in energy over time.

The focus here is on *Ionoacoustics*, energy input is considered to be from high

energy particles and thereby their dose in matter is of importance. The dose is defined directly as the amount of energy deposited by ionizing radiation per unit mass. The following definition of the isothermal compressibility coefficient is considered:

$$\kappa = -\frac{1}{V} \left(\frac{\partial V}{\partial p} \right)_T = \frac{C_p}{\rho c^2 C_v}, \quad (2.28)$$

and eq. (2.26) can be rewritten in terms of dose D :

$$\delta p = \frac{\beta}{\kappa C_V} \delta D = \Gamma \rho \delta D = \frac{\beta \rho c^2}{C_p} \delta D. \quad (2.29)$$

C_V and C_p are the isochoric and isobaric heat capacities, respectively. The *Grüneisen-parameter* Γ is discussed later.

In thermal confinement the *heating function* $\mathcal{H}(\mathbf{r}, t)$ is introduced as the thermal energy converted per unit volume and per unit time:

$$\rho C_V \frac{\partial T(\mathbf{r}, t)}{\partial t} = \mathcal{H}(\mathbf{r}, t). \quad (2.30)$$

It can easily be justified that this heating function can be written as a multiplication of a spatial and a temporal part from the fact that the used target material will always behave as described independent from the time profile, i.e. will later protons be as continuously slowed down as the first ones. Here it is assumed that no significant changes in the target material occur, which is justified for normal liquids and gases. For crystalline matter local changes due to the ionizing tracks are expected. Nevertheless, with the particle fluence used in the presented experiments, the overlapping of such tracks is unlikely, and the experiments were all conducted in water. A description of a source term is derived, hence the solution of eq. (2.6) in eq. (2.23) is found to be:

$$p(\mathbf{r}, t) = \frac{\beta}{4\pi C_p} \frac{\partial}{\partial t} \int d\mathbf{r}' \frac{\mathcal{H}_s(\mathbf{r}')}{|\mathbf{r} - \mathbf{r}'|} \mathcal{H}_t \left(t - \frac{|\mathbf{r} - \mathbf{r}'|}{c} \right). \quad (2.31)$$

Now, a second, very important time scale is introduced: the *stress relaxation time*:

$$\tau_s = \frac{d_c}{c}. \quad (2.32)$$

An energy input is considered *stress confined*, when the time for heating up the characteristic dimension is shorter than the time of acoustic signals passing through this length. Phenomenologically, any excitation with a pulse width shorter than the stress relaxation time can be considered instantaneously, which reduces this problem to well studied *initial value problems*. Nevertheless, this does not mean

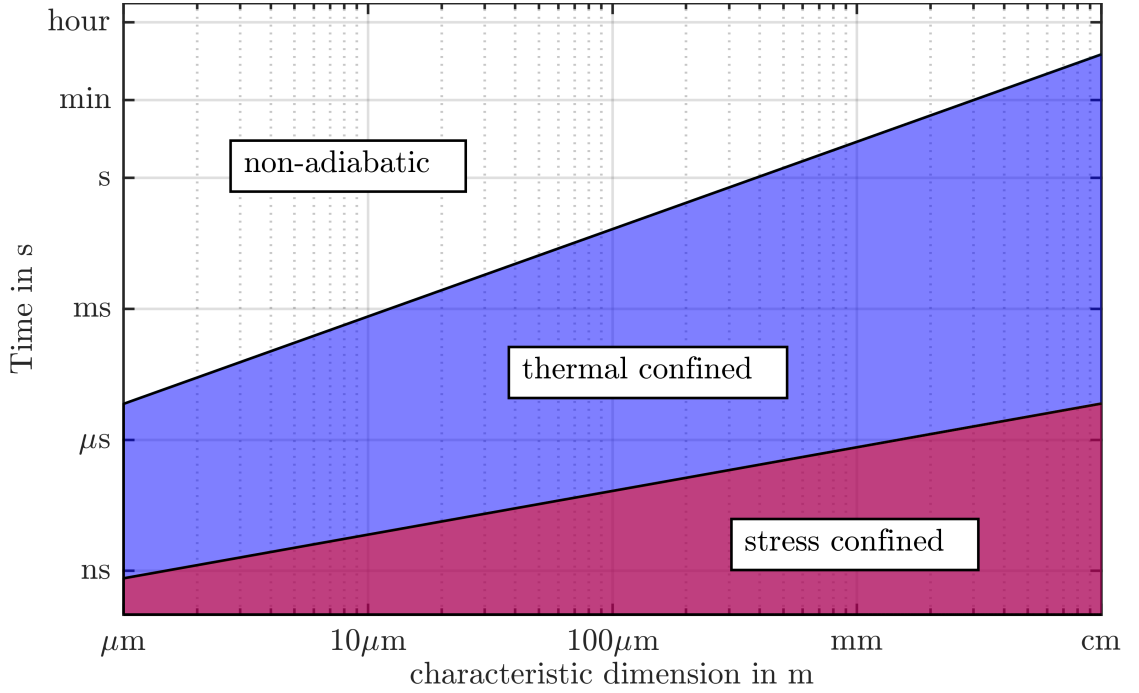


Figure 2.2.: Stress and Thermal confinement shown as a function of heating pulse length and diameter of heated area.

that the signal from a stress confined irradiation only contains the spatial form of a unipolar pulse, since the received signal is also a differentiation in time. Stress confinement means that the contribution of the temporal function can not be distinguished any more, as any pulse length shorter is “covered“ by the broader spatial contribution. Furthermore, it does not mean that the pulse shape, specifically the rising time, can be neglected, as very well demonstrated in Jones *et al.* (2016a, Figure 4). Here, the difference in pressure amplitude from rectangular and Gaussian shaped pulses are compared. While the step function rise shows a constant pressure amplitude in stress confinement, the amplitude even decreases for Gaussian pulses. We will come back to this discussing the question where the exact source of the ultrasound signal is.

If the temporal heating function is considered to be in *stress confinement*, eq. (2.31) can be simplified to

$$p(\mathbf{r}, t) = \frac{\beta}{4\pi C_p} \frac{\partial}{\partial t} \frac{1}{ct} \int d\mathbf{r}' \mathcal{H}_s(\mathbf{r}') \delta\left(t - \frac{|\mathbf{r} - \mathbf{r}'|}{c}\right). \quad (2.33)$$

The dimensionless Grüneisen parameter can be used to quantify the transfer from heat to pressure:

$$\Gamma = V \cdot \left(\frac{\partial p}{\partial E} \right) = \frac{\beta}{\kappa \rho C_V} = \frac{\beta c^2}{C_p}. \quad (2.34)$$

With this, the initial pressure can be written as

$$p_o(\mathbf{r}) = \Gamma \mathcal{H}_s(\mathbf{r}'), \quad (2.35)$$

which simplifies eq. (2.33), as it provides the direct correlation between the heating input from any kind of pulsed source to the related pressure wave:

$$p(\mathbf{r}, t) = \frac{1}{4\pi c^2} \frac{\partial}{\partial t} \frac{1}{ct} \int d\mathbf{r}' p_o(\mathbf{r}') \delta\left(t - \frac{|\mathbf{r} - \mathbf{r}'|}{c}\right). \quad (2.36)$$

The Grüneisen parameter in water can be estimated following Wang and Wu (2007):

$$\Gamma_w(T) = 0.0043 + 0.0053T, \quad (2.37)$$

with the temperature T in °C. As an example, the initial pressure from 1 Gy in water with a temperature of 37°C excited by a short pulse can be estimated:

$$p_o = \Gamma_w(37^\circ\text{C}) \rho_w(37^\circ\text{C}) D = 0.2 \cdot 993.33 \text{ kgm}^{-3} \cdot 1 \text{ J/kg} = 198.6 \text{ Pa}. \quad (2.38)$$

This result and also this estimation has to be interpreted with care, as an almost unrealistic energy confinement in space *and* time is assumed. This means in order to achieve this pressure at the source, an infinitesimal small volume with ideally sharp boundaries is assumed, excited by an infinitesimal short pulse. While the requirement of a short pulse can be fulfilled, demonstrated later in chapter 5, the sharp spatial boundaries will be challenging and is therefore only an estimation of the upper limit. Keeping also in mind that this is the maximum value at the source and the pressure amplitude will drop with at least $1/r$, this is a dynamic pressure level which is challenging to detect with standard ultrasound devices. For comparison, clinical ultrasound devices are able to produce several MPa of pressure amplitude, exceeding the static atmospheric pressure of 0.1 MPa. As it will be shown later in chapter 5, the measurement of ionoacoustic signals requires high averaging and amplification. However, in order to determine the dose, an absolute measurement of the pressure would be necessary.

Equation (2.33) can be further interpreted in terms of convoluted functions, as shown in Jones *et al.* (2016a, Appendix B). The temporal heating function can be written as a convolution of itself with a Dirac-delta function, the neutral element of the convolution:

$$\mathcal{H}_t(t) = \int_{-\infty}^{\infty} \mathcal{H}_t(t - \tau) \delta(\tau) d\tau \equiv \mathcal{H}_t(t) \otimes \delta(t). \quad (2.39)$$

This can be used to rewrite eq. (2.31) as:

$$p(\mathbf{r}, t) = \partial_t \left[\mathcal{H}_t \otimes \underbrace{\frac{\beta}{4\pi C_p} \left(\int d\mathbf{r}' \frac{1}{|\mathbf{r} - \mathbf{r}'|} \mathcal{H}_s \delta(t') \right) \Big|_{t'=t-\frac{|\mathbf{r}-\mathbf{r}'|}{c}}}_{P_\delta} \right]. \quad (2.40)$$

Here, the spatial part is summarized as P_δ and can be interpreted as the generic spatial signal which is then „blurred“ by the temporal function. Furthermore, when applying a Dirac-delta function as temporal heating function, the pressure signal reduces again to the time derivative of the volume integral, as discussed above in the context of stress confinement.

$$p(\mathbf{r}, t) = \partial_t [\mathcal{H}_t \otimes P_\delta] = \partial_t \mathcal{H}_t \otimes P_\delta = \mathcal{H}_t \otimes \partial_t P_\delta. \quad (2.41)$$

This interpretation is following the derivation in Jones *et al.* (2016a) and it can be useful in some applications. One obvious use is the realization that the temporal and spatial heating functions are independent from each other, which has been assumed before. In a case with short pulses or a well-known pulse structure, the generic spatial signal can be retrieved by deconvolution, as demonstrated in Jones *et al.* (2016b). Deconvolution is a non-trivial computational process which is sensitive to noise and also subjective, i.e. any realistic function can be tried in a deconvolution and will receive a result which is up to the experimentalist interpretation. This means that the quality of a deconvolution approach is dependent on the reasonable choice of input data, e.g. noise reduced and well fitted temporal profile measurements.

On the other hand, with this knowledge simulation studies on temporal profile dependencies have been significantly simplified. Simulations with only delta spike excitations are easier to handle from a computational point of view, and the desired pulse structure can be convolved later quickly on demand instead of being part of a long simulation¹. It will be shown later that running ionoacoustical simulations with a delta spike excitation and in a second step adding the correct temporal profile is advantageous (see section 2.3 for more).

2.2. Influences on Ionoacoustical Signals

It can be concluded from section 2.1 that a pulsed ion bunch is generating a pressure wave containing spatial and temporal information of the energy input. With

¹The correctness has been verified in a comparative simulation.

this distinct knowledge on the temporal structure of the used ion bunch, the expected signal is only the first derivative of the spatial heating function, or the second derivative of the temperature gradient. As discussed before in section 1.1, the depth-dose profile can be uniquely described and an important feature in medical application is the determination of the range. The different experimental modalities will be described in chapter 5, therefore only general topics are discussed here. In the following, it is important to distinguish the ideal *pressure wave* from the expected measured *signal*, mainly given as a voltage amplitude. It will be shown that several experimental circumstances are able to alter the signal considerably, so that certain interpretations of an experimental signal, that were derived from previous pressure calculations, need to be well justified.

2.2.1. General Model of Signal Generation

In section 2.1, a general description of how a temperature gradient produces a pressure wave is derived. Now the focus is on explicit heating functions and therefore the spatial distributions of energy which can be expected in the experiments presented in chapter 5. For simplicity, the detector point is placed at the origin, i.e. $\mathbf{r} = (0, 0, 0)$, and a short term excitations is assumed, i.e. $\mathcal{H}_t = \delta(t)$. The arriving pressure is now the temporal differentiation of the summation over a sphere expanding from the origin, the *scanning sphere*.

Disc Source

First a disc source is considered, i.e. a cylinder with given radius R , a height or thickness d , and at a distance r_D from the origin. Three cases can be distinguished in time: before the scanning sphere is touching the source, during, and after. The first and last are trivially zero, no pressure source is providing any signal here. Let us consider $r_D \leq ct \leq r_D + d$ or $ct \leq \sqrt{R^2 + r_D^2}$, whichever is smaller, where then $p(\mathbf{r}') = p_0$. Only azimuth angles up to the disc lateral size are considered as θ' . Equation (2.36) is used to calculate the distribution as follows:

$$\begin{aligned}
 p(\mathbf{r}, t) &= \frac{1}{4\pi c^2} \partial_t \left[\frac{1}{ct} \int d\mathbf{r}' p_0 \delta \left(t - \frac{|\mathbf{r}'|}{c} \right) \right] \\
 &= \frac{p_0}{4\pi c^2} \partial_t \left[\frac{1}{c^2 t} \int d\mathbf{r}' \delta(ct - |\mathbf{r}'|) \right] \\
 &= \frac{p_0}{4\pi c^2} \partial_t \left[\frac{1}{c^2 t} \int_0^{2\pi} \int_0^{\theta'} (ct)^2 \sin \theta d\theta d\phi \right] \\
 &= \frac{p_0}{2c^2} \partial_t [t(1 - \cos \theta')] = \frac{p_0}{2c^2} \partial_t \left[t \left(1 - \frac{l}{ct} \right) \right] = \frac{p_0}{2c^2}.
 \end{aligned}$$

It can be seen that for the specific time, when the scanning sphere is passing through the disc source, a constant signal is received with an amplitude $p_0/2c^2$. Indicated by the upper limit for ct , the length of this signal is the corresponding time of flight from either the thickness of the disc d or the distance from the detector point to the edge of the disc, i.e. $\sqrt{R^2 + r_D^2}$. It has to be noted that this example includes an idealized temporal profile and a homogeneous distribution of initial pressure, which is a non-realistic simplification. In the following, Bragg curve shaped heating functions are considered.

Bragg Curve Shaped Source and Reflection

An analytical model can be used to describe a simplified proton dose profile, e.g. from Bortfeld and Schlegel (1996), Bortfeld (1997), and directly calculate the spherical integral. Figure 2.3 shows a configuration of a 20 MeV proton Bragg curve and the corresponding pressure wave deriving from a direct calculation of the spherical integral, as described later in section 2.3.1. This configuration already assumes a typical measurement setup, which is described later in chapter 3. This is an axial measurement of the generated pressure including a reflective surface in the field of view. This configuration is used for now without further motivation, as the justification for the measurement configuration will become clear in section 4.1.

For the calculation of these Bragg curves, the following formula for the energy E and the stopping power S of protons in water at the depth z has been used (Bortfeld, 1997):

$$E(z) = \frac{1}{\alpha^{1/\xi}} (R_0 - z)^{1/\xi}, \quad (2.42)$$

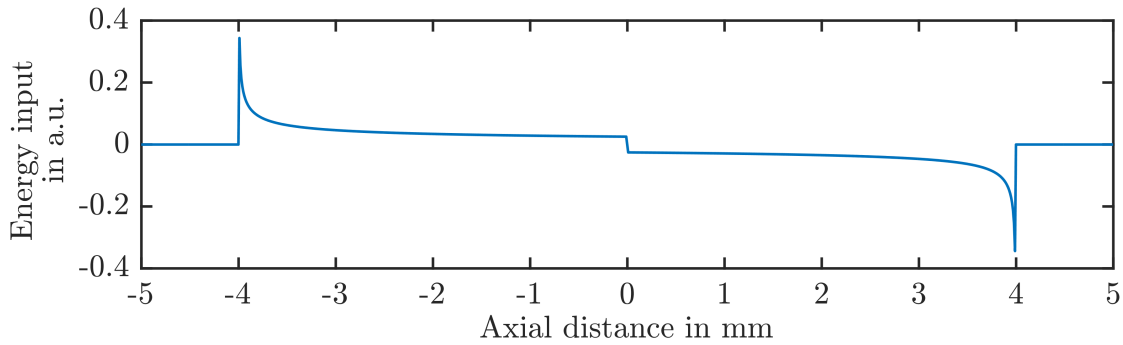
$$\Rightarrow S(z) = -\frac{dE}{dz} = \frac{1}{\xi\alpha^{1/\xi}} (R_0 - z)^{1/\xi-1}, \quad (2.43)$$

with $\alpha = 0.0022$ and $\xi = 1.77$. The required range of protons in water is specified with R_0 . Two Bragg curves are placed behind each other assuming a perfect reflection on a closed end, i.e. the width of the reflective surface and the possible energy loss in any kind of entrance foil is neglected². The acoustic reflection is depending on the change of acoustic impedance $Z = \rho c$ at a surface. The reflectivity coefficient R_M is then given as:

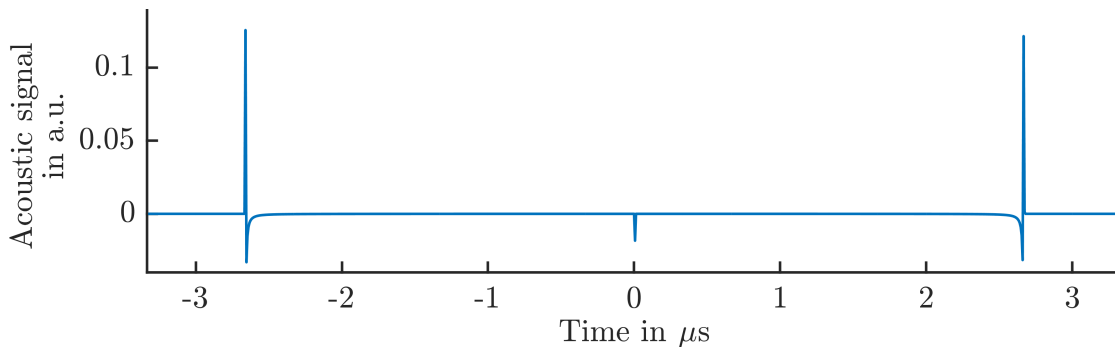
$$R_M = \frac{Z_1 - Z_2}{Z_1 + Z_2}, \quad (2.44)$$

²That means no losses due to transmission and no further frequency depending modifications. For thin entrance foils from water to air, this assumption is reasonably justified.

where the acoustic wave is travelling from a material with acoustic impedance Z_1 into a material with acoustic impedance Z_2 . From water to air, $R_M = -0.99$ which is an almost perfect reflection. So for this simple calculation, the second half of the energy input was just inverted to simulate the phase shift at the reflection. With a quick comparison to fig. 4.1, the signals do fit quite well showing 3 distinct signal parts. In this comparison, the source locations of the signal can be identified. It is to be noted that the proposed analytical description of a Bragg curve represents a very idealistic dose profile. Broader distributions are expected from realistic proton beams as barely any broadening due to energy uncertainties is included. The approximation does however include empirical estimations for range straggling and other processes. This approximation can be used in order to get into the description and understanding of measured signals. Also, with this analytical approach expected signals can be calculated in a straightforward and fast manner for point detectors, but the initiating heating function has to be considered ideal,



(a) Bragg peak shape heating function as input for forward simulation.



(b) Resulting acoustic pressure wave for single point detector.

Figure 2.3.: Analytical simulation using a simplified Bragg peak source. This was done in a direct calculation of the spherical integral expanding over an analytical function for Bragg peak ionizations. Details in 2.3.1, Jones *et al.* (2015), and Bortfeld and Schlegel (1996).

as realistic distributions will always be broader.

As emphasized before, the pressure wave is equivalent to the spatial gradient of the source, thus the sharp rise of the Bragg peak front is seen followed by the slow decay towards the entrance in the first signal part. This will be called the *direct signal*, as it is directly travelling from the source to the detector. The maximum of this curve is the zero-crossing of the first derivative, which will be used later in the evaluation of the measured signals. The 3rd signal derives from the reflection, hence is called the *reflection signal*. The Bragg peak is observed from its back, hence the lower part is arriving first followed by the sharp distal edge. Additionally, the amplitude is inverted due to the reflection on a closed end.

The *entrance signal*, in this work also referred to as the *window signal*, between the direct and reflection signal is a short, unipolar, and negative signal deriving from the negative gradient at the border between direct ionization and its reflection.

The spatial input has been normalized such that:

$$1 \equiv \frac{1}{N} \int dV \mathcal{H}_s(\mathbf{r}), \quad (2.45)$$

where N is the normalization constant for the spatial heat input excluding the reflection. By convolving later the time profile in J/s, the result will be in pressure units.

2.2.2. Non-Delta Spike Excitations

As a next step, non-stressconfined excitations need to be addressed, i.e. longer pulse widths and Gaussian pulse fronts. In Jones *et al.* (2016a) it is shown that the measured signal can be interpreted as the convolution of the spatial heating function, the temporal heating function, and the response function of the detector. The latter would incorporate all electronic frequency modifications from amplifiers, filters, detector surfaces and similar. By assuming a delta spike excitation as the temporal heating function, the generic spatial signal of ionoacoustics was studied. To simulate the effect of a non-instantaneous heating, other temporal functions can be incorporated in the simulation, which would be computationally cumbersome. Instead, the signal assuming a delta spike excitation is calculated and the time derivative of the desired temporal function is convolved in the next step, achieving the exact same result. This has been motivated before, e.g. starting from eq. (2.40). The full signal not considering detector depending parameters is hence written as:

$$p(\mathbf{r}, t) = \mathcal{H}_s(\mathbf{r}') \otimes \delta_t \mathcal{H}_t(t). \quad (2.46)$$

This will provide the pressure in units of Pa/s when using a normalized spatial heat input and a temporal heat input in units of J/s.

2.2.3. Realistic Detector Surfaces

A spatially extended detector is considered next, which will be a summation of different \mathbf{r} over the detector surface. This would then emulate an extended single element detector. The signal detection can be assumed to be practically instantaneous, so the superposition of signals detected at different detector points can enhance or destroy the signal after summation, e.g. if the corresponding time-of-flight between two points corresponds to a phase shift of π . Imagine a line of detectors trying to detect an incoming plane wave under an angle. Instead of a single push, different elements of the detector surface will see maxima and minima simultaneously, i.e. a destructive interference. Hence, the selection of detectors is crucial and depends on the expected pressure wave, since the form of the surface will add a frequency bandwidth just by respecting interferences of the signal over the surface.

The effect of geometrical properties of the detector is summarized as the *spatial impulse response SIR* (Jensen and Svendsen, 1992):

$$\text{SIR}(\mathbf{r}', t) = \int_S \frac{\delta\left(t - \frac{|\mathbf{r} - \mathbf{r}'|}{c}\right)}{|\mathbf{r} - \mathbf{r}'|} d\mathbf{r}'. \quad (2.47)$$

In general, the SIR is a low-pass filter and will shift the frequency content to lower values, i.e. blur the signal in time domain. The SIR can be calculated for any detector geometry, but a specific source point has to be assumed. This gives the opportunity to optimize the surface to a specific source structure, but can blur the signal when the detector is misaligned.

For a focused transducer, the 6 dB pulse-echo beam diameter W_{beam} is given by:

$$W_{\text{beam}}(-6 \text{ dB}) = 1.02 \frac{Fc}{fD}, \quad (2.48)$$

with the focal length F , the material speed of sound c , the frequency f , and the element diameter D (Olympus NDT INC., 2001). This provides a reasonable minimal measurable spot size. A calculation of a realistic SIR is then an average of points inside this beam diameter.

2.2.4. Influences of Realistic Detectors Electronics

Additionally to the SIR, the intrinsic material properties of the detector have to be considered. This includes the resonances of the piezo material, backing material, amplifier and oscilloscope bandwidth, and is summarized as the *electrical impulse response EIR*, which can be considered a band-pass filter. Together with the SIR,

the complete modifications of the signal by a realistic detector is the *total impulse response TIR* (Caballero *et al.*, 2013):

$$\text{TIR}(\mathbf{r}', t) = \text{SIR}(\mathbf{r}', t) \otimes \text{EIR}(t). \quad (2.49)$$

Although there are some approaches trying to predict the EIR of specific measurement systems, the most practical solution is a measurement with a well-known calibration setup. If the sound source can be described well enough and modified by a previously calculated SIR respecting the involved detector geometry, the remaining modification of the signal is assumed to be caused by the EIR.

The transfer function of the used detector system is very important, as it can add considerable phase-shifts during the measurement. It is to be noted here again, that the SIR can add strong spatial dependence, e.g. with spherical focused transducers. This is the main reason for the strict separation between pressure wave signals from calculations and experimentally measured signals.

2.2.5. Attenuation in Water

Besides the $1/r$ drop in amplitude due to the spherical wave evaluation, the pressure amplitude is reduced exponentially due to absorption and scattering. The absorption in water is rather low, but the effect has to be considered for heterogeneous tissue or long distances. The absorption is depending on the distance x and the frequency f of the signal, and can be described as:

$$p(x, f) = p_0 e^{-\alpha f^2 x}, \quad (2.50)$$

where α is the absorption coefficient. For water with a temperature of 25 °C $\alpha = 22 \times 10^{-17} \text{ s}^2/\text{cm}$ (Pinkerton, 1949). The initial pressure at $x = 0$ is given as p_0 . Over a distance of 25 cm, this results in an attenuation of half a percent for 1 MHz and 42 % for 10 MHz.

2.2.6. Dispersion

The dispersion of a wave is known as the effect of phase velocity change as a function of frequency. For a wave propagating in a bulk medium or free space where it is not bounded or can be assumed unbounded, dispersion is caused by and only by attenuation. That means, attenuation is the sufficient and necessary condition for having dispersion. The relationship which connects dispersion and attenuation is the Kramers-Kronig relationship (O'Donnell *et al.*, 1981). This relationship has been verified experimentally for ultrasound in Lee *et al.* (1990) and He (1999).

We follow Barthel and Nolle (1952), King McCubbin (1954), Carstensen (1954),

and Gedanitz (2010) to that water is considered a non-dispersive medium for ultrasound waves up to a frequency of 25 MHz.

2.3. Simulation Studies

In this section, the used simulation techniques and some examples are presented. Before details on the actual measurements are shown, the multiple sources of signal modifications are studied and by that, the ramifications on the signal measurements are investigated.

2.3.1. Direct Integration applied to the General Solution

Equation (2.31) can be directly solved for a single, infinitesimal detector point over time. For simplicity, this detector point is chosen to be at $\mathbf{r} = (0, 0, 0)$ and the evaluation of the scanning sphere is calculated in spherical coordinates. The integral to solve for a delta spike excitation is then reduced to:

$$p(\mathbf{r}, t) = \frac{\beta}{4\pi C_p} \partial_t \int_0^{R_{max}} dr \int_0^\pi d\theta \int_0^{2\pi} d\phi r \sin\theta H_s \delta\left(t - \frac{r}{c}\right). \quad (2.51)$$

This method is quick and suitable for easy cases, like simple geometrical objects. The calculations are reduced to a surface integral and a differentiation, once the ϕ integration is carried out. A Matlab script has been developed which offers simple symmetric spatial heating functions like those discussed in section 2.2. It has been used to study the simple case described in section 2.2.1, but it is not sufficient to study a realistic case. First, several simplifications are assumed, the most important one is the homogeneity of the simulated medium, i.e. only water. Second, simulating an extended detector surface would require the same full calculation on a grid over this detector surface and thereby losing the advantage in time compared to a “full” simulation. And last but not least, the evaluation of the surface integral over the provided spatial heating function requires an analytical description of those functions. That is possible for disc or slab sources, but the analytical model for Bragg peak ionization is not sufficient. It is of course a first step for understanding signal parts and origins, but it lacks some advanced features of the proton depth dose distributions (Bortfeld and Schlegel, 1996, Bortfeld, 1997). Also, the simple approximation using a power law and a finite range is not valid for heavy ions, as it barely includes the mixed radiation field effect of the *dose tail* following the Bragg peak. In Jones *et al.* (2016a) a full detector study for protons in the medical energy range has been made. As this specific group is focused on the full reconstruction of the dose distribution, the described approach has been used for multiple detector surface points, i.e. for cases with $\mathbf{r} \neq (0, 0, 0)$.

2.3.2. Global Finite-Difference Method using k-Wave

For a complete simulation of the generated pressure field, an open source Matlab toolbox called k-Wave (Cox *et al.*, 2007, Treeby and Cox, 2010) is available. With this, it is possible to define heterogeneous media in terms of density and speed of sound, complex detector surfaces, phantom geometries, and arbitrary sources. The last feature is used to include Geant4 Monte Carlo simulations of conducted experiments and convert them to initial pressures as described in section 2.1. It is also possible to simulate non-instantaneous excitations, i.e. longer pulse widths exceeding the stress confinement or longer pulse rise times and Gaussian shaped pulses.

The approach to solve the first order coupled acoustic equations in k-Wave is a so called pseudo-spectral method. A basic computational problem is the discretization of partial differentiation. One approach is the so-called *finite difference method*, or FD, which simply replaces the differentiation by the difference between two sampling points on a simulation grid divided by a discrete difference. One can improve this approximation by considering not only neighbouring grid points but including the next 2, 3, etc. points in some type of fit. A Fourier series can be used to fit the grid points, which has the advantageous feature of fitting automatically to the complete grid. For that reason, pseudo-spectral methods are called global methods compared to local FD methods. Also, the basis of the Fourier series are sinusoidal functions, so only two grid points per maximum wavelength are needed to describe this function completely. This can reduce the computational requirements on the simulation grid by about one order of magnitude per simulated dimension compared to FD methods. With the use of this property of the Fourier transformation:

$$\mathcal{F}\{\partial_x f(x)\} = -\frac{1}{2\pi} \int f(x) (-ik_x) e^{-ik_x x} dx = ik_x \mathcal{F}\{f(x)\}, \quad (2.52)$$

the spatial derivatives can easily be calculated.

More than in *non-global* simulation algorithms, the choice of spatial and temporal dimensions is important. As the spatial grid spacing Δx is defining the *sampling frequency*, the maximum transported frequency is given by the *Nyquist limit*, stating that the maximum frequency in a sampled signal should be half the sampling frequency in order to avoid aliasing or other sampling errors. Hence:

$$f_{max} = \frac{c}{2\Delta x} = \frac{1.5 \mu\text{m/ns}}{2 \times 10 \mu\text{m}} = 75 \text{ MHz}, \quad (2.53)$$

given for the smallest used spacing Δx in the presented simulations, assuming two sampling points for the smallest wavelength on the grid, and the approximate speed of sound c in water. This is sufficient as measured signals never exceeded

10 MHz. Additionally, the temporal time step Δt is coupled to the given spacing Δx . In order to avoid phase errors, Δt should be chosen such that the distance a wave can travel in the given medium during a single time step is significantly smaller than the grid spacing Δx . This ratio is given in the one-dimensional *Courant-Friedrichs-Lewy* (CFL) number (Courant *et al.*, 1928):

$$\text{CFL} \equiv c \frac{\Delta t}{\Delta x}. \quad (2.54)$$

A CFL number of 0.3 typically provided a good balance between accuracy and computational speed for weakly heterogeneous media. With a grid spacing Δx of 10 μm , this would result in a time step of 2 ns (Treeby *et al.*, 2012).

2.3.3. Calculation of SIR using Field II

With the Matlab toolbox Field II, SIR-functions of arbitrarily shaped and apodized, i.e. with inhomogeneous sensitivity in the detector material itself distributed over the detection surface, ultrasound transducers can be calculated (Jensen, 1996, Jensen and Svendsen, 1992). This is done by propagating spherical waves from defined field points towards detector points and the field point dependent detector response is retrieved. A large transducer surface is split into smaller triangles, and the result of the corner points are used for averaging. This reduces the computational burden. For a realistic detector SIR, the contributions of several field points inside the transducers beam diameter are accumulated.

2.3.4. Simulation Examples

Now, different examples of simulation studies are shown.

2.3.4.1. Disc Source Example

As a first rather artificial example the disc source example already described in section 2.2.1 is investigated again with the k-Wave program. The simple geometry of this source can be used to study the influence of detector distances. Results from a disc with radius of 5 mm R and 1 mm thickness D are shown in fig. 2.5, a schematic overview of the setup is given in fig. 2.4. The normalized pressure traces are given for increasing detector distances r_d from bottom to top, ranging from 1 mm to 11 mm respectively. In this example, a single point detector on a central axis to the disc source has been used and a short pulse excitation of 60 ns, i.e. stress confined. Two signal parts can be identified, a constant, rectangular part with a width of 666 ns and a changing, later part, both arriving at later times as the detector moves away from the source. For a detector distance of 1 mm, the

time difference of the rising edges is $2.7 \mu\text{s}$ and the signal parts are almost overlapping at 11 mm. The width of the later signal part increases from 190 ns to 600 ns. To understand these pressure traces, the differences to previously shown ionoacoustic signals need to be emphasized. First, the dimensions of this source are rather extreme considering the steep rises, the large transversal width, and rather short thickness. Also, the short excitation is not visible, but a constant high pressure field. This is due to the fact that here a large, homogeneously heated source is studied instead of the spatial gradient in the Bragg curve. It is therefore convenient to consider this source as the sum of single elements all sending a compression and a rarefaction pulse. Those elements are synchronised due to the short pulse width and the homogeneous pressure inside the disc. Hence, all those elements emit a pressure signal which is forming in superposition a planar wave according to Huygens' principle. This planar wave contains a compression going outwards from all edges and a rarefaction going inwards. At the point detector, this planar wave is not observed all at once, but delayed due to the different distances of the single sending elements of the source to the point detector. This results in the first rising edge of the pressure signal deriving from the compression pulse of the source point with the shortest distance. In the next time step, the compression of the next points arrive, which are now all points lying on a sphere with radius $c(\Delta t + t)$ around the detector. These positive contributions are overlapping with the negative rarefaction of the previous points. As long as the scanning sphere is expanding through disc, more compression than rarefaction is encountered, hence the overall signal is constantly positive. This changes once the backside of the

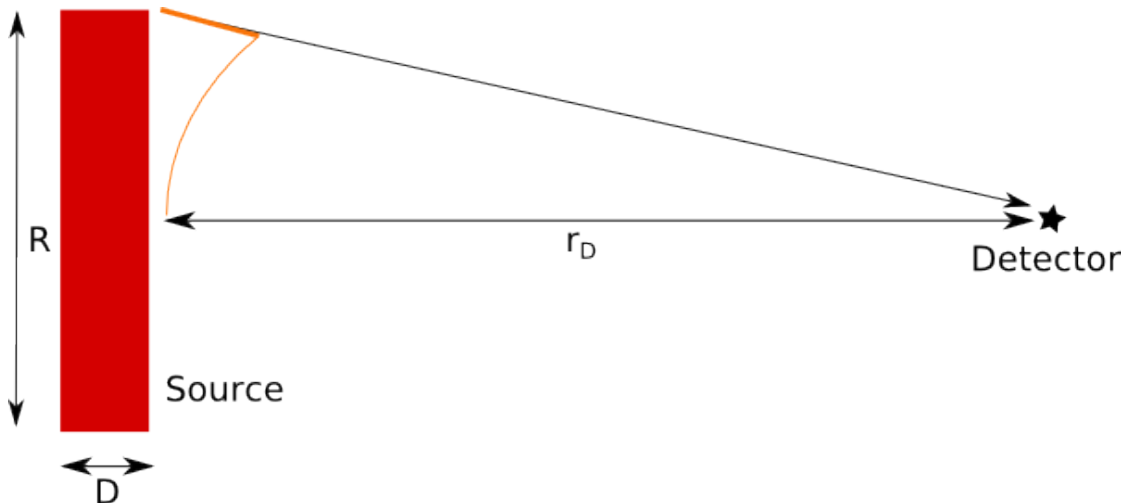


Figure 2.4.: Sketch of disc source example setup including relevant dimensions for the discussion.

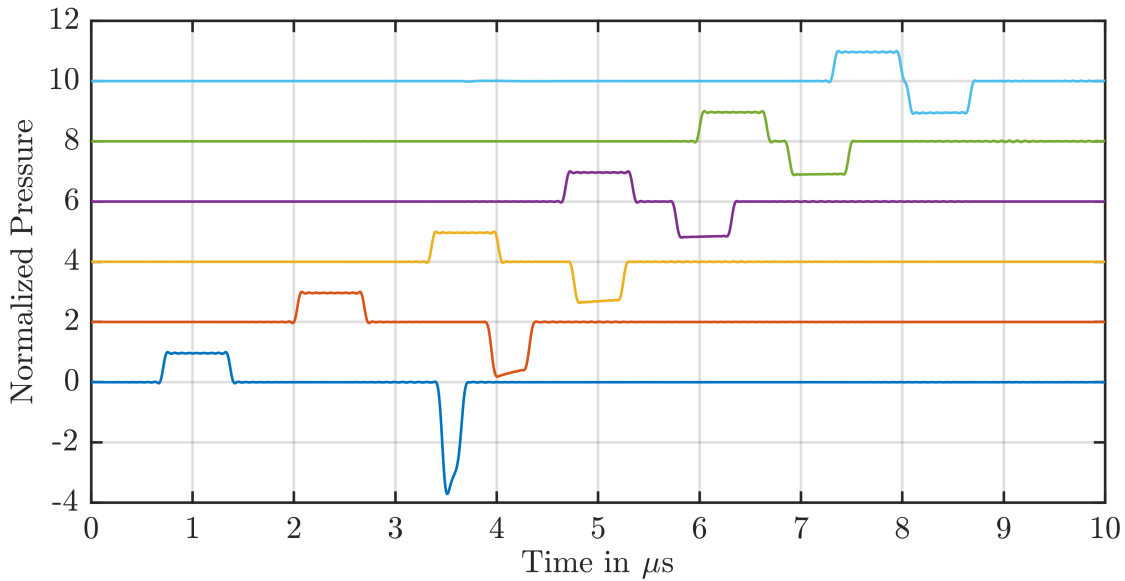


Figure 2.5.: Simulation example for detector distance relationship. As source, a disk with 5 mm radius R and 1 mm thickness D was excited for 60 ns. The normalized pressure traces for different distance r_d of the point to the source are plotted from bottom to top increasing from 1 mm to 11 mm in steps of 2 mm each. Two signal parts can be identified, one corresponding to the thickness of the disk and one for the outer edge or the radius. While moving the detector point away from the source on axis, the thickness provides a constant signal, while the edge is observed with different angles, and the signals are overlapping as the difference between these two distances is decreasing.

source is reached. Now a part of the scanning sphere is leaving the source, hence the amount of compression is equal to the amount of rarefaction contributions, so the result is zero. It can be concluded that the width of the first signal corresponds to the thickness of the disc. In the example with 1 mm thickness this results in the 666 ns of the first signal part.

The second part derives from the outer edges of the disc facing away from the central axis on which the detector point is located. Hence, only the rarefaction contribution is seen travelling inwards of the source. The time of flight of this signal in this case and for a distance of 1 mm is:

$$t = \frac{\sqrt{r_d^2 + R^2}}{c} \Rightarrow 3.39 \mu\text{s}. \quad (2.55)$$

The width of this signal part is given by the length observed with the changing angle as the detector moves away. Hence, this is given by the difference of the time

of flight of the first sending element of this edge to the last one:

$$t = \frac{\sqrt{(r_d + D)^2 + R^2} - \sqrt{r_d^2 + R^2}}{c} \Rightarrow \frac{\sqrt{29} \text{ mm} - \sqrt{26} \text{ mm}}{1.5 \text{ mm}/\mu\text{s}} = 190 \text{ ns.} \quad (2.56)$$

This value is increasing with the detector distance. In a far field approximation where $r_d \gg R$, the radius can be neglected in this calculation and a width of this signal again corresponding to the thickness of the source is received.

2.3.4.2. Pulse Width and Shape Dependency

After a study on the spatial heating input, the focus is now on the influence of different temporal profiles. An analytical Bragg peak signal is used and different forms of temporal profiles are convolved, i.e. a Gaussian shape, a rectangular pulse, and a smoothed rectangular pulse emulating the expected pulse shape from the MLL chopper. The description of this specific beam pulse shaping device is given in 5.1. The signal is detected by a single point detector. The signals shown here

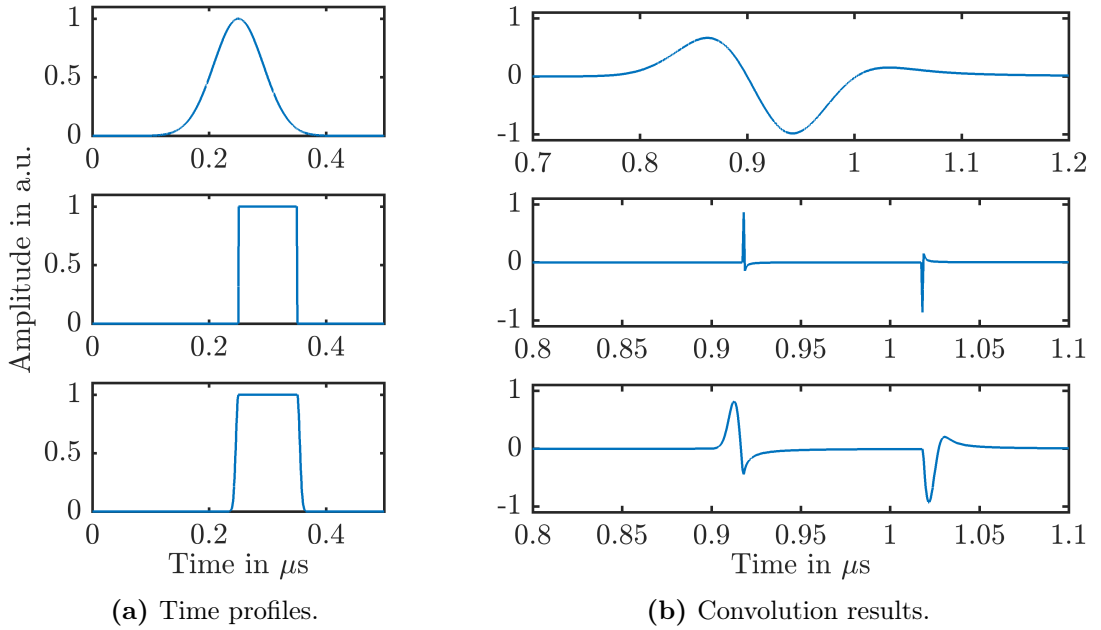


Figure 2.6.: Influence of different temporal profiles. Left: Time profile of 100 ns Gaussian, rectangular and smoothed rectangular (chopper-like) pulses. Right: Convolution result on simulated pressure traces from monoenergetic 20 MeV proton beams. Only the direct signal is shown.

are therefore the idealized available signal if only accelerator depending parameters are considered. A summary of convolutions with 100 ns pulses of different shapes are given in fig. 2.6. It can be seen in the details that the sharp features from the original signal are lost especially in the Gaussian case, compared to the signal incorporating rectangular shaped excitations, where the sharp rise with the long pulse results in two distinguishable peaks.

The influence of the pulse width for the Gaussian and rectangular case are studied next. Figure 2.7a shows the maximum signal amplitude in dependence of the pulse width for Gaussian and rectangular pulses. The pulses are normalized to one, meaning that the simulated delivered energy is constant for all pulses, but spread over a longer time. Otherwise, the rectangular signal would remain constant as the instantaneous current is constant. Additionally to the decrease in amplitude due to the normalization at longer pulses scaling with $1/t_{pulse}$, the instantaneous current is decreasing as well with another factor $1/t_{pulse}$ as a Gaussian pulse is acting as a low pass filter on the signal. The effect can be seen in the frequency content of a 100 ns Gaussian displayed in fig. 2.7b.

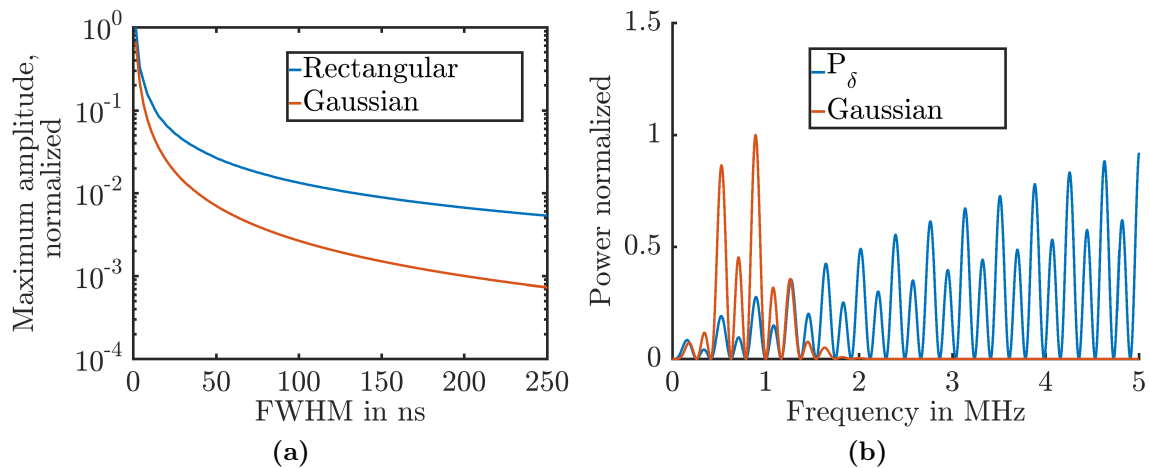


Figure 2.7.: a) Study of the influence of the pulse width on the acoustic amplitude after the convolution of Gaussian and rectangular pulse profiles. b) Frequency content of an ionoacoustic signal convolved with a 100 ns Gaussian pulse compared to the generic pressure signal.

2.3.4.3. Influence of a Realistic Spatial Impulse Response

From fig. 2.6 rather high frequency signals are expected when using the pulsing instrumentation in the later presented proof of principle experiments, where rectangular and Gaussian temporal shapes are provided. In the following the spatial

impulse response of an often used transducer with a main frequency of 3.5 MHz with an 1" spherical focus is studied. The SIR is calculated with the FieldII software and averaged over multiple source points inside the beam diameter. This SIR is then convolved with the signal from the study on the pulse shape shown in fig. 2.6.

Figure 2.8 is showing the results of this study for a 100 ns Gaussian pulse and a sharp rectangular pulse. The blue curves are the original signals, the influence of the SIR is in red. The signals have been shifted in time for a better view. It can be seen that the SIR again reduces the frequency content of the signal as lower frequencies are preferred. Most visible is the loss of informations in the rectangular pulse case, where the two signals from the temporal begin and end of the pulse are blurred into one bipolar pulse similar to the Gaussian pulse case. It can be seen here that the SIR acts as a low-pass filter and can alter a signal considerably, but however is not introducing a phase-shift such that important timing information would be lost. In fig. 2.8, a positive peak is followed by a negative peak, allowing the interpretation as a compression followed by a rarefaction. For an arbitrary measured signal with unknown TIR, this interpretation cannot be directly made. The EIR could introduce phase shifts leading to inverted signals. An interpretation in terms of compression and rarefaction is then only valid if such phase shifts can be excluded or deconvolved with a known TIR.

Another study with the FieldII SIR calculation is shown in fig. 2.9. Here, the SIR function is calculated for a 10 MHz spherical focused ultrasound transducer

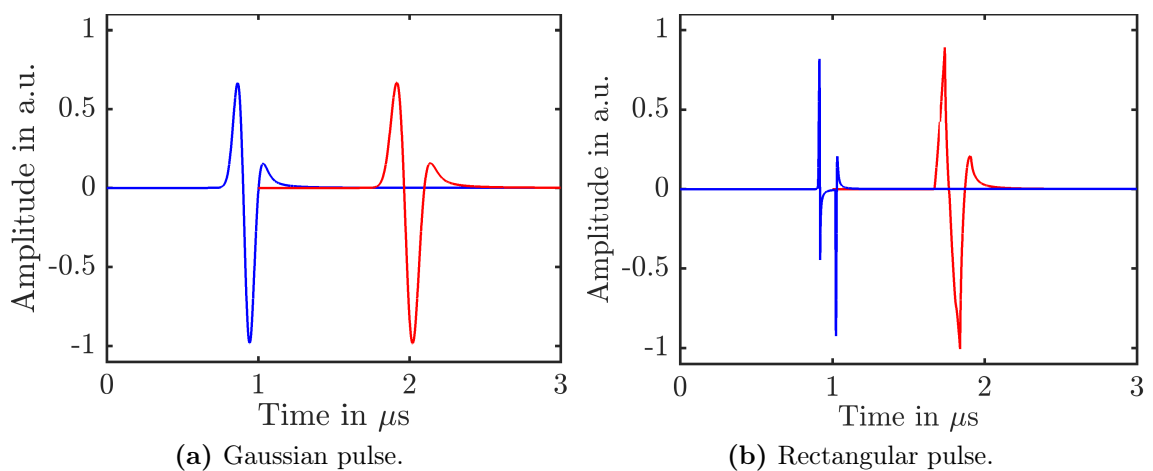


Figure 2.8.: SIR influence of a 3.5 MHz spherical focus transducer observing a Gaussian and a rectangular pulse in (a) and (b) respectively. The blue signal is before the application of the SIR-filter, the red signal is the result. The blue signals are the same as in fig. 2.7b.

scanning source locations at different points along the central axis. This is emulating the signal change during a z-scan of the transducer from an ideal, delta spike excitation. Since the transducer is simulated with perfect geometrical conditions, there is one ideal single source point which is the centre of the sphere defining the detector surface. The spherical wave evaluated from this centre is perfectly matched to the designed transducer surface, hence the delta spike excitation is reproduced. This is shown as the red signal in fig. 2.9. Once the detector is out of focus, this matching is lost and the spherical wave is reaching the detector at different points in time. This stretches the signal in time and the formerly sharp information is lost. This is also visible in the frequency spectra in fig. 2.9b.

It is shown here the possible strong spatial dependence of the signal acquisition by using a spherical focused detector. This is usually done in order to enhance the measured signal and is reasonable if the expected shape of the source is known, in this case spherically symmetric. However, this introduces the experimental challenge of aligning the detector, i.e. matching the expected pressure wave front to the detector shape. For measurements with a single source, this is usually justified. For several sources, flat surface detectors are to be considered, if possible phase shifts are required to be minimal.

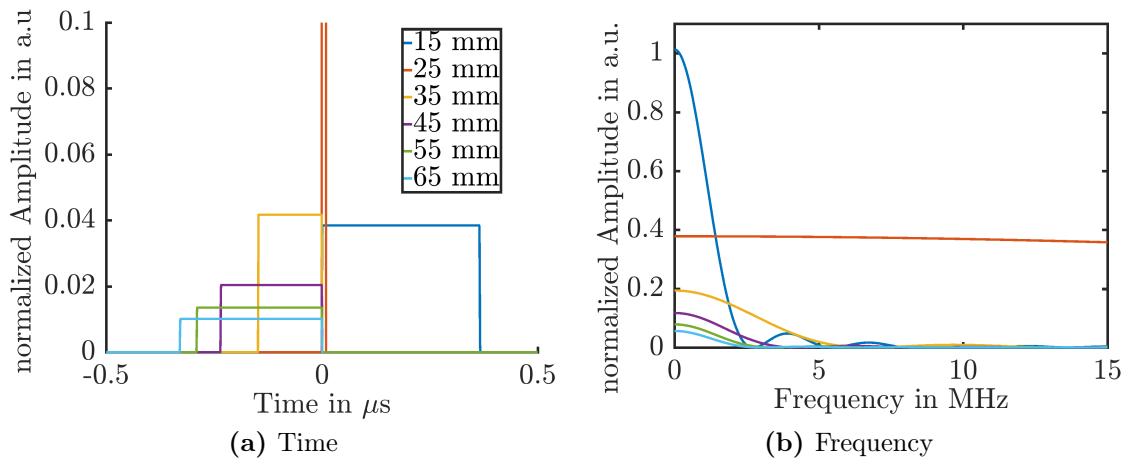


Figure 2.9.: SIR study on z position dependency. For a spherical focused transducer, the SIR is calculated for several source locations along the beam axis. The red signal is the ideal position in focus. a) Simulated pressure trace depending on different z-positions around the optimal focus position. The signals are normalized in amplitude and time (i.e. corrected by the different beam axis position) to the ideal focus position in red. b) Frequency spectra of the signals in (a).

2.4. Conclusion

In this chapter the generation of pressure from several patterns of pulsed dose deposition was derived. Only adiabatic heating processes can result in measurable pressure waves, hence only thermal and stress confined heatings need to be considered. Pressure amplitudes can be expected in the order of 200 Pa for 1 Gy under idealistic conditions. Finally, in selected simulations the important characteristics of the detector system have been analysed. If the spatial heating is considered as it is, which is the property to be measured, the temporal heating is optimized by using short and step-like pulses. Additionally, the spatial configuration of the used transducer is important, as signal informations are lost quickly with mismatched detector surfaces.

The value of that closed linear system:

$$p(\mathbf{r}, t) = \mathcal{H}_s(\mathbf{r}') \otimes \delta_t \mathcal{H}_t(t) \otimes TIR(\mathbf{r}, t), \quad (2.57)$$

i.e. the full description of the measured pressure traces as the convolution of spatial heating, temporal heating, and detector specific impulse response function, can not be underestimated. Once that system is fully described, signals can be predicted, measured traces deconvolved, and new detectors analysed and optimized theoretically.

3. Experimental Tools and Methods

Und der Haifisch der hat Zähne,
und die trägt er im Gesicht.
Und Macheath der hat ein Messer,
doch das Messer sieht man nicht.

From *Die Moritat von Mackie Messer*
by KURT WEIL and BERTHOLD BRECHT

This chapter introduces the equipment used for ionoacoustic experiments along with an introduction to the systems used for accelerating charged particles as well as the tools for measuring and simulating dose, and detecting ultrasound signals.

3.1. General Experimental Setup and Beam Properties

All experiments presented in this thesis were performed with pulsed ion beams stopped in a water phantom. Figure 3.1 is a schematic view of the used experimental setup. Particles are stopped in a water phantom and the ionoacoustic pressure wave is detected by an ultrasound hydrophone or transducer. The beam enters the phantom from the side through an air channel with a length of some centimetres and a 50 μm Kapton foil except for the experiments at clinical facilities. Due to the long range in these high energy proton experiments (see section 5.2), the beam was coming from the top through the water surface instead. In all cases, the detector was mounted on a motorized stage and the water temperature monitored. The data acquisition (DAQ) and control of these motorized stages had to be done remotely for radiation protection reasons. For this purpose, a software and *graphical user interface (GUI)* was written in LabView. Details on this software framework is given in section 3.7.

The temperature was measured with a PT100 thermometer coupled to a measuring converter, which is then readout by a digitizing voltmeter (PicoLog1216, PicoTechnology, UK). The accuracy of this temperature measurement has been determined to ± 1 K. The deionized water used in these experiments provided stable temperature conditions, and no short-term fluctuations in the temperature measurement was observed. The precision of this used temperature measurement can therefore be estimated to 0.1 K, corresponding to the 12-bit digitizing resolution of the voltmeter. The consequences of this accuracy and precision is discussed in section 5.1.

The signal from the hydrophone was amplified by at least 60 dB, bandpass filtered and then recorded by a digital oscilloscope (RTM2034, Rhode&Schwarz and PicoScope6404, PicoTechnology). Additionally to the acoustic transducer, a scintillator for the detection of scattered particles was used on site. As the temporal beam width is important this was mainly used in combination with a time-amplitude-converter (TAC) and multichannel analyser (MCA). For a range measurements at clinical facilities, this scintillator signal also provided the trigger signal for the TOF measurements. Further details, if required, are given in the specific description of the experimental studies in chapter 5.

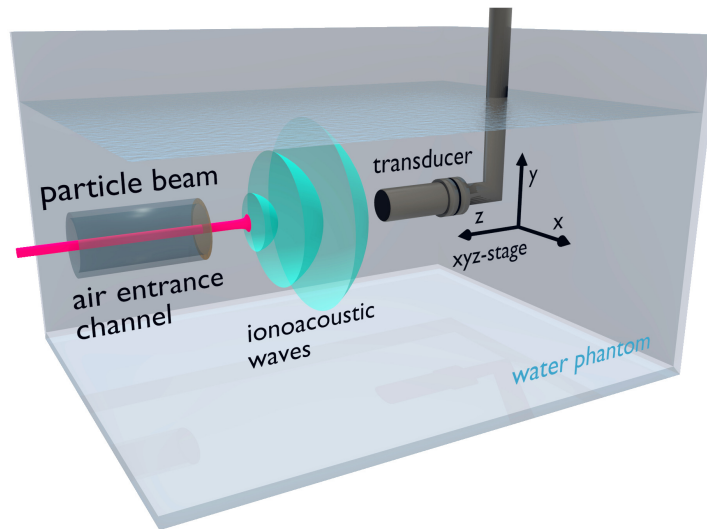


Figure 3.1.: Sketch of the ionoacoustic setup from Assmann *et al.* (2015).

3.2. Accelerating Particles

Charged particles can gain energy by passing an electric field depending on the field strength and the charge of the particle. When passing a magnetic field, the Lorentz force acting orthogonally to the field and direction of the charged particles momentum will result in a curved trajectory. A modern accelerator is a clever combination of magnetic and electric fields. However, a very practical limit in size for accelerators is the so called breakdown voltage. While applying high electric fields on an insulator, at some point a current can be induced due to material weakness. In metals, the point where free electrons can be pulled out of the surface might be reached, which would result in a collapse of the accelerator. This accelerating field strength is typically in the order of 10 MV/m to 20 MV/m. A summary of accelerator types used in this work is given here and their characteristics are underlined.

3.2.1. Particle Accelerators investigated for Ionoacoustics

A simple way to accelerate charged particles is an electrostatic linear accelerator. In this type, particles pass a static electric field on a linear vacuum tube once and are then guided towards the experiment. This type of accelerators provides rather low energetic particles up to some tens of MeV/u and is here mainly used for experimental studies. The details can vary greatly from machine to machine, but a common feature is the high energy precision. As the electric field can be

precisely stabilized, dE/E of those machines can easily be in the order of 10^{-3} . The MLL Tandem Van-de-Graaff accelerator in Garching (Assmann *et al.*, 1974), where most of the reported experiments have been performed, provides a maximum acceleration voltage of about 12 MV. Particles from various sources can be extracted and pulsed before the main acceleration, which is a two-step process at the MLL Tandem. Ions carrying an additional negative charge are accelerated towards the positively charged terminal in the middle of the accelerator. Here, they pass a *stripper foil* removing electrons from the negative ion. The now positive ion is accelerated once more towards the grounded end, hence tandem. With additional voltage stabilization on the accelerating electric field as well as analysing and selecting magnets, an energy precision of $dE/E = 10^{-4}$ can be reached.

As the magnitude of the accelerating electric fields is limited, circular accelerators use the passage through an electric field several times. One of the first implementations was the cyclotron. Two electrodes in the shape of a “D” (*Dees*) are located between the two poles of an electromagnet. This magnet bends the charged particles on a orbit passing a gap between those two Dees several times. Along this gap, an electric field is applied accelerating particles with every passage. This field needs to be changed in polarity for every passage, therefore an oscillating field is used, typically in the order of 60 MHz. The cyclotron resonance frequency is given as

$$f = \frac{qB}{2\pi m}, \quad (3.1)$$

with the particle charge q and mass m and the magnetic field strength B . As the particles are bended by the magnetic field, its strength limits the maximally achieved energy, i.e. their speed for a given accelerator size, and cyclotrons are typically specially designed for one type of particle. In a non-relativistic approximation, the following formula can be found to describe the maximal energy of the particles depending on their charge q , mass m , and the magnetic field strength B and radius R of the accelerator:

$$E = \frac{q^2 B^2 R^2}{2m}. \quad (3.2)$$

This approximation is true for non-relativistic energies, as it assumes a constant mass. With this simplification, the particle orbit increases linearly with the particle velocity, hence the orbit time is constant and an oscillating electric field with a constant frequency can be applied. However, in the case of medical beam energies, typically up to 230 MeV for protons, the relativistic gain in mass has to be considered. This can be compensated by either adapting the accelerating frequency, which would be a *synchrocyclotron*, or by increasing the magnetic field towards larger orbits, which is called *isochronous cyclotron*. On a synchrocyclotron, the frequency is decreased to compensate the longer round trip times, typically from

100 MHz down to 60 MHz. This will also produce inherently a bunched beam, again specifically for one particle type, as the charge to mass ratio is fixed. Normal, isochronous cyclotrons also have a pulse structure, the so-called *RF-structure* resulting from the oscillating electric field. For medical irradiations over seconds, this is not of importance, for nuclear imaging it might be. We will call this RF-structure the micro structure of the beam, in contrast to the macro structure, which for a cyclotron is considered to be a (quasi) continuous beam. Additionally, in the case of synchrocyclotron, a sub-macro structure is present, which is a microsecond pulse repeated with about 1 kHz forming the pulse train macro structure.

Finally, a synchrotron is a combination of linear accelerating parts and bending and focusing magnets. In order to keep the charged particles on a fixed orbit, the magnetic field is increased. This *ramp up* of the magnetic field is setting the limit for the total acceleration time or pulse repetition rate. For older accelerators this is typically in the order of seconds, but novel developments working on the *rapid cycle medical synchrotrons* (RCMS) are expected to achieve pulse repetition rates of 30 Hz (Trbojevic *et al.*, 2011). This offers a high flexibility of accelerating particle types with high energy precision. These accelerators are typically large and are mostly used in scientific research, e.g. at the *Gesellschaft für Schwerionenforschung* (GSI) in Darmstadt, Germany or the *Large Hadron Collider* (LHC) in Geneva, Switzerland, but also at the *Heidelberger Ionentherapiezentrum* (HIT), a medical facility providing carbon and proton beams, or the *J. Slater Proton Therapy Center* in Loma Linda, USA, which uses only protons and is one of the oldest still running proton therapy centres.

More details are discussed in the specific explanation of the experimental environments in chapter 5. A short summary on the pulsing properties of the used accelerators is given in table 3.1.

Laser Plasma Acceleration

Traditional accelerators are limited by the static break-down voltage of 10 MV/m to 20 MV/m. However, the electric field strength in a high intensity, femto second laser pulse can easily reach TV/m, which can be used to accelerate particles from thin target foils. An often used model is the *target-normal-sheet-acceleration* (TNSA), where the strong electric field pushes a cloud of electrons out of this target foil. This charge separation is then pulling the remaining nuclei. Besides the fact that the production of the required laser pulse is experimentally challenging, the resulting ion beam differs considerably from the output of standard particle accelerators. The resulting beam has a polyenergetic spectrum, the beam is highly divergent, the particle fluence is several orders of magnitude higher than from typical accelerators, and the pulse width is in the order of nanoseconds, although this

Table 3.1.: Summary of particle accelerators used for ionoacoustic measurements with relevant pulsing parameters. GSI pulse lengths are given for a single pulse in the fast extraction mode.

Accelerator Type	Pulse length	Particles per pulse
MLL Linear	>1 ns	$1 \times 10^5 - 1 \times 10^7$
LEX Laser Plasma Acc.	ca. 1 ns	$>1 \times 10^8$
UPENN isochronous cyclotron	>19 μ s	6×10^6
CAL synchrocyclotron	ca. 4 μ s	1.2×10^7
GSI synchrotron	100 ns	$<10 \times 10^{10}$

is quickly extended due to the large time-of-flight differences in the polyenergetic beam (Daido *et al.*, 2012, Macchi *et al.*, 2013). Nevertheless, with a dedicated energy selection, the acoustic signal from short and intense *laser accelerated ion* (LION) pulses have been detected and used as a first approach to sophisticated methods in signal evaluation. Details are given in section 5.4.

3.2.2. Typical Beam Properties for Medical Applications

To offer treatment of deep seated tumours, ranges in water of up to 30 cm are needed. This corresponds to an energy of up to 230 MeV for protons and 430 MeV/u for carbon ions. The dose rate is typically in the order of Gy/(Lmin). A typical fraction entails the delivery¹ of 2 GyE to 3 GyE, which results in a treatment time of some minutes, not accounting for the positioning of the patient or unexpected complications (Durante and Paganetti, 2016).

As Ionoacoustics relies on a pulsed beam, the temporal beam profile is important and depends on the accelerator type. For linear accelerators and isochronous cyclotrons, the pulse width is mainly determined by the accelerating frequency, if the source current is constant. As the accelerating frequencies are typically in the order of 60 MHz, both the micro and macro structure are not suited for acoustic measurements, unless there are modifications resulting in pulses of some microseconds². Further details are discussed in chapter 5.

A synchrocyclotron will inherently produce a pulsed beam. As the frequency is adapted to the pulsed particle source, only the matching energy will be on a stable orbit until extraction (Henrotin *et al.*, 2016). Typical pulse widths are 5 μ s to

¹The unit GyE is a dose weighted by the *relative biological effectiveness* RBE, taking into account that different types of radiation transfer energy with different efficiency.

²This can be a combination of lateral and longitudinal electric fields (chopper and buncher) as in Rohrer *et al.* (1984) or a pulsed source as in Jones *et al.* (2015)

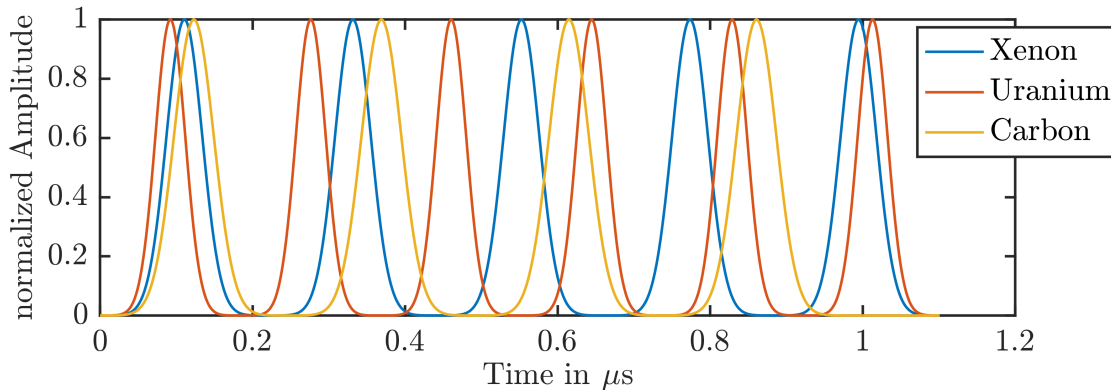


Figure 3.2.: Calculated pulse profile for GSI experiments. This takes the circumference of the synchrotron, the exiting accelerating frequency, and the final speed of the particles into account

10 μs . These are ideal conditions for ionoacoustic measurements with high energy proton beams.

For a synchrotron, a micro structure is given by the radiofrequency of the linearly accelerating parts as well, and the overall profile is given by the orbit time at the final energy. In the beginning, medical synchrotrons traditionally apply a *slow extraction*, i.e. the continuous draining of the accelerator. One possibility is the use of a *septum*, where parts of the beam can be *peeled off* while the main part stays in the ring, thus achieving irradiation times longer than the circulation time. In a *fast extraction*, the full particle content of the synchrotron can be extracted all at once. Hence the maximum pulse width is determined by the orbit time. Additionally, the accelerating electric field can be used to bunch the beam, which then can be used for Ionoacoustics. For the experiments at the GSI synchrotron, the expected temporal pulse shape can be calculated from the known circumference, the final velocity of the particles, and the *extraction frequency*, i.e. the frequency of the electrical accelerating field at the time the particle intentionally leaves the synchrotron. Relevant detailed values are given in table 3.2. The final velocity v_{exit} of the particles is calculated as the fraction of the speed of light β_γ :

$$\beta_\gamma = \sqrt{1 - \left(\frac{E_0}{E_0 + E_k}\right)^2}, \quad (3.3)$$

where E_0 and E_k are the rest and kinetic energy, respectively. This will provide a orbit time of roughly 1 μs for beam energies used in this thesis. This pulse is now bunched with the provided *exiting frequency* f_{exit} and an *angle of acceptance* α of 90° , which is the fraction of the modulating sinusoidal wave used for acceleration. In other words, only $\pi/2$ of the wave with frequency f_{exit} is used. Hence, the

effective single pulse width in the resulting micro pulse is given by:

$$t_{single} = \frac{\alpha}{360^\circ f_{exit}}. \quad (3.4)$$

These time values were used to calculate the expected Gaussian pulse train displayed in fig. 3.2.

Table 3.2.: Relevant values for calculating the temporal pulse shape at the GSI synchrotron with fast extraction.

	²³⁸ U	¹²⁴ Xe	¹² C
m ₀ in u	238.050	123.905	12.011
f _{exit} in MHz	5.4	4.5	4.0
Circumference	216 m		
E _{exit}	300 MeV/u	200 MeV/u	

3.3. Calculating Dose Depositions

A quick overview on different calculation approaches is given here. We can distinguish between using tabulated stopping power values and advanced Monte Carlo codes.

3.3.1. Using Stopping Power Tables

One approach to calculate a depth dose profile is by using stopping power tables given mainly by ICRU (2014b). Starting with the desired initial kinetic energy, the energy lost on the next step is retrieved from this database. The energy loss is integrated until the remaining energy is zero. This is the strict application of eq. (1.2). This approach has been implemented using the libdEdx programming interface³ (Lühr *et al.*, 2012). With this the depth profile by looping through the energy values can be calculated rather quickly and is applied in the simulated annealing approach explained later in section 4.5.

However, this approach can only provide linear information and is not including any range straggling nor lateral scattering or nuclear interactions. Also, for heavier ions all possible lighter fragments would need to be included.

³A very handy tool which is also the basis for the well used android app *electronic stopping power*.

3.3.2. Monte Carlo in SRIM and Geant4

The term *Monte Carlo* is used as a general keyword for simulation codes based on single particle tracking rather than the mathematical approach to solving integrals with the use of well distributed random numbers. Two different programs were used in this thesis, SRIM (Stopping and Ranges of Ions in Matter) (Ziegler *et al.*, 1985, 2010) and Geant4 (Agostinelli *et al.*, 2003). SRIM was one of the first programs designed to calculate the energy loss of charged particles in matter with a focus on low energies. In order to keep run times low for the computational power of the mid 80's, the full calculation of collisional energy loss in matter is simplified with the help of fit functions to experimental data. Most significant is the use of the so called *magic formula* which simplifies the calculations of the scattering angle in the nuclear stopping contributing to the energy loss by coulomb interactions. As this approximation only has a deviation of 2% to measured experimental data, SRIM is mostly reliably used for low energy simulations with particle energies below 1 MeV/u (Ziegler *et al.*, 1985). It does, however, neglect nuclear reactions.

Geant4 on the other hand was designed for high energy interactions. In simulations using the Geant4 libraries, particles are proceeded and evaluated through a simulation grid and all possible interaction are calculated until the particle would leave the simulated geometry or reaches a predefined lower energy threshold. The energy loss is thereby divided in a continuous and discrete part. Below a given energy threshold the energy loss is continuous and above it the energy loss is simulated by the explicit production of secondary particles.

For the continuous energy loss, stopping power tables are pre-calculated specific to the given simulated media. From this stopping power tables, *range* and *inverse range* tables are calculated and used during the simulation run of a single particle. Specific processes contributing to the energy loss are not involved in the calculation at that moment. In contrast, the production of secondary particles with kinetic energies above the production threshold is sampled by each individual energy loss process or nuclear reaction.

With the presented algorithms, complex dose distributions are calculated including also statistical processes, i.e. scattering in all directions and the evaluation of possible daughter nuclei and other secondary particles. In order to obtain a valid profile which is not influenced by the random scattering, sufficient amount of particles need to be simulated in order to get full 3D dose information.

3.4. Measuring Dose with established Methods

In order to compare the ionoacoustic measurements presented later in chapters 4 and 5, selected established dose measurements are introduced. This quick overview

is focused on the possibilities to receive ranges in water phantom measurements, mainly applied in the clinical, regular quality assurance measurements.

3.4.1. Radiochromic Films

The effect of ionizing radiation can be made visible with radio sensitive plastic material (Reinhardt *et al.*, 2012). In a sophisticated radiochromic film, such as EBT3, an active layer of radio sensitive material is sandwiched between clear polyester sheet. In total, these film have a thickness around 300 μm . When exposed to ionizing radiation, the active layer is polymerized and thereby changes its colour and a measurement of the absorbance can be correlated to the amount of exposed dose. The dose range that can be measured with such films is 0.1 Gy to 10 Gy. The radiosensitive layer is not recovering, which means that films can only be used once. During beam times, such radiochromic films can be used for a quick localisation of radiation, i.e. checking and measuring spot sizes and particles fluence. For an absolute quantitative dosimetry, these films need to be calibrated. This requires the precise irradiation of one film per production batch and measurement of the optical density with a film scanner. This provides the specific dose response curve, which is not linear (Reinhardt *et al.*, 2012).

When bundled together in a stack, these films can be used to measure the range of charged particles. One sheet of EBT3 radiochromic film is equivalent to 350 μm water. This means, when irradiating a stack axial, the dose in slices of 350 μm can be followed layer by layer. By this, the resolution limit of these stack measurements is given. For low energetic particles, i.e. energies from 10 MeV to 50 MeV for protons corresponding to ranges in water from 1 mm to 25 mm, stack measurements using EBT3 films are a valid measurement method of the range of charged particles. Smaller ranges are not properly resolved and longer ranges would require many layers of films. Another possibility is the irradiation of the radiochromic film *edge-on*, i.e. from the side through the sheet. This requires a fixed mounting of the film and is limited by the length of the film in beam direction. However, in order to characterize higher energies of charged particle beams, a reusable, online method is more suitable.

3.4.2. Ionization chambers

A very common measurement tool of ionizing radiation is the ionization chamber IC. In a gas volume, charged particles generated by ionizing radiation are separated and collected with a high electric field. The collected charge or current can be correlated to dose deposited in the gas volume. The applied electrical field is lower than in Geiger-Müller counters, where a higher electrical field is applied to generate a multiplication effect, enhancing the resulting current. Moving such an

ionization chamber in a water phantom along the beam axis will give the localized ionization, which can be summed together to the Bragg curve. For the purpose of range measurements, such an ionization chamber can be considered similar to the radiochromic films described above, but with online read out.

Two commonly used types of ionization chambers are available, cylindrical or *thimble* chambers and parallel-plate chambers. In the cylindrical form, an inner central anode is surrounded by a conductive surface being the cathode. Arranging several of such pencil-like chambers in an array allows measurements of the particle beam with certain lateral resolution. Parallel-plate chambers are shaped like a disc, with circular collecting electrodes separated by a small gap, typically 2mm or less. These electrodes can be very thin, allowing for much more accurate near-surface dose measurements than with a cylindrical chamber.

One special application to be noted here is the PTW peakfinder (PTW Freiburg, Germany). This is a water column with one fixed and one moveable parallel plate ionization chamber with a precise motorized stage. With this precise positioning, depth dose profiles can be measured with a resolution of up to 50 μm (Tessonnier *et al.*, 2017).

3.5. Measuring Dynamic Pressure and Ultrasound

Although ultrasound is an everyday technique, a precise measurement of dynamic pressure is challenging. As it will be shown later on, the expected pressure amplitudes in the case of ionoacoustic measurements are in the order of some Pascal and are not in the small banded frequency range of medical imaging applications, but range from tens of kHz to some MHz.

3.5.1. Piezoelectric Effect

Discovered by Jacques and Pierre Curie in 1880, piezoelectricity is the electric charge that accumulates in certain crystals when mechanical stress is applied due to the change in the electric dipole moment (Jacques Curie, 1880). This effect is also reversible: applying a voltage to these crystals will cause them to deform. It is therefore the method for measuring and producing dynamic pressure fields, i.e. sound waves.

Different crystal materials are available using piezoelectricity for e.g. igniters or precise stepping motors. For the measurement of ultrasound, there are two commonly used:

- **PZT** Lead zirconate titanate, a crystal material commonly used in transducers for medical and material science.

- **PVDF** Polyvinylidene fluoride, a foil material which can be made very thin. This is rather used in sensitive hydrophones.

Most transducers, i.e. devices producing *and* measuring ultrasound, use PZT crystals as the active medium. As a general rule of thumb, PZT is an order of magnitude more effective in producing ultrasound than PVDF, but also an order of magnitude less sensitive in receiving. For the generation of ultrasound, high bandwidth pulses with amplitudes in the order of some 100s of Volts are needed. As PVDF is typically used in thin foils mounted on a proper surface, they usually do not withstand high amplitudes and are therefore not used for generating ultrasound waves. As usual, the specific application will decide on material and size of the detector as a general engineering task.

Recently, the development of solid state based ultrasound devices (*capacitive micromachined ultrasonic transducers* cMUT) gained more and more interest. Here, two micromachined electrodes are produced around a capacitive gap. With the change of the distance between these electrodes, a change in capacity can be measured, and such micromachined devices are able to produce and measure ultrasound with the same quality as PZT, but with only a fraction of the cost (Haller and Khuri-Yakub, 1996, Khuri-Yakub *et al.*, 2000).

3.5.2. Different Forms of Detectors

Perhaps the most ordinary form of PZT transducers incorporates cut crystals in basically any form, from small pieces aligned in an array to almost 2" single elements. They have a wide-spread use in medical imaging applications and material quality control, e.g. the checking of weld seams or inner material defects. These applications require the generation of ultrasound, hence PZT is used.

For rather scientific applications, PVDF based hydrophones are used. Usually sold in ready-to-use sheets, they can be easily tailored and mounted on detector housings. The typical usage does not require the generation of ultrasound, e.g. calibration measurements or detecting of whale noises⁴. Those hydrophones are covered with an impedance matched plastic material for protection, but for high sensitive calibrations, bare detectors are available. Again, depending on the application, the PVDF can be mounted on the tip of a needle or in the middle of a membrane, thus giving the name of these types of hydrophones. Needle hydrophones are used when the positioning of a small detection point is important in order to detect ultrasound at precise positions in space. Membrane hydrophones tend to be bulky, but can be very broadband.

⁴Our own hydrophone, the C305X, is intentionally a *whale catcher*, a handy fact when passing U.S. Customs.

3.5.3. Calibration of PZT Transducers

Ultrasound transducers are usually not calibrated. A calibration can mean two different things. We can try to measure the sensitivity of a transducer in order to transfer measured voltage signals to pressure units. For a typical application like medical imaging, this is not important. In ultrasound imaging, the amplitude is only a measure of the reflectivity of an object and provides the contrast in the image. In first order, the absolute pressure value does not matter. A calibration can also mean the identification of the frequency capabilities of the measurement system, consisting of influences from the detector, amplification, and the oscilloscope. As described before in eq. (2.49), the total impulse response function (TIR) takes an important role on the final signal shape. Also, the TIR can then be used in the retrieval algorithm evaluation described in section 4.5.

Two different methods have been applied in order to determine the sensitivity of transducers used in this thesis. With the use of a calibrated hydrophone, the transducer's sensitivity can be measured in the substitution method. A stable, broadband source is measured first with the calibrated hydrophone, then with the unknown transducer in the position of the highest amplitude. A comparison of the frequency depending magnitudes provides a sensitivity curve for the unknown transducer. This method is strongly depending on the stability of the source and a separation of the SIR and EIR is barely possible.

Another approach is determining the EIR of a transducer with a simulated SIR in a measurement of a photoacoustic source. Here, the frequency content of simple targets can be determined in calculations (Caballero *et al.*, 2013).

3.6. Used Hydrophones and Transducers

In the following, the used ultrasound devices are listed and characterized.

3.6.1. PA Needle Hydrophone

The Needle Hydrophone from Precision Acoustics (Precision Acoustics, Dorchester, UK) is a calibrated Hydrophone with PVDF mounted on a 1 mm diameter needle. This hydrophone was used to calibrate the Olympus PZT transducers. The provided sensitivity is given in fig. 3.3. The relative uncertainty on the measured pressure is 15 %.

3.6.2. Olympus PZT

The workhorse in the presented experiments are single element PZT immersion transducers from Olympus (Olympus Europe, Hamburg, Germany). Those detec-

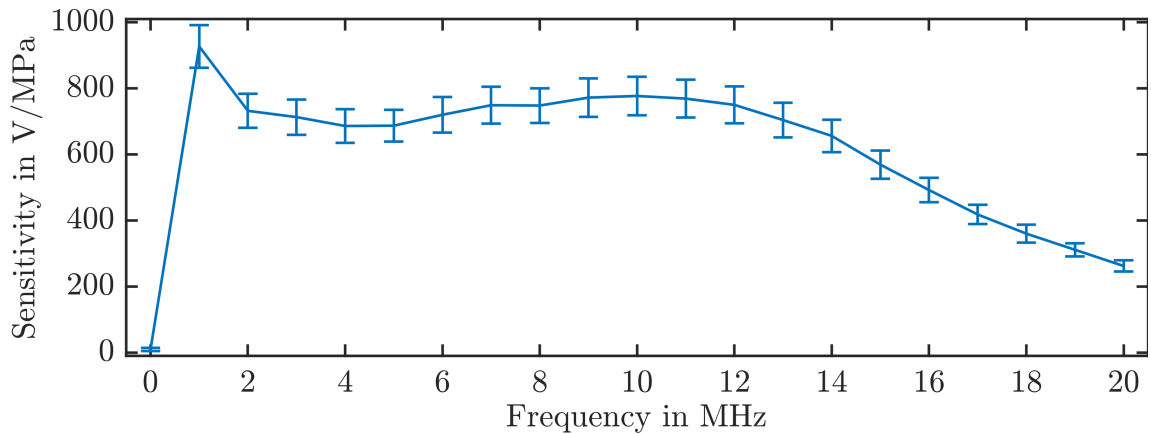


Figure 3.3.: Sensitivity of the PA needle hydrophone as provided by the manufacturer.

tors are usually not calibrated for an absolute pressure measurement, but have been calibrated against the PA needle hydrophone (Duque, 2016). The spherically focused transducers have a focal spot size of 1 mm, and a 6 dB field depth of 10 mm. Sources measured inside this field depth can be considered comparable in amplitude and frequency, and no disturbance of the signal is expected due to the SIR of these spherically focused transducers.

Construction

The active element is a PZT crystal contacted on both sides. The housing is the ground connection. Behind the active element is a backing layer, i.e. a filling of the detector that dampens ultrasound at the back of the active element. This reduces reflections from the backside of the transducer. The active element is covered by

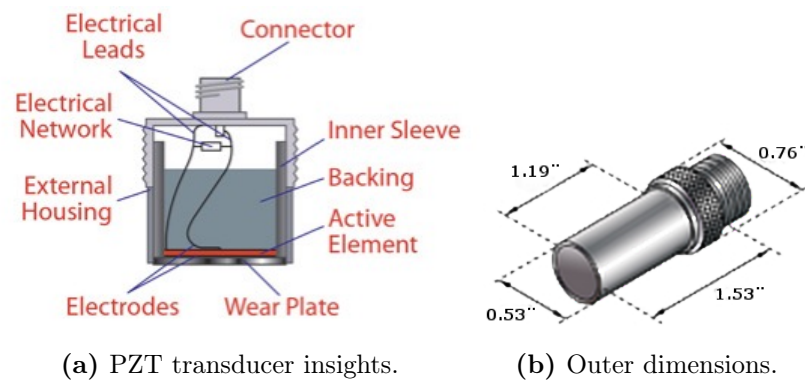


Figure 3.4.: Olympus PZT overview.

a $\lambda/4$ plate to match the impedances to water. Dimensions and insights are given in fig. 3.4. The active element can be flat or spherically curved. The first one is a good source for planar waves, the curved can measure ultrasound from small sources, that are smaller than the diameter of the active element.

Frequency and Sensitivity

The PZT transducers are matched to a main frequency by choosing the thickness of the crystal equal to $\lambda/2$ and the thickness of the matching layer of $\lambda/4$, where λ is the wavelength corresponding to the desired frequency. Hence the bandwidth is changing for the several considered transducers. As an example, the frequency bandwidth and sensitivity of the 3.5 MHz is given in fig. 3.5 as derived from calibration studies. The given frequency of those PZT transducers is meant as the main sending frequency, i.e. due to the thickness of the crystal the best frequency to generate ultrasound. The sending spectrum in fig. 3.5a peaks therefore at around 3.5 MHz. The receiving spectrum has additional sensitivities, in fig. 3.5b around 1 MHz. This is mainly due to the fact, that lower frequencies can transport energy into the resonator more efficiently.

Due to the flat or focused surface of the active element, these transducers are very directional. Basically only waves directly from the front are measured.

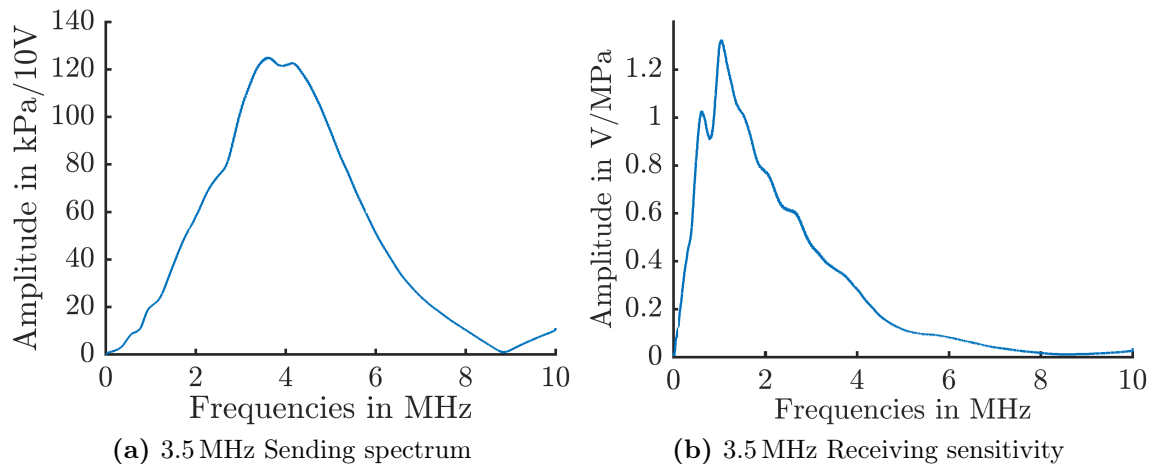


Figure 3.5.: Sending capabilities and receiving sensitivity of the 3.5 MHz spherical focused transducer V382 from Olympus measured with the PA calibrated needle hydrophone.

3.6.3. Cetacean C305X

The C305X is a single element PVDF⁵ hydrophone from CRT (Cetacean Research Technology, Seattle, WA, USA), intentionally designed to record whales. This hydrophone has been calibrated against a calibrated hydrophone from collaborates, which is presented in section 5.2.2. The X version of this hydrophone included a 33 dB pre-amplifier and a DC filter in the voltage supply. The hydrophone was modified with an aluminium shield around the cable connected to the ground of the amplifier voltage supply, which reduces the noise level by roughly two thirds.

Construction

The manufacturer provided no detailed information on the actual inner dimension and material of this hydrophone, which is also due to variations in the manufacturing process. The precise position of the sensitive element inside the hydrophone and the sound velocity of the casting material needed to be determined, as in the course of the measurements at clinical facilities a remaining offset in the absolute range measurements was found. After incorporating the actual position of the active element, this offset could be removed and accurate results were achieved. The characterization of the hydrophone included a CT-scan and an analysis by ultrasound means. Figure 3.6b shows an image of the hydrophone and CT scan side view. One can identify the active element next to the wires connecting it to the pre-amplifier. It is visible that this active element is not symmetric inside the plastic coverage. Hence, the orientation matters in the absolute evaluation of the measurements. As seen in fig. 3.6a, one can distinguish these two sides with the imprinted symbol of the manufacturer. Also, a sealing bond on the side of the hydrophone revealed the actual position of the sensitive volume and was used for levelling the hydrophone correctly.

Ultrasound Measurements on the C305X

In order to determine the actual dimensions and material sound velocities, the CRT C305X was scanned with an ultrasound transducer and the signals from both, the reflection signals recorded by the transmitting transducer and the recorded signal in the C305X, are measured and compared (Baumann, 2016). The setup and schematic is shown in fig. 3.7. From the bottom of a water phantom, an ultrasound signal was generated with a sending transducer. This ultrasound signal was travelling upwards towards the water surface, reflected at that surface, and then recorded by the sender again. The signals from both ultrasound devices, the send-

⁵Although not explicitly stated, this can be assumed. From the manufacturer side it is *a pressure sensitive foil material*.



(a) Top view of the C305X provided by CRT.

(b) CT image of the C305X.

Figure 3.6.: The CRT C305X inside out. a) Front view taken from manufacturer website. b) CT scan side view.

ing transducer and the scanned hydrophone C305X, are recorded simultaneously with an oscilloscope. The sound velocities were determined by the time of flight of the signal from the source transducer to the water surface and back, once with and once without the hydrophone in the path. By identifying all possible reflections and absorptions, the different run times could be compared to actual dimension. These measurements provided the following results for the thickness of front side s_f , the thickness of the back side s_b , the thickness of the active element s_d , and the speed of sound of the cover material c_{Hydro} :

$$\begin{aligned}
 s_b &= 4.19 \pm 0.03 \text{ mm} \\
 s_f &= 6.51 \pm 0.04 \text{ mm} \\
 s_d &= 0.60 \pm 0.06 \text{ mm} \\
 c_{Hydro} &= 1.89 \pm 0.01 \text{ mm}/\mu\text{s}
 \end{aligned}$$

These values have been used to correct the water depth in the absolute range measurements at the clinical synchrocyclotron, see section 5.2. In order to determine

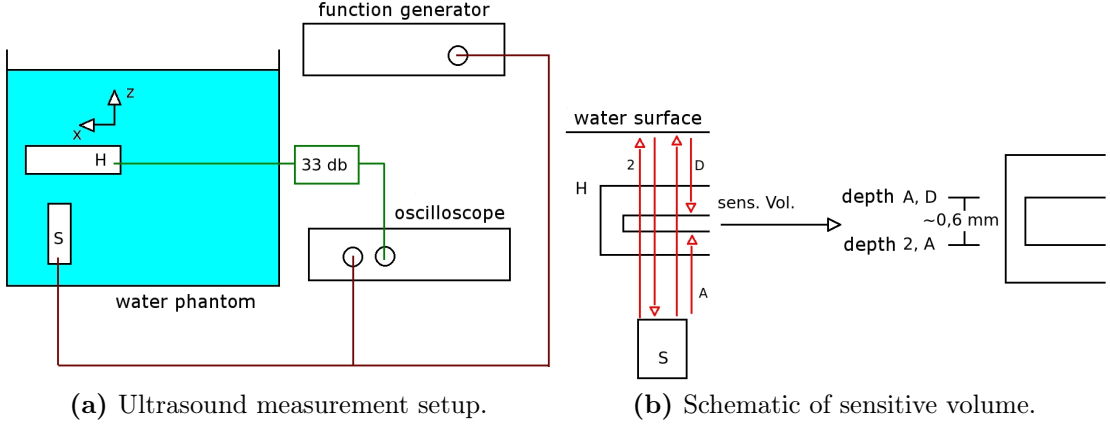


Figure 3.7.: Setup and schematics of the ultrasound measurements on the C305X hydrophone.

the range, the actually measured distance between the Bragg peak and the active element is assumed to be water. But the distance would then be overestimated, if this hydrophone was levelled with the active element at the water surface. Let us assume that the distance from the Bragg peak to the active element consists of the distance to the surface of the detector and the current thickness of the detector and the Bragg peak is faced with the front part of the C305X. The measured time then correctly consists of:

$$t_{cor} = \frac{s_{BP \leftrightarrow DS}}{c_{H_2O}} + \frac{s_f}{c_{Hydro}}. \quad (3.5)$$

It will be easier to simply multiply the derived TOF from the measurements with the sound velocity of the used water. Hence, the error will then be:

$$t_{simple} - t_{cor} = \frac{s_{BP \leftrightarrow DS} + s_f}{c_{H_2O}} - \left(\frac{s_{BP \leftrightarrow DS}}{c_{H_2O}} + \frac{s_f}{c_{Hydro}} \right) = \frac{s_f (c_{Hydro} - c_{H_2O})}{c_{H_2O} c_{Hydro}}, \quad (3.6)$$

which is positive. Hence, the distance between Bragg peak and the active element is overestimated if only the speed of sound in water is used. In order to use this simplification, this error is added to the measured depth of the hydrophone from which this simplified distance, Bragg peak to detector, will be subtracted. The corrected depth for using just the speed of sound in water will then be:

$$s_{newdepth} = s_{olddepth} + \frac{s_f (c_{Hydro} - c_{H_2O})}{c_{Hydro}}. \quad (3.7)$$

It would have been equally possible to correct both values to the detector surface, i.e. the depth of water by the current thickness f and the TOF by the time the signal passes this thickness s_f :

$$t_f = \frac{s_f}{v_{Hydro}}. \quad (3.8)$$

Frequency and Sensitivity Band

The provided frequency response and receiving pattern measurements for the considered hydrophone are shown in fig. 3.8. It is clear that this is a bi-directional detector with a smooth frequency response. The upper limit in the sensitive frequency band is mainly given by the built-in pre-amplifier.

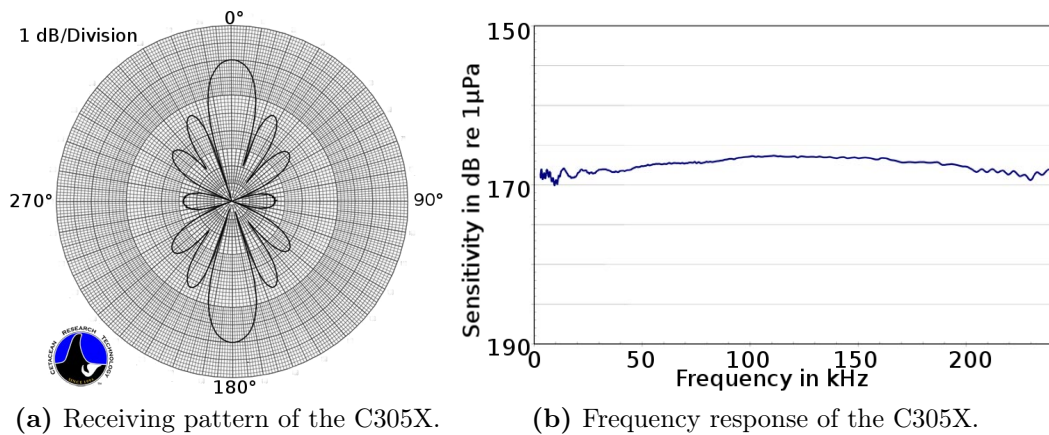


Figure 3.8.: Provided frequency bandwidth measurements and receiving pattern.

3.7. DAQ Software and Hardware

The presented data was acquired by a LabView program combining previously provided graphical user interfaces (GUI) and general purpose motor control software adapted to the used motor control card (Lehrack, 2014). Temperature, motor positions corresponding to the detector position, and oscilloscope signal were recorded and stored with a fixed file format which was kept over the last 3 years. This now provides access to all measured data with the same read-in routine. The export directly to a Matlab binary file was included and the text file only kept for backwards compatibility. The schematic of the software is given in fig. 3.9.

During this thesis, two different oscilloscopes had been used. In the beginning, a RTM2034 from Rohde&Schwarz had been used, later replaced by a PicoScope 6404 from Picotech. Both Oscilloscopes are 4-channel devices with a sampling frequency of 1 GHz and a bandwidth of 350 MHz, and provided reasonable remote capabilities via USB or Ethernet interfaces. The PicoScope 6404 is a pure USB/PC oscilloscope, i.e. it has no own monitor or knobs, and needs to be controlled by a computer. However, the main difference between these two oscilloscopes is the waveform rate, i.e. the frequency with which single traces are recorded and stored to the computer. The PicoScope 6404 can do this with a rate of 1 kHz, which

is much faster than the RTM2034. On the other hand, the RTM offers post-processing functions as averaging and filtering on the device before transferring to the computer. The fast waveform sampling rate of the PicoScope 6404 enabled the recording of every sub-macro pulse during the beam time at CAL, which is described later in section 5.2.3.

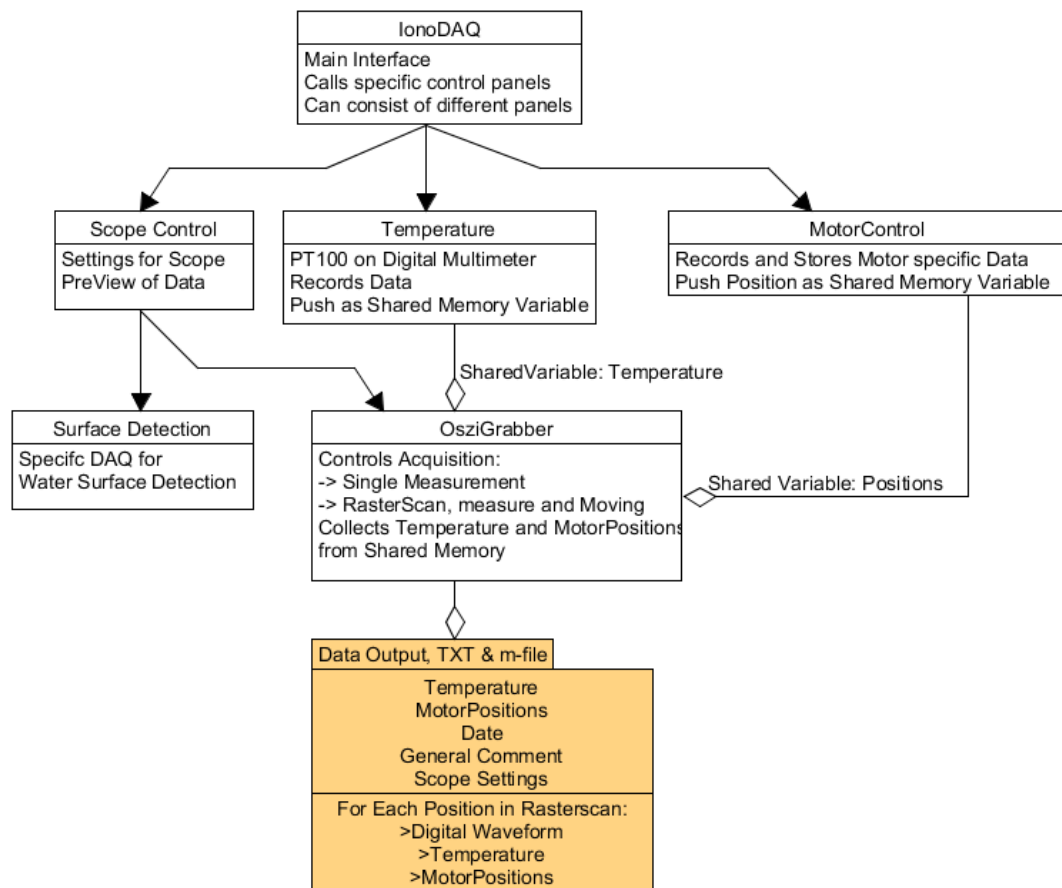


Figure 3.9.: IonoDAQ Software schematic.

4. Evaluation Techniques

LORD POLONIUS

Though this be madness, yet there is method
in 't. Will you walk out of the air, my lord?

HAMLET

Into my grave.

LORD POLONIUS

Indeed, that is out o' the air.

From *Hamlet* by WILLIAM SHAKESPEARE

4.1. Signal Origin

After the construction of a reasonable model, the measured signal can be analysed and the reconstruction concluded. As this work is focused on range determination, axial measurement positions are mostly used as this is the most promising geometry for measuring the range. In other positions the location of the detector needs to be known and taken into account. An extensive study on determining the range from non-axial positions and non-delta like excitations is presented in Jones *et al.* (2016a,b). The general setup has been introduced in chapter 3, and a common measured signal is shown in fig. 4.1.

Typically, this generic signal consists of up to 3 parts, all generated at different gradients:

1. A *direct signal* deriving from the Bragg peak front,
2. An *entrance signal*, in this work refereed to as a so-called *window signal*, from the entrance of the ions into the water phantom,
3. A *reflection signal* which is the reflection of the backward travelling part of the direct signal at the entrance foil.

Details of those 3 signals will vary depending on the shape of the dose distribution and the frequency response of the used detectors, as it has been demonstrated in section 2.3.4. Depending on how clear those signal parts can be separated, different approaches can be used in the evaluation. Consequences and implementations in the experiment are discussed in chapter 5. For the following evaluation techniques, it is beneficial to summarize the origin of these 3 signals thoughtfully, where only stress confined heatings are considered and the possible influences from a realistic transfer function is ignored for now.

The direct signal is generated at the Bragg peak and travels directly to the detector. This signal can be considered the most basic pressure generation observed by a typical detector in the one-dimensional field of view. As quantitatively derived in section 2.1.4, the heat induced by the ionization produces a positive pressure front as long as the heating is ongoing. As soon as the pulse width time is over and no additional heat is added, a negative pressure follows. It is to be noted that this is not a simple reverse process, i.e. an active cooling. Considering mass conservation, the compressed material in the positive front leaves an under-dense area behind it. The direct signal is therefore a bipolar signal representing the heated area along the observation direction of the detector. Depending on the beam spatial dimension, the signal can have different lengths depending on the observation angle. However, for short pulses, the expected pressure wave is the first order spatial derivative of the observed heating profile.

The window signal is generated at the entrance foil. The different materials with their different stopping powers and Grüneisenparameters will produce different temperature gradients. Especially at the border to water, this step results in a unipolar, negative pulse. The pressure amplitude of this signal will always be negative, as this marks the end of the heating function in water. Observed from the front, this will hence be negative. This signal can be very sharp, as the spatial dimension is given by the surface between the corresponding materials. The source location of the window signal front is at the water surface border. This can be either at an entrance foil, or directly air. This will be the exact spot from where the range in water is measured.

The reflection signal's origin is the same as the direct signal at the Bragg peak, but going in the opposite direction. It is then reflected at the air surface and detected. It is important to note two differences on the signal compared to the direct one. First, due to the reflection the Bragg peak is observed from the other side than before with the direct signal. Since the ionization is not symmetric in axial directions, i.e. the sharp front has a different temperature gradient compared to the plateau region, the reflection signal starts with a lower positive pressure from

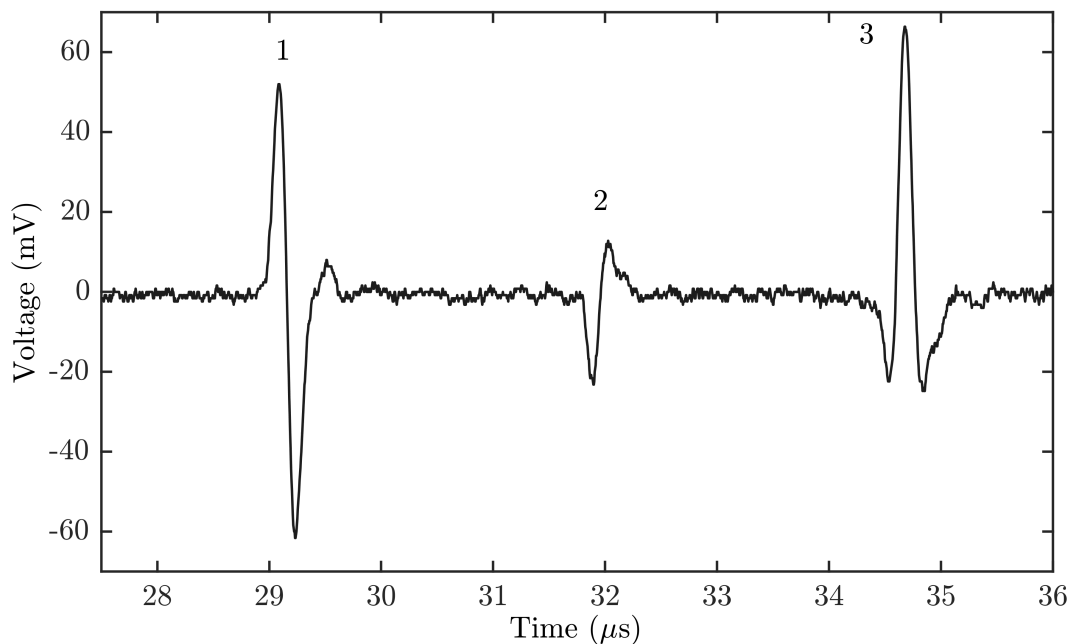


Figure 4.1.: Example of ionoacoustical signal, taken from Assmann *et al.* (2015). The signal was measured from a 120 ns 20 MeV proton pulse in a setup shown in fig. 3.1. The used transducer is a 3.5 MHz cylindrical focused PZT with a diameter of 0.5". Three distinct signals are visible, which are discussed in details in the text: (1) a *direct signal*, (2) a so-called *window signal*, and (3) a *reflection signal*.

the plateau followed by a negative pressure from the Bragg peak front. Second, the surface to air is always a closed end, as the acoustic impedance of air is much lower than in water or foil material. Hence, the reflection introduces a phase shift of π , an inversion in the amplitude. The final signal is then also bipolar starting with a lower, negative peak followed by a stronger positive peak. The location of this reflection is not the same as the origin of the window signal, if an entrance foil is used. When comparing the received ranges from the different metrics, the thickness of the entrance foil has to be taken into account.

In the example signal shown in fig. 4.1, a third peak at the direct and reflection signal is visible. This derives from the finite temporal pulse width of the signal. The exact details on the pulse generation in this specific example is given in section 5.1 and can be considered a rectangular pulse with a pulse width of 120 ns. At each temporal gradient a full spatial signal is generated, hence at the rise *and* fall of this temporal pulse, but with different amplitude, first a positive compression, then a negative rarefaction. For the direct signal, this means that the negative spatial signal from the turn-on temporal part is superposing the negative spatial signal of the turn-off part and vice-versa for the reflection signal. The third peak of the direct signal is hence the spatial signal of the plateau region generated at the turn-off part, while the reflection signal is the distal fall-off, respectively.

Additionally, the presented signal in fig. 4.1 is including the detector transfer function of a cylindrical focused transducer. It is to be noted that all 3 signal parts derive from different source location, and it is thus challenging to acquire all of these signals with a strong spatially dependent SIR. Hence, for measurements with high energetic, i.e. long ranged in water, heavy charged particles, it is not recommended to use a strongly focused transducer. In such a case, unintuitive differences between the direct and reflection signal can occur, making the direct interpretation of the measured signals difficult. In the cases presented here, no strong modification of the signal was seen, as the detectors were chosen such that possible influences of the SIR are low and the expected signal centre frequency is covered by the detector bandwidth. Hence, the measured signals are considerably similar to the previously presented pressure wave calculations and treated equally in this thesis. It is to be noted here again that the correct choice of matching detectors is a basic prerequisite for a good quality measurement. However, as this is a rather general engineering task, this will not be further discussed in full details.

4.1.1. Signal Elements following Albul et al

The derivation given in the section above is rather specific to the historical point of view of the experimental setup used in our group. The proof of principle experiments described later in chapter 5 were done with the ultrasound transducer axial to the beam. A more general description is given in Albul *et al.* (2004) and

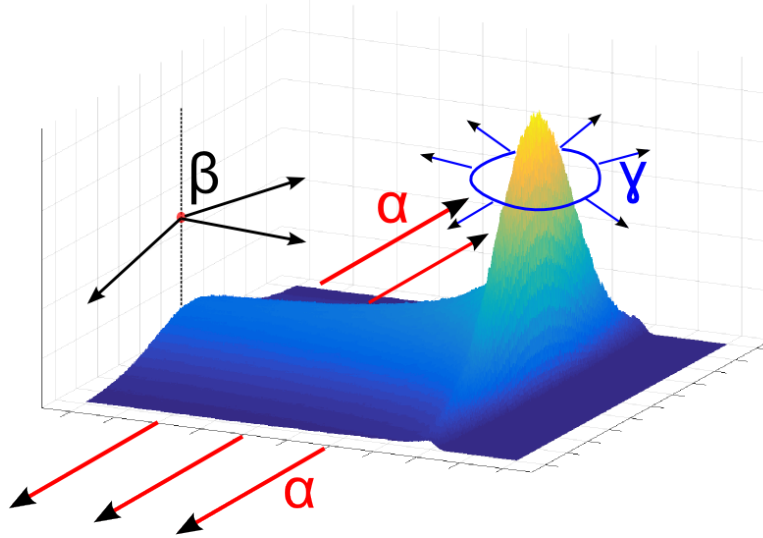


Figure 4.2.: Signal overview following Albul *et al.* (2004). Based on an exemplary, simulated dose distribution, 3 different source locations are marked with the according signal part dedicated to that source location: α , β , and γ . The β and γ signals correspond to the window and direct signal in fig. 4.1. The α signal is generated at the plateau region of the Bragg curve and travels laterally. This signal is hence not detected in axial detector configurations, which are the mainly applied configuration in the here described experiments.

this notation has been adopted in Jones *et al.* (2014). A descriptive overview is shown in fig. 4.2.

In Albul *et al.* (2004), 3 signal parts are identified and attributed to 3 different source locations. These signals are named α , β , and γ . The β signal is ascribed to the gradient at the water entrance. This corresponds to the entrance or window signal in our description. The source location of the γ signal is identified as the Bragg peak. Therefore, it corresponds to the direct signal and the reflection signal. In the work of Albul and co-workers, the reflection was not discussed and even intentionally not recorded.

The remaining α signal is generated by the cylindrical shape of the plateau region and evolves laterally. This signal component is hence not detectable in axial detector configurations and is therefore not used in the here described range evaluation techniques. For any tomographic approach, i.e. a full reconstruction of the heat distribution, measurements from different angles have to be done. This can be done e.g. with an ultrasound array. The possibilities and positioning dependent errors in such measurement scans are discussed in Jones *et al.* (2015), Kellnberger *et al.* (2016), and Patch *et al.* (2016).

4.2. Relative Evaluation

The signal shown in fig. 4.1 is one of the signals that is often used for demonstrating the basic range evaluation in ionoacoustics. As in this example 3 distinct signals are visible, it is possible to measure a range in a straightforward manner. Following the construction of a realistic heating function in section 2.2.1 and fig. 2.3, the origin of each of those 3 signals can be identified. It is now possible to use the time difference between those signals together with a calculated speed of sound and determine the range. This method is called *relative*, as it is independent from a comparison to another detector, which will be discussed in section 4.3. The measured pressure signal is identified as the first derivative of the heating function, i.e. the Bragg peak. As the focus is on range determination, the actual peak position is measured which corresponds to a zero crossing in the signal¹, because the zero crossing of the first derivative corresponds to an extremum in the original function. The points to extract in each part of the signal are therefore:

- the first zero crossing of the direct and reflection signal,
- an edge point in the window signal, optimally 50% between the peak and base value.

With those 3 points identified, two independent measurements for the range are available, i.e.

- the time difference between the direct and window signal, and
- half the difference between the direct and reflection signal corrected by the foil thickness,

both multiplied with the corresponding speed of sound. These considerations are only valid as long as the resulting signal is not blurred or disturbed. In the typical measurement setup, the matching of all components and choice of proper transducers are important, as discussed in more details in chapter 5. The example in fig. 4.1 was recorded using an inverting, broadband amplifier, hence inverted such that the measured voltage in the direct signal is positive, as expected from a compression pulse acting on the transducer surface. In general, the EIR and SIR of the detector system needs to be known and extracted from the measurements before a discussion of the signals.

Looking back at the simulation with a reasonable Bragg curve heating function, it is to be noted that the source locations of the window and the reflection signal

¹It is also possible to calculate the discrete integral of the signal and search for the peak positions. Trivially, those methods are analytically equivalent and comparing studies showed no relevant difference in the results beyond computational differences or challenges.

are not the same if an entrance foil is used. The window signal is generated at the border from water to entrance foil, but the reflection happens at the air-foil surface. For thin, metallic foils this difference could be neglected, but for thicker foils, the run time through the foil material needs to be subtracted from the time difference between direct and reflection signal before converting to distances. Only the range of charged particles in water is considered excluding any other material before. This means, that range values are given in water only, starting at the water surface, either to a foil or air. If this foil effect is not corrected for, the ranges derived from the window signal will differ and, as the speed of sound in plastic or metal tends to be bigger than in water, the range derived from the reflection will be underestimated, if the lower speed of sound in water is assumed instead of the correct materials speed of sound.

As discussed before, pulse width and shape will influence the signal. Especially pulse width just above the stress confinement will blur out the signal, since now temporal and spatial turn on and turn off parts will overlap indistinguishably. Identifying the signal points stated above can be challenging, besides noise considerations, resulting in cumbersome evaluations of the data by selecting points manually. One attempt to overcome this burden is the usage of the envelope of the signal, a smooth curve outlining the extrema of a function. This will provide a unipolar pulse which can be easily analysed by a simple peak search. However, due to the asymmetry of the heating function, the maximum of the envelope is not the maximum of the integral, i.e. the zero crossing in the direct or reflection signal. But it can be used for evaluating relative shifts between different settings, i.e. the change in range due to different thicknesses of absorbing material and the calculation of the water equivalent path length of that absorber as long as scattering and broadening of the signal can be neglected.

4.3. Time-of-Flight Mode

For high energy proton data shown in section 5.2, the recorded waveforms only contained the direct signal part due to two main reasons. With ranges of about 300 mm, the loss in amplitude due to the $1/r$ drop of spherical waves is considerable. In order to detect the low amplitude signals, shown in detail later in section 5.2, the hydrophone was rather close to the Bragg peak compared to the range of protons in water². Second, with the larger range, the range straggling increases as well, resulting in Bragg peak widths of several millimetres. This also reduces the spatial temperature gradient, the energy is distributed broader. The

²The range of 20 MeV protons is about 4 mm and the detector distance around 25 mm. The range of 230 MeV protons is around 30 cm and the measurement was done at a distance of 5 cm and less.

measured signals from high energy proton beams are rather low in amplitude, Jones *et al.* (2015) reports 5 mPa/ 10^7 protons with a noise level of 27 mPa. As the direct signal itself is not very prominent a high averaging is required, and measuring the reflection and entrance signal in these circumstances remains challenging. In Albul *et al.* (2004), full signals of 200 MeV proton bunches with a pulse width of 70 ns and 4×10^{10} protons/pulse, i.e. 6.4 nC, were recorded, but not discussed in terms of range determination. The authors tried to avoid any reflection signal and therefore limited the recording time. They did, however, record the entrance signal, there called β signal, from lateral measurements. The focus of those studies was on the identification of acoustic signal sources correlated to their extraordinarily intense proton beam.

For an evaluation of ionoacoustic data with only the direct signal, a scintillator can be used to define the time of protons entering the water phantom. The time difference between this start and the arrival of the direct signal is then the time-of-flight from the Bragg peak to the detector. With a precise levelling of the hydrophone, this distance can be subtracted from the depth of the hydrophone and this will provide a measure for the range.

Contrary to the relative evaluation, two time signals need to be correlated. Previously, the signal was interpreted as the first order derivative of the spatial heating function, therefore the zero-crossing is identified as the corresponding spatial point. However, the highest pressure is generated at the point of the highest temperature gradient, temporal and spatial. Hence, the maximum of the pressure signal represents the highest dose deposition, i.e. the Bragg Peak spatially, and the inflection point of the time signal, i.e. the steepest point in the scintillator signal. If a Gaussian shaped temporal signal is assumed, the inflection point is located at $\mu \pm \sigma$. These inflection points, which are extracted from the scintillator signal need to be correlated to the maximum compression or the minimum rarefaction in the acoustic signal respectively, according to the inclination of the time signal.

In the experiments conducted in Pennsylvania reported in Jones *et al.* (2016b), the long pulse width not fulfilling the stress confinement limited the resolution in range determination. To overcome this, post-processing methods including a deconvolution of the long pulse have been studied rigorously. As shown in fig. 4.3 taken from that publication, deconvolving the experimental scintillator trace can improve the signal. Although the deconvolved signal seems to be sharper and includes more features, the results using this deconvolution do not show a notably improvement in term of the final precision, probably due to the computational uncertainties introduced by the deconvolution process. However, one interesting effect is that after the deconvolution, the time zero is the maximum of the scintillator trace. This will be useful in an automatic evaluation of ionoacoustic signals.

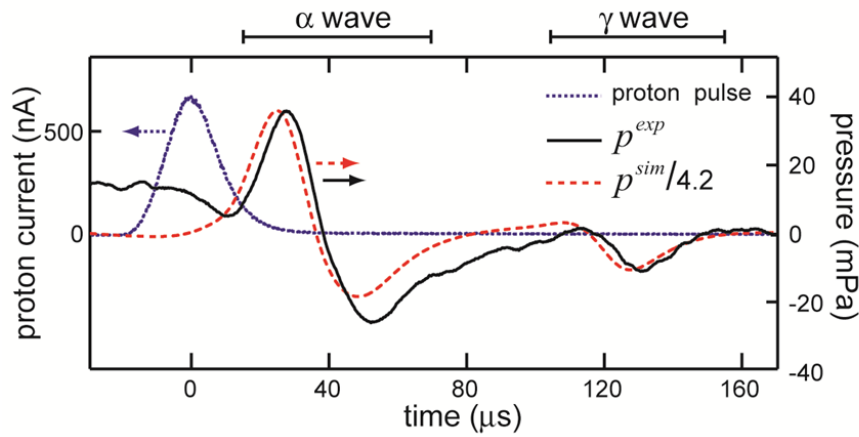
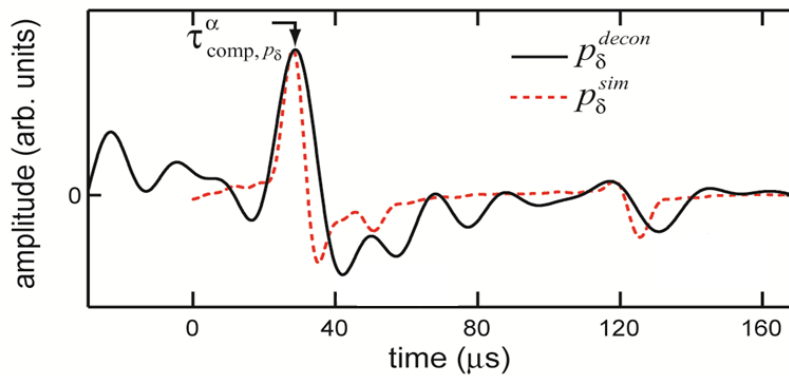
(a) Experimental data taken from Jones *et al.* (2016b).(b) Deconvolution result taken from Jones *et al.* (2016b)

Figure 4.3.: Demonstration of experimental data deconvolution taken from Jones *et al.* (2016b), compared to simulation data (red). From the top figure (a), the purple scintillator trace has been deconvolved from the black pressure trace, resulting in the bottom figure (b). The signal in (b) becomes sharper and aligned in time, meaning that the new time zero is the maximum of the scintillator trace. Comparative simulation data is shown in red.

4.4. Frequency Based Method or Autocorrelation Method

The previous descriptions are all based on temporal analysis, i.e. defining points on the time series and convert them to distances. Now, the frequency content of these signals is analysed. Figure 4.4a shows the frequency spectrum of the signal shown in fig. 4.1. Besides the main, broad distribution deriving from the trans-

ducer bandwidth centred around 3.5 MHz and heated area itself, a beating in the spectrum is seen. As the last part of the signal is identified as the reflection of the direct signal, the Fourier analysis will incorporate this as the beating, i.e. a repetition of the signal. This repetition can be used as this beating frequency corresponds to the relative time-of-flight already identified as the range of protons in water.

A valid approach to analyse the data with a frequency method would be an extraction of this inherent repetition of its own signal. The Fourier analysis \mathfrak{F} of the power spectrum of the signal $S(t)$ is therefore evaluated, i.e. the absolute value of the frequency spectrum:

$$N(t) = \mathfrak{F}^{-1} [\mathfrak{F} [S(t)]^2]. \quad (4.1)$$

This is also the autocorrelation of the signal following the Wiener-Khinchin-theorem (Wiener, 1930). The autocorrelation provides the self-similarity of the signal with itself and is therefore the method to analyse repetitive signals. In fig. 4.4b, a wavelength corresponding to the distance between the direct signal and its own reflection is visible and can be easily evaluated computationally. Compared to a cumbersome time-based analysis with a proper and fragile definition of points to extract, i.e. zero-crossings or thresholds, the implementation of the described method requires two Fourier transformations and a simple peak search and offers stable results with low computational demands. The thickness of the foil needs to be corrected as discussed in section 4.2.

As seen in fig. 4.4b) the absolute value of the resulting autocorrelation shows several distinct features. A DC part and a clear peak around 200 ns is shown, which can be considered an artefact of this transformation. The input power spectrum for the second Fourier transformation has only positive contribution, which explains the DC part. The corresponding wavelength of the overall transducer bandwidth of 5 MHz is 200 ns. This is basically the envelope of the displayed power spectrum in fig. 4.4a). Besides that, 2 peak pairs roughly below 3 μ s and at 5.5 μ s are visible. These peaks are deriving from the overall repetition of the signal in the window and reflection signal, respectively. As the reflection signal tends to be stronger, the evaluation will focus on this latter signal part only. The autocorrelation of the bipolar shaped signals is seen with two peaks. To give an explanation, an intuitive picture arises by shifting the direct signal through the complete waveform and add up the amplitudes. The negative tail of the direct signal is matching with the negative front of the reflection, hence providing a visible, negative autocorrelation signal. As the absolute value of the autocorrelation is plotted in fig. 4.4b, this is the first positive peak in each of the peak pairs respectively. Then, the positive front of the direct signal matches the positive tail of the reflection, resulting in the second, positive peak in the autocorrelation. As explained in the beginning of this chapter, the reflection signal is inverted compared to the direct signal, although

deriving from the same source location. The autocorrelation vanishes therefore at the zero-crossing of direct and reflection signal, i.e. where the direct and reflection signal overlap perfectly. Now, the positive front of the direct signal matches with the negative front of the reflection signal, and vice versa. Hence, the point to extract is the minimum between these two peaks at the largest distance. This will provide an evaluation comparable to a relative evaluation based on the reflection signal.

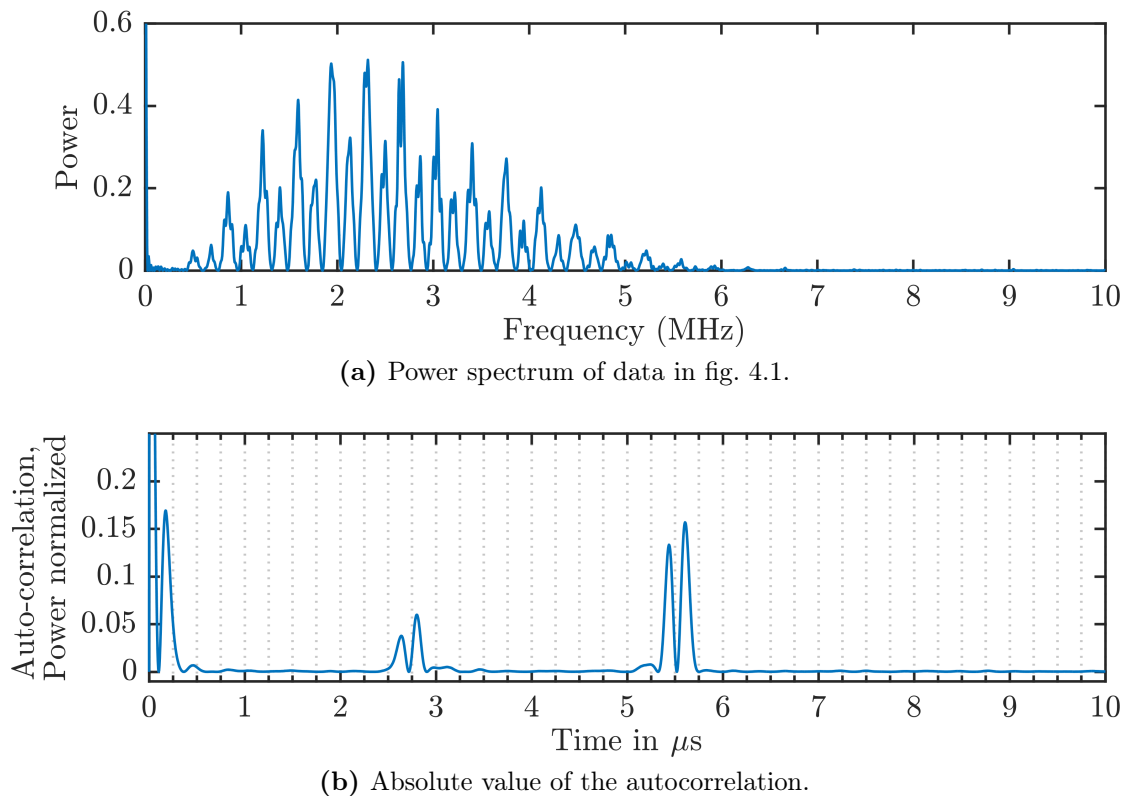
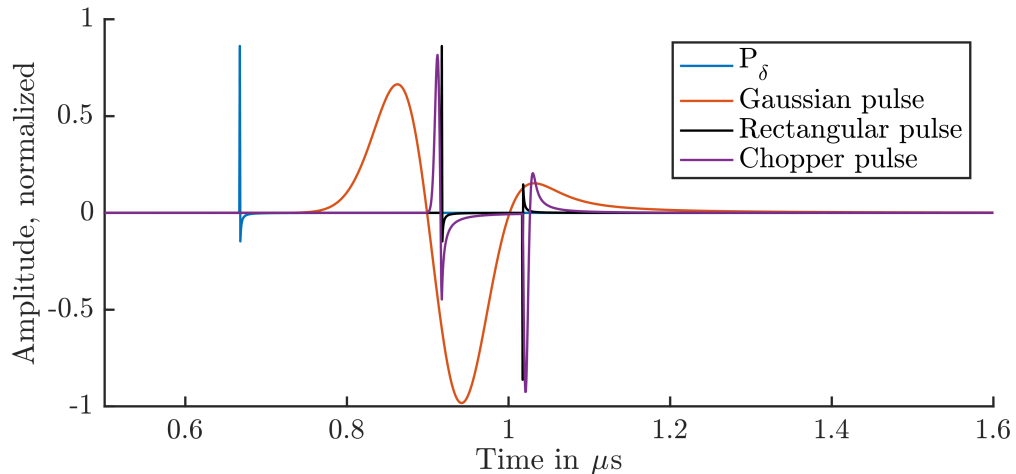
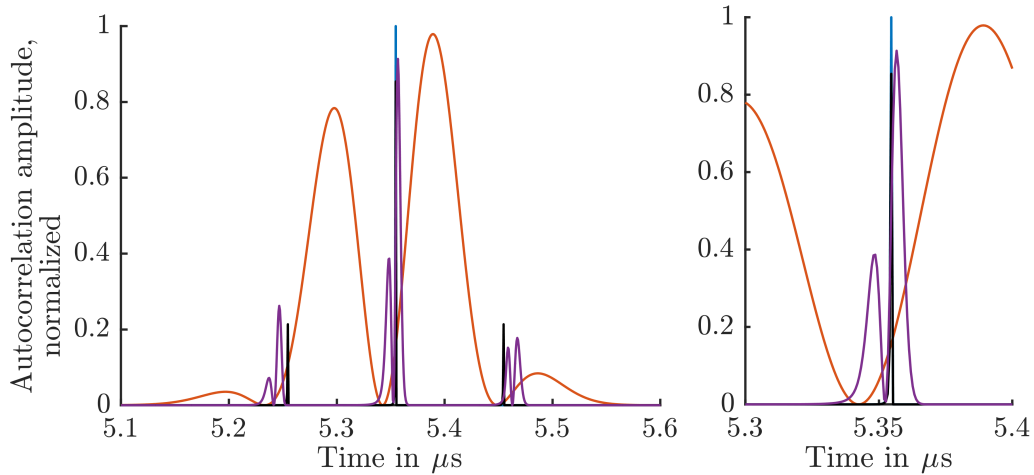


Figure 4.4.: Demonstration of the autocorrelation method on the example signal shown in fig. 4.1. (a) Power spectrum of an ionoacoustic signal. The bandwidth of the transducer and the spatial and temporal frequency content of the Ionoacoustic source is visible as the envelope of the signal. The signal is additionally modulated with the repetition of the signal itself, i.e. the reflection to the direct signal and to the window signal. This is visible as a beating with two different intensities. (b) Absolute value of the inverse Fourier transformation of the power spectrum in (a), providing the absolute value of the autocorrelation of the original signal. Two peaks are visible at two distinct positions corresponding to the repetition time of the window signal and the reflection signal with respect to the direct signal.



(a) Original Data.



(b) Absolute value of the autocorrelation

(c) autocorrelation zoom

Figure 4.5.: Result of autocorrelation analysis applied to simulation data presented in fig. 2.3. The original simulation data, derived from a delta spike excitation, is shown in blue, a convolution with a rectangular pulse with a pulse length of 100 ns in black, a MLL Chopper pulse in purple, and a convolution with a Gaussian profile with a FWHM of 100 ns in red. Amplitudes have been normalized and slightly adapted for a better view. Top Part: Original and convolved data focused on the direct signal. Bottom Part: Focused results of the second Fourier transformation. The blue peak is at $5.35 \mu\text{s}$, which corresponds to the correct range in this simulation.

In order to further understand the autocorrelation signals and the involved influences on the evaluation, a simulation of a 20 MeV proton beam stopped in water is investigated. Analysing a generic pressure signal provides a clear peak corre-

sponding to the time difference between direct and reflection signal, displayed as the blue signal in the lower part of fig. 4.5. Therefore the generic pressure from the simulation is analysed, additionally convolved with a 100 ns Gaussian pulse, a rectangular shaped pulse with a pulse width of 100 ns, and with a MLL chopper pulse of 100 ns. The latter is a rectangular pulse with smoothed edges with a rise time of 10 ns, which is expected at the MLL Tandem experiments described in chapter 5. This is also displayed in fig. 4.5, where the focus is on the direct signal only to demonstrate the effect of different pulse shapes on the signal. It is to be noted that the various influences on the signal shapes were presented and discussed before in section 2.2. The simulations presented here do not include any detector characteristics, as the purpose here is the study of proton beam properties, i.e. energy and pulse width, on the evaluation process. Detector dependent impulse response function should be accounted for in general in order to measure signals as clear as possible.

The convolution with the rectangular shape (black) can be interpreted as two delta excitation with a finite time difference. Hence, in the time domain two signals separated by the pulse width are observed. The two peaks have positive and negative amplitudes according to the gradient of the temporal heating function applied. Hence, turn on produces a positive signal, turn off a negative one.

In figs. 4.5b and 4.5c it can be seen that by applying a finite pulse width, a second signal appears. This is always the case for a bipolar pulse. As the provided heating function is very sharp, the pulses become bipolar after the convolution of the temporal profile. In the case of the rectangular signal, the rise of the main peak is coincident with the original peak at $5.35 \mu\text{s}$, which corresponds to twice the range in this simulation, i.e. the time difference from direct to reflected signal. The time difference between the two side signal after the second Fourier transformation is 100 ns, i.e. the pulse width. With the finite pulse length and the extreme case of a rectangular shape, the turn off part of the direct signal also matches the turn on part of the reflection, but this time difference is shortened by the pulse width, since the turn off signal is exactly delayed by that time.

A problem arises when assuming a Gaussian pulse shape (red). The minimum does not coincide with the desired value. In the enlarged view in the lower right part in fig. 4.5, the discrepancy is visible. The reason for this derives from the fact that convolving a Gaussian time profile is a basic low-pass filter removing high frequency components which would give this sharp peak. One possible approach is the use of a pulse width dependent study to correct the error which is made by using this minimum in the autocorrelation. This requires the provided pulse width as prior knowledge, which is reasonable without loss of generality, as the pulsed beam is the major prerequisite for Ionoacoustics and has been rigorously studied during the experiments. The correction can be calculated from simulation studies

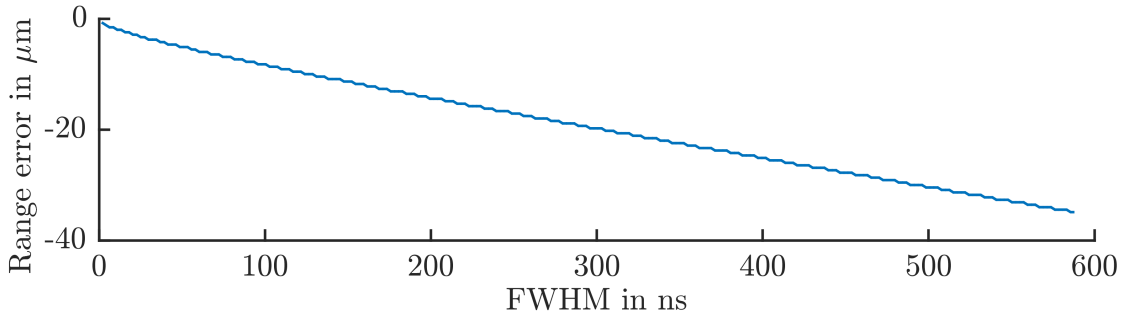


Figure 4.6.: Correction values derived from evaluation of simulations with different pulse lengths. This is the error associated to using the minimum between the peaks as shown in fig. 4.5.

on the temporal profile. Such a pulse width study is demonstrated in fig. 2.6, and results of the correction factor are shown in fig. 4.6 for a 20 MeV proton beam. These corrections are similar to the findings in Jones *et al.* (2016a) where this intrinsic error is obvious for zero-crossing metrics discussed *ibidem*. There, the solution is the deconvolution of the temporal shape providing again the generic signal P_δ .

4.5. Retrieval of Polyenergetic Spectra

As described earlier in section 3.2.1, laser driven ion acceleration produces polyenergetic ion spectra but with a very short pulse width and high fluence. In order to reconstruct the energy spectrum, the broad energy distribution can be considered as a superposition of single energy heatings. Assuming that the signal is clearly separated in the known 3 parts, each energy in the spectrum results in a distinct pressure trace. Hence, the expected final signal is also a superposition of pressure traces from mono energetic heating functions. A *simulated annealing algorithm* (Khachaturyan *et al.*, 1979, 1981) can be used in order to find a good fit of a predicted pressure trace to measured signals. Figure 4.7 is a flowchart of this procedure, which has been developed in Yang (2017). Starting with an initial guess, the fit quality of an original spectrum is compared against a modified spectrum. The difference between those energy spectra is applied randomly and depending on the *temperature* of the state, hence the modification will decrease during the *annealing*. From these spectra the actual heating functions and finally the expected pressure trace can be calculated. If this pressure prediction from the modified spectrum is a better fit to a measured signal than the one from the original spectrum, the latter will be replaced by the modified one. If not, the modified spectrum is rejected with a probability of p or the modified spectrum is used

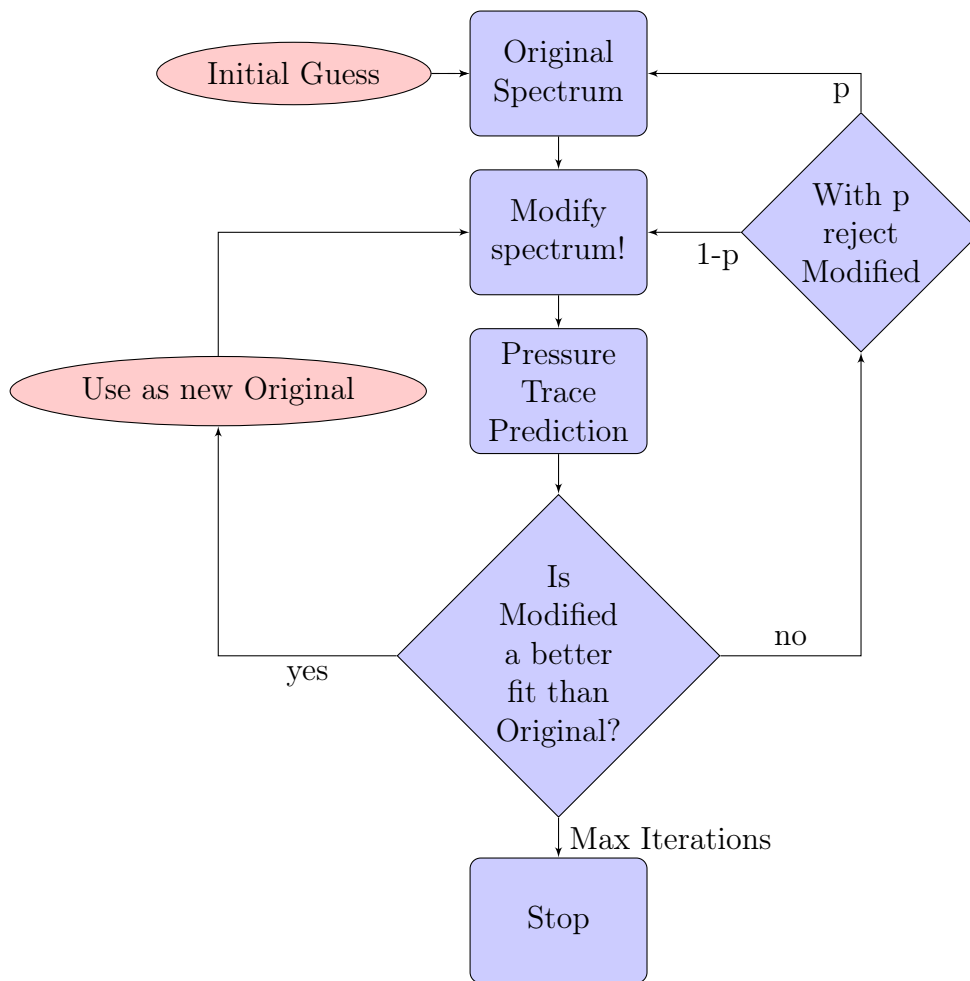


Figure 4.7.: Flowchart of simulated annealing procedure.

despite the worse fit. This step is introduced in order to ensure that the final state is an actual global minimum, i.e. the best fit of the predicted pressure trace to a measured signal. Generally speaking, this method fits a measured trace to a guess spectrum. As the spectrum can be predicted from any sources, a better fit of the guess spectrum is a closer guess of the acoustic source. After some guesses, a good description of a source is achieved that generates a spectrum close to the measured signal. As only one detector is used in this setup, the resulting energy spectra are measured in the field of view of this detector, i.e. along a line. However, the lateral size of this source in comparison to the detector size and the distance between the two does matter. Hence, the actual spot size of the irradiation had to be considered as a free parameter in the prediction of the pressure traces (Yang, 2017). The crucial part in this process is the correct prediction of the pressure trace which

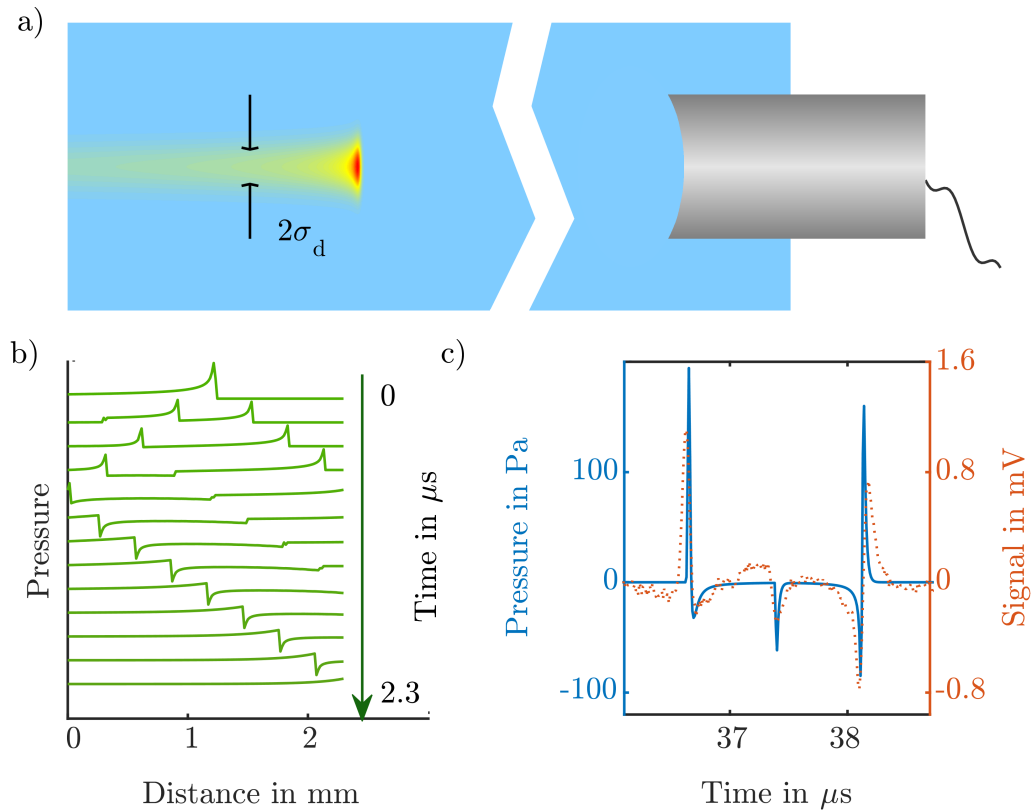


Figure 4.8.: Polyenergetic retrieval work flow taken from Yang (2017). (a) Schematic of the experimental setup. (b) Simulated pressure propagation. (c) Comparison of simulated pressure to measured transducer signal. This includes also filtering effects of amplifiers and transducer bandwidth. Starting from an initial guess on the energy spectrum, the final energy content of the measured signal is retrieved in an iterative process.

requires a full characterization of the transfer function of the ultrasound detector. In the experiments presented later, the detector system including its amplifier was calibrated with a known heating function from mono-energetic proton beams at the MLL Tandem. This completes the linear system from source to detection, including all elements in eq. (2.49). With this approach, fully theoretical studies and predictions can be made i.e. assuming any energy input expected signals can be predicted depending on machine and detector parameters. For the reconstruction of energy spectra from acoustic measurements, the term *Ion Bunch Energy Acoustic Tracing I-BEAT* has been introduced. The experimental implementation is described in section 5.4.

4.6. Conclusion on Evaluation Techniques

4.6.1. Comparison of the different methods

In order to appraise the presented evaluation methods, results from different range measurements are summarized here. This comparison focuses on the most precise data, which are 20 MeV protons measured at the MLL Tandem in Garching. The exact experimental details are given later where more sophisticated measurements are presented in chapter 5. The general setup details can be taken from fig. 3.1. Here, the focus is on relative evaluation methods, i.e. an extraction of zero-crossings on the one side and the according minimum value in the autocorrelation function (see section 4.2 and section 4.4 respectively for details on the methods). The results of these two evaluation methods are given as reflection and autocorrelation in table 4.1. The data was recorded over several beam times with slight changes affecting the range. Those changes are a higher energy of 21 MeV in July 2014, and different distances of air between the exit and entrances for all beam times. Those differences are respected in comparative simulations and the peak position is given in table 4.1. An error estimation is made in section 5.1.3 later on, which estimates the uncertainty of these simulation to be 28 μm .

The resulting ranges listed in table 4.1 reproduce the simulation prediction with a precision of 40 μm and below for the zero-crossing method and 100 μm and below for the autocorrelation method. These values are retrieved from a histogram fit of all calculated ranges to a normal distribution. Error estimations considering uncertainties in temperature measurements are discussed later. The focus of this summary given here is on the quality of the evaluation techniques itself. Besides, the temperature was stable during each of these measurements and only changed significantly when the water was changed. The values are generally over-estimated,

Table 4.1.: Summary of 20 MeV proton beam time results. Ionoacoustic range measurements are evaluated with different evaluation methods and compared to peak position retrieved from Geant4 simulations.

Beam time	Range from G4	Reflection	Autocorrelation
11/2013	4034 μm	4068 \pm 41 μm	4136 \pm 29 μm
07/2014	4423 μm	4490 \pm 19 μm	4561 \pm 63 μm
12/2014	4034 μm	4021 \pm 8 μm	4099 \pm 102 μm
03/2016	4030 μm	4028 \pm 7 μm	4086 \pm 2 μm
06/2016	4031 μm	4087 \pm 6 μm	4128 \pm 21 μm
01/2017	4028 μm	3949 \pm 17 μm	4089 \pm 13 μm

the zero-crossing method seems to reproduce the simulation results better than the autocorrelation. The differences between the two methods range from 60 μm to 140 μm . Compared to the simulation result, the relative error in accuracy is 1.5 % to 3.1 % for the autocorrelation method and 0.1 % to 1.9 % for the zero crossing method. A discussion and comparison of this and other range determination results is given in section 6.1.1.

4.6.2. Closing

In this section several evaluation techniques have been introduced. The order presented here can be read chronologically, as the methods became more sophisticated during the course of this thesis. With the development of the model based approach for the polyenergetic case, the used evaluation methods have been reviewed critically in simulation studies. With the full description of the functions contributing to the signal shape and especially its frequency content, a time based approach based on zero-crossings alone might not be sufficiently justified for future measurements. It is, however, when measured with a broadband amplifier and mono energetic short pulses very intuitive, as the measured trace is very close to the described generic pressure signal. Therefore, it can be simply integrated to receive the spatial heat distribution, hence the Bragg peak in a depth dose profile. Once this is not directly valid any more, a model based approach including all effecting parts in the measurement is needed. The requirement of a short pulse, or at least a defined rising edge, as well as matching of the detector's bandwidth to the expected signal will ensure the measurement of a signal with sufficient SNR. In order to fully evaluate the signal fast and accurately, the described frequency based approaches including a full calibration of the detector is intended in the development towards a reliable beam monitor for any pulsed particle beam.

5. Experimental Studies

Man muss schon sehr genau hinhören!

Der sprechende Hund from LORIENT

If I have seen further it is by standing on the
shoulders of giants.

ISAAC NEWTON in a letter to Robert Hooke

In this chapter, experiments which use the ionoacoustic range determination technique are presented. Again as with the evaluation methods, this chapter can be read chronologically from the first proof of principle with 20 MeV to the high energetic beams at medical beam facilities. Basic range measurements have been given exemplarily in section 4.6.1. Now, more advanced experiments using ionoacoustics are shown in section 5.1. Then, the experiments at high energy particle accelerators are presented, starting with the medical, pulsed cyclotron in UPENN in section 5.2.2, and the novel superconducting synchrocyclotron at CAL in section 5.2.3. Measurements with heavier ions at high energies at 200 MeV/u and 300 MeV/u are presented from the beam times at GSI in section 5.3. As a final experimental section, the experiments conducted at LEX with laser accelerated protons are shown in section 5.4, before this chapter is concluded in section 5.5.

5.1. Proof of Principle Experiments with 20 MeV

The basis of all presented experimental results in this thesis are proof of principle experiments with 20 MeV protons at the MLL Tandem accelerator in Garching (Assmann *et al.*, 1974, 2015). The rather easy access to this beam was used for general studies on new detectors and other DAQ devices, and the flexibility here allowed adaption to experimental conditions, which would not be possible at a certified medical facility. This proton beam can be efficiently chopped and bunched before the main acceleration. Hence pulse widths down to 1 ns are possible. The chopper is a series of fast switching electrical fields transversal to the beam axis. When synchronized to the particles speed, the constant (*continuous wave CW*) beam extracted from an intense source is transformed to a pulsed beam with maximum 5 MHz repetition frequency. The chopper hence reduces the duty cycle to almost arbitrary values. A buncher is a longitudinal electric field with a high amplitude. This will give the particles an additional energy variation further compressing (bunching) the beam pulse after the chopper. An intuitive picture is that particles in the front part of a longer pulse are decelerated while particles in the later part are further accelerated depending on the phase of the electrical buncher field. When synchronized and timed precisely, the arrival time of all particles at the experimental place can be synchronized to a few nanoseconds (Rohrer *et al.*, 1984). This is a rather sophisticated installation and is usually not available at a medical accelerator. The pulses available at the MLL Tandem with the use of the optional buncher are Gaussian shaped with a FWHM of 1 ns. Using only the chopper, the pulses have a step-function-like shape with a constant rise and fall time of 3 ns and a minimum FWHM of 46.4 ± 0.5 ns (Freiwang, 2014). For simplicity, this chopper setting will be referred to as 40 ns. It is also possible to apply an external logical signal, allowing basically any pulse width up to ms and arbitrary

pulse repetition with the same rise time of 3 ns.

The range in water of 20 MeV protons is only 4 mm and is therefore not considered for medical application, besides cell studies or surface lesions of small animals. A study of range measurements has been presented as a conclusion on the evaluation methods presented in the previous chapter, see section 4.6.1. The focus in the following is on advanced measurements, where the determination of the range can be considered the basis, or additional measurements and simulations, which were required in order to achieve the range precision and accuracy presented in section 4.6.1.

5.1.1. Simulation of Experiments with 20 MeV Protons

As a starting example, all parts of the simulation demonstrated in chapter 2 are brought together and compared to measured pressure signals. By investigating the basic properties of the ionoacoustic setup, the performance of applied simulations is evaluated.

The experimental setup consists of a water basin, already shown in fig. 3.1 and a PZT single element ultrasound transducer (Olympus PZT, see section 3.6.2 and setup details in section 3.1) with a spherical focus and an element size of 0.5". In this explicit setup with 20 MeV protons, the particles leave the vacuum through a 11 μm titanium foil, pass some centimetres of air, and enter the water tank through a 50 μm Kapton foil. The energy loss of 20 MeV protons before the water is calculated to be 480 keV. A selection of stopping power values for 20 MeV protons in relevant materials is given in table 5.1. The blue signal in fig. 5.1 is a measured signal under the experimental circumstances presented in section 3.1 and is given as an arbitrary example, which is now reproduced using the described ultrasound simulation techniques from section 2.3.

Table 5.1.: Stopping power values for different materials and 20 MeV proton beams. Data was derived with the libdEdx interface based on NIST PSTAR values (Lühr *et al.*, 2012, ICRU, 2014b).

Material	Mass stopping power in MeVcm^2/g	Density in g/cm^3	Stopping power in $\text{keV}/\mu\text{m}$
Air	0.027	1.2×10^{-3}	2.763×10^{-3}
Water	26.05	1	2.605
Kapton, Polyimidefilm	23.84	1.42	3.385
Titanium	17.50	4.54	7.945

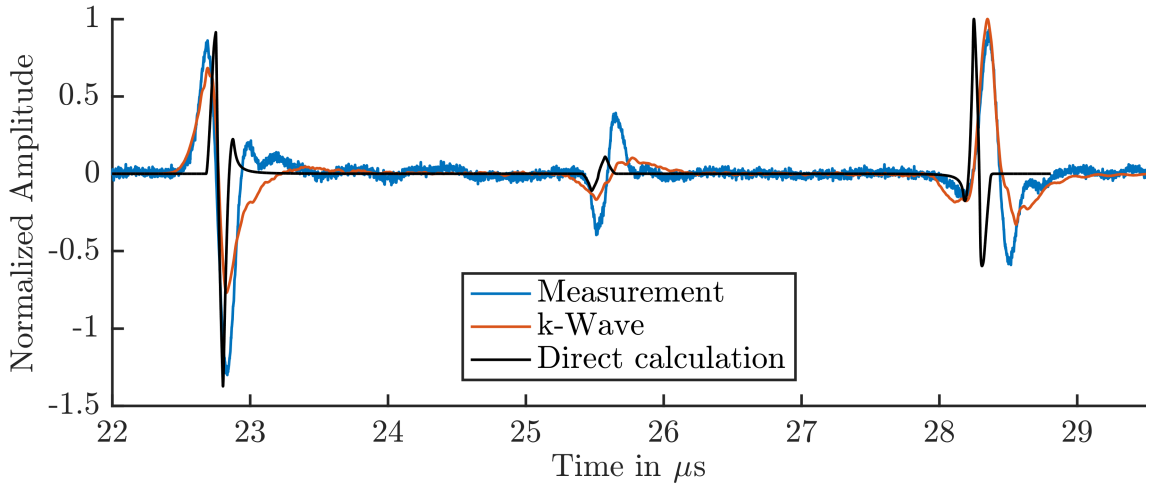


Figure 5.1.: Comparison of measurement signal with simulations. Here, a 3.5 MHz transducer with 0.5" diameter and 1" focal length, spherically focused, is simulated measuring a 40 ns pulse at the MLL Tandem accelerator.

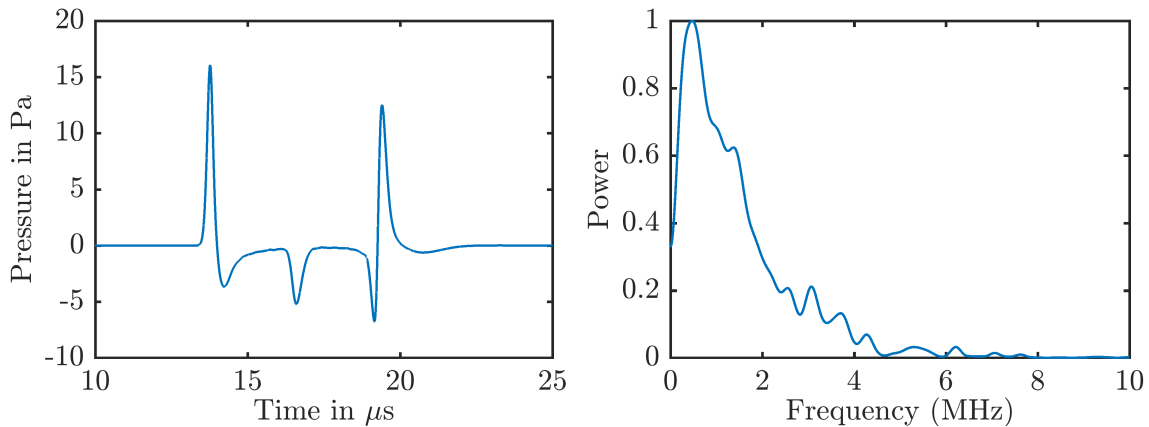
The signal in red in fig. 5.1 is the result of a k-Wave simulation (see section 2.3.2) including a 3.5 MHz spherically focused PZT transducer with an element size of 0.5" and a focal length of 1". The black signal is from a direct calculation for a single point detector (see section 2.3.1), the analytical description of the Bragg curve, and convolved with a theoretical SIR (see section 2.3.3). In order to match the example measurement, a 40 ns chopper-like rectangular pulse has been convolved, the signals are aligned by the first zero-crossing and the amplitudes are normalized by the maximum of the signal. In this case, this is the positive peak of reflection signal, since here the turn off temporal signal and the spatial signal from the plateau region are superimposed. This signal part is always larger in amplitude than the first positive peak of the direct signal. This can also be seen at the negative signal part of the direct signal, which corresponds to this positive peak at the reflection signal. The signal shape and timing is studied first, then the signal amplitude is addressed.

It is shown that the k-Wave result matches the correct timing and signal widths, but the direct calculation shows a better coverage of the high frequency parts, e.g. the second positive peak in the direct signal. It is to be noted that all the simulation signals use the same speed of sound and range, as well as the same temporal heating function. Hence, the mismatch for the direct calculation must derive from the spatial heating input and the fact that a single element detector blurred by a theoretical transfer function is not sufficient to emulate the broadening of the signal and the large scale detector. This broadening occurs on the spherical expansion of the direct signal and the reflection, which is covered realistically in

k-Wave, but is simplified in the analytical approach.

It can be summarized that both simulation techniques have their specific advantages and disadvantages. The direct calculation and its simplification quickly provided results in familiar signals, i.e. simulation signals similar to presented measurements in this specific setup. This fast simulation method can be used to study the signal shaping, i.e. from different temporal profiles and transducer surfaces, and new approaches for evaluations, but the heating input is not realistic and too sharp, at least for protons with higher beam energies. On the other hand, with k-Wave a realistic dose distribution from Geant4 simulations can be incorporated into the simulation as well as the correct pressure evaluation also at the reflection. This demands a longer simulation runtime compared to the direct calculation and is limited by the grid spacing, as is every finite element simulation. One problem arising during the following studies is the discrepancy in amplitude prediction between the measurements and simulations. Figure 5.2a shows a k-Wave simulation result for a 20 MeV proton beam in water, pulse width of 100 ns, 3×10^6 particles per pulse, and a distance of 25 mm from the Bragg peak. The size of the detector matches the PA needle Hydrophone, i.e. 1 mm^2 . The peak pressure in the simulation is 16 Pa compared to the measured pressure presented in section 5.1.5 of 12 Pa.

Additionally, all the simulations have problems estimating the amplitude of the window signal. In relation to the direct and reflection signal, the amplitude of the



(a) Simulation of 20 MeV ionoacoustic pressure. (b) Frequency spectrum of the signal shown in fig. 5.2a

Figure 5.2.: Simulation of 20 MeV ionoacoustic pressure. The experimental parameters match the setting of quantitative measurements, which are discussed in detail later in section 5.1.5. a) Simulated pressure amplitude. b) Frequency spectrum of the signal shown in a).

window signal is generally underestimated compared to the given measurement, as seen in fig. 5.1. This problem increases significantly in experiments with a thicker entrance foil prior to water. When a 300 μm Kapton foil was used instead of 50 μm Kapton with 20 MeV protons, the window signals amplitude was found to be in the order of the direct signal amplitude (see fig. 5.3a). Two effects need to be considered in order to understand this phenomenon. First, the thicker entrance foil further reduces the beam kinetic energies, and introduces additional scattering as well. Hence, the spatial gradient at the Bragg peak is reduced, which decreases the direct signal. Second, with a width of 300 μm , the absorption of beam energy in the entrance foil cannot be neglected. The stopping power of Kapton is about 30% higher than in water, and the acoustic impedance is about 2 times higher, hence the transmission from Kapton to water is about 2/3. The remaining third of the pressure inside the Kapton foil is then again reflected very efficiently at the surface to air, building up an etalon or a half-open-pipe. This provides a basic wavelength λ of 1.2 mm. This derives from the 300 μm Kapton foil defining the $\lambda/4$ in this half-open pipe and assuming a speed of sound of 2.2 mm/ μs in Kapton, this corresponds to a frequency of 1.8 MHz. For the 50 μm foil, this frequency would be 11 MHz, which is too high for the usually used PZT transducer. An example of a signal and frequency spectrum of the window signal only is given in fig. 5.3. Here, the stronger window signal compared to the direct and reflections signal is visible. In the frequency spectrum focusing on the window signal, a main peak at 1.6 MHz can be seen. Additionally, a peak at 3.2 MHz is visible, which would

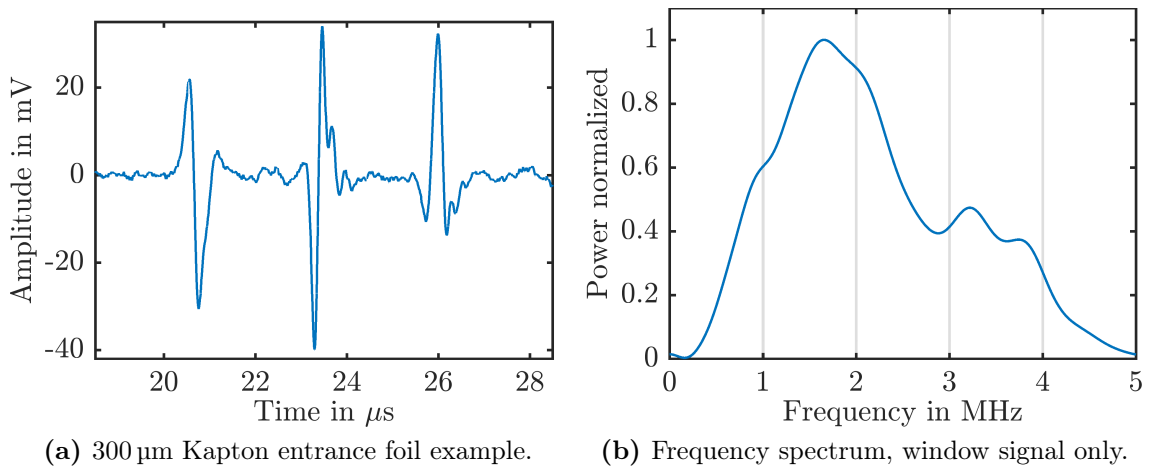


Figure 5.3.: Analysis of thick Kapton entrance foil. a) Example waveform for 20 MeV protons passing through 300 μm Kapton entrance foil. b) Frequency spectrum of a) from the window signal only. The peak frequencies are 1.6 MHz and 3.2 MHz, corresponding to the expected etalon frequencies.

correspond to $\lambda/2$ of this etalon. However, the 1.6 MHz is in good agreement with the previous rough calculation, considering the uncertainty of the speed of sound in Kapton and a possible expansion of the entrance foil due to heating during the experiment. Calculating backwards from the measured frequency of 1.6 MHz assuming the given speed of sound in Kapton of 2.2 mm/ μ s, a thickness of the Kapton entrance foil of 305 μ m is derived, corresponding to a relative difference of 1.8% to the known value. This can be considered in good agreement with the measured thickness of the foil material.

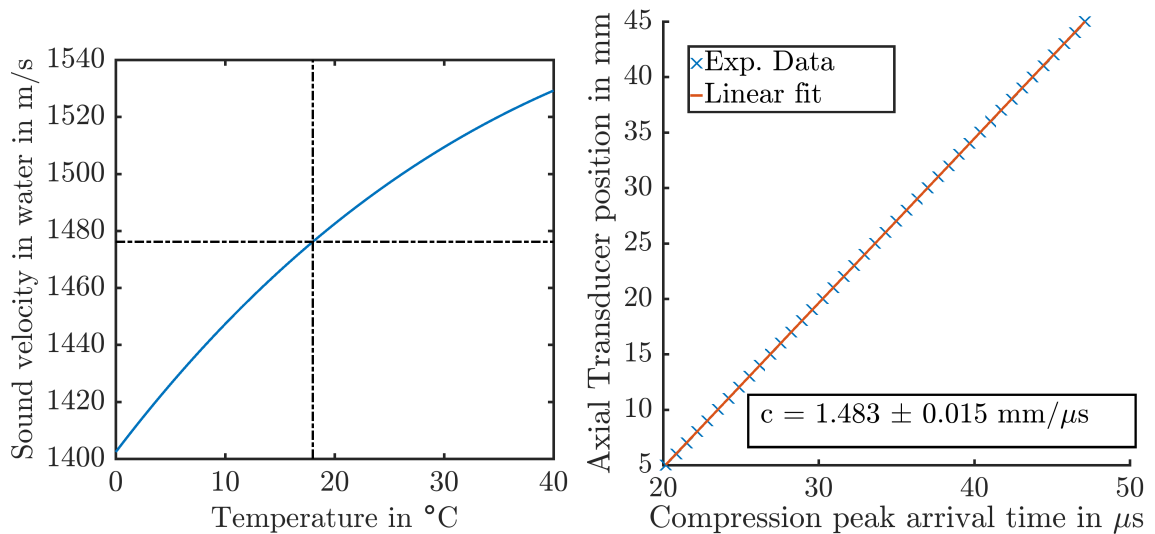
However, this etalon effect is not reproduced in any of the simulations. The energy loss in the foil is taken into account in the Geant4 simulation, thus reducing the final range in water of the used heating function. However, this energy loss in the foil material is not scored in the dose distribution. Furthermore, as the source of the window signal is in general a surface effect, a simulation based on grid values struggles to analyse these sharp edges. In order to avoid errors introduced by high frequencies, the given density and corresponding speed of sound distributions in the k-Wave simulation are smoothed before the calculation. Otherwise, the simulation becomes unstable very quickly. It is to be noted that this smoothing is usually not applied to the source pressure input and thus not effecting the Bragg peak region.

5.1.2. Deriving the Speed of Sound in Water Experimentally

For the evaluation of ionoacoustic range measurements, a precise knowledge of the actual speed of sound in water is essential. After all, measured flight times are converted to a distance using this speed of sound which is generally given as:

$$c = \sqrt{\frac{K_s}{\rho}} = \frac{1}{\sqrt{\rho\kappa}}, \quad (5.1)$$

where K_s is a coefficient of stiffness, the isentropic bulk modulus, κ the isothermal compression, and ρ the material density. While the K_s is a material dependent constant, the density changes with temperature and is therefore the main influence on the speed of sound in the presented experiments. Figure 5.4a shows the dependence for liquid distilled water, i.e. in pure standardized conditions. Those values are usually taken in laser interferometric measurements, which are precise measurements of a displacement of two transducers. The acoustic signal generated by one transducer and the receiving signal at another transducer are compared and phase matched, which gives a precise measurement of the path lengths and thereby a comparison of the speed of light with the speed of sound in water (Kroebel and Mahrt, 1976). However, as this is a rather elaborate measurement, multivariate polynomial fits have been found to retrieve the speed of sound quickly. In the



(a) Speed of sound in water for different temperatures. (b) Z-scan-data for speed of sound evaluation.

Figure 5.4.: Speed of sound evaluation conducted with a water temperature of 18.9°C . a) Speed of sound in water for different temperatures ranging from 0°C to 40°C derived from analytical fit to experimental values (Marczak, 1997). The value for a temperature of 18.9°C is marked. b) Transducer displacement plotted against the change in signal arrival time and fitted linearly.

pursuit of this work, the implementation proposed in Marczak (1997)¹ was used, which is derived from comparison to very precise speed of sound measurements and reproduces literature values with a small uncertainty of 0.03 m/s . The coefficients are given in table 5.2 and values are plotted in fig. 5.4a. However, for this formula the temperature of water needs to be known with high accuracy.

The speed of sound can also be retrieved in *z-scan measurements*. For this, the detector was moved along the *z*-axis, i.e. along the beam axis. The measured difference in arrival time of the signal plotted over the displacement of the detector is given in fig. 5.4b and provides a measurement of the speed of sound in-situ, assuming stable temperature and beam conditions during this measurement. This has been ensured with simultaneously recorded temperature values. In this section, it is investigated whether this *z-scan* measurement is a valid replacement for the temperature dependant fit.

As an example the measurement in fig. 5.4b, acquired at a temperature of 18.9°C ,

¹This decision was solely based on the fact that the described simulation tool k-Wave also uses this implementation from Marczak and co-workers. There are other implementations discussed in Robinson (2000).

Table 5.2.: The coefficients a_i of the fifth-order polynomial given by Marczak (1997), approximating the dependence of the speed of sound in water, c , on temperature.

i	0	1	2	3	4	5
a_i	1.402×10^3	5.038	-5.799×10^{-2}	3.287×10^{-4}	-1.398×10^{-6}	2.787×10^{-9}

provides the following values:

$$c_{meas} = 1.483 \pm 0.015 \text{ mm}/\mu\text{s},$$

$$c_{lit} = 1.479 \pm 0.003 \text{ mm}/\mu\text{s},$$

where c_{meas} is the measured speed of sound extracted from a linear fit in fig. 5.4b, and c_{lit} is the literature value from the described polynomial fit given in Marczak (1997) for the measured temperature in the presented experiment. The given uncertainties on the speed of sound values are discussed individually in the following. The z-scan measurement of the speed of sound is in good agreement with the provided fit value. In order to evaluate the given uncertainties for the z-scan measurements and the literature value derived from Marczak (1997), the influence of these two given speed of sounds in water on the measured ranges is investigated. The z-scan method providing c_{meas} is independent from the temperature measurements, as it is measuring the actual signal shift correlated to the displacement of the transducer. Sources of error are the precision of the motorized stage, the recording oscilloscope, and the beam stability. As only the arrival time of the peak pressure is measured, the frequency dependence of the focused transducer regarding the distance to the Bragg peak, as discussed in section 2.2, is not affecting the signal considerably. The given uncertainty for the measured speed of sound in water of $15 \mu\text{m}/\mu\text{s}$ is derived from the root-mean-square-error of the linear fit shown in fig. 5.4b.

For the fit value c_{lit} , a temperature is needed, which can be assumed to have an uncertainty of 1 K in the presented ionoacoustic measurements. This provided the uncertainty of the literature value given above of $3 \mu\text{m}/\mu\text{s}$. However, the fit presented in Marczak (1997) has an uncertainty to comparison measurements value which is 2 orders of magnitude lower than the error deriving from an uncertainty in temperature of 1 K.

Assuming no correlation between the speed of sound measurement and the temporal resolution of our oscilloscope, the linear error propagation formula for the uncertainty in the range measurement ΔR is generally given as:

$$\Delta R = R \sqrt{\left(\frac{\Delta c}{c}\right)^2 + \left(\frac{\Delta t}{t}\right)^2}, \quad (5.2)$$

where ΔR is the combined error estimation on the calculated distance or range, t and Δt the time and the uncertainty of the time measurements in the oscilloscope respectively, and c and Δc the speed of sound and the respective uncertainty. The temporal resolution of our recording oscilloscope is $\Delta t = 1$ ns, and for 20 MeV protons stopped in water the range of 4 mm corresponds to a time difference between direct and reflection signal of $t = 5.3$ μ s. Hence, the uncertainty in the range measurement using the different sound velocities and the corresponding uncertainties in the speed of sound measurements stated above is calculated to:

$$\begin{aligned}\Delta R(c_{meas}, \Delta c_{meas} = 15 \mu\text{m}/\mu\text{s}) &= 40.8 \mu\text{m}, \\ \Delta R(c_{lit}, \Delta c_{lit} = 3 \mu\text{m}/\mu\text{s}, \Delta T = 1 \text{ K}) &= 8.2 \mu\text{m}, \\ \Delta R(c_{lit}, \Delta T = 0 \text{ K}) &= 0.76 \mu\text{m}.\end{aligned}$$

For c_{lit} , the uncertainty ΔR has also been calculated assuming a perfect temperature measurement, emphasizing the potential of this precise fit. Comparing the resulting uncertainties deriving from different speed of sound measurement methods, it can be seen that the z-scan method is not precise enough in order to achieve the presented range values in section 4.6.1. Although it is possible to obtain the speed of sound in-situ with such a displacement z-scan method, the provided fit has been used exclusively for the evaluation of particles ranges in water. Otherwise, an additional precise measurement and evaluation of a z-scan would have been necessary for each conducted beam time. Nevertheless, an improvement in the accuracy of the temperature measurement is recommended for future measurements.

5.1.3. Calculating Ranges for 20 MeV protons

As discussed in section 4.1, the main objective of this thesis is the determination of the range of charged particles in water, starting from the here considered accessible low energies of 20 MeV protons. For comparison, Geant4 simulations (Agostinelli *et al.*, 2003) have been created, which included all relevant beam line elements and dimensions of all conducted beam times at the MLL. In this section the uncertainties of such a simulation are investigated.

As an example, a simulation incorporating the setup of the MLL beam time in March 2016 will be shown here. Here, the small energy uncertainty of the MLL Tandem of $dE/E = 1 \times 10^{-4}$ is used to restrict the sources of uncertainties to elements in the experimental setup. The elements involved are the 11 ± 1 μ m titanium foil as the vacuum exit window, an air gap of 85 ± 1 mm, and finally a 50 ± 5 μ m Kapton foil before the water phantom. The influence of uncertainties in the lengths of the air distance and the thickness of the involved foils is derived from a simulation including upper and lower boundaries, but a fixed temperature of 18 °C and ionization potential of water of 78.0 eV. This ionization potential is

the current recommendation of the ICRU. The resulting change in peak position is 20 μm .

Besides uncertainties of the geometrical properties of elements in the beam path, remaining uncertainties of such a simulation are the temperature dependent water density and the mean ionization potential of water. The density was derived from the measured temperature at the experiment and is adapted in the simulation accordingly. For the ionization potential of water the latest recommendation of ICRU of $78 \pm 3 \text{ eV}$ (ICRU, 2014a) is chosen. In order to estimate the influence of these two simulation intrinsic parameters independent from geometrical uncertainties, simulations were conducted with the maximum and minimum of the expected density from a change of 1 K in the water temperature. This was done for two typical temperature ranges around 24 $^{\circ}\text{C}$ and around 18 $^{\circ}\text{C}$. For the exemplary beam time of March 2016 presented here, the mean water temperature was 18 $^{\circ}\text{C}$. The used densities are given in table 5.3. The ionization potential was varied in the steps of 75.0 eV, 78.0 eV and 81.0 eV. The results are listed in table 5.4 and displayed in fig. 5.5.

The step size of the simulation, i.e. the resolution of the resulting dose distribution, was 10 μm in axial dimension. In fig. 5.5, the variation of the water density is grouped by the same colour. It can be seen that the change of the ionization potential used here has a bigger influence on the simulated dose distribution than the change in temperature, i.e. density. Both parameters are shifting the Bragg curves all together, while the relative distance from the Bragg peak to the R_{80} stays constant. In order to evaluate the effect of the density change, the R_{80} range has been extracted by a multi polynomial fit from the depth dose profiles instead of the Bragg peak itself. The exceptional use of the R_{80} here is only to quantify the small changes due to the density. The mean differences are given in the last column and row in table 5.4, where a change of 3 eV in the ionization potential will alter the peak by 19 μm , in this specific case. Combining the geometrical er-

Table 5.3.: Temperature dependent density of water as used in Geant4 simulations (Wagner and Pruß, 2002).

Temperature in $^{\circ}\text{C}$	Density of Water in g/cm^3
25	0.99704
24	0.99729
23	0.99754
19	0.99840
18	0.99859
17	0.99877

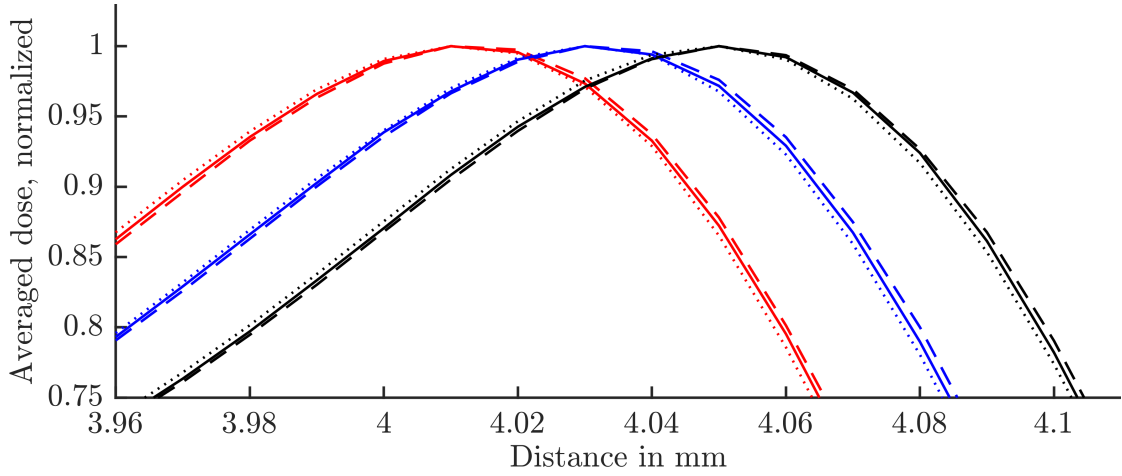


Figure 5.5.: Variation of the mean ionization potential and water temperature in Geant4 simulations for the experiments conducted in March 2016. Details on the ranges are given in table 5.4. Here given are the Bragg peaks of the normalized dose curves for a water temperature of 25 °C to 23 °C as dashed, solid, and dotted line, and an ionization potential of 75.0 eV, 78.0 eV and 81.0 eV in red, blue, and black, respectively.

Table 5.4.: R_{80} ranges resulting from a variation of the ionization potential and water temperature in Geant4 simulations for the beam time conducted in March 2016. The exceptional use of the R_{80} here is only to quantify the small changes due to the density. All values are given in μm . The last row and column give the mean differences, respectively, as an uncertainty estimate.

T in $^{\circ}\text{C}$	I_{pot} in eV	75.0 eV	78 eV	81.0 eV	Mean differences in $\mu\text{m}/3\text{eV}$
25 $^{\circ}\text{C}$		4060	4080	4098	19
24 $^{\circ}\text{C}$		4059	4079	4098	19
23 $^{\circ}\text{C}$		4058	4077	4096	19
19 $^{\circ}\text{C}$		4054	4074	4093	19
18 $^{\circ}\text{C}$		4054	4073	4092	19
17 $^{\circ}\text{C}$		4053	4073	4092	19
Mean differences in $\mu\text{m}/^{\circ}\text{C}$		0.8	1.0	0.9	—

rors, the error from the density, and the error induced by the uncertainty of the ionization potential of water by a linear propagation of uncertainties, this leads to a simulation uncertainty of 28 μm .

Corresponding acoustic measurements have been presented in the discussion on the evaluation methods in section 4.6.1, and the result of the relative evaluation based on the reflection signal is repeated here comparing to the peak position extracted from the corresponding Geant4 simulation:

$$\begin{aligned} R_{\text{ionoacoustic, SZ 3/16}} &= 4034 \pm 7 \mu\text{m}, \\ R_{\text{Sim}}(78 \text{ eV}, 18 \text{ }^\circ\text{C}) &= 4028 \pm 28 \mu\text{m}. \end{aligned}$$

The variation in the temperature in the dimension encountered in the experiments can be neglected in the simulation. Nevertheless, the influence of the uncertainty in the temperature measurement on the used speed of sound in water is discussed in section 5.1.2. The uncertainty of the ionoacoustic range given here is therefore only the standard deviation σ from a fit of all evaluated ranges to a normal distribution, which can be considered a measure for the reproducibility of ionoacoustic measurements. The achieved precision is comparable to other experimental range determination methods, which are briefly introduced in section 3.4. In comparison with thoughtfully conducted simulations, the measured ranges are in good agreement, also considering the even larger uncertainties from the variation of the ionization potential. Considering the good precision of ionoacoustic measurements, this can be seen as a confirmation of the proposed value for the ionization potential of 78 eV, at least in these experiments. With increasing energy, difficulties can be expected with the increase in range straggling. This is specifically discussed in the onset of section 5.2, where measurements at higher particles energies are described.

5.1.4. Absorption Wheel Measurements

The ionoacoustic method has also easy access to measuring the *water equivalent thicknesses* (WET). It is common practice in medical physics to characterize a beam not by its main energy, but its range in water, which is a rather practical approach. At the end, the range in water is what matters in medical physics, i.e. in treatment planning specifically. It is thus convenient to characterize absorbing materials by their equivalent thickness as if they were made of water by comparing the stopping power of these absorbing materials to water. In a medical beam line this can be e.g. any kind of beam monitors. For thin foils, the WET l_W is therefore (Newhauser and Zhang, 2015):

$$l_W = l_m \frac{\rho_m \overline{S_m}}{\rho_W \overline{S_W}} = l_m \frac{R_W}{R_m}, \quad (5.3)$$

where l_m is the physical, actual width of the absorbing material, $\overline{S_W}$ and $\overline{S_m}$ the mean proton mass stopping power, and R_W and R_m the range of protons in water and the material, respectively. The *water equivalent ratio* (WER) is the ratio of l_W/l_m . At the very heart of this concept, the question is by how much is the range decreased when introducing a certain material of some thickness into the beam. Hence, as Ionoacoustics actually measures the range of charged particles in water, the WET of an absorbing material, and subsequently its stopping power, can be retrieved from the decrease of the TOF between direct and reflection signal. This change of the TOF is corresponding to the reduction of the range in water after the energy loss caused by inserting more and more material into the beam path. Measurements of the WET of a plastic material are presented here, where the focus is on the achieved precision of the resulting stopping power values.

With the use of a specially designed energy degrading wheel, the range in water is measured with different thicknesses of absorber material before the water tank, starting from no material up to 1.7 mm. This wheel was 3D printed and the specific stopping power of the used plastic material (AR-M2, polyjet printing done by rapidobject, Leipzig) was not exactly known. The intended use of this wheel was an easy energy degradation in order to determine the energy resolution of future detectors, which makes a precise knowledge of the stopping power of the involving plastic material mandatory. From first estimates and simulations, the WER was expected to be 1.05. The density of the plastic material has been determined with the mass of the resulting wheel and the precise volume from the planning 3D-model required for the printing process, and measured to be $\rho_m = 1.094 \pm 0.005 \text{ g/cm}^3$. The setup contained the usual data acquisition, 60 dB amplification, and the 3.5 MHz PZT transducer from Olympus. In order to reduce the effect of scattering due to the wheel itself and the broadening of the signal due to a significant increase in the lateral spot size of the Bragg peak, the PZT transducer setup was placed very close to the wheel. This was the same detector setup as in the Ionoacoustic experiments described later in section 5.4, which is basically a modified KF-40 pipe (Aluminium pipe according to the ISO norm with an inner diameter of 40 mm). The diameter of this smaller experimental volume filled with deionized water was large enough to avoid reflections from the pipe wall. Conceptionally the elements in the beam path are the same, i.e. vacuum exit window with 11 μm titanium foil, a certain air gap from that exit to the wheel of some centimetres, and finally another 11 μm titanium foil as water entrance foil. Compared to the experiments described and reproduced in section 5.1.1, the energy loss before the entrance into water is reduced to 400 keV. With this energy loss before the stopping in water, the range of initially 20 MeV protons in water measured with this setup was $4120 \pm 8 \mu\text{m}$. The length of the tube was chosen such that the focus of the PZT transducer was at the expected range of 20 MeV protons in water.

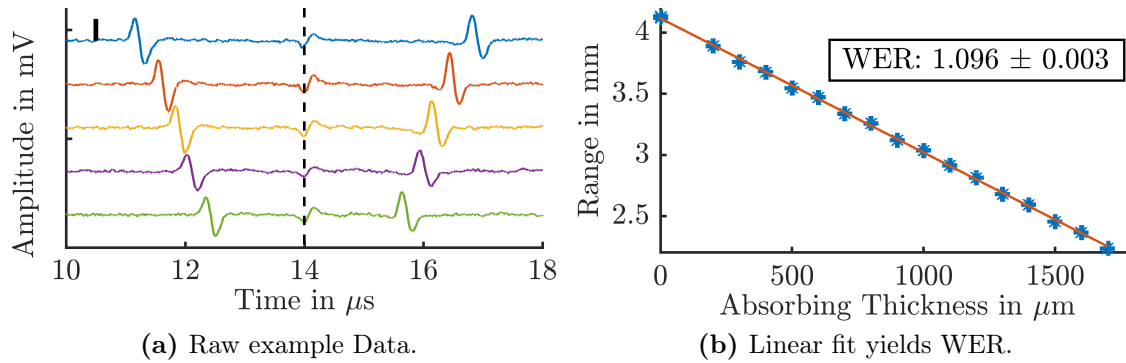


Figure 5.6.: Water equivalent ratio measurements with the modulating wheel. a) Raw example data for various plastic material thicknesses from zero up to 1.6 mm. As the range decreases with increasing thickness of the absorbing material, the time difference between direct and reflection signal decreases with constant window signal. The black bar indicates 1 mV. The dashed vertical line is indicating the constant position of the window signal despite moving decreasing ranges. b) Evaluated ranges as a function of absorbing material thickness with a linear fit and the corresponding measurement uncertainties.

Nevertheless, the field depth of this transducer ranges from 20 mm to 29 mm, i.e. no significant loss in amplitude is expected by a Bragg peak slightly out of focus in axial direction. In this detector setup, the speed of sound was determined in-situ by a pulse-echo measurement using the exact lengths of the KF-40 pipe. The calculated speed of sound from these pulse-echo-measurements were in good agreement with the speed of sound received from the multivariate polynomial fit calculated with a measured water temperature, which was taken when the KF-40 pipe was filled.

With increasing absorbing material, the distance between vacuum exit window and water entrance window is not changed. Instead, the absorbing material is replacing air in the beam path. It has to be ensured, that this reduction is not significant for the resulting range and thereby even compensating the range reducing effect of the absorbing material. The stopping power of air for 20 MeV protons is 2.8×10^{-3} keV/ μm and thereby 3 orders of magnitude lower than the corresponding stopping power of water (ICRU, 2014b). Measuring the WER over this long range of thicknesses is hence justified, as also the reduction of ranges in this order is linear with the increasing absorbing material. Example waveforms are shown in fig. 5.6a, where different thicknesses on the wheel reduce the time difference between direct and reflection signal with constant window signal. Already at this raw data, the effect of additional absorption on the range is visible, demonstrating the unique simplicity of the ionoacoustic method for range determination. Never-

theless, the signal width stays constant, which suggests that the broadening due to scattering in the absorbing material is negligible. The given black bar in fig. 5.6a indicates a signal amplitude of 1 mV.

The ranges were extracted from the raw data by applying the autocorrelation method, which is described in section 4.4. The difference between the ranges with and without material is the WET, divided by the material thickness is the WER. Plotting the measured ionoacoustic ranges as a function of the absorbing material thickness is assumed to show a linear dependency for most of the plastic material, e.g. PET (Polyethylene terephthalate) or PMMA (Polymethyl methacrylate), and in this small variation of material. The retrieved ranges are plotted against the used material thickness in fig. 5.6b. The WER extracted from a linear fit to these ranges is 1.096 ± 0.003 . The extracted WER is a positive value, although the inclination in fig. 5.6b is negative, which has been done for the reader's convenience. The given uncertainty of 3×10^{-3} was derived from the quotient of the range in water compared to the range in the material. Taking the WER of 1.096 and the measured range in water in this setup of $4120 \pm 8 \mu\text{m}$, the range in the plastic material is $3759 \pm 7 \mu\text{m}$. The linear combination of the uncertainties of the ranges in water and in material gives an uncertainty of 3×10^{-3} for the WER.

The difference of this WER to the first estimate was expected, as concurring measurement with silicon detectors by co-workers also showed the tendency to a higher WER than initially expected (Würl *et al.*, 2017). This discrepancy was the motivation for our acoustic measurements, and concluding measurements reproduced these WER results. With its precision at the lower beam energies, Ionoacoustics is a valid, comparative tool for determining the WER.

From this WER, the mass stopping power of the plastic material can be calculated:

$$S_m = \text{WER} \frac{\rho_W}{\rho_m} S_W = 1.0002 S_W. \quad (5.4)$$

Following that calculation, the mass stopping power of protons in the plastic material is 0.02 % higher than the mass stopping power of protons in water. However, the linear progression of uncertainties for the mass stopping power of protons in the plastic material provides a relative uncertainty of 0.5 %, which is one order of magnitude higher than the expected change in the stopping power. It can be concluded, that the used plastic material can be considered water-like, as the mass stopping powers barely differ.

With the WER of the plastic material, the stopping power $\rho_m S_m$ is calculated to be $2.850 \pm 0.008 \text{ keV}/\mu\text{m}$. Over this maximal length of 1.7 mm, the 20 MeV proton beam loses 4.845 MeV, corresponding to 24 % of the maximum beam energy. In Zhang and Newhauser (2009), *radiobiologically thin targets* are targets with a proton beam energy loss of less than 30 % of the total beam energy. Hence, the approximation with a single valued stopping power for the absorbing plastic material over a thickness of 1.7 mm is justified.

5.1.5. Dose Determination using Quantitative Pressure Measurements

As described in section 2.1, the measured pressure is directly linked to the applied energy deposition or dose via the Grüneisen parameter. By measuring with a calibrated, broadband needle hydrophone along the beam axis, the actual pressure at the source can be extrapolated. Details on this hydrophone are given in section 3.6.1. Figure 5.7a shows a measurement of a 20 MeV proton pulse measured with the PA calibrated needle hydrophone. With the use of a $1/r$ fit to peak pressure values measured at different distances, the pressure at the peak level can be extrapolated, here 115 ± 2 Pa. The error estimation of 2 Pa is given by the root-mean-square-error of the applied fit. The uncertainty given by the 15% relative uncertainty of the calibration data is 18 Pa.

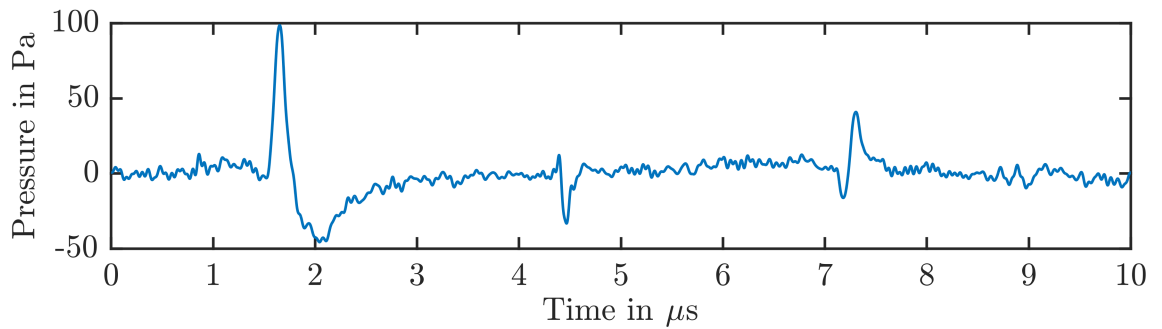
This measured pressure can be converted into a temperature increase using eq. (2.26) of 0.28 ± 0.05 mK. The used physical constants are listed in table 5.5. The Bragg peak volume can be estimated as a disk of 300 ± 30 μm thickness and 2.0 ± 0.2 mm diameter as the spot size. Hence:

$$\begin{aligned} V_{BP} &= 1.2 \pm 0.2 \times 10^{-9} \text{ m}^3 \Rightarrow m_{BP} = 1.2 \pm 0.2 \text{ mg} \\ dE = C_V m dT &= 1.4 \pm 0.3 \times 10^{-6} \text{ J} \Rightarrow D_{BP} = 1.1 \pm 0.3 \text{ Gy} \end{aligned}$$

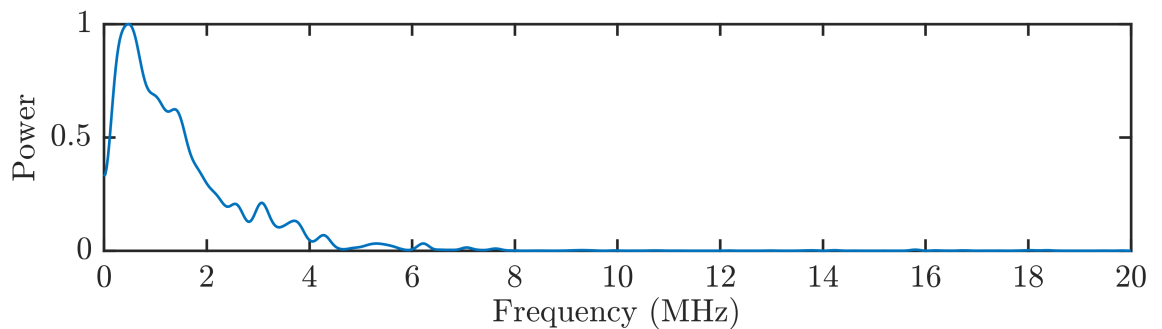
The actual dose deposited by the measured 20 MeV proton beam in water can be estimated by the beam current measured in the experiment of 5.1 ± 0.7 nA with a repetition rate of 9.7 kHz, resulting in a number of protons in a single measured pulse of $(3.2 \pm 0.5) \times 10^6$. Assuming that the complete kinetic energy is deposited in the water volume, the full proton bunch contains 10.4 ± 1.5 μJ .

Table 5.5.: Constant values used for quantitative pressure measurements for water at 18 °C (Kell, 1975).

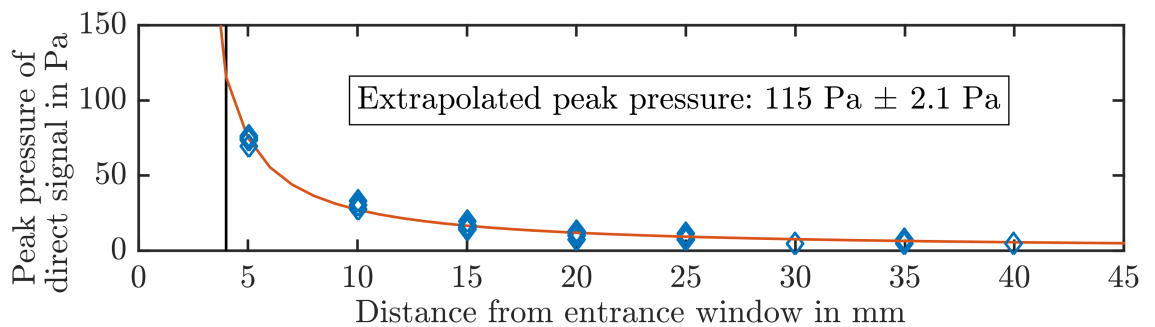
Name	Symbol	Value
volume expansion coef.	β	$1.85 \times 10^{-4} \text{ 1/K}$
isothermal compressibility coef.	κ	$4.62 \times 10^{-10} \text{ 1/Pa}$
density	ρ	998.5 kg/m^3
isochoric specific heat capacity	C_V	4184 J/(kg K)



(a) Absolute pressure measurement.



(b) Frequency spectrum of fig. 5.7a



(c) Extrapolation of pressure at source level.

Figure 5.7.: a) Absolute pressure measurement with a calibrated hydrophone from a 20 MeV proton beam, 100 ns pulse width, and 3×10^6 protons per pulse. b) Frequency spectrum of a). c) Extrapolation of absolute pressure at the Bragg peak location.

From a corresponding simulation the amount of energy deposited in the Bragg peak volume compared to the full dose is about 10%. Hence, the theoretical value of deposited energy in the Bragg peak is $1.04 \pm 0.15 \mu\text{J}$ or $0.8 \pm 0.1 \text{ Gy}$, using the same mass of $1.2 \pm 0.2 \text{ mg}$ as above.

The given estimations of the Bragg peak volume are rather rough, nevertheless

it demonstrates a possible way to measure dose from ionoacoustic data. The relative error between the dose estimation from the beam current and the dose from the pressure conversion is 28%. This is more than the uncertainty of the hydrophone calibration at the beginning. For a better result, the applied particle numbers should be measured more carefully. However, given the simplicity of the ionoacoustic method and the rough estimations on Bragg peak dimensions, it is demonstrated that a reasonable dose measurement is possible for this low monoenergetic proton beam. Considering the lower pressure amplitude in the upcoming experiments at medical accelerators, a good measurement of the applied dose is challenging, as this would also require a very specific and more thoughtful determination of the irradiated volume. The measured pressure trace with single element transducers will give an average of the observed heat distribution, i.e. energy deposition. Hence, the result will be worse in cases, where the distribution of energy cannot be simplified as in this example.

5.1.6. Coherent Ionoacoustics

Coherence is caused by the constant phase difference between two waves with the same frequency and waveform. This is the condition for local interference, i.e. the superposition of wave amplitudes at a certain point of detection, which can either be constructive or destructive. As the signal amplitude of the ionoacoustic measurements is rather weak, the possibility to enhance the amplitude with constant dose was studied. In order to achieve a coherent interference, different source locations have to be excited at different times, where the timing is defined by the runtime of the signal between the source locations. If matched to the detector location, constructive interference will occur. In this section, it is investigated, which combination of spatial and temporal heating functions can lead to an enhancement of the measured signal, while keeping the delivered dose constant. Starting from the fact that when using a long pulse only the temporal gradients at the beginning will produce a spatially defined signal, variations on the temporal form are one option to coherently interfere acoustic sources. Explicitly, instead of using one long pulse one might choose to modulate and thereby generate more signals but with less dose. Of course, this is limited by the possibilities of the accelerator, but is one way to maximize the measured signal by exploiting all available temporal gradients.

The pulsing system of the Tandem accelerator offers the possibility to realize almost any macro pulse structure, i.e. pulse width and repetition rate. The following investigation was therefore focused on a matching of the temporal form of the pulse to the given spatial conditions, thereby exploiting the good possibilities of the MLL Tandem in shaping temporal beam profiles. In order to get several different source locations, two options are possible:

- **Axial** The beam is modulated by its energy resulting in different ranges, hence different Bragg peaks on one line towards the detector.
- **Transversal** The beam is varied in its x- or y-direction but with the same energy.

As the typical transducer bandwidth is in the order of MHz, a pulse repetition of some μs and distances between the sources of some mm were needed. A required change in energy resulting in some mm change in range in a few μs was not possible at the MLL accelerator, obstructing the axial option stated above. Hence, a multi-slit collimator with a slit difference of 1.1 mm was designed. Broadly irradiated, this resulted in spatially separated beam stripes, as seen in fig. 5.8b (Doyle, 2016). These stripes were illuminated with a pulse train with a frequency around 1 MHz and the acoustic signals measured transverse in the same water phantom setup as in the MLL experiments mentioned before, i.e. described in section 5.1.4. Here, 20 MeV protons leave the vacuum through 11 μm titanium, pass some centimetre of air and a 0.5 mm aluminium scatter foil, then the multi-slit collimator as close as possible to the 50 μm Kapton foil as the water entrance foil. The collimator was positioned with a special holder, so that there was no interference with the beam, and broadening effect due to a long distance to the water basin was limited. The scatter foil was used to enlarge the beam spot smoothly, thus illuminating the collimator homogeneously. Some of the measured signals and a comparison to simulations are displayed in fig. 5.9.

Figure 5.9a is a first test shot through the multi-slit collimator with a single pulse of 120 ns pulse width, i.e. no intended temporal coherence yet. The pulse contained 768 fC/pulse, i.e. 4.8×10^6 protons/pulse. The signal is recorded with a 1 MHz focused PZT transducer in transversal direction and can be considered the

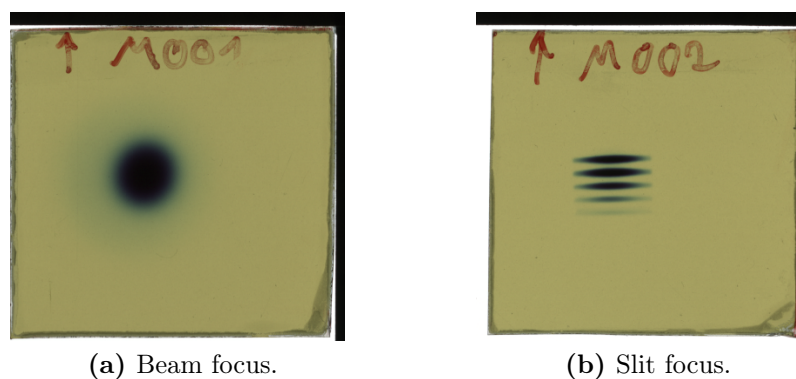


Figure 5.8.: Beam foci (a) without and (b) with multi-slit collimator, both measured with GafChromic films in the Bragg peak region.

basis signal. The maximum amplitude here is 1.9 mV. Longer pulses beyond the stress confinement will not further increase the signal amplitude. What is shown in fig. 5.9a is a sequence of γ signals induced at the BRagg peak observed in transverse direction. The range of 20 MeV protons in water is too short in order to separate α and γ signals. Hence, this pulse train here is dominated by the stronger γ signals from the Bragg peak. 5 positive and negative peaks are visible corresponding to the 5 illuminated slits of the collimator resulting in 5 different beam spots in the field of view of the detector. With the pulse width in stress confinement, only the spatial variation is observed in this oscillation. As already seen in the radiochromic measurements in fig. 5.8b, the beam intensity differs for the 5 beam spots. Hence, the observed amplitude is different additionally to the $1/r$ attenuation of the signal over the total length of the collimator of 1 cm. In fig. 5.9b the effect of coherence in this setup is demonstrated. Now, a pulse train of 5 consecutive micro pulses were used to match the peak difference already seen

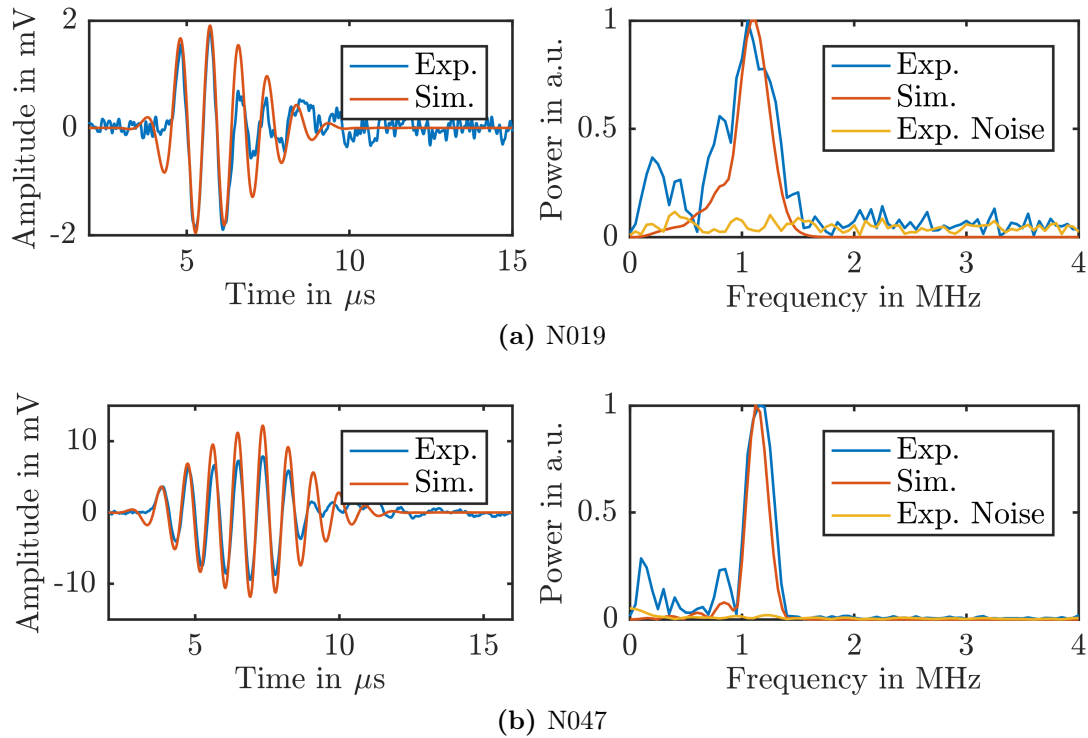


Figure 5.9.: Coherent ionoacoustics compared with simulations in time and frequency domain. The enhancement compared to the noise is indicated. a) Single shot measurement, i.e. only spatial modulation of the stripe foci. b) Example for pulse repetition frequency of 1.18 MHz demonstrating the full potential of the coherence approach.

in fig. 5.9a. The micro structure of this pulse train had a frequency of 1.18 MHz with a duty cycle of 50 %. This means, the 5 pulses in one sequence had a time difference of 850 ns and had a width of 425 ns. The macro structure of the pulsing was given by a 500 Hz repetition rate of these sub-macro pulse trains. Each of these 5 pulses contained 3.16 pC/pulse, which is about 4 times more than in the previous case in fig. 5.9a due to the longer pulse width. Converting down to the amount of particles per ns, this number stays constant given the usual fluctuation of the source. The maximum measured amplitude is 7.8 mV. The micro structure is supposed to match the runtime of the signals from one spot to the next, meaning that the signal of a spot excited in the previous pulse arrives at the neighbouring spot when the next pulse arrives. The first arriving peak is therefore not enhanced, as it directly travels towards the detector without passing another spot. The next peak was initially excited at the second spot² with the first pulse, and then enhanced at the first spot by the second pulse. This logic continues for the other signals following. For the ideal case shown in the simulation result in red in fig. 5.9b assuming 5 equally excited beam spots in 5 sequential pulses, the last beam spot will pass all other spots and is enhanced by a pulse at each spot, resulting in signal amplitude for the 5th peak 5 times higher than the first signal peak. Comparing to the measured signal, this is not completely the case, which is due to the unequal intensity in the different beam spots, which is already seen in the single pulse signal in fig. 5.9a. The signal enhancement due to the coherence is clearly visible, also in the corresponding frequency spectra in fig. 5.9. The excitation frequency at 1.18 MHz is dominating comparing the pulse train signal to the single pulse signal, and the signal amplitude is 4 times higher in the coherence case with the same level of pulse current. It is to be noted that this is not due to the 4 times longer pulse width and the 5 consecutive pulses. The signal amplitude is determined by the spatial and temporal gradient. The case in fig. 5.9b has therefore to be compared to a full pulse of 2.1 μ s, which is the described pulse train pushed together. With such a long pulse, only the signal amplitude of about 2 mV is expected as in fig. 5.9a. Only by stretching the pulse in 5 consecutive pulse, the signal amplitude was increased by a factor of 4.

One interesting application of this enhancement would be the measurement with a micro- or mini-beam collimator (Prezado *et al.*, 2012, Prezado and Fois, 2013, Peucelle *et al.*, 2015, Sammer *et al.*, 2017). Here, similar to our multi-slit collimator, only small beams are used in the irradiation instead of a broad distribution. This is motivated by the fact that sparsely irradiated tissue has a better recovering probability and the lateral scattering blurs the dose distribution in the tumour region efficiently enough to ensure homogeneous coverage. Hence, a spatially fraction-

²Here, first, second etc. spot is counting the order in the field of view of the detector. The first spot is the spot closest to the detector providing the first signal in the recording.

ated beam pattern is given and could be observed transversally assuming proper pulsing.

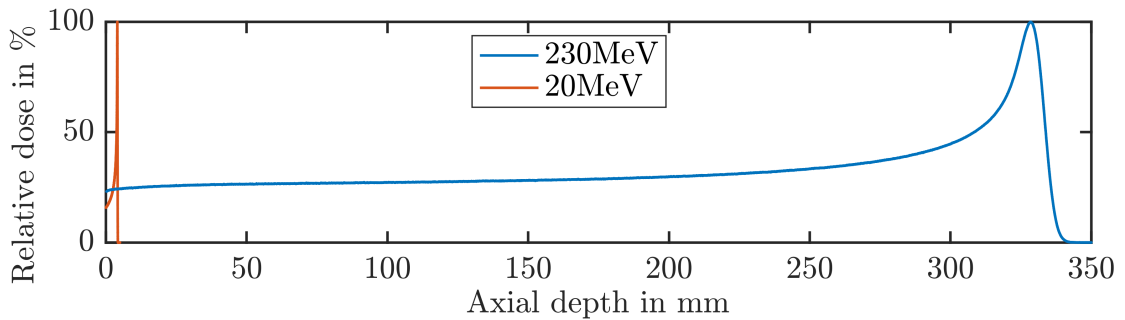
5.2. Measurements at Medical Accelerators up to 230 MeV Protons

Measurements at medical proton accelerators provide broader Bragg peaks than the 20 MeV proton beam experiments at MLL. The absolute evaluation method is therefore applied relying on the time-of-flight difference between the rising edge of a scintillator pulse to the compression peak of the ionoacoustic signal. Two different experimental campaigns are presented, one conducted at the Roberts Protons Centre at the University of Pennsylvania (UPENN) in Philadelphia, USA, the second at the Centre-Antoine-Lacassagne (CAL) in Nice, France. The measurements were conducted in a water phantom irradiated from the top. Comparative simulations have been done accompanying the measurements.

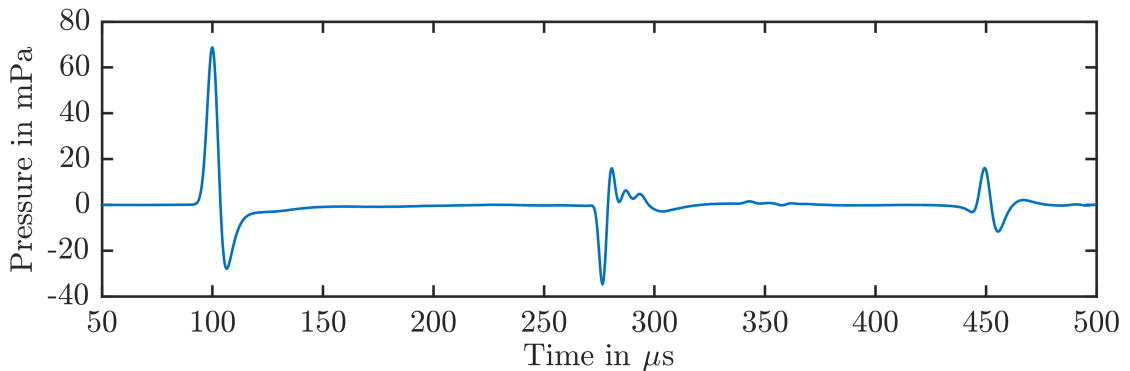
5.2.1. From 20 MeV to 200 MeV

In order to estimate the signals expected at medical accelerators from high energy protons, studies have been done using Geant4 and k-Wave (Lehrack *et al.*, 2016). Before looking at the simulation results, it is worthwhile to summarize typical properties. In general, a lower frequency signal can be expected, since the dose (or temperature) gradients at those high energies are reduced. Instead of roughly 300 μm Bragg peak width as seen with 20 MeV protons in water, several millimetres even in the rising edge are encountered. Also, typical pulse widths are in the order of several microseconds and spot sizes are up to 10 millimetres at clinical proton accelerators. The dimensions can be seen in fig. 1.2a and fig. 5.10a, showing the depth dose profiles from 20 MeV and 230 MeV proton beams. Figure 5.10b shows the ionoacoustic result derived in a k-Wave simulation. In these simulations, the SIR is automatically included as specific detector points on the simulation grid have to be specified. Only there, the dynamic pressure is recorded. For memory saving reasons, the simulations are always executed assuming a short pulse excitation and any temporal profile is convolved later. The simulation shown in fig. 5.10b is matched for the accelerator at CAL in Nice with the CRT hydrophone C305X in a water phantom, see section 5.2.3 and section 3.6.3 for details. The EIR of the C305X was not measured, only the area of 1.44 mm^2 of the flat, squared, sensitive detection area, along with an estimated pulse width of 4 μs and a reasonable distance to the source of 7.5 cm was considered. It can be expected that an actual measurement will show reduced amplitude especially for the entrance signal. This

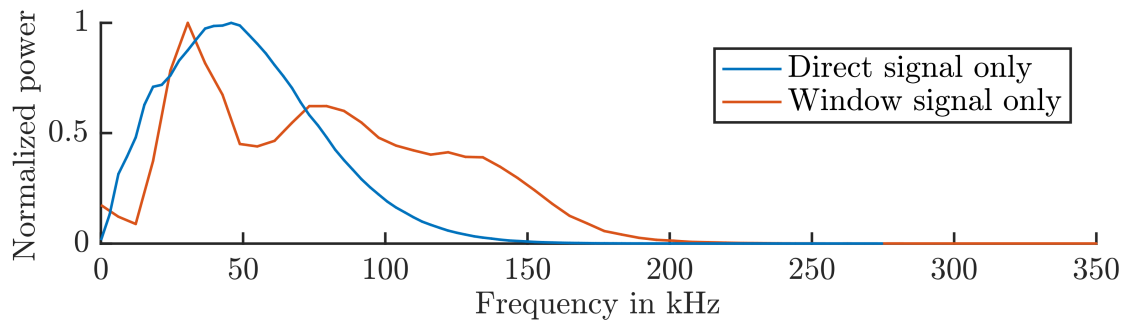
part is difficult to simulate because in this setup the phantom entrance is the water surface.



(a) Geant4 Simulation of 20 MeV and 230 MeV proton beams in water.



(b) K-Wave simulation from a 200 MeV proton beam in water, temporal pulse width of $3.7 \mu\text{s}$ and Gaussian shape.



(c) Frequency spectrum from individual signal components shown in fig. 5.10b.

Figure 5.10.: Simulations using medical beam properties. a) Comparing depth dose profile for 20 MeV and 230 MeV proton beams in water. The Bragg peak FWHM is $300 \mu\text{m}$ and 28 mm for 20 MeV and 230 MeV respectively. b) K-Wave simulation of a 200 MeV proton beam in water tailored to the experimental conditions at CAL (see section 5.2.3 and section 3.6.3). c) Frequency spectrum from individual parts shown in fig. 5.10b.

The energy input of the simulation at that water surface is located at an impedance step with a large difference from water to air, producing a high frequency oscillation. This would require a small grid spacing, which is difficult with the current available computational resources when such a long range and distance to the detector needs to be simulated. A certain error in this entrance signal has therefore to be accepted. The main message is that the broader dose distribution, longitudinal and lateral, *and* the longer Gaussian proton pulses are pushing the frequency content down below 100 kHz. The Fourier spectrum of the individual signal parts, i.e. direct and entrance signal separated, is shown in fig. 5.10c. As these two parts are originating at different spatial gradients, the frequency content of the entrance signal is higher, but still covered in the hydrophones bandwidth. The peak pressure of the first signal is 70 mPa and reduces considerably for the reflection signal, as the distance to the detector is shorter compared to the distance from the Bragg peak to the water surface and back. As shown later in section 5.2.3, the measured pressure amplitudes are in good agreement with the simulated pressure. The acoustic amplitude is influenced by many factors, including temporal rise time, exact spatial configuration, precise transducer calibration in sensitivity and bandwidth, and finally a proper alignment of the hydrophone to the source. In Jones *et al.* (2016b), where a discrepancy between simulated and experimental acoustic amplitude in the order of a factor of 4 is reported, similar considerations are given, leaving this problem for future comparative studies. It is in this context to be noted again, that the amplitude does not influence the intended goal of reliable range verification, as long as sufficient SNR is achieved. This conclusion is also drawn in Nie *et al.* (2017), reporting on follow-up studies in UPENN, where k-Wave simulations are used for acoustic signal predictions in different materials.

5.2.2. Measurements at UPENN

At the University of Pennsylvania studies have been made at a clinical cyclotron (C230, Ion Beam Application IBA, Belgium), where pulsing on the ion source arc current generated 17 μ s pulses (Jones *et al.*, 2015). Normally, the beam generated at an isochronous synchrotron is quasi continuous, making ionoacoustic measurements infeasible. Thorough studies on the possibility to pulse this isochronous cyclotron have been done before in order to achieve pulse widths of 17 μ s for proton energies of 230 MeV. The estimated stress confinement for such a proton beam in water is 18.5 μ s. The acoustic pulses were thus generated in stress confinement, but the pulse width is close to the limit. The consequences of these pulse widths are discussed in the following.

During a 2-weeks-visit of this group between April and May 2016, evaluation techniques and used hardware, specifically two different hydrophones, were compared. The hydrophone used for medical proton experiments in this work is a bi-

directional Cetacean C305X (Cetacean Research Technology, Seattle, USA), with a total amplification of 73 dB (internal and external, see section 3.6.3), whereas UPENN used an omnidirectional calibrated B&K 8105 (Brül&Kjær, Nærum, Denmark) amplified by a manufacturer amplifier. This amplifier was set to provide signals with a sensitivity of 100 mV/Pa. Both hydrophones are comparable in sensitivity and frequency response. But since UPENN focused on Bragg peak tomography, i.e. full imaging of ionization in matter, they chose a device which could be placed in non-axial positions without realigning the detector surface. This was a first step of addressing implementation issues for those medical cases, where patient anatomy might inhibit perfect axial positions of the ultrasound device. Also, by measuring in lateral positions the detection of α and γ signal³ offers a direct opportunity for triangulation. In Jones *et al.* (2016a) the feasibility and possible caveats of such configurations have been studied extensively. A short summary of these findings is given in the outlook of this thesis, where possible transducer positions are discussed.

The experimental setup consisted of a water basin irradiated from the top. The artificially pulsed beam with highest possible energy of 230 MeV passed through an ionization chamber to measure the delivered current and then a block of solid water of 6.7 cm, reducing the range of the protons in water from 326 mm down to 257 mm, corresponding to a kinetic energy of the protons of 198 MeV. A scintillator coupled to a photomultiplier tube was used for pulse width measurements and later evaluation. During these test beamtimes, signals from the hydrophone and the photomultiplier tube were recorded with the same digital oscilloscope (Agilent DSO7104A, USA) and averaged over 1024 traces in order to minimize the influence of statistical uncertainties.

One of the outcomes of the joint beam times was a calibration of our uncalibrated cetacean hydrophone by the calibrated B&K hydrophone and thereby a repetition of the absolute pressure measurement already reported in Jones *et al.* (2015). The B&K 8105 from UPENN included a measurement of the sensitivity of the amplifier. With concurring measurements the signals from both hydrophones can be related and transferred to pressure units. The hydrophones were placed axially in a water phantom with irradiation from the top. With different distances from the Bragg peak the ionoacoustic signal was measured consecutively so that both hydrophones measured in the same position. The B&K 8105 provided signals with a sensitivity of 100 mV/Pa. When normalizing the measured signal traces by the applied beam current to mV/nA a conversion factor can be found from the comparison of the

³This notation was introduced by Albul *et al.* (2005) and Jones and co-workers adapted this notation. The α wave derives from the pre-distal part and propagates transversally, the γ part derives from the Bragg peak region and propagates spherically. See section 4.1.1 for details.

voltage amplitude from both hydrophones:

$$\frac{V_{C305} [\text{mV/nA}]}{V_{B\&K} [\text{mV/nA}]} = \kappa_{C305X} = 4.15, \quad (5.5)$$

providing a sensitivity for the C305X of 415 ± 85 mV/Pa.

Using a dataset measured at a distance of 35 mm to the Bragg Peak, the maximum pressure amplitude with a pulse charge of 0.96 pC was 35 ± 8 mPa for the C305X, yielding 36 ± 8 mPa/pC. This recording is shown in fig. 5.11. In this figure, the beam current is not corrected for, hence the difference in the maximum pressure amplitudes measured by the two hydrophones. However, for the measurement with the B&K 8105 the recorded pressure is 28 ± 4 mPa with a pulse charge of 0.84 pC, yielding 33 ± 5 mPa/pC. For the B&K 8105, a general measurement uncertainty of 15% is assumed. The two hydrophone measurements are in good agreement, the remaining difference can be attributed to fluctuations in the beam current and uncertainties in the pressure calibration. It is also visible, that the C305X is more sensitive to disturbances, as additional oscillations occur, which are not recorded by the B&K 8105. This additional noise in the C305X is overlaying a possible candidate for an entrance signal in the B&K 8105 signal trace at around 250 μs . The expected TOF difference between direct and entrance signal in this case was 173 μs using a speed of sound of 1.480 mm/ μs . As the SNR of this possible entrance signal is low and no reflection signal was recorded, a relative evaluation has not been further considered.

Besides the hydrophone calibration, the capability of the two hydrophones in determining range shifts has been examined. For this, the two hydrophones were placed next to each other with the bi-directional C305X directly on beam axis and the omni-directional B&K 8105 5 cm next to it. Considering the dimension of the beam spot of several millimetre, the distance from the Bragg peak of about 10 cm, and the omni-directional receiving characteristic of the B&K 8105, this offset can be neglected. With this fixed hydrophone position, additional layers of solid water with thicknesses of 2 mm, 3 mm and 5 mm were inserted, thus shifting the Bragg peak away from the hydrophones. The corresponding variation of the beam energy was between 198 MeV and 194.7 MeV. The changes in pressure peak arrival time compared to simultaneous captured scintillator signals are plotted against the added slices of solid water in fig. 5.12. This means, that an absolute evaluation has been applied here (see section 4.3), but without a levelling to the water surface, no absolute range was calculated. The dashed line in fig. 5.12 indicates the intended shifts in range, where the WER of 1.03 of solid water was applied and the first value was subtracted from all values, thus removing the general offset in the distance to the Bragg peak. The C305X difference to this theoretical value is within less than 0.5 mm with a standard deviation of $\sigma=1.6$ mm. The B&K 8105 had differences ranging from -0.8 mm to -1.5 mm and a standard deviation of

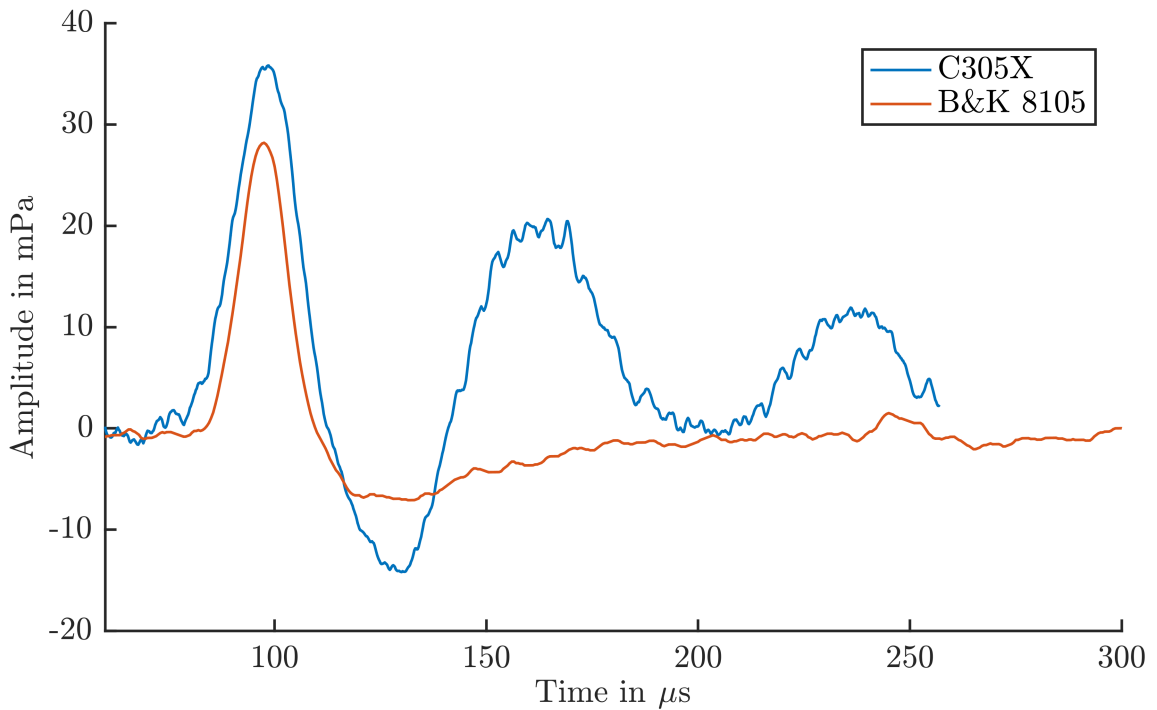


Figure 5.11.: Pressure traces recorded at UPENN. The C305X is given in blue, the B&K 8105 is given in red. The signals are averaged over 1024 traces and were measured at the same position relative to the beam.

$\sigma=1.0$ mm. These deviations are derived from a fit of all measured distances to a normal distribution.

Overall, both hydrophones are following the reduction of the range with a reasonable agreement. The C305X was more sensitive to disturbances during irradiation, hence the resulting peak arrival times are more deviated. Future measurements conducted by the colleagues at UPENN will benefit from a shorter pulse width. In Nie *et al.* (2017), a pulse width of 15 μ s is stated, indicating an improvement after the beam times presented here. The pulse width measurements conducted in these beam times were not sufficient for an improvement by deconvolution as proposed in Jones *et al.* (2016b). Especially with the unusual high noise in the C305X measurement data, the deconvolution fails as this noise is exceedingly amplified.

5.2.3. Measurements at the Synchrocyclotron at CAL

Additionally to the comparative experiment in Pennsylvania, range measurements have been conducted at the Centre-Antoine-Lacassagne in Nice, France in April 2015 and July 2016 (Lehrack *et al.*, 2017). At this hospital, a superconducting syn-

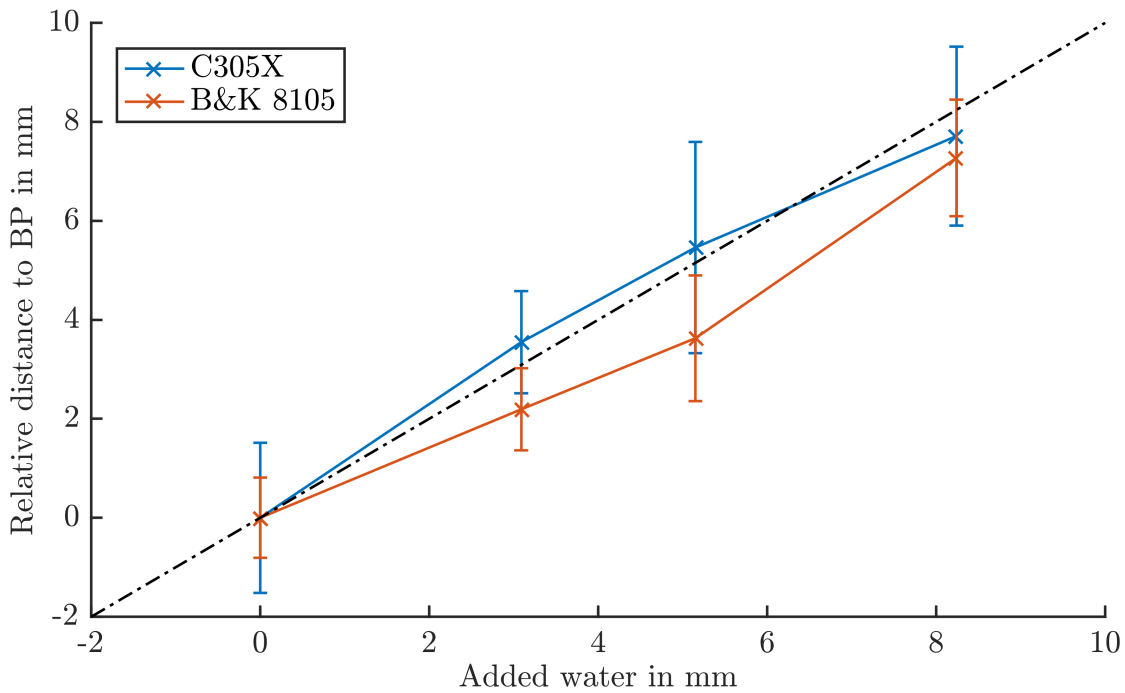


Figure 5.12.: Relative range shifts from ionoacoustic measurements at UPENN. The results from the C305X are given in blue, from the B&K 8105 are given in red. Plates of absorbing solid water with different thicknesses were insert in the beam path, thus shifting the peak pressure arrival time with increasing distance between Bragg peak and detector. The shifts relative to the first position are given here along with the expected shift given by the dashed, black line. The corresponding variation of proton beam energy was between 198 MeV and 194.7 MeV.

chrocyctron (S2C2, Ion Beam Applications IBA, Belgium) has been installed for a compact single room proton therapy facility. This is the first synchrocyctron for proton therapy in Europe, and the first S2C2 from IBA worldwide. As described before in section 3.2.1, this accelerator type produces an inherently bunched proton beam by compensating the relativistic gain in mass with an adapted, decreasing accelerating frequency from a so called *rotating capacitor* (Rotco). The cycle frequency of this Rotco also provided an easy acquisition trigger for the measurements. In the second beam time, a different, much faster oscilloscope was used, which enabled measurements of single pulses. Instead of collecting and averaging data on the oscilloscope, this averaging was done in post-processing, which allowed advanced correction methods in order to improve this averaging. Before the final results of the second beam time are presented, preparatory studies on the precision of this Rotco trigger are introduced.

5.2.3.1. Scintillator triggered Ionoacoustics

In order to achieve good SNR in the measured ionoacoustic signals, waveforms are typically averaged over 16 pulses per waveform in the 20 MeV case at MLL up to 1000 pulses for the medical proton beam energies. For this purpose, a stable trigger for the data acquisition is required. In the first measurements at CAL, a jitter on the trigger in the order of 1 μs has been detected, which blurred the averaged signal so that no range determination with a precision better than 1.5 mm was possible. In order to overcome this problem, studies have been made investigating the generation of a reliable trigger source, which will be independent from an accelerator deduced trigger. The question at hand was whether a scintillator detector setup could reliably provide such a trigger, yielding the time of protons entering the water phantom.

In order to test that, ionoacoustic measurements have been done at the MLL triggered with the *constant fraction discriminator* signal (CFD) of a plastic-scintillator and were compared in their reproducibility to *normal*, i.e. standard measurements triggered with the chopper signal (see section 5.1). The detector consists of a plastic - polystyrene p-terphenyl - absorbing material, light tight covered and attached to a *photo multiplier tube* (PMT) (Nuvia, Czech Republic). Usually, these particle detectors work in a low statistic regime with only a few events in order to reduce pile-up effects. Ideally, only one interaction is measured per single pulse and the tube has enough time to recharge. Pulse width informations are then gathered over several pulses in a histogram. One single event can therefore occur any time inside the pulse width time.

However, with a high current and intentional overloading, the rise time of the

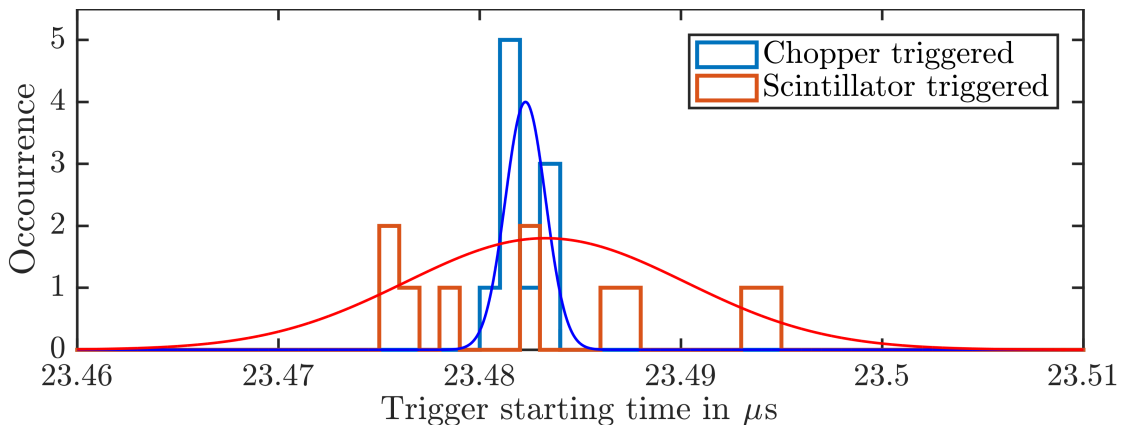


Figure 5.13.: Precision of different trigger sources at MLL. The standard deviation σ derived from a fit to a normal distribution is 1 ns and 7 ns for the chopper (blue) and the scintillator (red) triggered acquisition, respectively.

scintillator signal was stable enough to produce a precise trigger signal. With this high current, the probability of an interaction at the beginning of the pulse was high enough. Measurements of ionoacoustic signals at the MLL triggered with either the CFD or the chopper showed a variation of less than 7 ns for the scintillator triggered acquisition, as shown in fig. 5.13. In both cases, the deviation of the resulting measured ranges were $2 \mu\text{m}$. The measured absolute ranges were $4012 \pm 2 \mu\text{m}$ for the measurements triggered with the chopper, and $4009 \pm 2 \mu\text{m}$ for the measurements triggered with the PMT signal. As these values are in good agreement to each other with a high reproducibility for both trigger mechanisms, it is shown that a scintillator can be used as a reliable trigger for highly averaged ionoacoustic measurements.

In order to check the trigger precision at CAL, scintillator measurements were done triggered with the Rotco. These measurements of PMT signals were analysed in terms of its Shot-to-Shot fluctuations. This is by how much differs a single shot in its arrival time compared to the full average of all 1000 shots. These differences around the averaged mean of the PMT signals is shown in fig. 5.14a, showing no long term drift in the pulse arrival times. In fig. 5.14b, these arrival times are presented in a histogram view including a fit to a normal distribution. This fit provided a standard deviation of $\sigma = 402 \text{ ns}$. This means, the incoming pulses recorded by the PMT at CAL do vary in their mean by some hundreds of nanoseconds from Shot-to-Shot. With the fast oscilloscope, these differences was used to

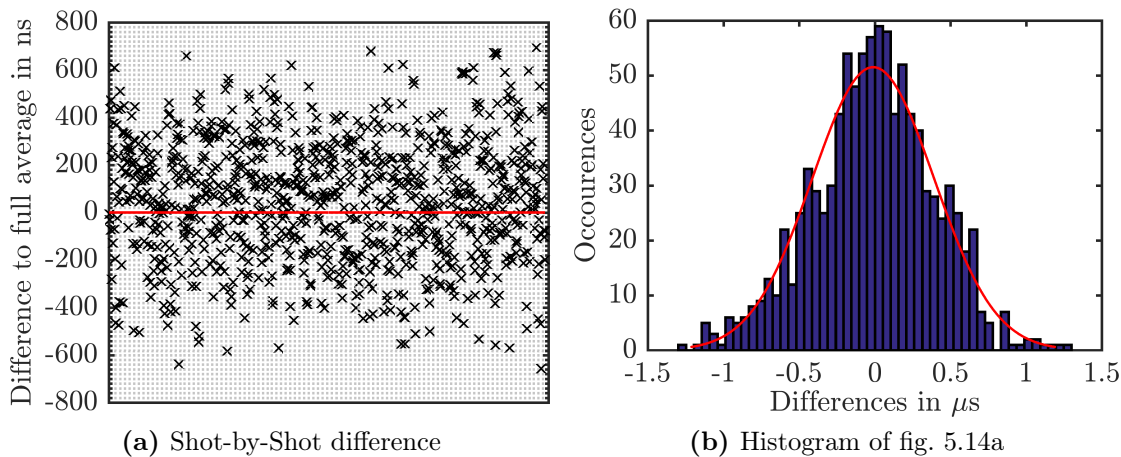


Figure 5.14.: Shot-by-Shot differences. For each PMT trace, the centre of a Gaussian fit was compared to the centre of the full average. This specific difference was used to correct the averaged acoustic waveform Shot-by-Shot. On the left, for a sequence of 1000 shots, this difference is directly given. The right is a histogram with a fit to normal distribution, providing a standard deviation of $\sigma = 402 \text{ ns}$.

correct each measured acoustic signal before averaging. However, no considerable improvement on the precision in range determination could be seen. This can be explained by the energy uncertainty dE of the accelerator of approximately 1 MeV. The resulting deviation in the Bragg peak position by this energy uncertainty is in the same order as the corrections done with this Shot-to-Shot differences.

5.2.3.2. Range Determination Results

The experiment consisted of a proton beam stopped in a water phantom with irradiation from the top through the water surface. Measurements were done with the Cetacean C305X hydrophone in axial position. The goal was a high precision

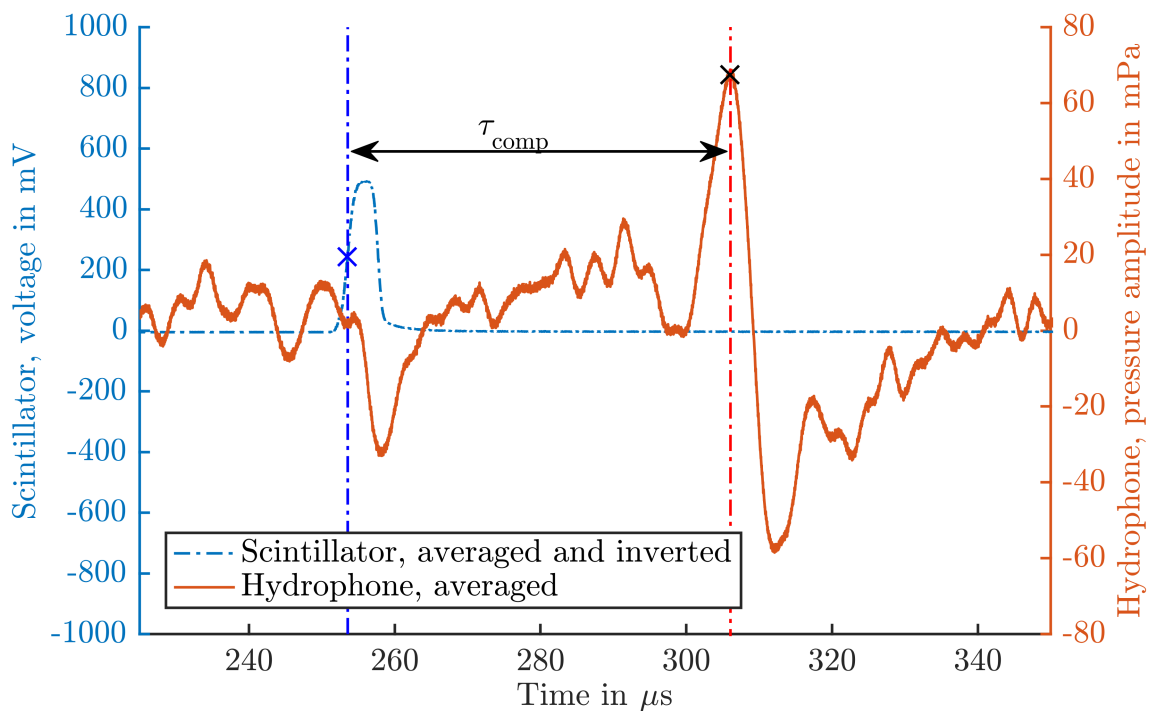


Figure 5.15.: Example of raw data acquired at CAL with a 220 MeV proton beam energy and added pressure calibration. Figure adapted from Lehrack *et al.* (2017). The inverted scintillator voltage is given in blue on the left y-axis, the pressure amplitude measured with the C305X in red on the right y-axis. Both signals are averaged over 1000 traces. Two relevant points for the absolute evaluation are indicated: the point of 50% rise time of the scintillator signal and the peak pressure arrival time. The time-of-flight difference between these two points τ_{comp} , provides the distance between the hydrophone and the Bragg peak.

5.2 Measurements at Medical Accelerators up to 230 MeV Protons 113

range determination with a clinically used proton beam energy.

Figure 5.15 shows an example of raw data acquired during these beam times. The pressure and the scintillator signal has been 1000-fold averaged and inverted. It is hence the resulting signal from 1000 2 pC bunches with a pulse width of 3.7 μ s, respectively. The resulting pressure amplitudes are comparable to the measurements in UPENN, which were done with about 1 pC and a pulse width of 17 μ s. Especially in the second beam time, a fast sampling oscilloscope (PicoScope 5000, Pico Technology, Cambridgeshire, UK) has been used, which was able to record these signals with a 1 kHz repetition rate. This offered the possibility for extensive post-processing beyond the averaging. Ranges were evaluated with the time-of-flight method, see section 4.3. The distance between the detector and the Bragg peak was derived from the time difference between the rising edge of the scintillator signal and the peak pressure of the acoustic signal. This is indicated in fig. 5.15 with τ_{comp} , which is similar to Jones *et al.* (2016b).

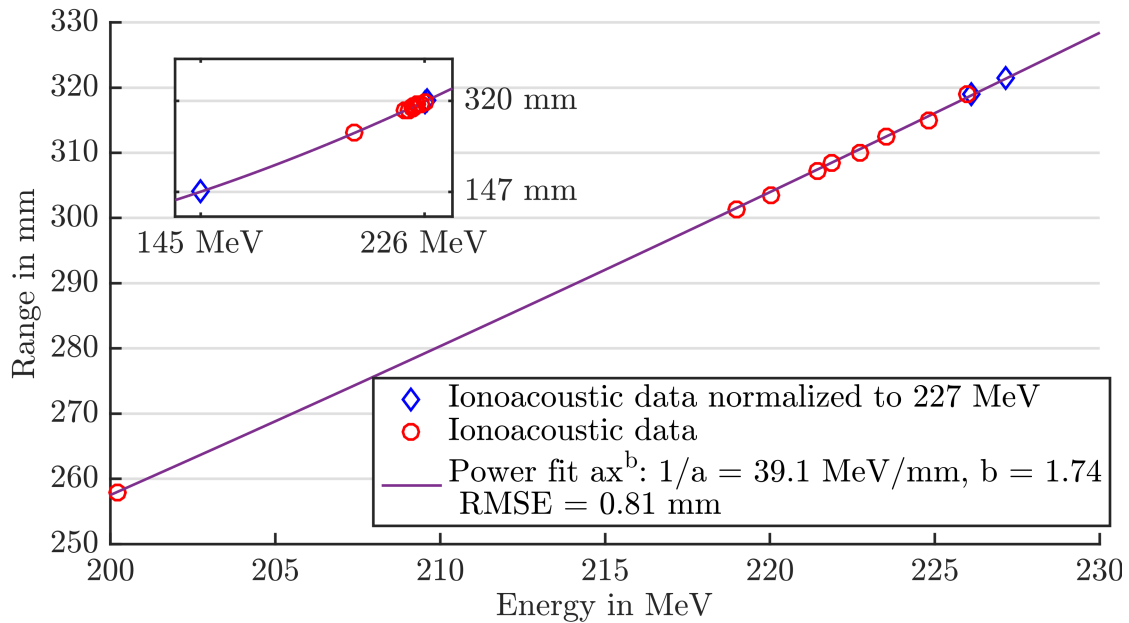


Figure 5.16.: Result of energy variation acquired at CAL, taken from Lehrack *et al.* (2017). The acquired peak positions for different proton beam energies assessed with different methods are given. In red are absolute measurements, where τ_{comp} was transferred to a range with the hydrophone's depth in water, see text for details. In blue, relative measurements are given, where the absolute range was measured relative to the range of the largest energy of 227 MeV. The range of this energy was derived from a power fit to ionisation chamber measurements, which is given in purple and was used to provided comparative range values.

In-depth studies on the C305X preceded these measurements. In basic ultrasound lab experiments summarized in section 3.6.3, the thickness and speed of sound of the casting material of this C305X was derived and an asymmetry of the inner sensitive volume was discovered. As all these information were included in the evaluation, the resulting ranges were precise and accurate less than 1 mm. Table 5.6 is a summary of these measurements for different initial proton beam energies.

The measured ranges from ionoacoustic measurements are plotted in fig. 5.16. A measurement with a large area parallel plate ionization chamber (IC, StingRay IBA Dosimetry, Schwarzenbruck) with 200 MeV proton beam energy has been conducted in the second beam time in April 2016, which can be directly compared

Table 5.6.: Summary of all absolute acoustic range measurements at CAL. The difference is (acoustical range - IC fit values). IC fit values are derived from a power fit to ionization chamber measurements, see fig. 5.16. σ is the standard deviation from a fit to a normal distribution. Since some of the values are single measurements, those values are not calculated. Indicated with a * are consecutive, comparative measurements. τ_{comp} is the time-of-flight difference used to derive the ionoacoustic range, as indicated in fig. 5.15. With the help of the IC fit, the deviation of the range $\sigma(\tau_{comp})$ was transferred to a deviation of the energy ΔE . Data shown in the bottom part of this table are from the first beam time and only relative to the highest energy, corresponding to the blue diamond data points in fig. 5.16. The range of this highest energy was set to the IC fit value, hence is only given in brackets.

Energy in MeV	Ionoacoustic Range in mm	Power fit to IC in mm	Difference in μm	$\sigma(\tau_{comp})$ in mm	ΔE in keV
200.21	258.0*	258.0*	-27	0.342	359.3
219.00	301.4	301.6	-156	0.111	109.1
220.00	303.5	304.0	-473	0.399	390.9
221.45	307.1	307.5	-367	0.394	384.1
221.87	308.3	308.5	-174	0.553	538.4
222.71	310.0	310.5	-531	-	-
223.55	312.4	312.6	-160	-	-
224.80	315.0	315.6	-646	-	-
226.00	319.1	318.5	564	-	-
227.13	(321.3)	321.3	-	0.7	-
226.13	319.1	318.9	224	1.3	-
145.0	148.0	147.2	819	5.4	-

5.2 Measurements at Medical Accelerators up to 230 MeV Protons 115

to ionoacoustic measurements as indicated in table 5.6. From this and existing IC measurements, a power fit has been created providing interpolated Bragg peak positions depending on the proton's initial beam energy. This fit is given as the purple line in fig. 5.16 and as *Power fit to IC* in table 5.6, showing the good accuracy of the range measurements conducted at CAL. Measurements from the first beam time have been included in fig. 5.16 by setting one of the measurements to the fit value of 227 MeV, and the remaining measurements in relation to this value. These measured ranges are given as blue diamonds in fig. 5.16 and titled *Ionoacoustic data normalized to 227 MeV*. The calculated IC fit was also used to transfer the deviation of the measured ranges $\sigma(\tau_{comp})$ to an energy uncertainty. Both approaches assume the IC measurements to provide a perfect, i.e. correct value.

With the use of the pressure calibration of the C305X against the B&K 8105 in Pennsylvania, the data from CAL were transferred to absolute pressure values as well. In fig. 5.15, a peak pressure value of 67 ± 10 mPa can be seen at a TOF distance of 75 mm from the Bragg peak. In order to compare these pressure values, a normalization to the applied charge per pulse is suitable, as proper pulse width conditions, i.e. stress confinement, can be assumed. In this example, this is 2 pC per 3.7 μ s which corresponds to 541 nA instantaneous current, i.e. the current per pulse. Hence, the accelerator at CAL provided 33 ± 5 mPa/pC. From the measurements at UPENN, a value of 25 ± 8 mPa/pC can be interpolated at the same distance of 75 mm to the Bragg peak. This linear interpolation has been done between two measurements at a distance of 56 mm and 86 mm to the Bragg peak, which had been conducted at UPENN in the course of the absolute pressure calibration (see section 5.2.2).

Although the C305X pressure measurement is in agreement with the UPENN result presented in this thesis, these values must be interpreted with great care. As it has been stated before, the maximum pressure amplitude depends on many parameters, especially pulse width and form, spot size, distance of the detector to the source, size of the detector, and finally the proton number. For a clear message, the variety of the measurements is too small. In this context, it is noteworthy, that a maximum peak pressure of 3.25 mPa/pC is reported in Jones *et al.* (2016b) incorporating similar experimental conditions as presented here, i.e. same hydrophone and distance to the Bragg peak. With this difference by one order of magnitude, it can be repeated again that the quality of the presented ionoacoustic range determinations is independent from a measurement of the pressure amplitude.

Unfortunately, as no explicit z-scan measurement has been done at CAL, an extrapolation of the pressure at the Bragg peak cannot be done, and thus no calculation of the dose from the acoustic measurements itself. The dose per shot can

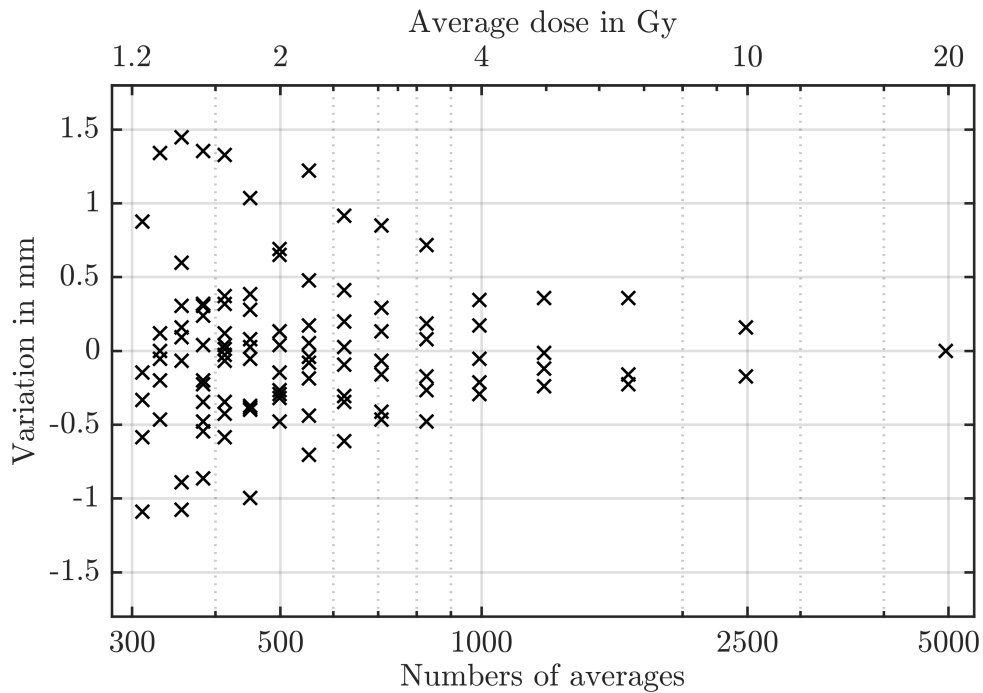


Figure 5.17.: Dose dependence of CAL measurements. From a sequence of 5000 shots, a different amount of averages was used for the range evaluation. The resulting ranges are plotted relative to the range from the full 5000-fold average. The amount of averages corresponds to the applied dose and the corresponding calculations are given in the text.

be estimated from Geant4 simulations providing the geometrical properties of the irradiation. The mass of the irradiated water volume can be estimated to 100 g, the deposited energy from a 2 pC proton pulse with 200 MeV kinetic energy is 4 mJ. Hence the dose per pulse can be estimated to 4 mGy. The dependence of the resulting precision in the range determination is plotted in fig. 5.17 against the required averages, which is connected to the applied dose. From the measurement of 5000 single 200 MeV proton pulses, after the correction for the scintillator deviation as described in the previous section, the traces were equally and randomly distributed and then averaged to multiple waveforms. The resulting picks were stored for later analysis. This has been done in order to prevent long term shifts from biasing the evaluation. In fig. 5.17 it is shown that the variation in the measured range is decreasing with increasing averages. This is clear from the correlation of averaging to the SNR. A precision of 1 mm can therefore be reached with 700 pulses or a dose of 2.8 Gy. For a decent SNR, at least 200 to 300 pulses needed to be averaged. With less pulses, the signal might still be visible, but is hardly analysed by computational means. A considerable improvement with more

than 1000 pulses per averaged waveform cannot be seen in fig. 5.17. This is due to the energy variation of the accelerator, but might also be attributed to the fact, that these 5000 single pulses were captured in packages of 5x1000 pulses with the irradiation stopped while saving each of these packages. Hence, an *inter-radiation* effect might be visible here, meaning slight changes which affected the range during the recording of each of these packages.

5.3. Measurements at the High Energy Synchrotron SIS18 at GSI

During the test beam time of the upgraded SIS18 in 2016 at GSI, ionoacoustic signals from high energy, heavy ion beams, specifically ^{12}C , ^{124}Xe , and ^{238}U ions were measured. The used charge state was 6+ for ^{12}C , 43+ for ^{124}Xe , and 63+ for ^{238}U . Although the measurements were focused on the range determination of these ions in water the scientific question behind these experiments is not primarily a medical one. As the GSI synchrotron offers a very precise monoenergetic beam with $dE/E = 1 \times 10^{-3}$, the ionoacoustic method benefits from the sharp Bragg peak at high effective charges. The focus of the following studies is set to a precise measurement of stopping power values for ions heavier than protons.

The setup for these experiments was as before a water phantom irradiated from the side, see fig. 3.1. At the experimental place in cave HTB, the vacuum exit foil of the vacuum beam line was a 100 μm stainless steel foil, and the water entrance foil a 300 μm Kapton foil. In between these two windows, the ions passed an air gap of 60 cm to 65 cm. The total energy loss of the particle on the way to the water was calculated to be 2.25 MeV/u for ^{12}C ions, 14.29 MeV/u for ^{124}Xe ions, and 21.2 MeV/u for ^{238}U ions. The range in water for ^{124}Xe and ^{238}U ions was reduced by the air gap and foil material by 1.375 mm. For ^{12}C ions, this reduction in the range in water was on average 1.4 mm and is listed in details in table 5.9. Further details on the characteristic Bragg peak dimensions for the considered irradiation are given in table 5.7, and depth dose profiles derived from Geant4 simulations are given in appendix A.

As the spot sizes and the Bragg peak widths are in the order of several millimetres, an unfocused 500 kHz 1" PZT transducer (V318, Olympus) was used. Pulses were defined by the fast extraction of the SIS18. At this acceleration modality the beam is bunched inside the synchrotron to a fraction of the round trip time. This resulted in a pulse train of intentionally produced 4-6 consecutive short pulses of around 100 ns FWHM equally stretched over 1 μs , as shown before in section 3.2.2 and fig. 3.2. Figure 5.18a shows an example of raw data acquired with a ^{238}U ion beam at 300 MeV/u. Examples of acoustic signals with ^{124}Xe and ^{12}C ions are

Table 5.7.: Expected dimensions from Geant4 simulations for the GSI experiments using ^{12}C , ^{124}Xe , and ^{238}U ions. These values include the energy loss in the experimental setup. The peak width is the FWHM of the measured Bragg curves. This was used as a first order approximation of the expected frequency (given as *exp. freq.*) given by the spatial heating function, using the peak width as $\lambda/2$.

Ion Type Charge state	Energy in MeV/u	Peak pos. in mm	Peak width in mm	Exp. freq. in kHz
^{12}C 6+	180	70.75	1.50	498
	200	85.58	1.80	415
	220	100.84	2.13	350
	240	117.07	2.49	300
^{124}Xe 43+	280	18.60	1.04	716
	290	19.78	1.06	704
	300	20.96	1.08	689
	310	22.18	1.11	674
	320	23.41	1.14	656
^{238}U 63+	250	10.41	1.26	594
	280	12.69	1.32	564
	290	13.48	1.35	555
	300	14.29	1.36	549

given in appendix A in figs. A.4 and A.5. With a range of roughly 10 mm, the signals are clearly separated in fig. 5.18a, but the beam pulse modulation overlays the signal by the turn on and off signals and is hence not clearly distinguishable. The intensity of the measured signals scales with the effective charge z_{eff} of the incident particle squared, which can be seen from the Bethe-Equation eq. (1.1). The pressure signal especially generated by the ^{238}U ion beam was so intense, that the measurements were done with only a few hundreds of particles per spill⁴. All the signals were thus measured in single shots without averaging, and high intensity shots even overloaded the still used 60 dB amplification. Nevertheless, single shot measurement with down to 200 ^{238}U particles per pulse were possible and no averaging was necessary.

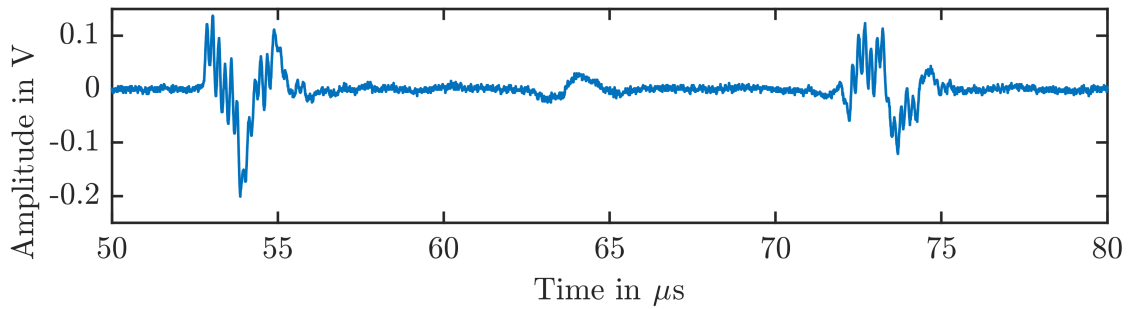
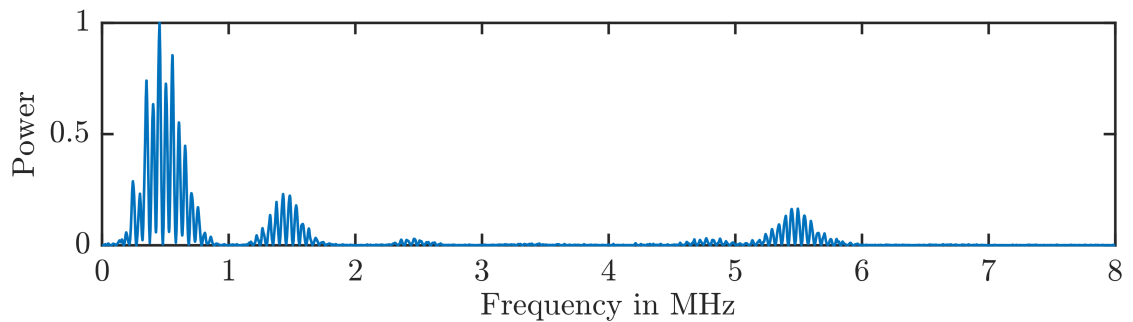
Simulations with k-Wave were done before the experiment in order to study expected signal shapes and bandwidth. An analysis of a single, delta-spike excitation

⁴This values is only estimated, as the threshold level for the beam monitors at GSI is 1×10^6 particles, but the particle current can be lowered further. These low values are therefore only guessed from the linearity of extraction below this threshold.

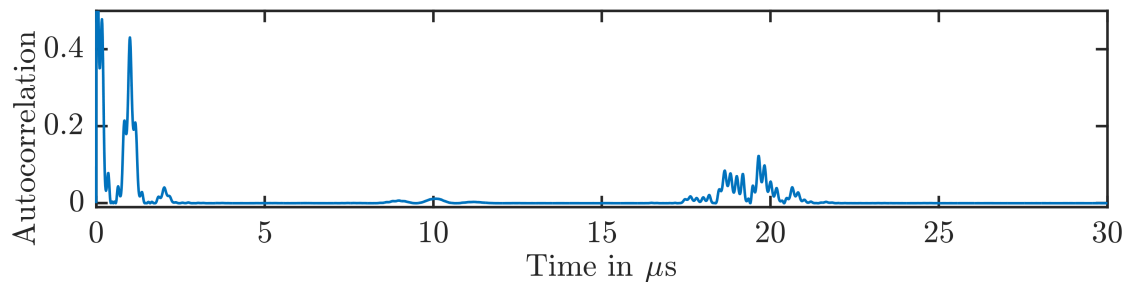
with 300 MeV/u ^{238}U is given in fig. A.7 and convolved with the expected pulse train in fig. A.8, both in appendix A. The simulation is including the given experimental setup and the SIR of the used detector, but not the EIR. Differences between simulation and measurement are probably due to additional modifications, especially acting on the phase of the signal, originating from the detector and the used amplifier. By choosing the rather low frequency PZT detector according to the expected main spatial frequencies, it was somehow expected that the high-frequency window signal is not recorded with full frequency details as given in this simulation. For the direct and reflection signal, the second part of this signal is missing in the simulation. With the uncertainty in the amplifier overloading and unexpected high signal amplitude, an unpredictable phase shift leading to a stretched signal in the measurement is possible. The expected spatial frequency as listed in table 5.7 can also be seen in the presented frequency spectrum in fig. A.8b. An interesting observation is that the pulse train is efficiently introducing the pulse repetition rate of 5.4 MHz, which is also visible in the measured frequency spectrum in fig. 5.18b despite the low design frequency of the used PZT detector. This improves the frequency based evaluation, as will be shown in

Table 5.8.: Results from time and frequency based analysis of GSI data compared to Geant4. The standard deviation σ is derived from a fit of all retrieved ranges to a normal distribution. The time based values here are derived from the reflection signal in order to be comparable to the autocorrelation value (given as *Autocorr.*).

Ion Type	Energy in MeV/u	Time based in mm	σ_{time} in μm	Autocorr. in mm	σ_{auto} in μm	Geant4 in mm
^{12}C	180	70.83	7.8	71.21	7.0	70.75
	200	85.28	59.4	85.62	41.1	85.58
	220	100.70	55.8	101.02	33.2	100.84
	240	116.75	7.6	117.14	6.5	117.07
^{124}Xe	280	18.60	4.6	18.65	1.5	18.60
	290	19.75	4.9	19.80	1.4	19.78
	300	20.92	8.4	20.96	1.7	20.96
	310	22.12	4.1	22.16	1.7	22.18
	320	23.33	4.3	23.36	1.7	23.41
^{238}U	250	10.48	8.3	10.32	26.4	10.41
	280	12.73	14.7	12.59	25.4	12.69
	290	13.50	6.4	13.39	21.6	13.48
	300	14.24	74.5	14.24	11.5	14.29

(a) Raw acoustic data from ^{238}U ion beam.

(b) Power spectrum.



(c) Autocorrelation.

Figure 5.18.: Demonstration of autocorrelation evaluation on GSI data. a) Example of raw data from ^{238}U ion beam with about 200 particles per pulse and 300 MeV/u. measured with a 500 kHz PZT, unfocused, 1" diameter of the active element. b) Power spectrum of the signal shown in a). c) Inverse Fourier transformation of b) resulting in a self-similarity spectrum. The contribution around 20 μs is resulting from the repetition of the direct signal by its reflection signal.

the following.

The default relative time based evaluation is possible, but cumbersome as no clear zero-crossing is visible. However, as the data is very stable due to the precise beam energy deriving from the synchrotron, an evaluation based on threshold

values provided promising results. For this evaluation the 50% rise time of the signal parts was used instead of the zero crossings as an estimate for the required TOF. The results of this time based evaluation are summarized in table 5.8. Here, an evaluation only based on the reflection signal is shown for simplicity, as this is the value which is comparable to the range evaluated with the autocorrelation approach. A complete set of tables with all results is given in appendix A.

In the next step, the data were analysed by its frequency content. The method based on the autocorrelation has been shown and discussed before in section 4.4 and fig. 4.4. In fig. 5.18b, the power spectrum of fig. 5.18a is plotted and several distinct features can be identified. The main peak around 500 kHz derives from the bandwidth of the used detector at this frequency as well as spatial heating function. The estimated spatial frequency based on the FWHM of the measured Bragg peaks is given in table 5.7. Overlaying this main peak is the beating deriving from the repetition of the direct signal, which is its reflection and the window signal. Also visible is the synchrotron extraction frequency of 5.4 MHz, which results in the turn on turn off oscillation of the signal. As described in section 4.4, by re-transforming the signal and analysing the minimum at the largest point in time in the autocorrelation spectrum, the signal repetition time around 20 μ s can be retrieved. The results of this evaluation are listed in table 5.8 as *autocorrelation*. The experimental results of the ^{12}C ion beam time differs from the results of the ^{124}Xe and ^{238}U ion beam times, as for ^{12}C comparative measurements are available. These comparative measurements were conducted with a precise range telescope, a water column of variable size which is similar to PTW Peakfinder. Hence, these two cases are discussed separately in the following.

5.3.1. Results from ^{124}Xe and ^{238}U Ion Beam Times

The evaluated ranges from acoustic measurements for ^{124}Xe and ^{238}U are compared to Geant4 simulations. Variations on the density and ionization potential of the water as well as geometrical properties of the beam line elements were applied in order to retrieve an uncertainty for the comparative simulation values. The applied variations had the same dimension as in section 5.1.3.

For the geometrical variations, a change in the resulting peak position by 30 μ m has been seen. The variation of the ionisation potential of water by 3 eV and the change in density resulting from ± 1 K temperature variations lead to a change in peak position of 10 μ m. Combining these two error contributions, the general uncertainty of the simulation values provided here is 32 μ m, independent from the ion type.

For the uncertainty on the acoustic range determination, the same approach as in section 5.1 is used. The uncertainty introduced by an error of 1 K in the speed of sound fit gives a range uncertainty of 42 μ m for ^{124}Xe ions and 29 μ m for ^{238}U

ions in the ionoacoustic measurements. Those values differ due to the different ranges and is dominated by the uncertainty in the speed of sound calculation due to the already discussed inaccuracy in the temperature measurement of 1 K, see section 5.1.2 for details.

The given precision σ in table 5.8 is the standard deviation derived from a fit of all measured ranges to a normal distribution, containing 20 to 50 measurements per energy. It represents therefore the precision of the evaluation and time measurement of the oscilloscope, and is comparable for ^{124}Xe and ^{238}U ions. The deviation measured with the autocorrelation evaluation method was transferred to an energy resolution and the values are listed in table A.8. A power fit has been created on the basis of simulation data, linking the measured peak position to corresponding beam energies. With this fit, the variation of the measured acoustic peak position was transferred to a variation of energy, similar to the proton data measured at CAL, see section 5.2.3. It is to be noted that this error in table A.8 does not include the uncertainty of the temperature measurements. However, assuming a possible improvement on the temperature measurement in following measurements, an energy determination from ionoacoustic measurements with a precision dE/E between 1×10^{-3} to 1×10^{-4} is possible, which would be in the same order of energy precision as provided by the GSI synchrotron.

The results of the measured ranges are in general in good agreement to the comparative simulations for all ion types. As seen in the comparative evaluation on proton data in section 4.6.1, the autocorrelation values tend to be slightly higher than the time-based evaluation. With the longer range this trend becomes less pronounced, as also the time-based evaluation using threshold levels instead of the zero-crossing is expected to provide slightly overestimated ranges. Nevertheless, the autocorrelation method is able to provide these results almost directly without a subjective interpretation of the signal in itself. These complicated temporal signals are a good example for this, making the evaluation almost independent from the explicit knowledge of the temporal beam structure. This means, that single sharp pulses are not always necessary, or longer pulse are not needed to be deconvolved in a noise sensitive procedure. This objective algorithm in the autocorrelation method is therefore recommended for an automatic online evaluation. Additionally, with single pulse measurements, such an evaluation is even further simplified.

5.3.2. Results from ^{12}C Ion Beam Time

^{12}C ion beams with energies of 180 MeV/u, 200 MeV/u, 220 MeV/u and 240 MeV/u have been measured, and the same evaluation and corresponding Geant4 simulation as with ^{124}Xe and ^{238}U ions have been conducted. The results for the range measurements are given in table 5.8. With the long range, the uncertainty due to the inaccuracy of the temperature measurement of 1 K increases to 175 μm .

Also, the given deviations of the evaluation in table 5.8 are changing considerably with the different beam energies. During the evaluation, *bad data* are selected and not considered. These are signals with e.g. insufficient SNR or considerable disturbances which influence the selection of signal point relevant for the evaluation. Nevertheless, with all careful selections, a large difference in the uncertainty at different beam energies remains. One possibility might be that a beam profile monitor was left in the beam for only a part of the measurements. The data for 200 MeV/u was measured several times during the day, which might be a reason for possible long term drifts. The other energy data was measured in shorter times in a dedicated variation of the beam energy.

For ^{12}C ions, additional range telescope measurements were available (Sihver *et al.*, 1998, Schardt *et al.*, 2008), conducted with a water column of variable length (WS). On the basis of these WS values, a power fit has been made, similar to section 5.2.3, allowing to interpolate range values for the energies of ^{12}C ions presented here. Those WS measurements were corrected for the energy loss in the air gap and foil material in front of the water phantom, thus providing the actual range in water for the given beam energy independent from the experimental setup and absorbing material in front of the water phantom. In table 5.9, the results of these range telescope measurements are compared to ionoacoustic measurements evaluated with the autocorrelation method and corrected by the expected reduction in range due to foil material. This correction has been derived specifically for the experimental setup at HTB from Geant4 simulations. It can be seen here, that the acoustic measurements and Geant4 simulations do agree well with these older range telescope measurements at a different beam line. The relative error of the ionoacoustic measurements compared to these range telescope measurement is

Table 5.9.: Comparison of range data from ^{12}C ion beams. The GSI water column (WS) ranges (Schardt *et al.*, 2008) are corrected for the energy loss before the water phantom. Hence, the difference in the peak position from simulations with and without absorbing material (cor) is added to ionoacoustic measurement values evaluated with the autocorrelation method (AC) already given in table 5.8. At last, the difference (WS-(AC+cor)) is given.

Energy in MeV	AC + cor. in mm	WS in mm	Difference in μm	G4 in mm
180	72.98	73.33	345	72.45
200	86.76	87.36	600	86.81
220	102.33	102.35	20	102.15
240	118.46	118.28	-180	118.39

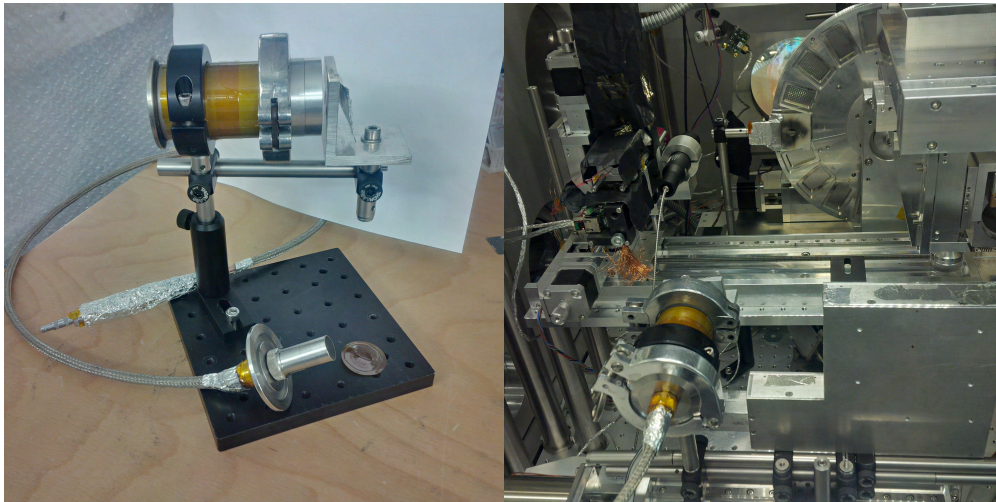
less than 1 %.

As ^{12}C ion beams are also used in particle treatment, the dose required for the signal amplitudes measured here is calculated. For that, an irradiated volume in the shape of a cylinder is estimated, similar to the dose studies done at CAL (see section 5.2.3). For a beam energy of 200 MeV/u, this cylinder has a length of 100 mm and a width of 10 mm, covering a large part of the pre-tail and the measured beam spot sizes. This provided a volume of 7.8 cm^3 and a mass of irradiated water of 7.8 g. The typical beam intensity was 1×10^8 ^{12}C particles per pulse, providing a total energy of 38 mJ. On this given mass, this would be a total dose of 4.9 Gy per pulse. Typical acoustic amplitudes were 200 mV after 60 dB amplification in single shot. This can be extrapolated to dose depending amplitude of 40.5 mV/Gy. With a typical noise level of 10 mV, the lowest detectable dose without averaging would be 0.25 Gy.

5.4. Demonstration with Laser Accelerated Particles at LEX

During the beam time of 2016, ionoacoustic measurements in the Laser ION experiment (LION) at the Laboratory for EXtreme photonics (LEX) were conducted. As the acceleration is done in vacuum, a special LIONo-acoustic detector has been developed. This consisted of a simple KF-40-pipe with an entrance foil made of 11 μm titanium on the one side and a special flange on the other side mounting the detector. This detector was filled with deionised water. Before recording, the signals were amplified by 60 dB. Figure 5.19 shows an image of the detector and the corresponding setup. The goal of these experiments was an energy diagnostic for laser accelerated ions. Usual spectrometers have problems with the high particle fluence in these experiments and the *electro-magnetic pulse* (EMP) signal, which disturbs the measurement. In ionoacoustics, the pressure is detected several microseconds after the interaction, which clearly separates EMP related disturbances from the measurement.

Different from the results of the experiments presented so far, the difficulty with laser accelerated particles is not the temporal beam profile but the spatial heating distribution in water. The energy spectrum is polyenergetic up to a cut off energy of typical 15 MeV in the case of LEX (Gao *et al.*, 2017). Without any modification, the resulting heating function would have been simply exponentially decreasing towards the detector and no significant spatial gradient would have been expected, which would be separable from a *simple* photoacoustic signal of the high power laser pulse hitting the reflective entrance foil. Hence, the initial beam was guided through a doublet of permanent magnetic quadrupoles (PMQ).



(a) The LIONo-acoustic detector. (b) Setup overview in the LION chamber.

Figure 5.19.: Images of the LIONo-acoustic setup and detector. a) The detector with the ultrasound transducer on the bottom and a pinhole in front, electrically insulated from the vacuum chamber itself to avoid noise from scattered protons impinging on the pipe. b) Setup overview inside the LION chamber with the LIONo-acoustic detector moved to the side. On top right corner the target wheel is visible, which is the place of the laser interaction.

These quadrupoles were not only focusing the otherwise highly divergent beam but also generating energy dependent focal spots (Rösch, 2015, Rösch *et al.*, 2017). This approach can be used as an energy selection system in the proton energy range from 6 MeV to 10 MeV, which resulted in Bragg peaks separated from the entrance foil. Nevertheless, the energy spread was still in the order of 2% to 3%. Furthermore, this energy selection resulted in distinct foci of single energies but other energies are still present and blurring the spatial distribution. In order to reconstruct this polyenergetic spectrum simulated annealing in combination with SRIM calculations were used (Yang, 2017). In this context, the term *Ion Bunch Energy Acoustic Tracing I-BEAT* has been introduced, which is the reconstruction of broad energy spectra using ionoacoustic measurements by applying a simulated annealing algorithm. The concepts of this approach have been already discussed in section 4.5.

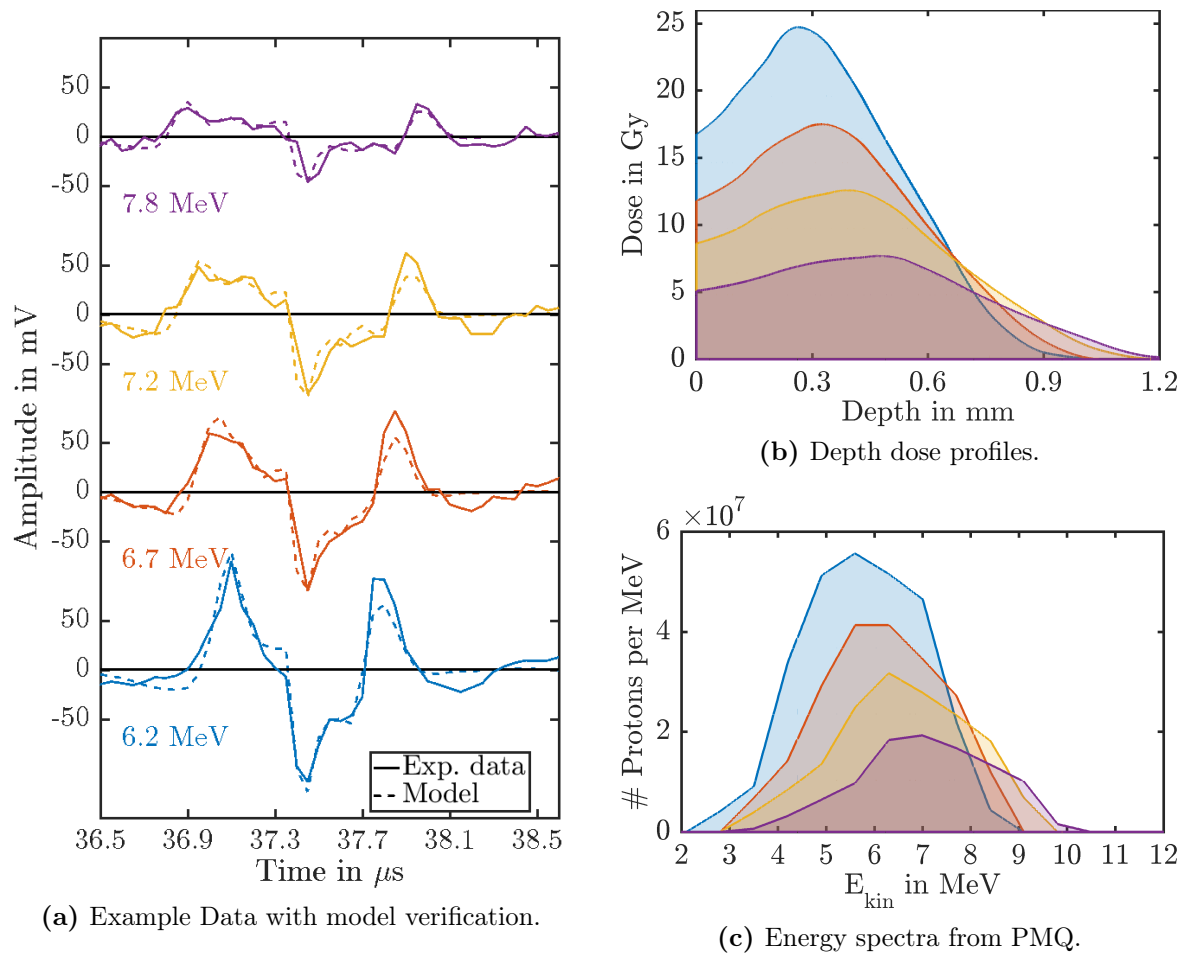


Figure 5.20.: Results of I-BEAT reconstruction of data measured at LEX (Yang, 2017). a) Raw experimental data with intended energies defined by the permanent quadrupole doublet and reduced by the entrance foil material. b) Heating function and c) energy spectrum reconstructed with described simulated annealing algorithm. This included a calibration of the detector, which made a reconstruction of an energy spectrum with absolute value possible.

Figure 5.20 shows results from these measurements. In this example, the energy focus of the PMQ was set to be in the range of 7 MeV to 8.5 MeV. In fig. 5.20a, acoustic raw data from single shots for these different energies are shown. Similar to fig. 5.6a, the distance between the direct and reflection signal is increasing with increasing energy, while the window signal stays constant. With the simulated annealing approach, the depth dose distribution and corresponding energy spectrum was derived, which is shown in the right part of fig. 5.20. The shown energy spectra have a trend corresponding to the PMQ energy selection setting,

but are broader compared to the expectation given by the PMQ design energies. This is because these PMQ are designed to focus all particles in that energy range to focal spots along the beam axis, hence lower energy particles also contribute to the depth dose profile, shifting the energy spectrum towards lower energies. The reconstructed spectra agree within 15 % compared to simulated PMQ design spectra (Yang, 2017).

In order to quantify these measurements, calibrations with monoenergetic beams had been done previously. Therefore, the exact same setup has been installed at the MLL Tandem and irradiated with a 10 MeV proton beam. From these precise measurements in terms of provided energy, the TIR of the complete setup including the amplifier has been measured and incorporated in the simulated annealing algorithm. With this correct TIR, the calculation of a comparative pressure trace from an estimated energy distribution is improved. This then reduces artefacts and in general the noise in the resulting energy spectra. Additionally, the pressure amplitude is well correlated to the input beam current. With the stable proton source at the MLL, the beam current was measured and associated with the signal amplitude. This allowed the reconstruction of an absolute energy spectrum in units of particles/MeV without an explicit pressure calibration of the transducer. Although subject to some uncertainty, this is for these laser accelerated ion beams one of only a few existing online method for energy spectrum reconstruction. Other usual methods for measuring energy spectra are neither online, like gafchromic stack measurements, or rather specific for a small energy range, like Thompson parabolas, and basically all of these methods cannot handle the high fluence of Laser driven accelerators. For the measurements of pulsed, focused laser-accelerated ion beam, the ionoacoustic method presented here as I-BEAT is comparable to existing experimental methods in terms of energy resolution and offers many advantages as the online measurement in this harsh environment.

5.5. Conclusion on Experimental Studies

Different range measurements have been presented, from low energy 20 MeV to 230 MeV protons, and high energetic heavy ions ^{12}C , ^{124}Xe , and ^{238}U . All presented cases are in good agreement with the conducted simulations, or if available, with comparing ionization chamber measurements.

The acoustic pressure has been measured with different proton beam energies and verified with k-Wave simulations. With a proton beam energy of 20 MeV, a pressure at source level of 115 ± 2 Pa was extrapolated for a 100 ns rectangular pulse containing 3×10^6 particles per pulse (480 fC). At a typical distance of 25 mm corresponding to the focal length of the used PZT transducer, this measured pres-

sure reduces to 12 ± 2 Pa. In a corresponding k-Wave simulation, the simulated pressure amplitude was 16 Pa at a distance of 25 mm.

With a proton beam energy of 220 MeV, a pressure of 67 ± 10 mPa was measured at a distance of 7.5 cm from the Bragg peak using a Gaussian pulse with $3.7 \mu\text{s}$ FWHM and 1.2×10^7 particles per pulse (2 pC). This pressure is in good agreement with a corresponding simulation providing a pressure amplitude of 70 mPa at this distance (fig. 5.10b). No extrapolation to the pressure level at the Bragg peak from data measured at CAL could be done. Nevertheless, the pressure at source level derived from the corresponding simulations with a delta-spike excitation was 5.5 Pa. This value has been calculated from the simulated dose distribution that was used in the k-Wave simulation. The maximum dose per voxel in this Geant4 simulation was 44.64 mGy for the used 1.2×10^7 protons per bunch. Remaining general problems in the determination of acoustic pressure amplitudes are discussed in the next chapter, which will lead to an outlook on ionoacoustic topics beyond this thesis.

Figure 5.21 is a summary of all measured proton range uncertainties presented in this chapter plotted against the used detector frequency, as far as this is meaningful. These uncertainties are the standard deviation σ deduced from a fit of all evaluated ranges to a normal distribution. The broadband hydrophones are listed to the left in this plot. The abbreviation RF stands for *ripple filter*, an energy modulator for the 20 MeV proton beam used to broaden the Bragg peak spatial distributions to study low-frequency detectors. A lot of effort has been put in collecting measurements with the Olympus V382, the 3.5 MHz, spherical focused PZT transducer, hence some of the measurement revealed ranges with a precision of $1 \mu\text{m}$, a result limited by the sampling frequency of the oscilloscope.

It is noteworthy, that all those results are at least one order of magnitude below the theoretical ultrasound resolution and only show a weak dependence on the detector centre frequency. The axial resolution limit is defined by the minimal distance between two surfaces, which can be distinguished in axial direction. It is hence depending of the wavelength of the emitted ultrasound wave. For 3.5 MHz, this yields an axial resolution limit of 0.5 mm. However, this limit does not apply for the evaluation, as the ultrasound deriving from a single acoustic source induced by charged particles stopped in water is measured instead. Additionally, for monoenergetic beams there is only one source point which is required to be separated from the entrance foil, i.e. a range larger than this resolution limit, a condition which is easily satisfied. Hence, the limitation is not the basic wavelength of the signal, but rather the bandwidth and phase shifting properties of the detector and its amplifier as well as the spatial gradient of the heating source. It is also to be noted once again, that the signal amplitude is not the crucial parameter. For the presented evaluation techniques, a measurement of time differences is conducted.

Two basic sources of uncertainties can be stated here, which currently provide the largest errors in the presented range determinations: The accuracy of the speed of sound in water, and the broad dose distribution for protons in stopped in water at beam energies above 150 MeV.

The sound velocity was determined by the water temperature with a high-order polynomial fit to the precise literature measurements (Marczak, 1997). The uncertainty in the temperature measurements was estimated to be 1 K, and is directly translating into a variance in the applied speed of sound. This uncertainty in the temperature measurement results in variance of the measured ranges of 20 MeV protons in water of 8 μm . The presented in-situ method with a z -scan measurement is not comparable to this. However, the literature values for the speed of sound in

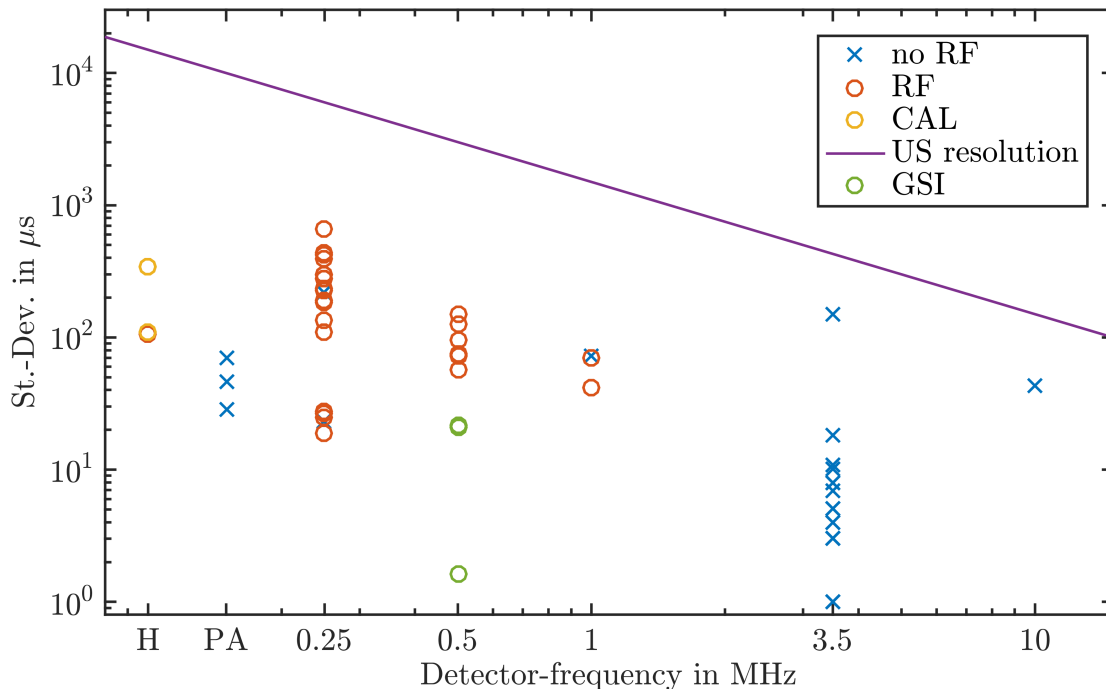


Figure 5.21.: Summary of the achieved precisions of evaluated ranges depending on the used detector frequency. Measurements conducted at different accelerators and different beam properties are separated: clinical (yellow), MLL without filtering (blue), MLL with RF *ripple filter* (red), and GSI (green). The theoretical axial resolution limit is provided. The abbreviation on the abscissa H is marking the measurements with the Cetacean C305X, mainly at CAL, see section 5.2.3, and PA is marking the Precision Acoustic needle hydrophone measurements at the MLL, see section 5.1.5. A detailed description of these ultrasound devices is given in chapter 3.

water can be determined with the used fit more accurately, hence an improvement in the temperature measurement will improve the uncertainty in the ionoacoustic range determination.

Nevertheless, the most precise results were achieved with 20 MeV protons, which provide highly confined spatial dose distributions. The results from measurements at clinical proton beam energies show inevitable a lower precision as the range straggling increases with the higher beam energy and reduces the spatial gradient in the dose distribution. Additionally, the precision in delivered energy dE/E at high energy medical accelerators is less than at the linear accelerator. The resulting uncertainties reported for the measurements at CAL in section 5.2.3 are limited by the given uncertainty of 1 MeV in beam energy. However, an improvement in accelerator technology for the sake of a precise acoustic range determination is not necessary. If an ionoacoustic measurement is able to determine the range of protons in a patient online with a precision of less than 1 mm, currently used safety margins in the treatment planning of 1 mm plus 3% could be decreased, hence sparing healthy tissue otherwise included in this margin. Promising results encouraging future research in this direction have been achieved and demonstrated for experiments in a water phantom throughout this last chapter.

6. Discussion and Outlook

And now for something completely different.

MONTY PYTHON

6.1. Summary on comparative Methods

This thesis presented many ionoacoustic studies in water and the basics of the acoustic signal generated by the energy loss of charged particles were extensively addressed. It has been demonstrated what the source of that acoustic signal is and how it can be measured and evaluated. The focus of this work was on range determination, a quantity that is depending on the particle initial kinetic energy. It has to be discussed, in which way an acoustic measurement can be used as an energy monitor for pulsed, charged particles on the one side and as an in-vivo range determination tool on the other side. At first, a summary of comparative measurements in the experiment and in simulations conducted in the course of this work is given.

6.1.1. Comparing Ionoacoustic Results to other experimental Methods

Throughout this thesis, many results of acoustic measurements are given providing range information down to precisions of some μm . It has to be discussed, to which extent this precision from ionoacoustic measurements is reliable, and how a fair comparison to other methods can be made.

In order to address these questions, comparative experimental methods are needed using established techniques. In the framework of this thesis, these are measurements e.g. with GafChromic films or depth dose profiles from ionization chamber measurements. Although only a few direct comparisons are given, the agreement to IC measurements is very good. Ionoacoustic measurements have been presented in this thesis for a wide range of energies and intensities, mono- and polyenergetic, and using different ions, all with comparable precision and accuracy of less than 1 mm in range determination.

During the experiments at CAL described in section 5.2.3, a depth dose profile from a 200 MeV proton beam in water was measured with a large diameter IC. From this and pre-existing measurements, the peak position for several energies has been extracted. From these positions, a power fit has been done in order to interpolate peak positions for arbitrary energies. This has been done for two reasons. First of all, the machine settings are optimized in terms of ranges in water and not in energies. This is a practical approach since during patients irradiation the range in water is the quantity that matters. Small variations in the actual energy are thereby tolerated, if during quality assurance an accurate range

in water is ensured¹. The measurements were conducted with the highest available energy ensuring the highest beam intensity. With small variation e.g. from different temperatures, the correlation from energy to range in water needed to be rechecked for our purposes. In this check, the range for certain energy settings of the machine is measured and then labelled with the corresponding energy. This means, that „200 MeV“ can have different effective ranges in water varying from time to time or from one therapy centre to another (Bäumer *et al.*, 2017). As the treatment planning is based on the actual range in water, this procedure is justified. It is, however, confusing for an accelerator physicist who wants to characterize the beam in terms of energy. Additionally, the range in water is typically given with the R_{80} value, but with ionoacoustics the actual Bragg peak position is measured. Depth dose profiles from IC measurements had therefore to be re-evaluated. This re-evaluation for the CAL measurements had been done with a direct IC measurement following an acoustic measurement with a 200 MeV proton beam and other pre-existing measurements which had been done shortly before the beam time. From these measurements, the peak value had been extracted with a multi-polynomial fit and a power fit had been done correlating the applied beam energy to this Bragg peak position. This fit has been used in order to interpolate values for the proton range in water, i.e. the Bragg peak position. The resulting values from this power fit are in good agreement with the acoustic measurement, as shown in table 5.6. For a proton beam energy of 200 MeV, a comparative measurement has been done consecutively, yielding the same value for the range in water of 258.0 ± 0.3 mm from IC and ionoacoustic measurements.

For the measurements at the GSI SIS18 with ^{12}C ions, water column measurements have been shown for comparison in section 5.3. These precise IC measurements have been conducted before at a different experimental place at the GSI SIS18, but have been corrected by stopping power calculations for any absorbing material in the beam line. This means, the energy loss in the specific entrance foil, air gap etc. has been calculated and the effective reduction of the range due to this specific energy loss has been obtained in a ATIMA calculation². Adding this reduction to the measured peak position of carbon ions in water provided a range value for beam energies from 50 MeV/u to 400 MeV/u independent from the specific experimental setup and its different absorbing materials before the water basin. The described reduction needed to be calculated for the ionoacoustic setup as well, and then a comparison to these older water column measurements was possible, as shown in section 5.3.2 and table 5.9. The resulting difference between the corrected ionoacoustic values does not exceed 600 μm , which is less than 1 %

¹One could exaggerate: a medical physicist does not care about the exact energy, as long as the range in water is accurate.

²A program developed at GSI which calculates amongst others the energy loss of protons and heavy ions in matter. Details see <http://web-docs.gsi.de/~weick/atima/>

of the total range, and the precision of the ionoacoustic measurements evaluated with the auto-correlation method is below 50 μm . Assuming the uncertainty of the temperature measurement of 1 K, the precision of the ionoacoustic measurement increases to 175 μm . In conclusion, after correcting the measured peak positions for the absorbing material specific for the used experimental place, the results are in good agreement to the water column measurements and also to conducted Geant4 simulations. Furthermore, the experimental results of ionoacoustic range determination for ^{124}Xe and ^{238}U ion beams are also in good agreement to conducted simulations within 100 μm .

For a comparison to other studies besides this thesis, currently two other groups need to be mentioned, although the experimental circumstances were different: At the University of Pennsylvania Kevin Jones and co-workers, and at the department of physics in Milwaukee Sarah Patch and co-workers. Comparative measurements had been conducted at UPENN and were presented in section 5.2.2. Besides these measurements, in Jones *et al.* (2016b), a range determination of a 230 MeV proton beam in lateral measurement positions with a precision of 2 mm is reported. Here, the range has been verified before with a multilayer ionization chamber. The results had been improved by the deconvolution of the rather long but still stress confined temporal pulse profile. Nevertheless, a rather large offset in the determination of the Bragg peak of 4.5 mm remains. It is expected that a more basic determination of the ultrasound properties similar to the preparing studies presented in section 3.6.3 of the used B&K 8105 will reduce this error offset. Jones and co-workers discuss the difficulties in determining the actual acoustic centre of the used hydrophone. As it turns out, the actual measurement of the ultrasound signal with such a spherical detector is complex, resulting in a frequency depending phase shift influencing the measured arrival time of the acoustic pulse (Jacobsen *et al.*, 2004). In the work of Jones and co-workers, a calibration of the detector similar to the approach described in section 3.6.3 was not possible. Consequently, the offset in the Bragg peak determination was accepted and the solution to this specific problem left for future experiments.

First ionoacoustic measurements with clinical ultrasound arrays are presented in Patch *et al.* (2016) and additional simulation work in Patch *et al.* (2017). Here, the ionoacoustic range determination with a 96-element ultrasound array is demonstrated with a chopped 50 MeV proton beam, corresponding to a range in water of 20 mm, and a pulse width of 1.7 μs in simple water phantoms and first heterogeneous phantoms including an oil-filled bubble. In Patch *et al.* (2016) a range determination of this proton beam in axial measurement position with a precision of 1.2 mm in plain water and 1.5 mm for the heterogeneous phantom is presented. The comparison has been made to SRIM Monte Carlo Simulation supported by spot size measurements from GafChromic films. A further comparison to an es-

tablished experimental method has not been done. However, the value of the work of Patch and co-workers is the successful demonstration of a clinical ultrasound device for ionoacoustic range determinations, although in special experimental circumstances including a specially pulsed low range proton beam with rather high doses.

6.1.2. Comparing Ionoacoustic in Simulations

Besides these experimental methods, comparative simulations have been presented. The conducted simulations can be separated in ion interaction and transport as well as acoustic propagation simulations. The used techniques have been presented in chapter 2, which are Geant4 for particle simulations and k-Wave for the acoustic evaluation.

Geant4 can be used to get a realistic dose distribution for acoustic simulations. On the basis of these simulations, the initial pressure is calculated, as demonstrated in section 2.1.4. However, retrieving Bragg peak position with a required accuracy remains challenging, as it has been shown in section 5.1.3. Here, for low energetic protons, the uncertainties in the simulation itself with the ionisation potential and geometrical variations leads to an uncertainty of 28 μm for 20 MeV protons. Considering the resulting variation, those simulations have an accuracy in the same order of magnitude as the ionoacoustic measurements, both depending on the accuracy of the knowledge of the material properties. The most obvious issue is the measurement of the water temperature, which is directly influencing the used speed of sound and the density applied in the simulation. Here, the influence of a variation in temperature on the density is less pronounced than on the speed of sound. For the ionization potential the recommended value of 78.0 eV for water (ICRU, 2014a) was used throughout this thesis, resulting in comparable results. Especially in the experiments conducted at the MLL tandem, the possible sources of error in the simulation are only material dependent, as the energy precision is ensured by the calibrated 90° bending magnet after the acceleration. Hence, a simulation can incorporate this precise energy information and actually contribute to an accurate range prediction, as done in section 5.1.3. Here, the ionoacoustic measurements can be interpreted as a validation of the recommended value of the ionization potential.

One problem arising during the simulation studies is the correct prediction of pressure amplitudes in k-Wave simulations. Although the process in which ions stopping in water generate pressure has been carefully investigated, considerable differences between the simulated and measured acoustic amplitude up to a factor of 3.5 have been found in this thesis as well as in the topical literature (Jones *et al.*, 2016b, Nie *et al.*, 2017). Future improvements must include a thoughtful examination of the underlying pressure evaluation process in this simulation, especially

if the correct damping and attenuation of the pressure signal is included. The experimental results in terms of pressure amplitude per pulse charge presented in this thesis in section 5.2.2 and section 5.2.3 are comparable. With the same detector and amplifier at a distance of 7.5 cm, 25 ± 8 mPa/pC were measured at UPENN, 33 ± 5 mPa/pC were measured at CAL, both using proton beams with clinical beam energies. These stable experimental results suggest that uncertainties in the simulation can be reduced. Therefore, several points to be considered are discussed in the following.

The hydrophone calibration should be repeated on a broadband artificial source, covering acoustic frequencies in the range of 1 kHz to 500 kHz. As it has been seen in the course of transducer calibrations in Duque (2016), the quality of a calibration is directly linked to the quality of the calibration source, especially its bandwidth. If possible, a calibration as conducted with the LIONo-acoustic detector is desirable, where no direct translation to pressure units is necessary. If the hydrophone signal can be directly correlated to the kinetic energy of the proton beam in a fixed setup, a reconstruction of energy spectra as with the laser accelerated proton data is possible.

Furthermore, the prediction of initial pressure is considering a perfect translation from kinetic energy via dose and temperature increase to a dynamic pressure amplitude. This conversion is certainly efficient, as e.g. only a small part of the beam energy is transferred in nuclear reaction processes instead of electronic collisions. The conducted Geant4 simulation correctly computes the dose considering long range energy transfer in secondary particles such as prompt γ particles or neutrons. More pronounced is the uncertainty in the thermal properties, i.e. the volume expansion β , the conversion efficiency η , and compression coefficient κ . Especially β is subject to high variation depending on the temperature of water, therefore the most important parameter influencing the Grüneisenparameter. Throughout this thesis η has been considered to be 1 for simplicity, and there has been no direct indication that this conversion efficiency from dose to heat is much less. However, this conversion is expected to be less than 100%. Improvements can therefore be done by a thoughtful examination and re-measuring of these values for any clinically used material, which has been started in Nie *et al.* (2017), but did not lead yet to better pressure amplitude prediction in simulations. It can therefore be concluded, also for the presented direct integration of the ionoacoustic pressure in section 2.3.1, that the results in acoustic simulations are highly depending on the quality of the input parameters and dose calculations. This somewhat trivial statement raises the need for a thoughtful examination of all thermodynamic parameters influencing the Grüneisenparameter for all tissue related materials. This is further discussed in the context of heterogeneous phantom studies in the next section 6.2.2.

As many aspects of the ion beam are influencing the simulation outcome, especially in terms of pressure amplitude, the use of ionoacoustic for an absolute dose verification is questionable. High fluctuations on the amplitude measurements directly influence the transfer calculations from pressure amplitude to deposited energy. However, contrary to the calculations given in section 5.1.5 where the effective volume and characteristic dimensions are roughly estimated, in a medical environment the radiated volume would be well defined by the treatment plan. On the other side, the use of monoenergetic proton beams as used throughout this thesis is somehow idealized, as in clinical treatment several spots or energy layers are stacked up delivering a homogeneous dose covering the full planned treatment volume. From the measurement of a pressure amplitude itself, only a calculation of the deposited energy is possible. Although it may be possible to obtain a dose estimation from ionoacoustic measurement, the determination of ranges is the key measurement.

6.2. Feasibility of medical Ionoacoustics

6.2.1. Technical Requirements

The requirements for the generation of measurable acoustic signals from charged particle beams has been examined before. In this section a summary of technical requirements is given, which are necessary for a ionoacoustic measurements with clinically used beam. The aspects to consider are the pulsing of the beam, the effective charge of the used particles, the possible positioning of the ultrasound device, and the properties of the medium. All these parameters need to be optimized in order to ensure a sufficient Signal-to-Noise-Ratio (SNR) in the measurement. Combined with a sufficient time resolution of the measured signal and a correct speed of sound in tissue a good ionoacoustic range determination is ensured.

6.2.1.1. Pulse Widths

Most important is the pulsing on a rather small time scale window. Short pulses are required to fulfil thermal confinement in the first place and producing adiabatic processes. On the other hand, high frequency beams, e.g. the approximate 60 MHz oscillation of an isochronous cyclotron, are too fast, thereby not producing any measurable temperature increase. As mentioned in section 3.2.1, the upcoming new generation of synchrocyclotron produces inherently bunched pulses, providing ideal conditions for ionoacoustic measurements. At CAL, range determination results with a precision and accuracy of less than 1 mm were achieved with a pulse width of 3.7 μ s (Lehrack *et al.*, 2017). Currently existing medical accelerators,

which are mainly isochronous cyclotrons for protons, will require additional pulsing as e.g. used in Jones *et al.* (2014). This pulsing on the source is achieved by applying a fast pulse on the arc current for IBA's cyclotrons. As shown in section 5.2.2, pulse widths of $17\ \mu\text{s}$ FWHM were achieved with beam conditions dictating a stress confinement of $18.5\ \mu\text{s}$. With such pulses, range determinations results with a precision around 2 mm were achieved (Jones *et al.*, 2016b). This approach is limited, as the arc current cannot be quenched fast enough. The ignition and distinction of the required plasma is limited. Accelerators produced by the company Varian, e.g. the accelerators at the *Rinecker-Proton-Therapy-Centre* (RPTC) in Munich or *Paul-Scherrer-Institut* (PSI) in Villingen, inject the ions from the source to the cyclotron by a deflector in order to control the delivery. This could be used for a more efficient pulsing instead of the modulation of the arc current. The installation of a complex chopper-buncher system as used for the 20 MeV proton beam experiments in this thesis is challenging due to the space restrictions between source and main acceleration, and is too complex when placed on the high energy side after the acceleration.

The advantage of the synchrocyclotron can already be seen in the different experimental results comparing UPENN and CAL (see section 5.2.2 and section 5.2.3). As the accelerator in CAL provided irradiation at shorter pulses with comparable beam currents, ranges of protons in water have been measured with accuracy and precision better than 1 mm (Lehrack *et al.*, 2017) in ideal axial position. Taking into account the comparative range determination presented in fig. 5.12, the better range precision can be attributed to the better beam condition at CAL, regarding ionoacoustic measurements. In order to overcome disadvantages due to the longer pulses, UPENN developed an evaluation procedure based on the deconvolution of the measured temporal pulse. As this is a complex and noise-sensitive method, the demonstrated improvement on the range determination is low. In Jones *et al.* (2016b), an improvement of the error in the range determination of 30% is achieved, with a final precision of the range of protons in water of 2 mm. The limitation is here at the spatial heating function of the high energetic proton beam, but it shows a possible evaluation method for pulse widths close to the stress confinement. The measurements presented in Jones *et al.* (2016b), from which these number are taken from, show that after the removal of influences by the pulse width the uncertainties in the acoustic measurement properties of the used hydrophone remained.

6.2.1.2. Beam Charge and Intensity

One of the challenges already arising with protons at those high energies is the increasing range straggling resulting in broad spatial gradients and thereby lower

frequencies and signal amplitudes. As this is rather generic to the basic physical behaviour, this could only be compensated by higher intensities and better hydrophones. With the presented results in this thesis, those options are exhausted. Two of the most sensitive low-frequency hydrophones commercially available have been used and compared, and their results were presented. The used dose rate in those experiments were at the clinical limit. One remaining option is the use of heavier ions. The results of the measurements at GSI especially using carbon ions showed that the same precision can be achieved despite complicated pulse structures. The higher transferred energies of heavier ions are also in favour of ionoacoustics. In the ongoing argument of photon vs. charged particle therapy, an ionoacoustic in-vivo range determination on carbon ions can be more easily achieved as the acoustic amplitudes are expected to be at least one order of magnitude higher than with protons due to the increase in the effective charge of the used incident particles. However, this requires the use of a fast pulsing as the fast extraction used in the presented experiments conducted at GSI, which is typically not implemented at clinical accelerators.

One method to improve the accuracy of the absolute range determination proposed in Lehrack *et al.* (2016) was the use of an additional transducer at the bottom of the water phantom. Currently in the medical measurements, the accuracy is also limited by the precise levelling to the water surface. The ultrasound pre-studies described in section 3.6.3 also tested how good the hydrophone can be positioned between such a transducer and the water surface. Ideally, the ionoacoustic signal could be captured with a good transducer instead of the C305X hydrophone. In that case, this positioning could be done inherently with a simple pulse-echo-measurement conducted by the same transducer. Unfortunately, this was not possible during the beam times at CAL, as the signal amplitude was at the detection limit even for the sensitive hydrophone. A PZT based transducer with a similar sensitivity as the C305X is not available and cannot be foreseen. Nevertheless, the combination of a sensitive hydrophone with a positioning transducer would be an improvement for the determination of the distance to the water surface required in the currently conducted evaluation of measurements with medical proton beam energies.

6.2.1.3. Angular and Patient-site Dependence

In Jones *et al.* (2016a), the error in determining the proton range in water was studied and fig. 6.1 has been taken from there. Going towards medical applications, the ideal axial measurement position of the ultrasound detector cannot be ensured, as it has been rigorously exploited in this thesis. In fig. 6.1, the systematic error in the determination of the range is given in millimetre depending on the transducer position. For a systematic error of ± 1 mm, the maximum angle between the beam

axis and the detector is given as $\Theta < 20$ deg. This angle θ corresponds to a half-open angle. For a detector distance of 5 cm, the circular area inside that angle would be 10.5 cm^2 with a radius of 1.8 cm. Considering the C305X with a detector size of $2 \times 2 \text{ cm}^2$, possible variations in the position relative to the beam axis is less than a centimetre. The question that arises is how to compensate the error in a non-axial measurement position. With only one detector, a triangulation, as presented in section 6.2.2, is not possible. However, for simple pencil beams, the runtime of the different signal elements, i.e. α and γ signal, can be evaluated. This can yield a range, if the position of the hydrophone is precisely known and the data acquisition of the hydrophone is correctly triggered with the protons entering the water phantom. This is also achieved with a successful deconvolution of the temporal profile, after which the new t_0 is the peak value of the scintillator trace, see fig. 4.3. The range of the protons in water is then calculated by assuming that the source of the recorded α and γ signals are on a straight line. For this evaluation, the signals must be clearly separated. There are distinct positions, where the runtime of these signals is equal, thus blurring the signal. The systematic error is plotted in fig. 6.1a in a 2D distribution, and in fig. 6.1b as a line-out in front of the Bragg peak. The pulse width used in these studies was a delta spike excitations in order to neglect the pulse width dependency. This plot shows, that for non-axial measurement configurations, which are probably all clinical situations, an array of multiple detectors enabling triangulation is necessary.

And finally, the treatment site must allow ultrasound measurements. For the lower abdomen and other soft-tissue regions, generating and measuring ultrasound is a

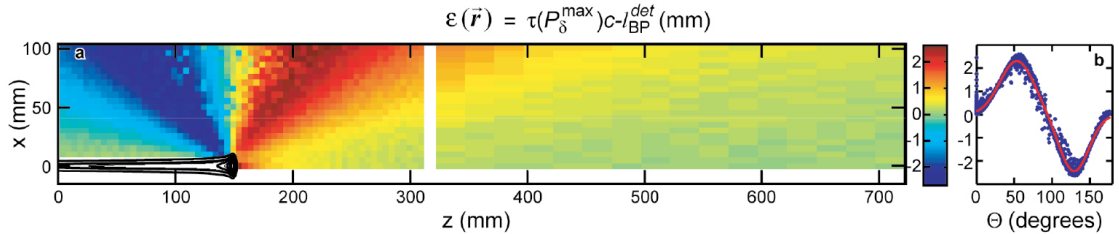


Figure 6.1.: The systematic error in determining the Bragg peak distance, taken from Jones *et al.* (2016a). Based on simulated measurements with a single element transducer and short pulses, the proposed absolute range determination relies on the clear distinction of α and γ signal in the recorded waveform. a) In positions with similar distances to the sources of these signal, a constant, position depending error is found and given as red and blue marking over- and underestimations in the determination of the range in water. This colour-coded error is given in mm. b) Angular dependence of this systematic error, where θ is the angle between the beam axis and the detector. It corresponds to a line-out in front of the beam.

clinical daily routine. Tumour sites in the lung are more complicated, as the air is preventing the efficient progression of ultrasound. Nevertheless, tumours close to the ribs might be possible to image with ultrasound, hence an ionoacoustic signal could be detected. Treatment of these body regions, where organ movement is the biggest challenge, could then benefit from an in-vivo range and position determination. Ultrasound is usually not applied at head regions, as the skull bone is highly reflective and absorbing, thus preventing any imaging ultrasound with required image resolution. However, the ionoacoustic signal has been shown to be in the lower ultrasound frequency. For the presented experimental studies in section 5.2, the detected main frequency did not exceed 20 kHz. Although no imaging might be feasible, the detection of ionoacoustic signals might be possible, as this lower frequency is less damped in the skull bone. However, compared to currently applied methods by fixing the patients head, the additional benefit from an ionoacoustic range determination might be low. The ideal treatment site is the lower abdomen, especially the prostate. Here, an ultrasound probe can be positioned rectal close to the organ, which would allow measurements of ionoacoustic signals close to the Bragg peak.

6.2.2. Heterogeneous Studies

Despite the technical considerations discussed above, one of the next challenges will be studies in heterogeneous phantoms. First studies using the k-Wave function for converting CT data to acoustic properties have been done recently, and a short summary and outlook on this topic is given here.

For the beginning, ideal cases are assumed, where perfect point transducers are placed freely in realistic CT-scans. As a typical fraction amounts to a dose of 2 Gy, signals can be expected suitable to determine ranges with a precision of ± 1 mm. This can be seen in the dose study conducted at CAL, see fig. 5.17. Additional reflection and absorption on multiple tissue surfaces will lower the signal amplitude. On the other hand, with a normal body temperature of 37 °C the Grüneisen parameter is twice as high as with 20 °C, doubling the expected signal amplitude. As so far no relative evaluation on high energetic, medical ionoacoustic measurements was possible, basic US reconstruction was studied. In a triangulation setup including multiple detector elements, the common source of a single signal can be recovered. Such a procedure can be considered state-of-the-art and is hence not explained further in this thesis. A measurement of the range would be possible, if the window signal could be detected and reconstructed, which would yield the entrance of the protons into the phantom. If this setup would also be able to produce ultrasound with MHz frequencies, an image of the tumour region could be made and directly combined with the ionoacoustic measurement of the irradiation. This is a clear advantage compared to the co-registration of other clinical imaging

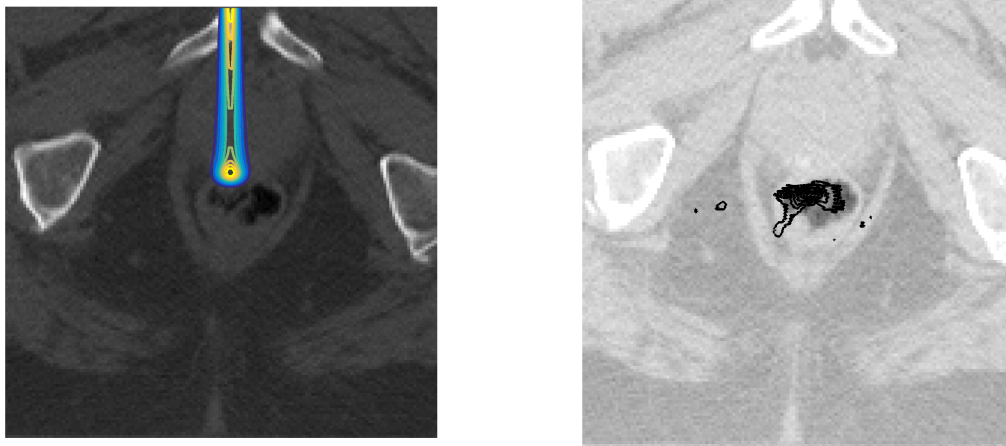
methods, e.g. CT and MRT, since with this ultrasound setup, imaging and measurement device is the same. In Patch *et al.* (2016) and Kellnberger *et al.* (2016) the possibility of such an ionoacoustic co-registration with low energy protons has been demonstrated, i.e. synchronizing the ionoacoustic measurement with an ultrasound imaging method, either standard clinical ultrasound or photoacoustic imaging. This synchronization requires a precise trigger, as used in the measurements in Lehrack *et al.* (2017). Different to normal ultrasound imaging with a pulse-echo-method, the measurement of the ionoacoustic signal has to be correctly synchronized for such a co-registration and for the required high averaging.

First simulation studies have been conducted using doses from realistic treatment planning systems on actual patient data (Sommer, 2017, Jones *et al.*, 2017b,a). The expected pressure signal arriving on a detector can then be simulated with k-Wave and the signals used for the development of evaluation techniques. As a first step, the expected acoustic signal was simulated and the discussion focuses on the propagation of ultrasound. It is expected that an acoustic signal is somehow generated, as already shown in Hayakawa *et al.* (1995), once the pulsing and spatial requirements are fulfilled. Due to rather large differences in the Grüneisen parameter for human tissues, a factor of 3 in pressure amplitude can be expected e.g. between fat ($\Gamma = 0.8$ (Yao *et al.*, 2014)) and soft tissue ($\Gamma = 0.25$ (Jones *et al.*, 2017a)). An ionoacoustic simulation included in a treatment planning work flow could also include the calculation of a *calibration shot*, optimized for highest pressure amplitude.

In Jones *et al.* (2017a) the computation times are a little more than 10 minutes on a moderate computation system. This is including specifically the C++ optimized binary executable of k-Wave (Jaros *et al.*, 2016) as well as low-frequency settings in the simulation, i.e. a rather large spacing and minimized absorbing boundaries. The results reported in Jones *et al.* (2017a) are in the order of 1 mm, but are finally limited by the resolution of the underlying CT-image. Including high resolution images of a full organ simulations can easily scale up the run time of such a pressure prediction to several days (Sommer, 2017). One way to face this challenge are better computation methods exploiting the high throughput of parallel computing or graphic card based codes (GPU) (Jaros *et al.*, 2015). Especially the GPU based code of k-Wave can reduce the run-times by at least one order of magnitude, but is limited by the memory size of the provided graphic cards. With memory requirements extending to 20 Gb, especially with medium grids defined by CT-images, this is not an option.

Besides these technical considerations, the approach of this forward calculation based on CT-images will incorporate the same limitations as usual treatments planning: the conversion from Hounsfield-Units to acoustic properties. Similar to the empirical values for the stopping power (Schneider *et al.*, 1996), relationships

for acoustic parameters in human tissues are available (Mast, 2000), but are limited in precision, hence limiting the results of a direct evaluation as well (Cox *et al.*, 2009, Jones *et al.*, 2017a). This problem could be circumvented by considering a relative, in this sense full image based approach. As indicated in Kellnberger *et al.* (2016) and Patch *et al.* (2016), a combined ionoacoustic measurement and imaging device would incorporate acoustic imperfection in an unscaled image, which would give at least a rough verification on the daily correctness of the dose delivery. This procedure would then only require a simple tomographic reconstruction of the ionoacoustic measurements on several receiving elements, but delayed as the acoustic source is not the detector itself. Figure 6.2 should give an impression of such an image. It is based on a k-Wave simulation done in Sommer (2017) including density and speed of sound from CT-data and pencil beam dose input from the CERR treatment planning system. The simulation input is in fig. 6.2a. The pressure detected by an array of ultrasound elements positioned axial to the beam was then fed into 3D planar FFT reconstruction provided by k-Wave. The positioning of the detector element should emulate an ultrasound probe in the patients rectum. This reconstruction resulted in the black overlay in fig. 6.2b. Here, this reconstructed pressure was overlaid on the density distribution used in the simulation.



(a) Simulation input from treatment planning. (b) Reconstructed pressure on density image.

Figure 6.2.: Possible reconstruction of initial pressure simulated with an array of ultrasound elements. a) Possible treatment plan of a prostate. b) Pressure reconstruction based on ionoacoustic measurements.

This attempt shown here can be considered a rather artistic impression, as this image was produced with a crude registration of the underlying image and the reconstruction output. Nevertheless, the reconstruction can be done in a few seconds, compared to several minutes of acquisition time for PET Imaging (Parodi, 2016). Considering an actual ultrasound measurement from an optimized calibration, such an image can be envisioned as a tool for daily in-vivo range verification. Additionally, this will be an actual real-time, in-vivo image of the range in the patient tissue. Recently, simulation studies progressing this idea have been presented in Patch *et al.* (2017). In the work flow presented in that publication, range estimations with an average error not greater than 2 mm were possible using a standard US array.

6.3. Ionoacoustic as a general Ion Energy Monitor

Different than the development in the medical field, experimental studies involving ionoacoustics have been conducted on a more basic scientific direction. That means, other than in medical applications, the measurements can be restricted to perfect angles, i.e. axial, allowing precise relative data evaluations. One example is the LIONO-acoustic experiments on laser accelerated ions and the simulated annealing involved. The underlying method in this model based approach is successful due to its simplifications on the surrounding geometries and homogeneous materials. An ionoacoustic particle energy monitor exploiting this full model description can be envisioned which could also be a simple daily QA tool (Lehrack *et al.*, 2017).

Although limited to pulsed beams, several applications might benefit from such an energy monitor. Especially in the field of laser plasma acceleration, measuring particle beams faces challenges due to high particle fluxes and EMPs from high intense laser field. Normal scintillation detection using sensitive PMT will saturate quickly or have inefficient signal generation, e.g. by lowering beam currents or measuring non-axial. So far, no other electronic online method has been demonstrated which is sustaining high particles fluxes and still able to measure with a sufficient accuracy. Worthwhile to mention are spectrum measurements with stacks of radiochromic films, which are only usable for a single shot, or Thompson parabola setups, which usually are tailored for parts of the beam. Additionally, due to the speed of sound of the signal, EMP induced disturbances are clearly separated from the pressure detection. With the modelling approach implementing a simulated annealing algorithm, a simple acoustic detection system was able to determine the full energy spectrum quantitatively calibrated on a Shot-by-Shot basis. With further improvements and reasonable prior information, those single shot measurements can be transferred to a full energy or range spectrum in a few

seconds well adapted to current repetition rates of laser driven sources.

In the framework of the polyenergetic retrieval algorithm it has been shown that the full reconstruction of the irradiated volume is beneficial. The reconstruction algorithm relied on the uniform spot size in order to calculate expected pressure signals. However, a first 3D setup has been designed, where the acoustic signal can be recorded from the axial and lateral detector position simultaneously. With such a detector setup including ultrasound transducers in lateral position, a beam positioning is also possible.

As it has been shown in the measurement with the absorption wheel, the ionoacoustic range determination is a simple, yet effective tool for determining small range shifts. In section 5.1.4, the stopping power of MR-A2 plastic has been determined via the measurement of the water-equivalent ratio. With the precise determination of the range in water, this stopping power was determined with an estimated relative error of 0.5%. In combination with the good results measured at GSI (see section 5.3), stopping power values for heavier ions can be determined with similar precision. As pointed out in Montanari and Dimitriou (2017), especially the stopping power of heavier ions in water is of interest.

Appendices

A. GSI Results

In this appendix, the full tables containing the results of the GSI beam times are given, as well as depth dose profiles from the conducted Geant4 simulations and additional, exemplary acoustic measurements. The details of the setup and evaluation methods are explained in section 4.4 and section 5.3.

The tables are separated by the used ion type and applied evaluation methods. All given peaks and ranges are Bragg peak positions. The provided σ are derived from a fit of all measured ranges to a normal distribution. *Reflection* refers to the result from an evaluation based on the reflection signal using appropriate threshold levels instead of zero-crossings. This was necessary since the pulse train blurred clear zero-crossings. *Window* refers to the results with the use of the window signal instead of the reflection. For ^{12}C ions, comparative measurements conducted with the water column are listed as *WS ranges*. These time based results are given in the tables A.1, A.4 and A.6.

In the frequency based tables, the centroid and minimum evaluation is given. The centroid can be used as a first approach to the correct minimum in the autocorrelation. However, this is not the correct value but this metrics is calculated faster. The minimum closest to that centroid is the correct value, and given in the corresponding column. These results are given in the tables A.2, A.5 and A.7

In table A.3, the differences from one energy step to the next for ^{12}C ions is given. This shows that despite the discrepancy in the absolute values, the relative shifts are in good agreement for all presented energy values.

In figs. A.1 to A.3, the depth dose profiles of ^{12}C , ^{124}Xe , and ^{238}U ions for all used energies are given, respectively. The presented depth dose profiles for ^{12}C ions in fig. A.1 are simulated without absorbing material in front of the water phantom. In the simulations for ^{124}Xe and ^{238}U ions, the vacuum exit foil air gap and Kapton foil as the water entrance foil is included.

In figs. A.4 and A.5 additional acoustic measurements are given for a 300 MeV/u ^{124}Xe ions and a 200 MeV ^{12}C ions, respectively. An exemplary comparison of different used PZT transducers is given for a measurement with ^{124}Xe ions in fig. A.6. In figs. A.7 and A.8, an analysis with the autocorrelation method is given for simulated pressure traces from a k-wave simulation with a 300 MeV ^{238}U ion beam. In fig. A.7, the result of a single delta spike excitation is given. In fig. A.8, the calculated pulse train profile for an exiting frequency of 5.5 MHz as presented in fig. 3.2 has been convolved. For both, the 0.5 MHz PZT transducer used in the

experiments has been included as the geometry of the pressure sensor, however without additional signal modifications which would emulate an EIR function.

Energy in MeV/u	G4 peak in mm	WS ranges in mm	Reflection in mm	σ_{ref} in μm	Window in mm	σ_w in μm
180	70.75	73.32	70.83	7.8	70.99	49.8
200	85.58	87.36	85.28	59.4	86.45	92.1
220	100.84	102.35	100.70	55.8	101.90	114.3
240	117.07	118.28	116.76	7.6	117.85	21.2

Table A.1.: Results from ^{12}C ions at GSI, time based.

Energy in MeV/u	Centroid in mm	σ_c in μm	Minimum in mm	σ_{min} in μm
180	71.64	20.6	71.21	7.0
200	86.11	100.7	85.62	41.1
220	101.52	43.7	101.02	33.2
240	117.87	13.7	117.14	6.5

Table A.2.: Results from ^{12}C ions at GSI, frequency based.

Energy in MeV/u	Δ G4 peak in mm	Δ WS in mm	Δ Ref. in mm	Δ Window in mm	Δ Cent. in mm	Δ Min. in mm
180	0.00	0.00	0.00	0.00	0.00	0.00
200	14.42	14.03	14.30	15.46	14.46	14.32
220	15.13	15.00	15.57	15.45	15.41	15.48
240	16.18	15.93	16.06	15.96	16.36	16.12

Table A.3.: Difference in the resulting ranges in water for different beam energies for ^{12}C ions at GSI. Here the consistency in a relative measurement is shown.

Energy in MeV/u	G4 peak in mm	Reflection in mm	σ_{ref} in μm	Window in mm	σ_w in μm
250	10.41	10.47	8.3	11.03	17.6
280	12.69	12.73	14.7	13.03	11.5
290	13.48	13.50	6.4	13.81	12.2
300	14.29	14.23	74.5	14.60	58.8

Table A.4.: Results from ^{238}U ions at GSI, time based.

Energy in MeV/u	Centroid in mm	$\sigma_{centroid}$ in mm	Minimum in mm	σ_{min} in mm
250	10.54	45.2	10.32	26.4
280	12.60	15.0	12.59	25.4
290	13.33	13.0	13.39	21.6
300	14.25	19.2	14.24	11.2

Table A.5.: Results from ^{238}U ions at GSI, frequency based.

Energy in MeV/u	G4 peak in mm	Reflection in mm	σ_{ref} in μm	Window in mm	σ_w in μm
280	18.60	18.60	4.6	18.58	14.1
290	19.78	19.75	4.9	20.00	7.3
300	20.96	20.92	8.4	21.16	13.7
310	22.18	22.12	4.1	22.11	22.2
320	23.41	23.33	4.3	23.37	114.4

Table A.6.: Results from ^{124}Xe ions at GSI, time based.

Energy in MeV/u	Centroid in mm	σ_c in μm	Minimum in mm	σ_{min} in μm
280	18.69	4.3	18.65	1.5
290	19.84	4.9	19.80	1.5
300	20.97	17.4	20.96	1.7
310	22.16	6.1	22.15	1.7
320	23.36	5.4	23.36	1.7

Table A.7.: Results from ^{124}Xe ions at GSI, frequency based.

Table A.8.: Range uncertainties translated to energy uncertainty via power fit based on simulation values.

Ion Type	Energy in MeV/u	σ_{auto} in μm	σ in keV/u
^{12}C	180	7.0	10.4
	200	41.1	55.8
	220	33.2	42.4
	240	6.5	7.7
^{124}Xe	280	1.5	13.2
	290	1.4	12.4
	300	1.7	14.4
	310	1.7	14.4
	320	1.7	14.4
^{238}U	250	8.3	113.9
	280	14.7	185.9
	290	6.4	78.8
	300	11.2	134.8

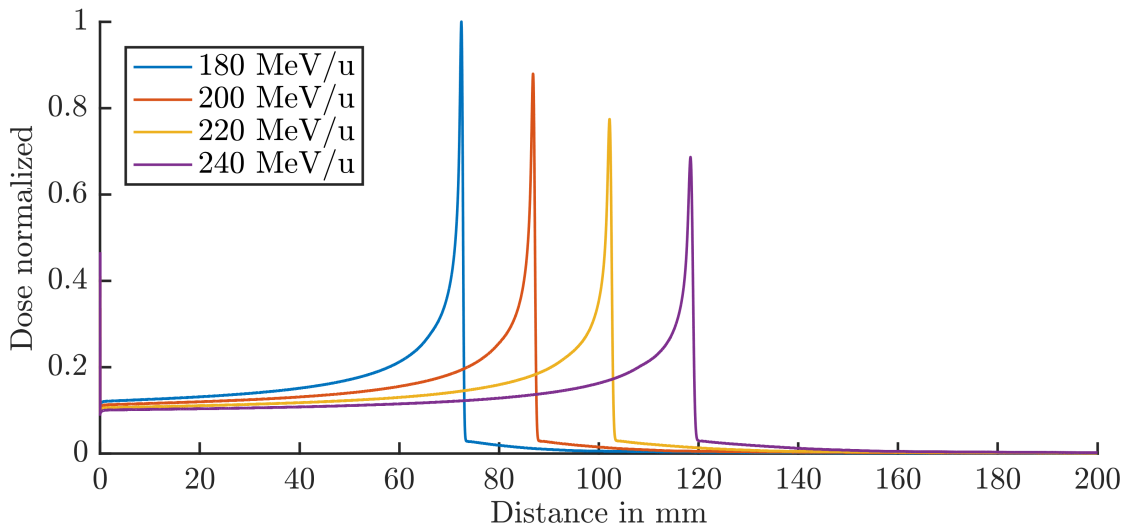


Figure A.1.: ^{12}C ion depth dose profile, taken from a Geant4 simulation not including absorbing material as vacuum exit foil, air gap, and water phantom entrance foil.

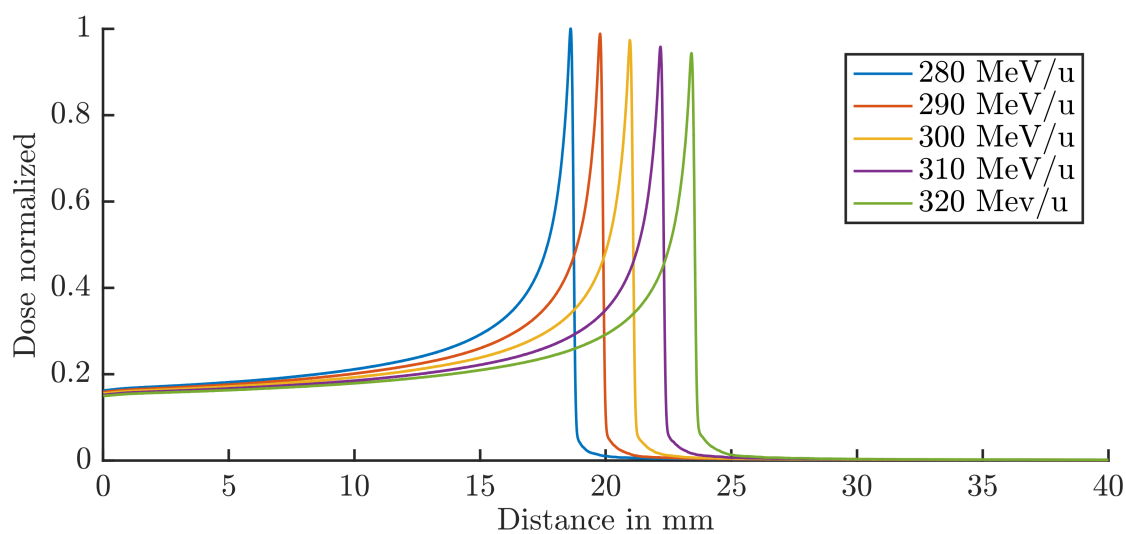


Figure A.2.: ^{124}Xe ion depth dose profile, taken from a Geant4 simulation including all absorbing material of the experimental setup.

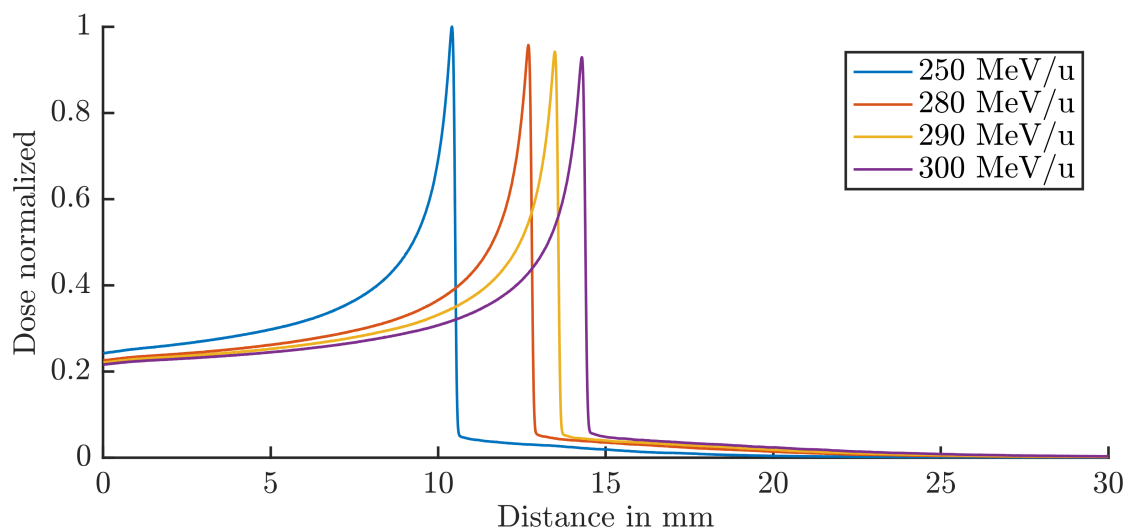


Figure A.3.: ^{238}U ion depth dose profile, taken from a Geant4 simulation including all absorbing material of the experimental setup.

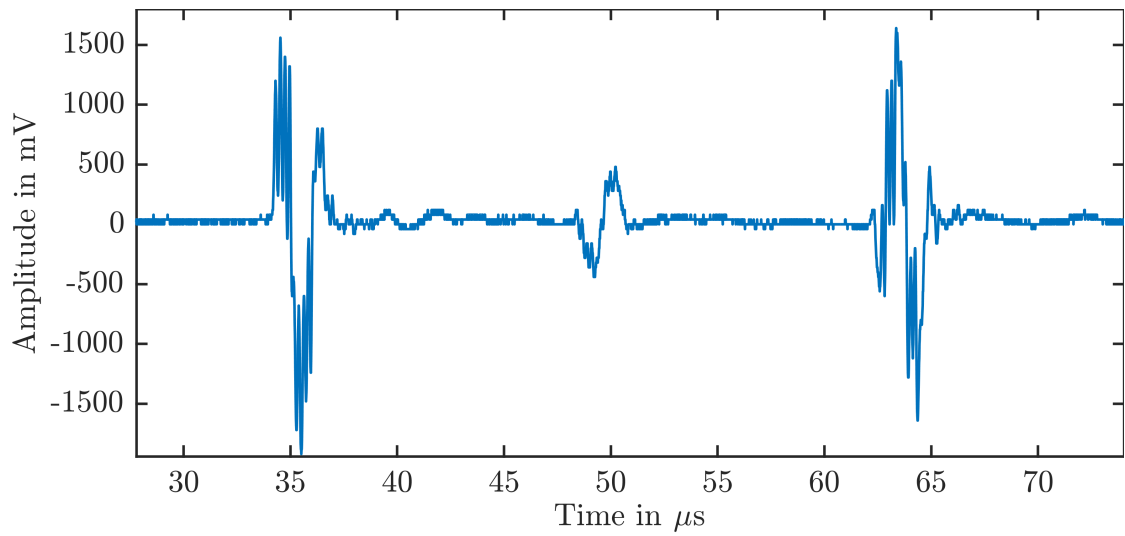


Figure A.4.: Ionoacoustic example of 300 MeV/u ^{124}Xe ions in water.

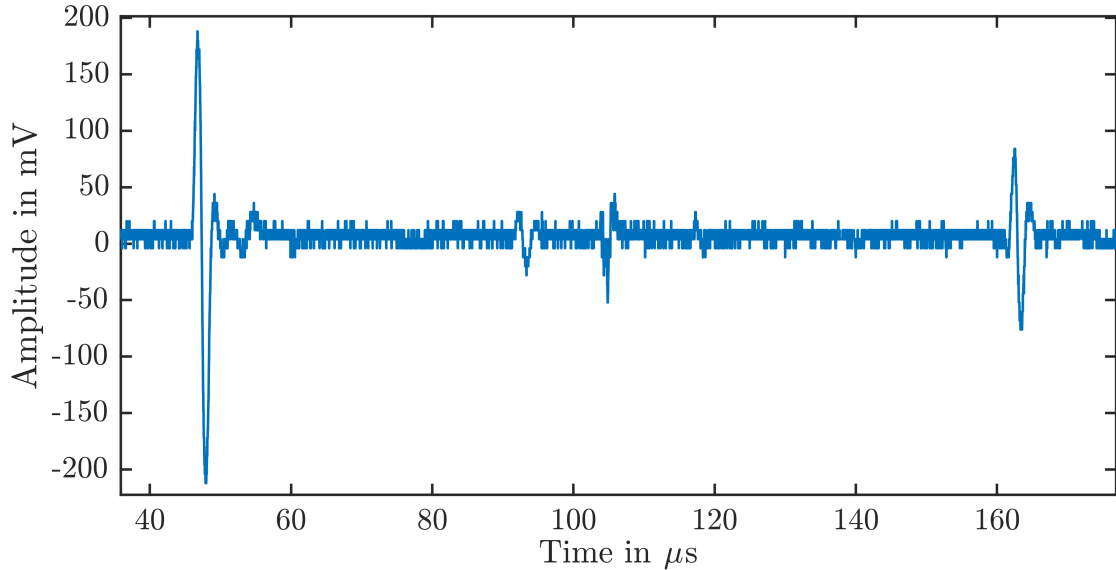
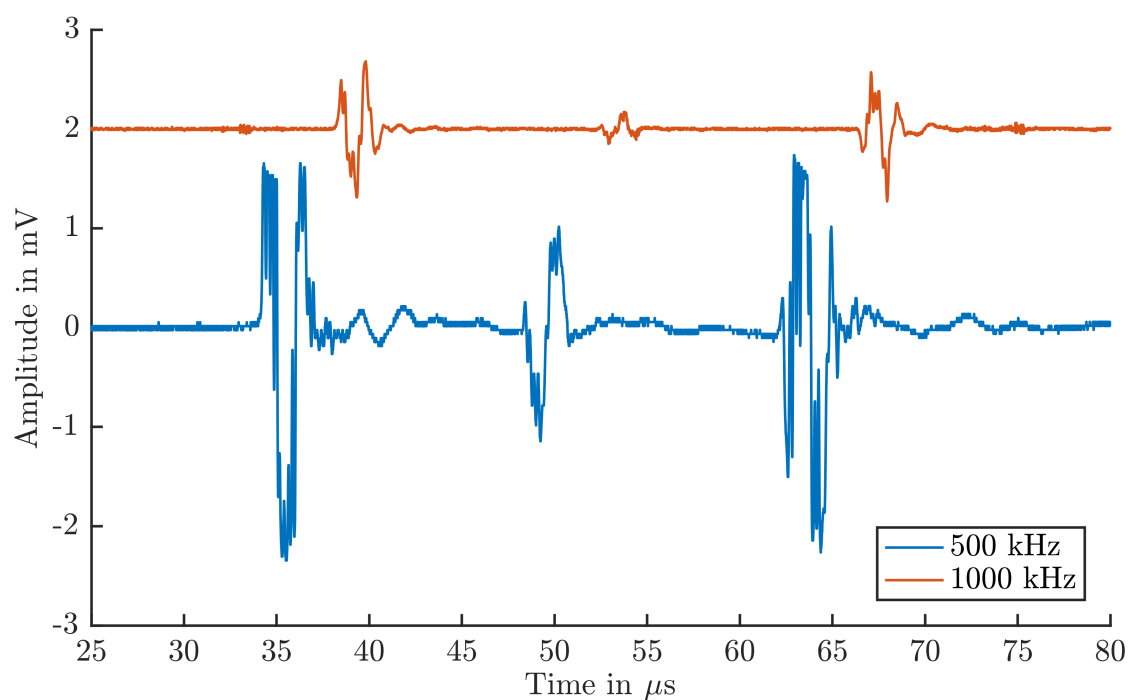
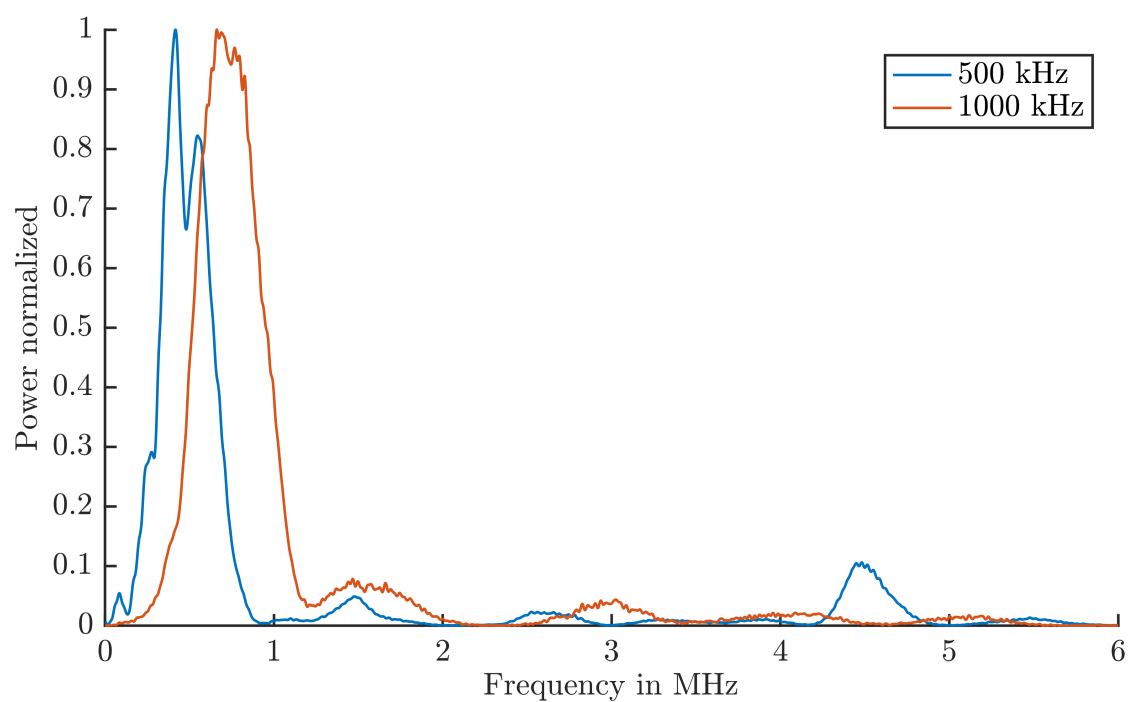


Figure A.5.: Ionoacoustic example of 200 MeV/u ^{12}C ions in water.



(a) Ionoacoustic amplitude.



(b) Frequency spectrum

Figure A.6.: Exemplary measurement of ^{124}Xe ions with different PZT transducers. a) Ionoacoustic signal of ^{124}Xe ions measured with a 1" diameter 500 kHz flat surface transducer in blue and a 0.5" diameter 1 MHz spherically focused transducer in red. b) Frequency spectra of a).

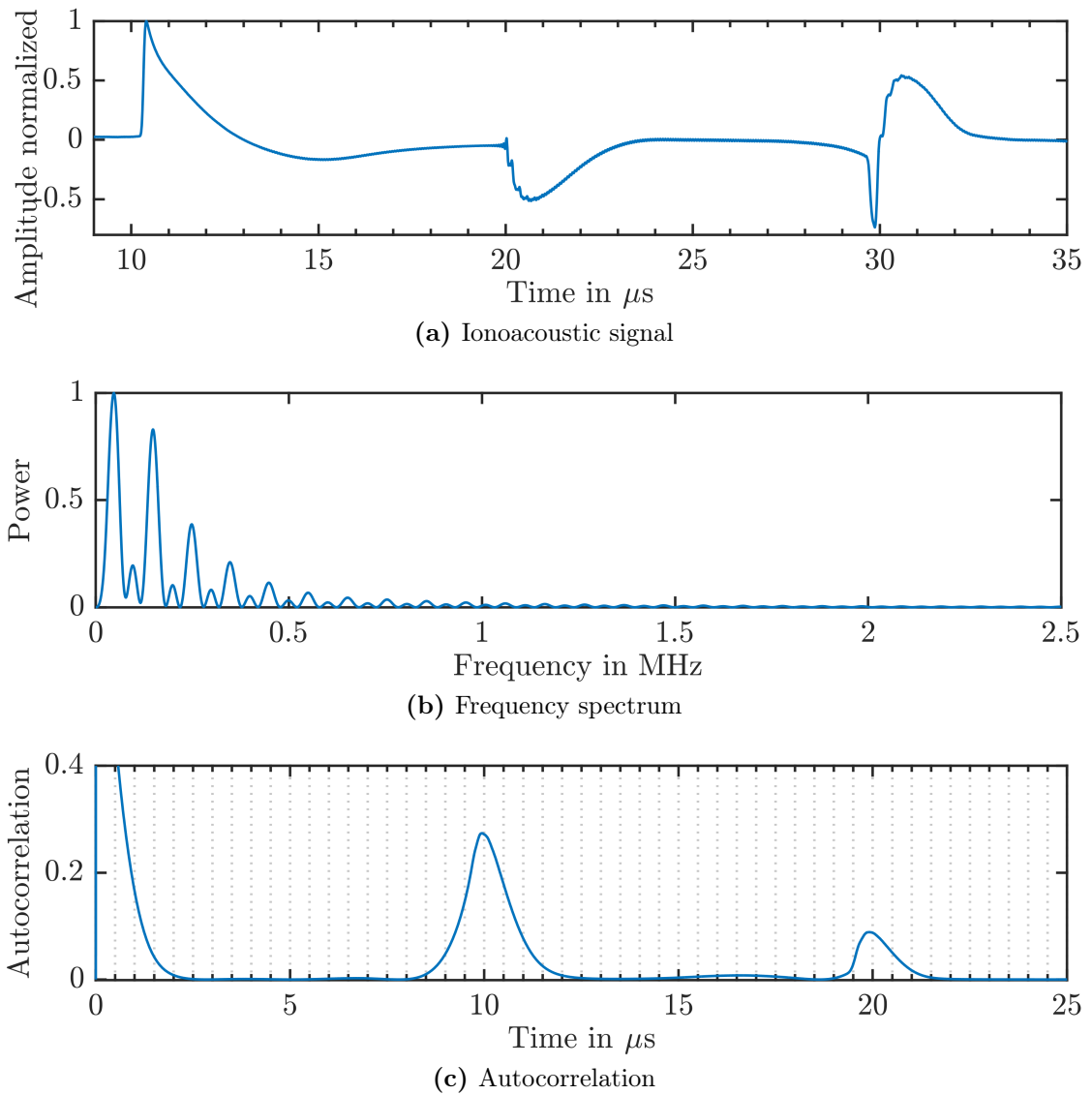


Figure A.7.: Autocorrelation analysis on k-Wave simulation data from single pulse ^{238}U ions.

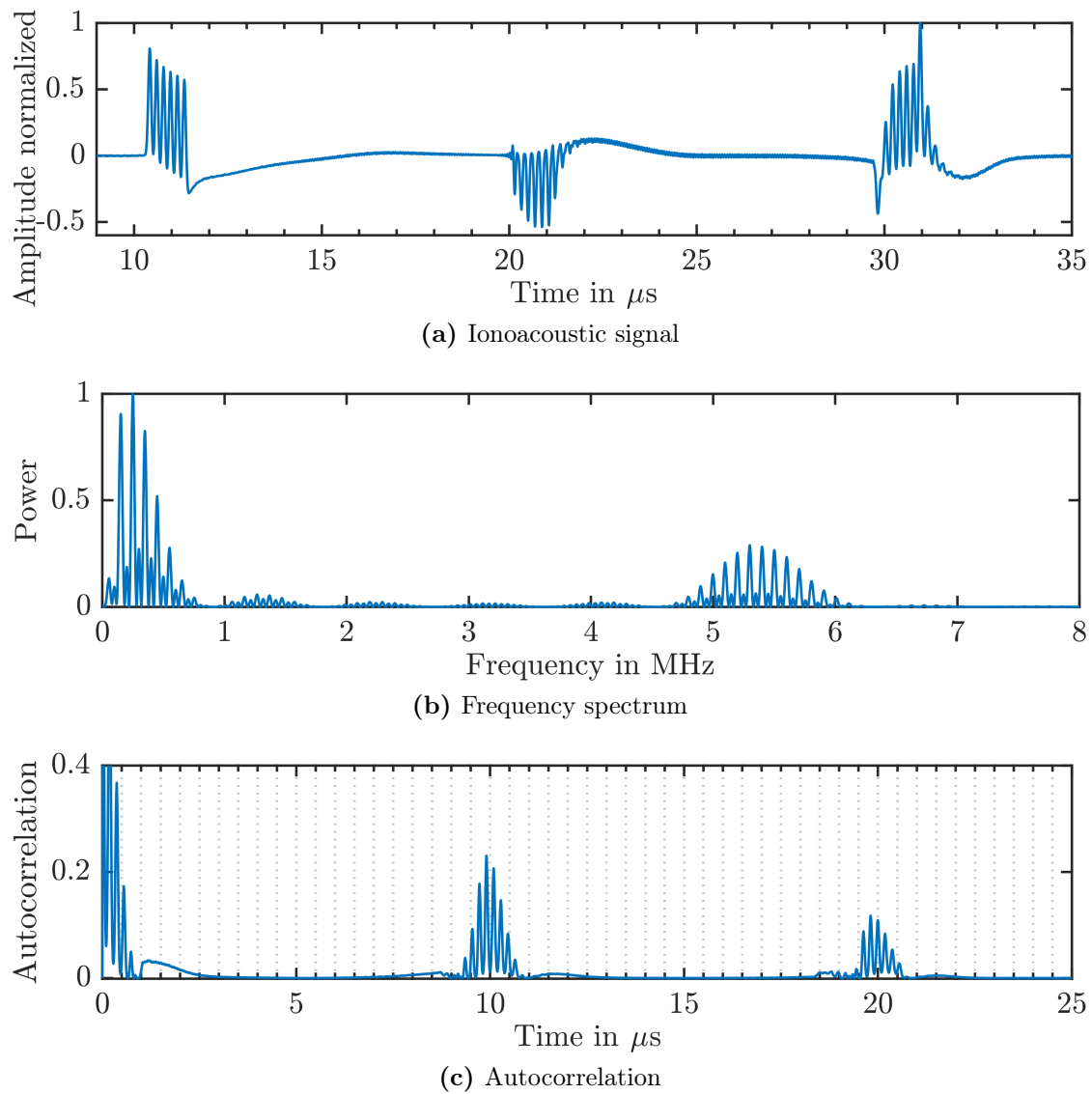


Figure A.8.: Autocorrelation analysis on k-Wave simulation data from ^{238}U ions using the GSI pulse train as temporal profile.

B. Additional Data from 20 MeV proton beam

In this appendix, more data from experiments at the 20 MeV proton beam at the MLL tandem is given.

Figure B.1 is a demonstration of a 2D raster scan. A 3.5 MHz PZT transducer has been moved in front of a 20 MeV proton beam stopped in water. For a second raster scan, 500 μm aluminium has been introduced in the beam path before the water phantom, thus enlarging the Bragg peak area due to scattering. The effect is visible in a 2D representation of the acoustic amplitude and in lineouts along the x and y direction.

Figure B.2 shows a study of longer pulses for a 20 MeV proton beam stopped in water measured at the MLL tandem. The pulse width was varied from 190 ns to 1030 ns. A 3.5 MHz PZT transducer was used for the measurements. Starting with pulses just above the stress confinement in fig. B.2a, the temporal signal is separated in fig. B.2c into 6 spatial signals. The sharp edges of the temporal profile achieved by the MLL chopper is generating a full spatial signal including direct, window, and reflection signal at the rise and the fall of the pulse. In fig. B.2b, the pulse width is not long enough to separate the spatial contribution in the direct and the reflection signal, but the window signal is separated. This is due to the different spatial gradients producing these signal parts, and the border between water and the entrance window is smaller than the Bragg peak area.

Figure B.3 is an example of a lateral measurement at a 20 MeV proton beam stopped in water acquired at the MLL tandem. The used transducer was a 10 MHz PZT transducer and the proton beam pulse width was 473 ns. It is to be noted that the strong signal here is still the γ signal deriving from the Bragg peak and thus overlaying a possible α signal. For 20 MeV protons the range is too short to distinguish a possible α signal in lateral measurements. The smaller signal shortly following is the β or window signal, which is seen since this signal starts with a negative peak. A α signal would always start with a positive pressure contribution.

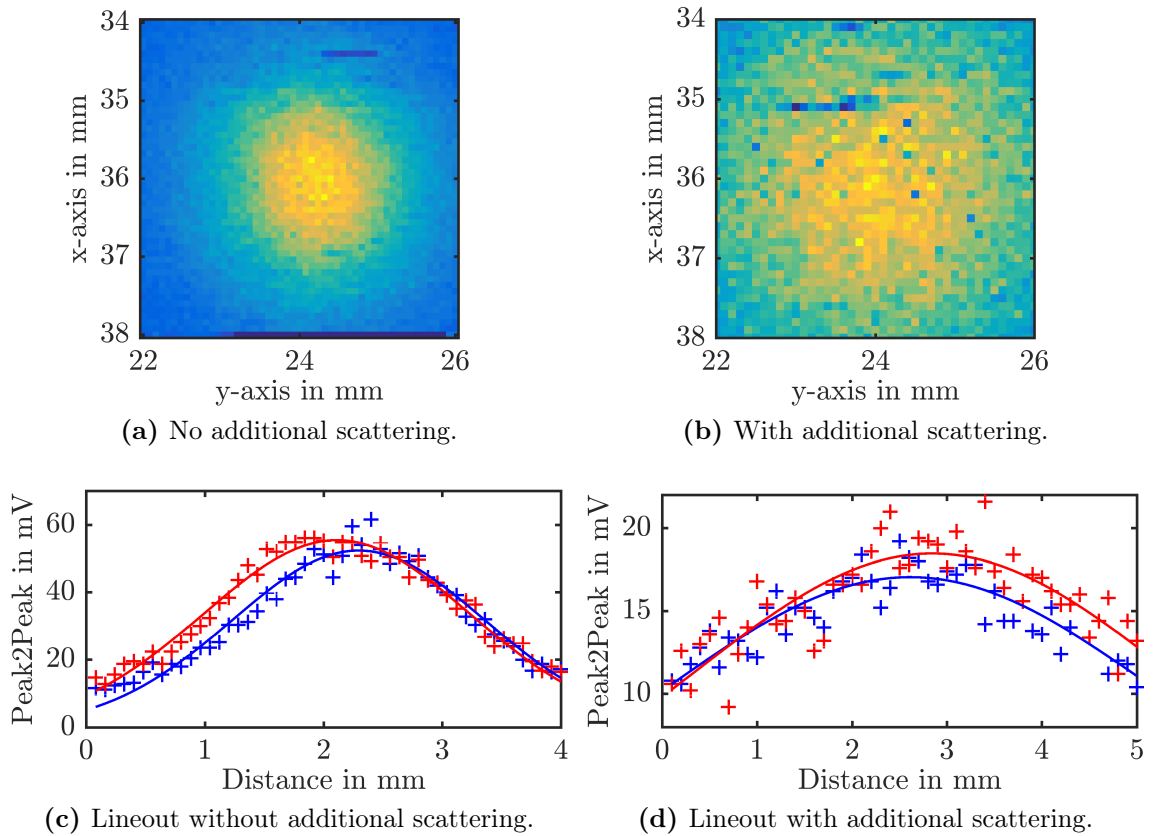
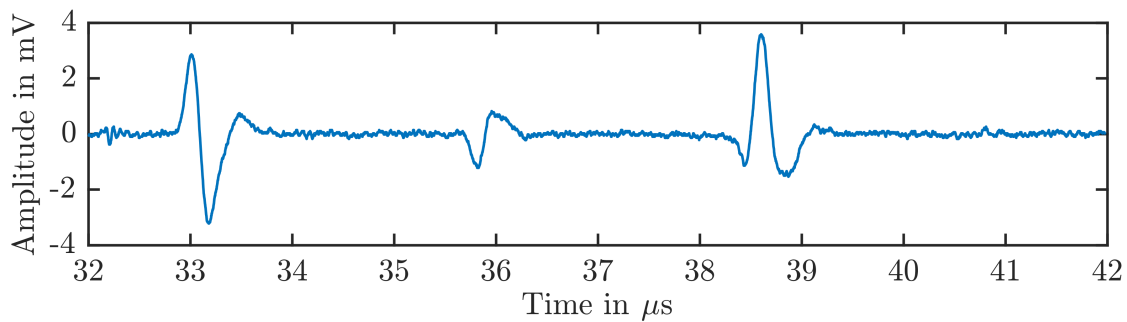
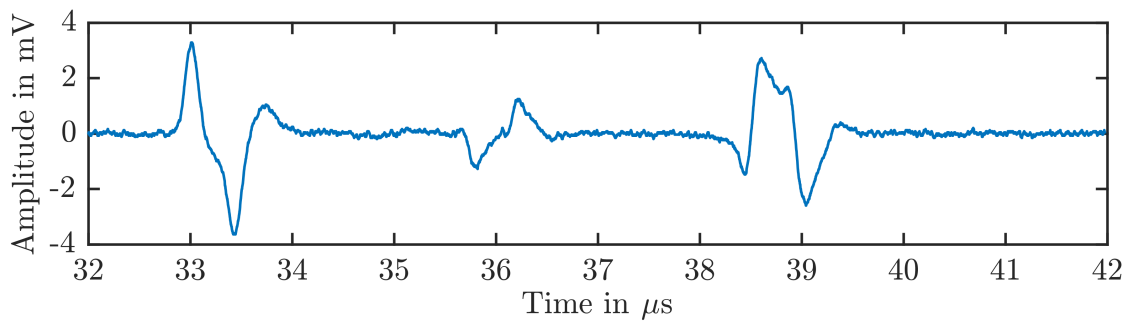


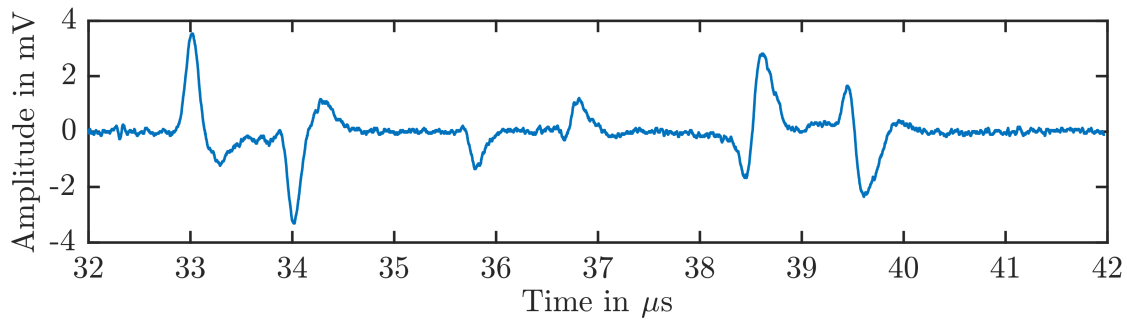
Figure B.1.: (a) 2D raster scan of 20 MeV protons. (b) Same as in fig. (a) but with additional scattering from a 500 μm aluminium. In (c) and (d), corresponding line outs in x (blue) and y (red) direction are given.



(a) 190 ns 20 MeV protons stopped water



(b) 470 ns 20 MeV protons stopped water



(c) 1030 ns 20 MeV protons stopped water

Figure B.2.: Pulse width study at the MLL tandem.

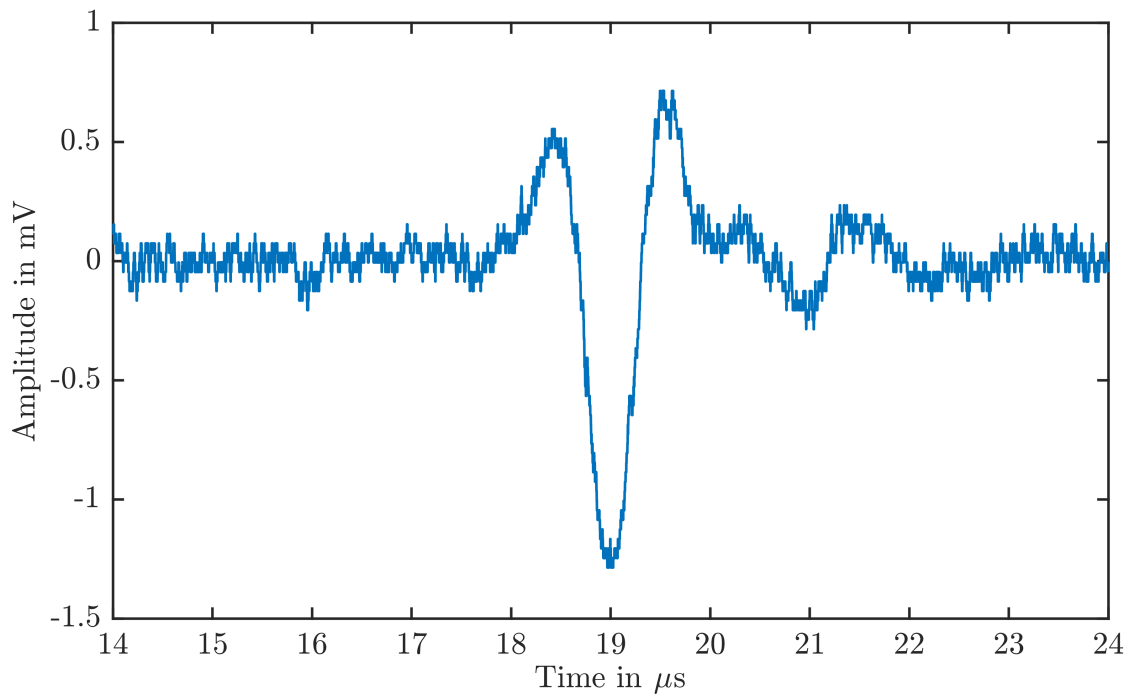


Figure B.3.: Example of a lateral measurement with a 20 MeV proton beam stopped in water. This example was measured with a 10 MHz PZT transducer and a proton beam pulse width of 473 ns at the MLL tandem.

C. Relevant Publications by the Author

Ionoacoustic characterization of the proton Bragg peak with submillimeter accuracy

W. Assmann^{a)}

Department for Medical Physics, Ludwig-Maximilians-Universität München, Am Coulombwall 1, Garching 85748, Germany

S. Kellnberger

Institute for Biological and Medical Imaging, Technische Universität München and Helmholtz Zentrum München, Ingolstädter Landstrasse 1, Neuherberg 85764, Germany

S. Reinhardt, S. Lehrack, A. Edlich, and P. G. Thirolf

Department for Medical Physics, Ludwig-Maximilians-Universität München, Am Coulombwall 1, Garching 85748, Germany

M. Moser and G. Dollinger

Institute for Applied Physics and Measurement Technology, Universität der Bundeswehr, Werner-Heisenberg-Weg 39, Neubiberg 85577, Germany

M. Omar and V. Ntziachristos

Institute for Biological and Medical Imaging, Technische Universität München and Helmholtz Zentrum München, Ingolstädter Landstrasse 1, Neuherberg 85764, Germany

K. Parodi

Department for Medical Physics, Ludwig-Maximilians-Universität München, Am Coulombwall 1, Garching 85748, Germany

(Received 6 August 2014; revised 3 December 2014; accepted for publication 7 December 2014; published 9 January 2015)

Purpose: Range verification in ion beam therapy relies to date on nuclear imaging techniques which require complex and costly detector systems. A different approach is the detection of thermoacoustic signals that are generated due to localized energy loss of ion beams in tissue (ionoacoustics). Aim of this work was to study experimentally the achievable position resolution of ionoacoustics under idealized conditions using high frequency ultrasonic transducers and a specifically selected probing beam.

Methods: A water phantom was irradiated by a pulsed 20 MeV proton beam with varying pulse intensity and length. The acoustic signal of single proton pulses was measured by different PZT-based ultrasound detectors (3.5 and 10 MHz central frequencies). The proton dose distribution in water was calculated by Geant4 and used as input for simulation of the generated acoustic wave by the matlab toolbox *k-WAVE*.

Results: In measurements from this study, a clear signal of the Bragg peak was observed for an energy deposition as low as 10^{12} eV. The signal amplitude showed a linear increase with particle number per pulse and thus, dose. Bragg peak position measurements were reproducible within $\pm 30 \mu\text{m}$ and agreed with Geant4 simulations to better than $100 \mu\text{m}$. The ionoacoustic signal pattern allowed for a detailed analysis of the Bragg peak and could be well reproduced by *k-WAVE* simulations.

Conclusions: The authors have studied the ionoacoustic signal of the Bragg peak in experiments using a 20 MeV proton beam with its correspondingly localized energy deposition, demonstrating submillimeter position resolution and providing a deep insight in the correlation between the acoustic signal and Bragg peak shape. These results, together with earlier experiments and new simulations (including the results in this study) at higher energies, suggest ionoacoustics as a technique for range verification in particle therapy at locations, where the tumor can be localized by ultrasound imaging. This acoustic range verification approach could offer the possibility of combining anatomical ultrasound and Bragg peak imaging, but further studies are required for translation of these findings to clinical application. © 2015 American Association of Physicists in Medicine. [<http://dx.doi.org/10.1118/1.4905047>]

Key words: proton therapy, *in vivo* range verification, thermoacoustics

1. INTRODUCTION

Ion beams are of increasing interest in radiation oncology, as they offer a more advantageous dose distribution than photons for external beam radiotherapy, with a characteristic dose maximum at their end of range (Bragg peak) and, in case of protons, no dose behind.¹ Therefore, a more conformal therapeutic dose can be applied to the tumor while sparing the surrounding healthy tissue, even if organs at risk are in striking distance. This makes, however, a precise positioning of the Bragg peak inside the tumor volume a challenging demand. Range uncertainties can have very different reasons, for example, patient and organ motion or conversion of CT Hounsfield values to relative ion stopping powers and are commonly perceived among the greatest issues for effective deployment of ion beam therapy.² Hence, different techniques, such as positron emission tomography³ or prompt gamma imaging,⁴ are currently under investigation at the clinical or experimental level to measure *in vivo* the Bragg peak position, ideally in real-time during the therapeutic irradiation.⁵ However, these methods rely on complex instrumentation and a not straightforward correlation between the emerging nuclear-induced secondary radiation and the Coulomb-induced dose deposition, so that a Bragg peak positioning accuracy better than a few millimeters cannot be expected in clinical situations.

A potentially more accurate non-nuclear technique for direct localization of the Bragg peak position during the irradiation could be based on the thermoacoustic effect.^{6,7} This effect is widely used in optoacoustics, where pressure waves are induced by the local absorption of light.^{8–11} In ion beam irradiation, local heat with a corresponding pressure pulse can be created by the energy deposition of an ion bunch (“ionoacoustic effect”), especially at the Bragg peak position. Deposition of a typical therapeutic dose of particles will increase the temperature of the irradiated volume by less than a millikelvin. Nevertheless, if the ion pulse is deposited within a short time window in a constrained tissue volume (microseconds and millimeters), it will lead to an ultrasound signal in the 0.1–10 MHz frequency range.¹² Detection of this ionoacoustic signal would allow for a much simpler and direct Bragg peak position determination compared to the nuclear-based techniques.

The ionoacoustic effect had long been considered for detection of neutrinos^{13,14} or high energy particles in general, and a first test of this technique was performed with proton energies above 150 MeV by Sulak *et al.* in 1979.¹⁵ In their experiment, the thermoacoustic origin of the measured ultrasound signals was clearly proven. First ionoacoustic experiments with focus on particle therapy have been performed by the group at the Proton Medical Research Center Tsukuba in water and in tissue, showing the applicability of ionoacoustics at clinical conditions.¹⁶ In particular, ionoacoustic ultrasound signals, even during proton therapy of a liver tumor, have been observed by Hayakawa *et al.*,¹⁷ but the spatial resolution was limited to some millimeters due to the used broad beam delivery technique and low-frequency acoustic instrumentation. The ionoacoustic effect was also studied at therapeutically

relevant energies by comparing experiments and simulations in water,^{18,19} and quite recently, has found new interest^{20,21} in the context of scanning beam irradiation²² and for proton beam characterization.²³ To further promote the ionoacoustic technique for *in vivo* dosimetry in particle therapy, a substantially improved position resolution and a deeper understanding of the underlying mechanisms would be essential.^{18,19} As a first step, we have measured the achievable Bragg peak position resolution of the method in a water phantom under optimized conditions using focused megahertz ultrasound transducers for a specifically selected probing beam of 20 MeV protons and pulsed time structure.²⁴ For such an energy deposition localized both in space and time, we demonstrate in this contribution ionoacoustic that Bragg peak localization can be achieved within a submillimeter range, in agreement with Monte Carlo calculations. Finally, we present a preliminary extrapolation of our results to higher energy beams.

2. MATERIAL AND METHODS

2.A. Experimental setup

The ionoacoustic effect of a proton beam in water was studied using the setup shown in Fig. 1 under various experimental conditions. To prove the achievable submillimeter accuracy in Bragg peak position determination, we have chosen a proton energy of 20 MeV \pm 10 keV from the tandem accelerator of the Maier-Leibnitz-Laboratory of the LMU and TU Munich. According to Geant4 simulations²⁵ at this energy, our beam has about 4 mm range in water and a very sharp Bragg peak of only 0.3 mm FWHM. We used a multicusp ion source,²⁶ which delivers a negative hydrogen beam of up to 18 μ A at 130 keV source voltage within an emittance of 4 π mm mrad. This beam was reduced in size and divergence for injection into the tandem accelerator to currents between 1 nA and 10 μ A, and, thus, the number of particles within a 1 μ s pulse could be varied between 10⁴ and 10⁸. Proton pulse widths from 8 ns to 4.3 μ s and a rise time of 3 ns were produced by means of a chopper/buncher system²⁷ at repetition frequencies between 1 and 10 kHz, which also delivered a trigger for the data acquisition system.

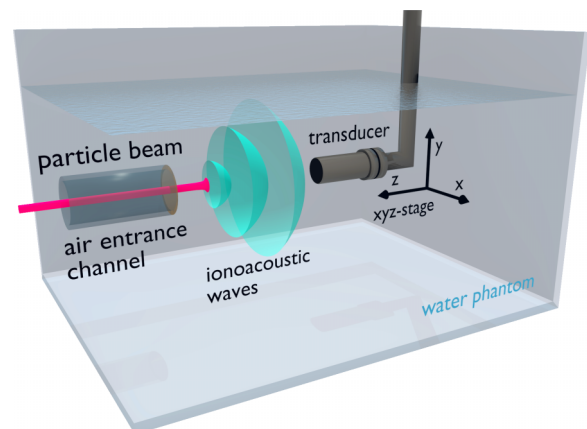


Fig. 1. Setup used for ionoacoustic experiments: Water phantom with air-filled entrance channel, separated by a polyimide entrance foil to water, and ultrasound transducer mounted onto a remote controlled *xyz*-stage.

The protons left the beam line vacuum through an 11.4 μm titanium foil, and entered a water phantom ($33 \times 18 \times 19 \text{ cm}^3$) via a 79 mm long air-filled entrance channel through a 50 μm thick polyimide entrance window. The beam spot cross section was adjusted to an area of about 2 mm.² The particle current was measured with 10% accuracy by a Faraday cup immediately before the beam exit to air, where the beam focus could also be seen on a cesium iodide (CsI) scintillating screen. The water phantom was filled with deionized water and stabilized within $\pm 1^\circ\text{C}$ to temperatures between 25 $^\circ\text{C}$ and 35 $^\circ\text{C}$. The measured temperature has been used to calculate the speed of sound for each individual experiment. Thermoacoustic signals induced by the particle energy deposition in water were measured by piezo-composite (PZT) based ultrasound immersion transducers (Videoscan, Olympus), which can be adapted to the desired frequency range and, hence, resolution. We used either a cylindrically focused 3.5 MHz transducer (38.1 mm focal distance, 76.3% bandwidth) or a spherically focused transducer at 10 MHz central frequency (25.4 mm focal distance, 73.5% bandwidth). The position of the detectors was on the beam axis (axial, Fig. 1), on the distal side of the Bragg peak, at focal distance. The transducers had an active diameter of 12.7 mm and were mounted on a motorized xyz -stage with 10 μm position accuracy. Signals were amplified with a low-noise 63 dB amplifier and stored with a digital oscilloscope at 500 MS/s sampling rate after averaging of 16 events.

2.B. Theory and computational modeling

Stopping of MeV protons in water is mainly due to electronic interactions taking less than a nanosecond. Energetic secondary electrons are produced by ionization, which first thermalize within about 10^{-15} s, and afterward transfer their energy via electron–phonon coupling to the atoms along the ion track. In a time window from 10^{-14} to 10^{-9} s and a few nanometers distance from the track, atoms in the proton Bragg peak region can reach temperatures of some hundred Kelvins.²⁸ On a macroscopic scale, a bunch of 10^6 protons of 20 MeV deposits in the stopping region 3.2×10^{-6} J in total, of which about 1×10^{-6} J is concentrated in the Bragg peak volume. This energy input produces a temperature increase of around 0.3 mK, which causes a pressure rise of 2.5 hPa.²⁹

The generation and propagation of pressure waves in water due to transient temperature increase $T(r,t)$ can be described by the general thermoacoustic equation³⁰

$$\left(\nabla^2 - \frac{1}{v_s^2} \frac{\partial^2}{\partial t^2} \right) p(\vec{r},t) = - \frac{\beta}{\kappa v_s^2} \frac{\partial^2 T(\vec{r},t)}{\partial t^2}, \quad (1)$$

with the induced pressure $p(r,t)$, the acoustic speed of sound in water v_s , the thermal coefficient of volumetric expansion β , and the isothermal compressibility κ . The thermal relaxation time τ_{th} amounts to 570 ms, considering a Bragg peak FWHM of 300 μm at 20 MeV, therefore, $\tau_p \ll \tau_{\text{th}}$ (τ_p proton pulse width) and the condition of thermal confinement is always fulfilled. Then, the heat equation can be reduced to $\rho C_V (\partial/\partial t (T(\vec{r},t))) = H(\vec{r},t)$, with the mass density ρ and

specific heat capacity at constant volume C_V . Furthermore, for short pulse durations, where stress confinement is fulfilled, i.e., $\tau_p < \tau_s$, (here, thermal stress relaxation time τ_s is about 200 ns),³⁰ the heating function $H(\vec{r},t)$ can be separated into its temporal and spatial components to $H(\vec{r},t) = Q(\vec{r}')H(t')$. With this simplification, Eq. (1) can be solved analytically for pressure $p(r,t)$ resulting in expression^{31,32}

$$p(\vec{r},t) = \frac{\beta}{4\pi v_s \kappa \rho C_V} \frac{\partial}{\partial t} \int_{A(t)} \frac{Q(\vec{r}')}{R} dA', \quad (2)$$

where the source term $Q(\vec{r}')$ is the energy deposition density (J/m^3) represented by the Bragg curve, integrated for $R = |\vec{r} - \vec{r}'|$ and $A(t)$ is the surface, on which $R = v_s t$ and is, thus, a function of time.

For calculating the proton dose deposition in water, we used Geant4 (Ref. 25) (version 9.6.p01) and activated the QGSP_BIC_HP 2.0 physics lists for handling of the main electromagnetic and nuclear processes. The still controversial value of the ionization potential of water was set to 78 eV, according to the latest recommendation of Sigmund *et al.*,³³ which was also adopted in other recent investigations with different ion species.³⁴ At the considered low-proton beam energy of this study, uncertainties in the knowledge of the ionization potential and the density of water (dependent on the temperature) were found to have only a minor influence (e.g., below 10 μm for 3 eV variation) on the simulated Bragg peak position. The largest uncertainty is introduced by measurement errors in the beam path geometry (air gap, foil thicknesses), which is calculated to be 30 μm .

The output of Geant4 was used as input to the k -WAVE simulation engine,³⁵ in order to simulate the entire chain, from the proton energy transfer to the medium to the generation of the acoustic wave and its propagation until detection. Correspondingly, the forward model consisted of a 3D matrix with $30 \times 30 \times 10 \mu\text{m}^3$ grid size spacing (similar to the used Geant4 scoring), and a volume size of $13.2 \times 13.2 \times 32 \text{ mm}^3$ in x , y , and z direction. In addition to simulations for 20 MeV protons, explorative simulations were performed at a higher, more clinically relevant energy of 150 MeV, using a volume size of $40.0 \times 40.0 \times 200.0 \text{ mm}^3$ with $0.5 \times 0.5 \times 0.5 \text{ mm}^3$ grid spacing. An air–water interface (neglecting the polyimide foil) was modeled using a heterogeneous distribution of sound speed in the acoustic propagation medium, assigning 343 ms^{-1} to air and using a temperature corrected value for water. The particle pulse duration was simulated by modifying the time varying pressure source term from 1 ns to 10 μs . To correct for the limited bandwidth of our transducers, we filtered the simulated ionoacoustic signals with a Butterworth band-pass ranging from 2.24 to 5.01 MHz for the 3.5 MHz transducer and 6.27 to 13.55 MHz for the 10 MHz transducer, respectively.

3. RESULTS

3.A. Bragg peak position resolution

A typical pattern of ionoacoustic ultrasound waves is shown in Fig. 2; the time scale is chosen according to the signal arrival time at the detector. Two distinguished pulses,

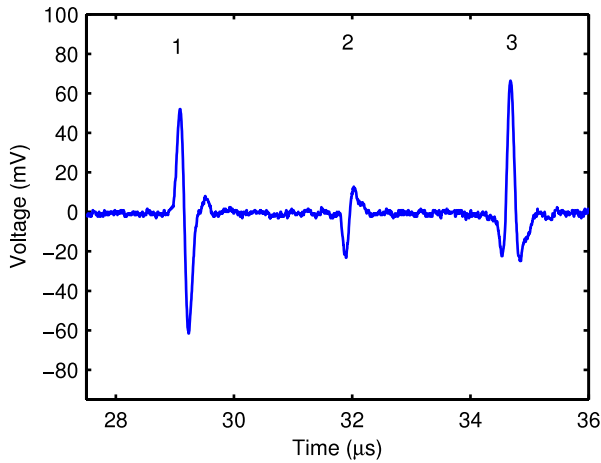


Fig. 2. Example of an ionoacoustic signal from a 110 ns ion pulse with 2×10^6 protons, recorded with a 3.5 MHz ultrasound transducer (pulse average of 16 samples, see also text).

corresponding to the Bragg peak location (1) and, about $3 \mu\text{s}$ later, to the beginning of the energy loss at the entrance foil (2) can be clearly resolved, together with additional acoustic echoes (3) of the reflected waves at the entrance interface, arriving another $3 \mu\text{s}$ later. The first ionoacoustic signal exhibits the typical bipolar pulse shape also known from opto- or thermoacoustic imaging.²⁹ At the entrance foil, however, the initial pressure spike produces a negative acoustic signal at the detector position, followed by a postpulse oscillation. The time difference between the positive peak 1 and the negative peak 2 amounts to $\Delta t_{12} = 2.80 \mu\text{s}$. Neglecting the proton traveling time in water and considering the acoustic speed of sound in water $v_s = 1507 \text{ ms}^{-1}$ (29°C), this corresponds to a distance of $\Delta x_{12} = 4.23 \text{ mm}$ of the Bragg peak from the entrance foil. The time difference of the acoustic echo Δt_{13} between signal 1 and 3 amounts to twice Δt_{12} .

The precision of the Bragg peak position determination with the ionoacoustic technique in water was checked in repeated experiments by varying the position of the transducer

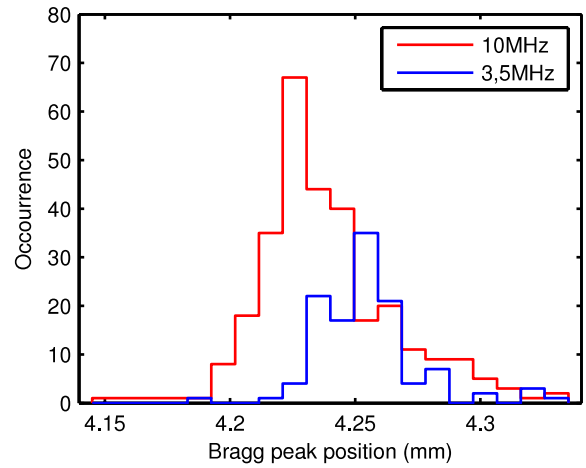


Fig. 3. Bragg peak position: Distance in water from the Bragg peak to the entrance foil, measured at different detection points along the axial position with 3.5 and 10.0 MHz transducers and 250 ns pulse width, calculated from the positive signal 1 to negative signal 2 distance (see Fig. 2).

in axial direction around the focal zone, using a pulsed beam delivery with a 250 ns ion pulse width. For each position, an independent value of Δt_{12} was determined. The resulting mean values are $4239 \pm 30 \mu\text{m}$ and $4255 \pm 30 \mu\text{m}$ for the 3.5 and 10 MHz transducer, respectively (Fig. 3). This result has to be compared to the Geant4 simulation, which gives $4060 \mu\text{m}$ for the Bragg peak distance from the polyimide entrance foil. The mean difference of $187 \mu\text{m}$ will be discussed later in context of ultrasound wave simulations.

3.B. Sensitivity of ionoacoustics to lateral heterogeneities

The sensitivity to lateral heterogeneities in the beam path, which represents a major source of range uncertainty in clinical scenarios,² was tested in another experiment with a 0.52 mm thick Al degrader plate covering either the complete or half of the beam profile before entrance into water. In Fig. 4(a), the corresponding pulse sequences are shown, where

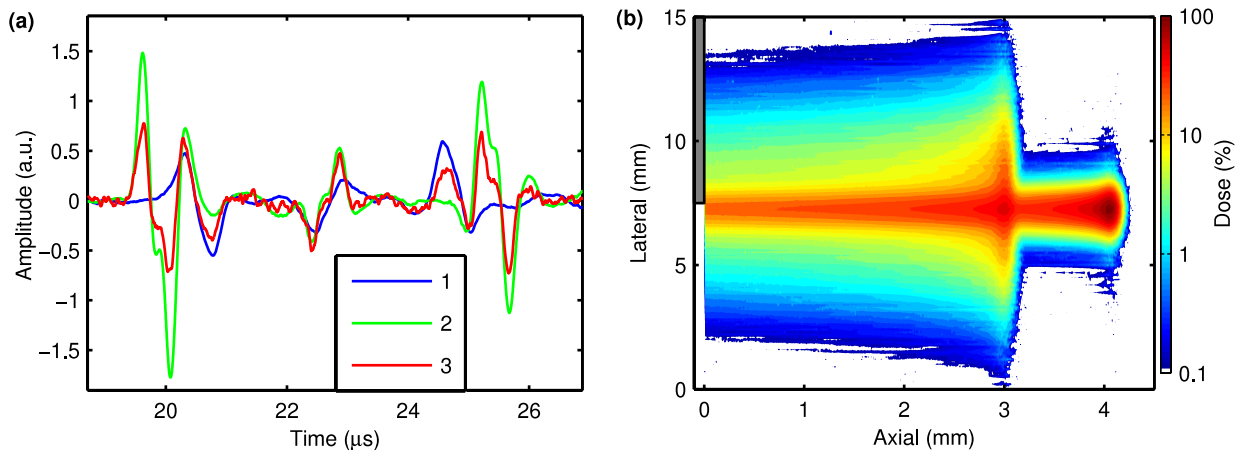


Fig. 4. (a) Measured ionoacoustic signals with 0.52 mm thick Al-degrader in three different positions (473 ns proton pulse width, 10 MHz transducer on a fixed position in beam axis): (1) with and (2) without Al degrader, (3) Al degrader covering half of the beam spot. (b) Geant4 simulation of the relative deposited dose for position (3), total projection in x - z -plane, Al-plate position marked.

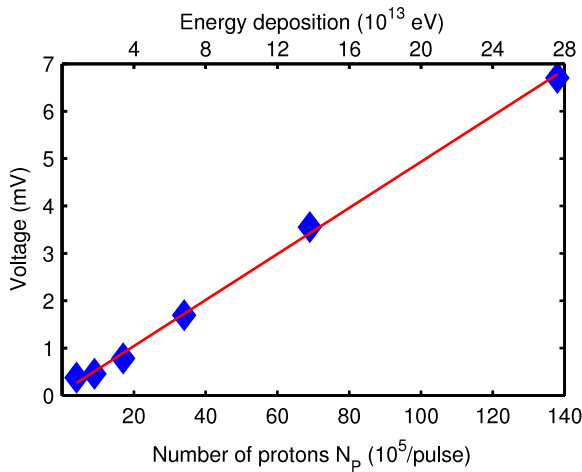


Fig. 5. Acoustic signal amplitude of a 473 ns proton bunch (16 pulses average) as function of particle number and total energy deposition per pulse, along with a linear polynomial fit (red line).

the effect of the two absorber configurations can be clearly distinguished. The measured Bragg peak reduction by $1068 \pm 30 \mu\text{m}$ in presence of the full absorber agrees well with the expectation of $1060 \mu\text{m}$ from a Geant4 simulation [Fig. 4(b)].

3.C. Ionoacoustic signal dependence on delivered dose

The relation between beam intensity and acoustic signal amplitude was measured by varying the particle number from about 10^5 to 10^7 protons/pulse at a constant pulse width of 473 ns. These particle numbers correspond to a total deposited energy between 10^{12} and 10^{14} eV. The polynomial fit of the data (Fig. 5) shows a linear relation with a detection limit for this setup in the range of 10^5 particles/pulse with averaging of 16 events. This corresponds to an estimated dose deposition threshold of about 1.6 Gy in the Bragg peak region (typical therapeutic doses are around 2 Gy).

3.D. Dependence of the signal pattern on the proton pulse width

To study the influence of the particle pulse width variation on the acoustic waveform pattern, we performed measurements using proton beam bunches with pulse lengths between 8 ns and $4.37 \mu\text{s}$ (Fig. 6). As an example, Fig. 6(a) shows the bipolar Bragg peak response to four different pulse durations. For pulse widths above 200 ns, the distance between the positive and negative pulse reflects the time duration of the proton pulse. For particle pulse durations below 200 ns, however, the peak–peak distance approaches a value of 132 ± 25 ns, independent also of the transducer mean frequency [Fig. 6(b)].

3.E. k-WAVE simulations

In order to understand this effect and the origin of the measured ionoacoustic signals in general, 3D *k*-WAVE simulations³⁵ have been performed. Due to computational time and memory consumption, at first a pointlike detector was assumed and the polyimide entrance window has been omitted. In Fig. 7, an example of such a *k*-WAVE simulation is presented and compared to the corresponding measurement with 1029 ns pulse width. Allowing for simplifications, the measured signal pattern is well reproduced. The simulation can also give information about the frequency spectrum of the pressure pulses, which is restricted in the measured ionoacoustic signals due to the limited frequency range of the transducers. The main spectral components are found to be centered around 1.5 MHz.

Varying the ion pulse width in the simulation, the experimentally seen linear relationship of the peak–peak distance with the pulse width above 200 ns can be well reproduced, but the final minimum peak–peak distance approaches 90 ns, compared to the measured 132 ± 25 ns. Therefore, a more realistic detector geometry was used in our simulation, as the spherical shaped detector surface of the transducer can produce, in contrast to a pointlike detector, a time broadening in the ionoacoustic signal. Incorporating the real detector

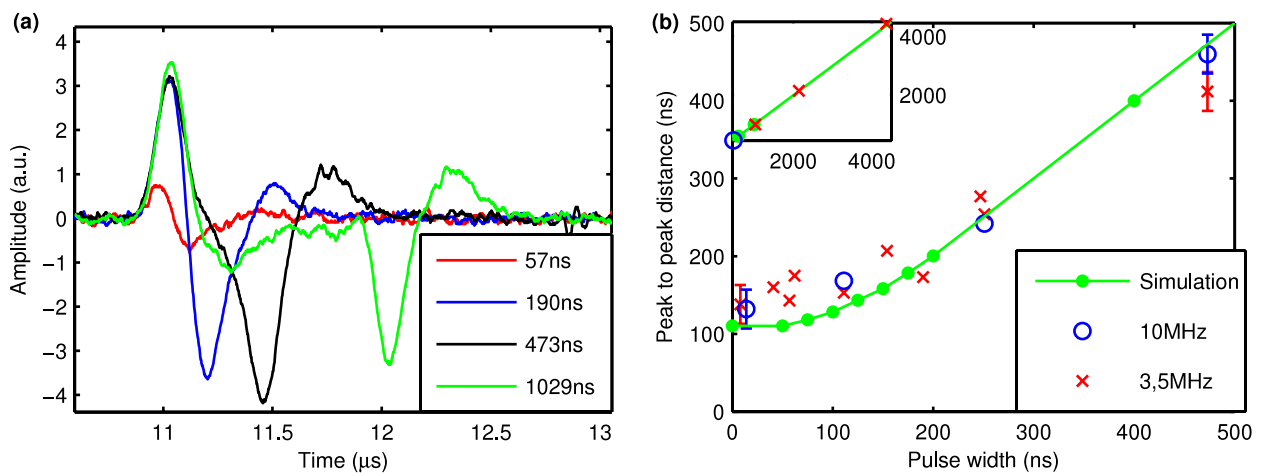


Fig. 6. Particle beam measurements with different temporal profiles. (a) Ionoacoustic signal amplitude as a function of varying particle pulse width. (b) Positive-negative-peak distance for different particle pulse widths (8–473 ns, inset 1.0–4.3 μs) compared to *k*-WAVE simulations with realistic detector geometry (see text).

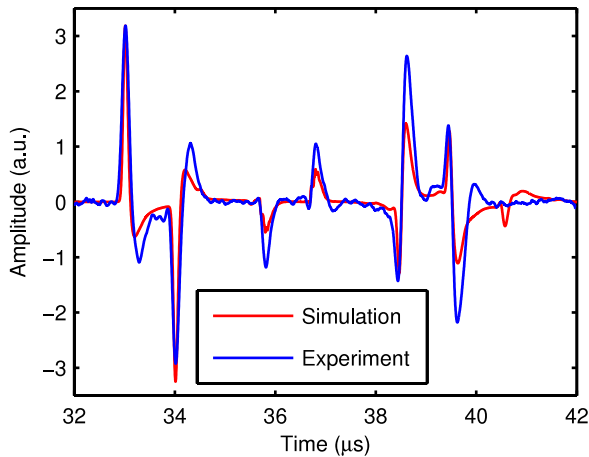


Fig. 7. Ionoacoustic signal pattern measured with a 3.5 MHz transducer and 1029 ns pulse width, compared to a k -WAVE simulation (normalized to the first peak, pointlike detector assumed).

geometry in the simulation, the minimum value increases to 110 ns, which matches the observed value within the experimental errors [Fig. 6(b)].

The reported values can be related to the ionoacoustic signal creation. The FWHM of the Bragg peak is about $300\ \mu\text{m}$, therefore, for pulse widths above 200 ns, stress confinement is not fulfilled and the distance between the positive and negative Bragg peak signal mirrors the pulse duration. Below this width, in stress confinement, the positive and negative signal components are fusing and now providing an image of the Bragg curve gradients [Fig. 6(a)]. According to the thermoacoustic theory [Eq. (2)], the amplitude maximum of the pressure pulse is situated at the gradient maximum of the dose distribution. Mathematical derivation of the Geant4 simulated Bragg peak provides about $120\ \mu\text{m}$ distance between the steepest gradients left and right of the peak maximum, corresponding to 80 ns. This value is close to the 90 ns minimal positive–negative signal distance extracted from the k -WAVE simulation, when using a pointlike detector geometry which neglects time broadening effects. The experimentally observed minimum value is 132 ± 25 ns. Therefore, taking into account the distance from the distal fall-off (where the ionoacoustic signal is created) to the Bragg peak, one has to subtract approximately half of this minimum peak-to-peak distance, i.e., 66 ns or $100\ \mu\text{m}$, respectively, from the measured values (Fig. 3). This yields an experimental mean value of $4147 \pm 45\ \mu\text{m}$. Considering the assumption of stress confinement and the estimated uncertainty of the Geant4 simulation, this value is close to the calculated Bragg peak position of $4060\ \mu\text{m}$.

Extrapolation from our results to higher, more therapy relevant energies in k -WAVE simulations is complicated due to the many influencing parameters, such as space and time distribution of the dose deposition, transducer characteristics and position, and phantom geometry. Notwithstanding, to get a rough estimate of the expected signal pattern and amplitude, which can be compared to our measurements, we calculated with Geant4 the dose distribution of a 150 MeV “pencil beam” entering a water phantom with a Gaussian shaped lateral beam profile with $\sigma = 3.0$ mm, which we scaled by the number

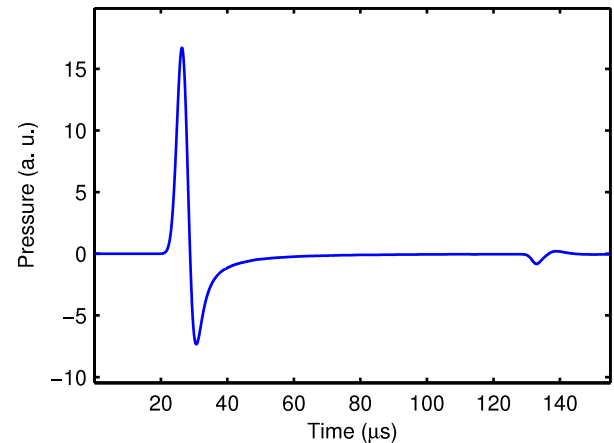


Fig. 8. Ionoacoustic signal pattern at 150 MeV simulated by k -WAVE (see text).

of protons to a maximum dose of 0.1 Gy. Taking this input for the k -WAVE simulation and a beam pulse profile with $\sigma = 1.5\ \mu\text{s}$ we get an acoustic signal amplitude, which is a factor of 2 smaller than for the same peak dose as in the present experiment at the same detector position, but comparing only pointlike detectors. In Fig. 8, an example of a typical signal pattern at 150 MeV is shown, limited to the two pulses from the Bragg peak and the beam entrance region. Note the larger time scale compared to Figs. 6(a) and 7, which is attributed to the broader Bragg peak and the longer proton pulse.

4. DISCUSSION AND CONCLUSION

Detection of ionoacoustic signals at high proton energies has been demonstrated by several measurements in the past.^{15–19} So far, all reported ionoacoustic experiments have been performed in broad beam geometry, i.e., with beam spot sizes in the centimeter range, and proton energies of more than 100 MeV. Moreover, for acoustic detection, hydrophones have been used with an upper cut-off frequency of 300 kHz.^{15,16,19} The only measurement during a therapeutic irradiation¹⁷ was made at conditions, where the entire tumor volume was irradiated at once, requiring also a dose distribution laterally and longitudinally extended over several centimeters with the so-called passive scattering technique. In this scenario, the corresponding ultrasound waves have a complex structure, from which the underlying dose distribution has to be reconstructed,³⁶ with only limited accuracy for resolving the spread out Bragg peak (SOBP) distribution. A more advanced irradiation technique makes use of active scanning, where a narrow and quasi-monoenergetic proton pencil beam is scanned across the tumor volume with magnetic deflection, adjusting the Bragg peak position in depth by stepwise changes of the proton energy.²² This method has specific advantages for highly conformal tumor therapy, but is on the other hand very sensitive to delivery uncertainties, especially in the presence of organ motion.³⁷ Therefore, it would greatly benefit from online Bragg peak monitoring. Fortunately, owing to its intrinsic dose delivery confinement in time and space, beam scanning favors in itself an ionoacoustic approach for this purpose.

In our experiments with a narrow and very sharp Bragg peak from a 20 MeV pulsed proton beam stopping in a water phantom, the conditions for a high signal to noise ratio (SNR) of the ionoacoustic pulse are advantageous. In clinical situations, however, with proton energies above 100 MeV, the SNR will be reduced due to a higher noise level (thermal, scattering), lower signal amplitude because of the less sharp (in time and space) dose deposition, and, not least, the generally higher signal attenuation in tissue. Therefore, improving the SNR is the main challenge for ionoacoustics in clinical applications. Current tendency in therapy accelerator developments is, however, to increase the number of particles per ion pulse for reasons of reducing the overall treatment time, which would also increase the acoustic signal amplitude. In particular, emerging single room solutions for proton therapy rely on compact synchrocyclotron accelerators which offer substantially more protons per pulse than conventional cyclotrons.³⁸ Our *k*-WAVE simulation with beam parameters for 150 MeV protons expected from such a synchrocyclotron has revealed signal amplitudes which should be detectable with advanced ultrasound methods. We focused our simulation on proton beams, but it would be also interesting to explore ionoacoustics with heavier particles, such as ¹²C, where more dose is concentrated in the Bragg peak region, but on the other hand less particles are delivered per ion pulse.

At existing proton therapy devices which already use beam scanning techniques, only minor changes to the beam delivery will open the possibility to use ionoacoustics for ion range determination. Enhanced SNR will be obtained by an intensity modulation of the ion beam at one or more frequencies³⁹ in order to measure in the frequency domain, as recently demonstrated in optoacoustics.⁴⁰ Although the beam of a cyclotron is already modulated at frequencies between 50 and 100 MHz, a lower frequency modulation is required since the very high frequencies are damped within short distances from the Bragg peak and, thus, these frequencies are not detectable in the ionoacoustic signal. Frequencies in the range 100 kHz–10 MHz seem to be preferable to increase the SNR. Distance measurement would transform to a phase analysis in the frequency domain. An additional low-frequency modulation may be necessary to avoid ambiguities in distance measurement by phase analysis, for larger transit times between Bragg peak and ultrasound detector than the ultrasound can travel within one cycle of the modulated frequency. Detecting the same frequencies as the beam modulation by the ultrasound transducers filtered at small band widths or even by lock-in-amplifier techniques could further increase the SNR. Thus, online Bragg peak monitoring comes into reach already for existing proton or ion beam treatment facilities.

Recently, a compact laser-based acceleration scheme has also been proposed to reduce the rather high installation costs of a particle therapy unit.^{41,42} One characteristic feature of this new acceleration technique is the expected high pulse intensity of more than 10⁸ particles/ns. This would clearly enhance the ionoacoustic signal, and also generally favors ionoacoustics for monitoring these high laser-induced pulse intensities, where most electronic detectors suffer from saturation effects and electromagnetic pulse noise problems.

In conclusion, our results demonstrate that detection of ionoacoustic signals allows for a much simpler and direct Bragg peak position measurement compared to the nuclear-based techniques. In the considered (ideal) experimental conditions, the method gives the Bragg peak position with an accuracy below 100 μ m, allows for probing the Bragg peak width, and, with an appropriate detector array, could make real-time Bragg peak tomography possible.⁴³ Moreover, using ultrasound techniques, one could simultaneously detect the ionoacoustic signal of the Bragg peak and the conventional ultrasound echo for additional anatomical information of the tumor region avoiding coregistration and fusion errors. At the beginning of a tumor irradiation, one could think of a few “diagnostic shots” at critical positions with a special time (and space) profile of the ion beam to verify the actual ion range. Although applicability and clinical benefits will depend on the tumor location, it is anticipated that suitable sites will include the most frequent pelvic (e.g., prostate and rectum), gastrointestinal (e.g., liver and pancreas), and female breast tumors. Despite the expected challenges in SNR, extrapolation of our experimental findings to clinically relevant higher energies supports the promise of this technique for new (synchrocyclotron) or next (laser) generation ion accelerators. Hence, in future experiments at more therapy relevant energies, we will further explore and develop the ionoacoustic Bragg peak monitoring technique toward clinical applicability.

ACKNOWLEDGMENTS

This work was funded by the DFG Cluster of Excellence Munich Centre for Advanced Photonics (MAP). The authors kindly acknowledge support from I. Cortrie, G. Dedes, C. Gäbisch, T. Hellerer, A. Maaß, and G. Sergiadis. The authors declare no conflict of interest.

^{a)} Author to whom correspondence should be addressed. Electronic mail: walter.assmann@lmu.de

¹R. R. Wilson, “Radiological use of fast protons,” *Radiology* **47**, 487–491 (1946).

²H. Paganetti, “Range uncertainties in proton therapy and the role of Monte Carlo simulations,” *Phys. Med. Biol.* **57**, R99–R117 (2012).

³K. Parodi, H. Paganetti, H. A. Shih, S. Michaud, J. S. Loeffler, T. F. Delaney, N. J. Liebsch, J. E. Munzenrider, A. J. Fischman, A. Knopf, and T. Bortfeld, “Patient study of in vivo verification of beam delivery and range, using positron emission tomography and computed tomography imaging after proton therapy,” *Int. J. Radiat. Oncol., Biol., Phys.* **68**, 920–934 (2007).

⁴C. H. Min, C. H. Kim, M. Y. Youn, and J. W. Kim, “Prompt gamma measurements for locating the dose falloff region in the proton therapy,” *Appl. Phys. Lett.* **89**, 183517 (2006).

⁵A. C. Knopf and A. Lomax, “In vivo proton range verification: A review,” *Phys. Med. Biol.* **58**, R131–R160 (2013).

⁶T. Bowen, “Radiation-induced thermoacoustic soft tissue imaging,” in *Proceedings of the IEEE Ultrasonics Symposium* (IEEE, Piscataway, NJ, 1981) Vol. 2, pp. 817–822.

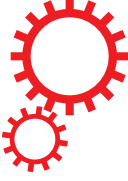
⁷T. Bowen, “Radiation-induced thermoacoustic imaging,” U.S. patent 4,385,634 (1983).

⁸V. Ntziachristos, J. Ripoll, L. H. V. Wang, and R. Weissleder, “Looking and listening to light: The evolution of whole-body photonic imaging,” *Nat. Biotechnol.* **23**, 313–320 (2005).

⁹H. F. Zhang, K. Maslov, G. Stoica, and L. H. V. Wang, “Functional photoacoustic microscopy for high-resolution and noninvasive in vivo imaging,” *Nat. Biotechnol.* **24**, 848–851 (2006).

- ¹⁰D. Razansky, M. Distel, C. Vinegoni, R. Ma, N. Perrimon, R. W. Koster, and V. Ntziachristos, "Multispectral opto-acoustic tomography of deep-seated fluorescent proteins in vivo," *Nat. Photonics* **3**, 412–417 (2009).
- ¹¹L. H. V. Wang and S. Hu, "Photoacoustic tomography: In vivo imaging from organelles to organs," *Science* **335**, 1458–1462 (2012).
- ¹²T. L. Szabo, *Diagnostic Ultrasound Imaging : Inside Out*, 2nd ed. (Academic, Amsterdam, 2013).
- ¹³G. A. Askariyan, B. A. Dolgoshein, A. N. Kalinovsky, and N. V. Mokhov, "Acoustic detection of high energy particle showers in water," *Nucl. Instrum. Methods* **164**, 267–278 (1979).
- ¹⁴N. A. Baily, "A review of the processes by which ultrasound is generated through the interaction of ionizing-radiation and irradiated materials—Some possible applications," *Med. Phys.* **19**, 525–532 (1992).
- ¹⁵L. Sulak, T. Armstrong, H. Baranger, M. Bregman, M. Levi, D. Mael, J. Strait, T. Bowen, A. E. Pifer, P. A. Polakos, H. Bradner, A. Parvulescu, W. V. Jones, and J. Learned, "Experimental studies of the acoustic signature of proton-beams traversing fluid media," *Nucl. Instrum. Methods* **161**, 203–217 (1979).
- ¹⁶J. Tada, Y. Hayakawa, K. Hosono, and T. Inada, "Time resolved properties of acoustic pulses generated in water and in soft-tissue by pulsed proton-beam irradiation—A possibility of doses distribution monitoring in proton radiation-therapy," *Med. Phys.* **18**, 1100–1105 (1991).
- ¹⁷Y. Hayakawa, J. Tada, N. Arai, K. Hosono, M. Sato, T. Wagai, H. Tsuji, and H. Tsujii, "Acoustic pulse generated in a patient during treatment by pulsed proton radiation beam," *Radiat. Oncol. Invest.* **3**, 42–45 (1995).
- ¹⁸V. I. Albul, V. B. Bychkov, S. S. Vasil'ev, K. E. Gusev, V. S. Demidov, E. V. Demidova, N. K. Krasnov, A. F. Kurchanov, V. E. Luk'yashin, and A. Y. Sokolov, "Acoustic field generated by a beam of protons stopping in a water medium," *Acoust. Phys.* **51**, 33–37 (2005).
- ¹⁹G. De Bonis, "Acoustic signals from proton beam interaction in water-comparing experimental data and Monte Carlo simulation," *Nucl. Instrum. Methods Phys. Res., Sect. A* **604**, S199–S202 (2009).
- ²⁰K. Stantz, F. Alsanea, and V. Moskvina, "BEST IN PHYSICS (THERAPY)—Use of radiation-induced ultrasound to image proton dosimetry," *Med. Phys.* **40**, 546 (2013).
- ²¹F. Alsanea, V. Moskvina, and K. Stantz, "SU-E-CAMPUS-T-02: Exploring radiation acoustics CT dosimeter design aspects for proton therapy," *Med. Phys.* **41**, 382 (2014).
- ²²A. R. Smith, "Vision 20/20: Proton therapy," *Med. Phys.* **36**, 556–568 (2009).
- ²³K. C. Jones, A. Witzum, C. M. Sehgal, and S. Avery, "Proton beam characterization by proton-induced acoustic emission: Simulation studies," *Phys. Med. Biol.* **59**, 6549 (2014).
- ²⁴S. Reinhardt, W. Assmann, S. Kellnberger, M. Omar, A. Fink, C. Gaebisch, P. Thirolf, M. Moser, G. Dollinger, G. Sergiadiis, V. Ntziachristos, and K. Parodi, "WE-D-BRF-02: Acoustic signal from the Bragg peak for range verification in proton therapy," *Med. Phys.* **41**, 495 (2014).
- ²⁵S. Agostinelli, J. Allison, K. Amako, J. Apostolakis, H. Araujo, P. Arce, M. Asai, D. Axen, S. Banerjee, G. Barrand, F. Behner, L. Bellagamba, J. Boudreau, L. Broglia, A. Brunengo, H. Burkhardt, S. Chauvie, J. Chuma, R. Chytracsek, G. Cooperman, G. Cosmo, P. Degtyarenko, A. Dell'Acqua, G. Depaola, D. Dietrich, R. Enami, A. Feliciello, C. Ferguson, H. Fesefeldt, G. Folger, F. Foppiano, A. Forti, S. Garelli, S. Giani, R. Giannitrapani, D. Gibin, J. J. G. Cadenas, I. Gonzalez, G. G. Abril, G. Greeniaus, W. Greiner, V. Grichine, A. Grossheim, S. Guatelli, P. Gumplinger, R. Hamatsu, K. Hashimoto, H. Hasui, A. Heikkinen, A. Howard, V. Ivanchenko, A. Johnson, F. W. Jones, J. Kallenbach, N. Kanaya, M. Kawabata, Y. Kawabata, M. Kawaguti, S. Kelner, P. Kent, A. Kimura, T. Kodama, R. Kokoulin, M. Kossov, H. Kurashige, E. Lamanna, T. Lampen, V. Lara, V. Lefebvre, F. Lei, M. Liendl, W. Lockman, F. Longo, S. Magni, M. Maire, E. Medernach, K. Minamimoto, P. M. de Freitas, Y. Morita, K. Murakami, M. Nagamatsu, R. Nartallo, P. Nieminen, T. Nishimura, K. Ohtsubo, M. Okamura, S. O'neale, Y. Oohata, K. Paech, J. Perl, A. Pfeiffer, M. G. Pia, F. Ranjard, A. Rybin, S. Sadilov, E. Di Salvo, G. Santin, T. Sasaki, N. Savvas, Y. Sawada, S. Scherer, S. Seil, V. Sirotenko, D. Smith, N. Starkov, H. Stoecker, J. Sulkimo, M. Takahata, S. Tanaka, E. Tcherniaev, E. S. Tehrani, M. Tropeano, P. Truscott, H. Uno, L. Urban, P. Urban, M. Verderi, A. Walkden, W. Wander, H. Weber, J. P. Wellisch, T. Wenaus, D. C. Williams, D. Wright, T. Yamada, H. Yoshida, and D. Zschiesche, "Geant4—a simulation toolkit," *Nucl. Instrum. Methods Phys. Res., Sect. A* **506**, 250–303 (2003).
- ²⁶M. Moser, P. Reichart, W. Carli, C. Greubel, K. Peeper, P. Hartung, and G. Dollinger, "High brilliance multicusp ion source for hydrogen microscopy at SNAKE," *Nucl. Instrum. Methods Phys. Res., Sect. B* **273**, 226–230 (2012).
- ²⁷L. Rohrer, H. Jakob, K. Rudolph, and S. J. Skorka, "The 4 gap double drift buncher at Munich," *Nucl. Instrum. Methods Phys. Res.* **220**, 161–164 (1984).
- ²⁸M. Toulemonde, E. Surdutovich, and A. V. Solov'yov, "Temperature and pressure spikes in ion-beam cancer therapy," *Phys. Rev. E* **80**, 031913 (2009).
- ²⁹L. V. Wang and H.-i. Wu, *Biomedical Optics : Principles and Imaging* (Wiley-Interscience, Hoboken, NJ, 2007).
- ³⁰L. V. Wang, "Tutorial on photoacoustic microscopy and computed tomography," *IEEE J. Sel. Top. Quantum Electron.* **14**, 171–179 (2008).
- ³¹B. T. Cox, S. Kara, S. R. Arridge, and P. C. Beard, "k-space propagation models for acoustically heterogeneous media: Application to biomedical photoacoustics," *J. Acoust. Soc. Am.* **121**, 3453–3464 (2007).
- ³²A. Rosenthal, D. Razansky, and V. Ntziachristos, "Fast semi-analytical model-based acoustic inversion for quantitative optoacoustic tomography," *IEEE Trans. Med. Imaging* **29**, 1275–1285 (2010).
- ³³P. Sigmund, A. Schinner, and H. Paul, "Errata and Addenda for ICRU Report 73, stopping of ions heavier than helium," *J. ICRU* **5**(1) (2009).
- ³⁴D. Sanchez-Parcerisa, A. Gemmel, O. Jakel, E. Rietzel, and K. Parodi, "Influence of the delta ray production threshold on water-to-air stopping power ratio calculations for carbon ion beam radiotherapy," *Phys. Med. Biol.* **58**, 145–158 (2013).
- ³⁵B. E. Treeby and B. T. Cox, "k-Wave: MATLAB toolbox for the simulation and reconstruction of photoacoustic wave fields," *J. Biomed. Opt.* **15**, 021314 (2010).
- ³⁶T. Terunuma, T. Sakae, Y. Hayakawa, A. Nohtomi, Y. Takada, K. Yasuoka, and A. Maruhashi, "Waveform simulation based on 3D dose distribution for acoustic wave generated by proton beam irradiation," *Med. Phys.* **34**, 3642–3648 (2007).
- ³⁷C. Grassberger, S. Dowdell, A. Lomax, G. Sharp, J. Shackelford, N. Choi, H. Willers, and H. Paganetti, "Motion interplay as a function of patient parameters and spot size in spot scanning proton therapy for lung Cancer," *Int. J. Radiat. Oncol., Biol., Phys.* **86**, 380–386 (2013).
- ³⁸W. Kleeven, M. Abs, E. Forton, S. Henrotin, Y. Jongen, V. Nuttens, Y. Paradis, E. Pearson, S. Quets, J. Van de Walle, P. Verbruggen, S. Zaremba, M. Conjat, J. Mandrillon, and P. Mandrillon, "The IBA superconducting synchrocyclotron project S2C2," in *Proceedings of Cyclotron 2013, Vancouver, BC, Canada*, edited by J. Thomson and V. Schaa (JACoW, CERN Geneva, 2014).
- ³⁹G. Dollinger, W. Assmann, K. Parodi, S. Kellnberger, and V. Ntziachristos, "A method and apparatus for determining an energy deposition of an ion beam," patent pending (2014).
- ⁴⁰S. Kellnberger, N. C. Deliolanis, D. Queiros, G. Sergiadiis, and V. Ntziachristos, "In vivo frequency domain optoacoustic tomography," *Opt. Lett.* **37**, 3423–3425 (2012).
- ⁴¹V. Malka, J. Faure, Y. A. Gauduel, E. Lefebvre, A. Rousse, and K. T. Phuoc, "Principles and applications of compact laser-plasma accelerators," *Nat. Phys.* **4**, 447–453 (2008).
- ⁴²H. Daido, M. Nishiuchi, and A. S. Pirozhkov, "Review of laser-driven ion sources and their applications," *Rep. Prog. Phys.* **75**, 056401 (2012).
- ⁴³V. Ntziachristos and D. Razansky, "Molecular imaging by means of multi-spectral optoacoustic tomography (MSOT)," *Chem. Rev.* **110**, 2783–2794 (2010).

SCIENTIFIC REPORTS



OPEN

Ionoacoustic tomography of the proton Bragg peak in combination with ultrasound and optoacoustic imaging

Received: 04 February 2016

Accepted: 07 June 2016

Published: 07 July 2016

Stephan Kellnberger^{1,2,*}, Walter Assmann^{3,*}, Sebastian Lehrack³, Sabine Reinhardt³, Peter Thirolf³, Daniel Queirós¹, George Sergiadis⁴, Günther Dollinger⁵, Katia Parodi³ & Vasilis Ntziachristos¹

Ions provide a more advantageous dose distribution than photons for external beam radiotherapy, due to their so-called inverse depth dose deposition and, in particular a characteristic dose maximum at their end-of-range (Bragg peak). The favorable physical interaction properties enable selective treatment of tumors while sparing surrounding healthy tissue, but optimal clinical use requires accurate monitoring of Bragg peak positioning inside tissue. We introduce ionoacoustic tomography based on detection of ion induced ultrasound waves as a technique to provide feedback on the ion beam profile. We demonstrate for 20 MeV protons that ion range imaging is possible with submillimeter accuracy and can be combined with clinical ultrasound and optoacoustic tomography of similar precision. Our results indicate a simple and direct possibility to correlate, *in-vivo* and in real-time, the conventional ultrasound echo of the tumor region with ionoacoustic tomography. Combined with optoacoustic tomography it offers a well suited pre-clinical imaging system.

Range uncertainties are among the greatest issues in ion beam therapy, and can have very different reasons: on the one hand range calculation inaccuracies in treatment planning (e.g. stopping power conversion from X-ray Computed Tomography [CT] images, CT artifacts), on the other hand inaccuracies of the actual irradiation (e.g. positioning of the patient and organ motion, physiological changes)^{1–3}. To compensate for the uncertainty in precisely placing the proton beam within tissue, safety margins are set around the tumor volume in treatment planning (typically 3.5% of the proton beam range¹), limiting the overall ability of proton therapy to provide maximum dose to the tumor and sparing surrounding healthy tissue⁴.

The importance of feedback during ion beam delivery is underscored by the consideration of various techniques for non-invasive localization of the Bragg peak position, typically based on the detection of nuclear reactions accompanying proton irradiation of tissue. Positron emission tomography (PET) is perhaps the most advanced method currently under clinical investigation^{5,6}, whereas the detection and imaging of prompt reaction gammas is just entering clinical testing^{7,8}. Both methods rely, however, on complex and bulky detector instrumentation and deliver only indirect information about the Bragg peak position. Another field, the development of compact laser-driven accelerators for ion-beam therapy^{9,10}, could similarly benefit by a technique that gives real-time feedback to the beam profile and energy deposition characteristics in order to optimize, calibrate, and standardize ion beam technology.

In this work we introduce ionoacoustic tomography (IAT) as a potent modality for high-resolution characterization of the Bragg peak spatial distribution¹¹. We hypothesized that by detecting and mathematically inverting the ultrasound waves produced upon transient stopping of ions by water/tissue we could reconstruct the deposited

¹Institute for Biological and Medical Imaging, Technische Universität München and Helmholtz Zentrum München, 85764 Neuherberg, Germany. ²Cardiovascular Research Center, Cardiology Division, Massachusetts General Hospital, Harvard Medical School, Boston, Massachusetts 02114, USA. ³Department for Medical Physics, Ludwig-Maximilians-Universität München, 85748 Garching, Germany. ⁴Department of Electrical and Computer Engineering, Aristotle University, 54124 Thessaloniki, Greece. ⁵Institute for Applied Physics and Measurement Technology, Universität der Bundeswehr, 85577 Neubiberg, Germany. *These authors contributed equally to this work. Correspondence and requests for materials should be addressed to V.N. (email: v.ntziachristos@tum.de)

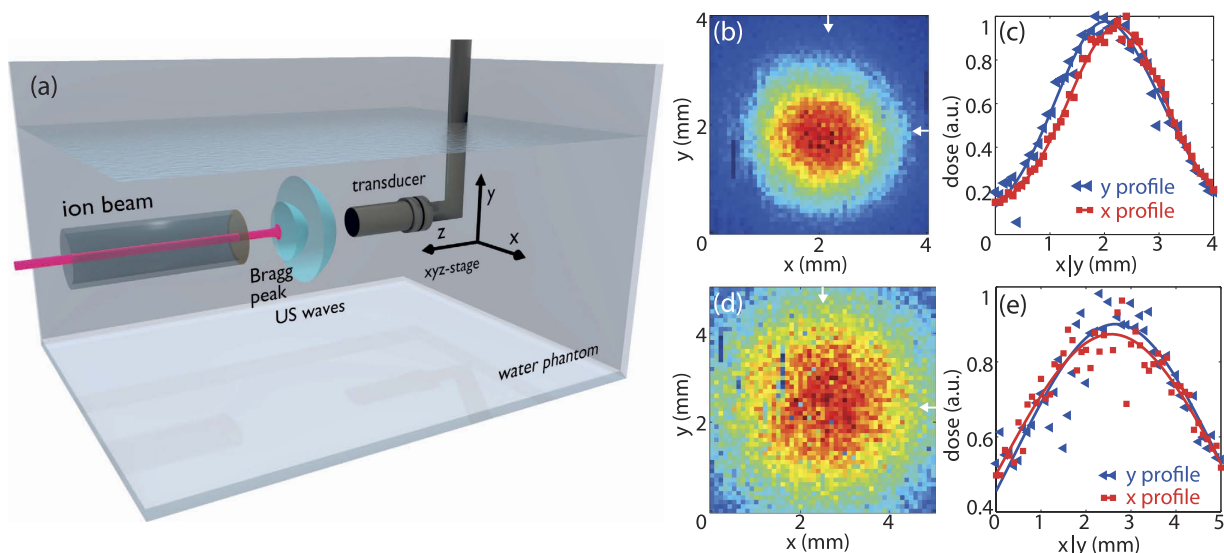


Figure 1. Experimental setup for 2D ionoacoustic imaging of proton beams. (a) Schematic of the 2D raster scan system using a focused high resolution acoustic wave sensor to characterize the proton dose distribution in water. Increased energy losses could be induced by means of an aluminum absorber inserted into the beam path. (b) Maximum intensity projection after raster scanning the proton beam. Arrows mark the position of the maximum. (c) Line profile of the Bragg peak in x and y direction, showing the measurement points (triangle and squares) and Gaussian fits to calculate the full width half maximum (FWHM). In x -direction, we determined the FWHM to be 2.4 ± 0.3 mm (red line) and in y -direction 2.3 ± 0.3 mm (blue line). (d) Bragg peak characterization with Al absorber. Maximum intensity projection of the particle beam after introducing a 0.5 mm Al sheet in the beam axis immediately after the vacuum exit window, arrows mark the maximum of the Bragg peak. (e) Line profile of the Bragg peak in x and y direction, illustrating scanning points and Gaussian fits to determine the FWHM.

dose profile. Such approach could yield a direct measure of energy deposition and enable ultrasound-diffraction limited imaging resolution (100–300 micrometers) within several centimeters penetration depth. The induction of acoustic waves using proton beams was first reported by Sulak *et al.*¹² in 1979, i.e. in the same time frame where optoacoustic (photoacoustic) imaging emerged¹³. Follow-up studies confirmed ultrasound detection from soft tissues even during tumor treatment, but were limited to single element acquisition and very low signal strength¹⁴. Using high frequency (up to 10 MHz) ultrasound transducers, we have recently shown one dimensional detection of ionoacoustic signals from a 20 MeV proton Bragg peak¹⁵. Besides several ionoacoustic simulation studies^{16–18}, in experiments at an advanced hospital-based cyclotron with 230 MeV protons ionoacoustic signals were observed around 10 kHz with hydrophones¹⁹. Alsanea *et al.*²⁰ demonstrated ionoacoustic tomography in simulations, however, no experimental study so far has revealed the spatial characteristics of proton beams. Here, we demonstrate submillimeter resolution three dimensional (3D) ionoacoustic tomography of the Bragg peak. We further combine IAT with ultrasound and optoacoustic imaging^{21–24} to demonstrate that not only Bragg peak profiles can be resolved with high resolution, but that they can also be co-registered to the underlying tissue morphology.

Results

Ionoacoustic imaging setup. To experimentally prove IAT we employed proton beams of 20 and 21 MeV provided by the Tandem accelerator of the Maier-Leibnitz-Laboratory (see Methods). According to Geant4 simulations²⁵, protons at this energy deliver a spatially confined Bragg peak with full-width-half-maximum (FWHM) of about 0.3 mm in beam direction and a range of approximately 4 mm in water, ideal for ionoacoustic characterization studies. Ionoacoustic signals were induced using a beam focus of about 1 mm FWHM (Supplementary Fig. S3(a)) and a proton pulse length of less than 200 ns, satisfying both thermal and stress confinement conditions (see Methods). For 2D raster scanning, we based image reconstruction of the Bragg peak on a maximum intensity projection of the acquired ionoacoustic data set while for 3D tomographic imaging we used the modified back-projection algorithm²⁶ or the model based reconstruction²⁷, similar to inversion methods applied in optoacoustic tomography^{28,29}.

2D ionoacoustic imaging of the Bragg peak. We first investigated the capability to image the Bragg peak with IAT in a two dimensional (2D) setting. Figure 1(a) shows the experimental 2D setup based on an uncalibrated 10 MHz single element focused ultrasound transducer located at focal distance of 25 mm from the expected Bragg peak position. We scanned the Bragg peak over a 4×4 mm² field of view in step sizes of 80 μ m. Figure 1(b) shows the maximum intensity projection (MIP), revealing a FWHM along the x - y axis of 2.4 ± 0.3 mm and 2.3 ± 0.3 mm as illustrated in Fig. 1(c). These values are in good agreement with a Geant4

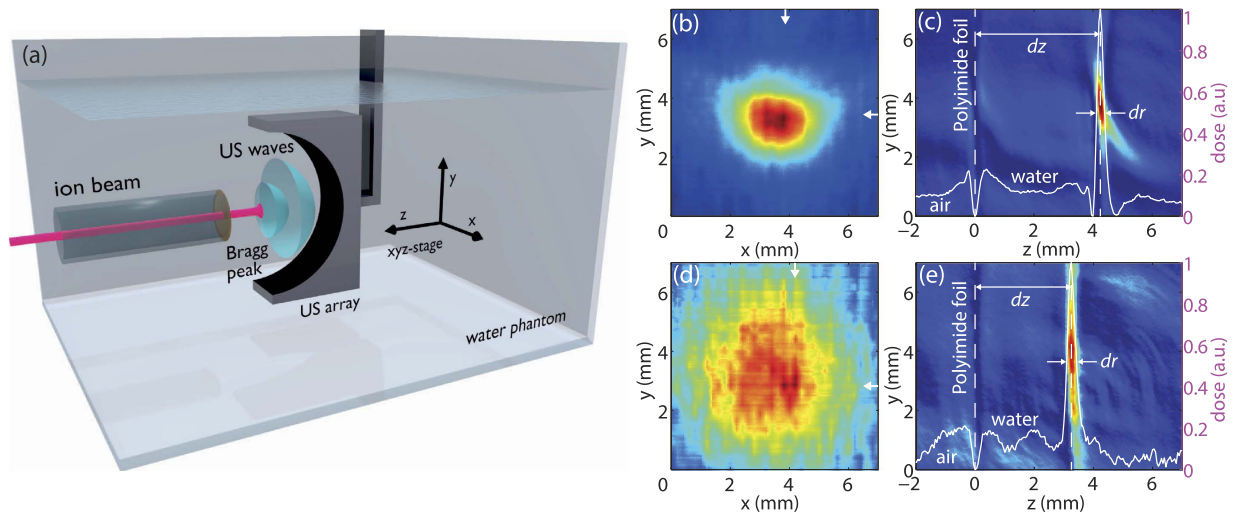


Figure 2. Three-dimensional tomographic scan of the Bragg peak. (a) Experimental setup for 3D ionoacoustic imaging. (b) Maximum intensity projection of the 3D reconstruction in the xy plane. The arrows indicate the position of the maximum in x and y axis. (c) Image of the reconstructed volume, showing the MIP in the yz -plane. The line profile depicts the position of the Bragg peak at a distance of 4.3 ± 0.2 mm from the polyimide foil and further reveals a longitudinal FWHM of the Bragg peak of 0.28 ± 0.05 mm. (d) Image of the Bragg peak after introducing an aluminum absorber in the beam path. The arrows indicate the position of the Bragg peak maximum. (e) Proton range determination using ionoacoustic tomography. The inserted aluminum absorber reduces the range of protons in water.

simulation based on the beam size measured with a radiochromic film located at the water phantom entrance foil (Supplementary Fig. S2(a)). Using k-Wave³⁰ to simulate ionoacoustic signal generation and propagation we found that 10^6 particles per pulse, corresponding to $1 \mu\text{J}$ stored energy in the Bragg peak volume generated a pressure wave of 67 Pa at the detector position. The induced ionoacoustic signals exhibit a signal to noise ratio (SNR) of about 40 dB after averaging 16 signals. These numbers are similar to SNR values measured in Assmann *et al.*¹⁵.

Upon confirming the fundamental ability to directly image the Bragg peak position and proton absorption distribution, we investigated the IAT detection sensitivity by introducing a 0.5 mm thick aluminum absorber in the proton beam after the vacuum exit before the 8 cm air gap. Geant4 simulations predict about a factor of two increase of the lateral spread due to the introduction of absorbing material into the beam (Supplementary Fig. S2(b)). Using IAT, we confirmed this prediction (Fig. 1(d,e)), revealing a beam profile measuring FWHM $x = 5.4 \pm 0.5$ mm and $y = 5.3 \pm 0.5$ mm. Due to the lower energy density in this experiment, SNR decreased to approximately 30 dB after averaging 16 events.

3D ionoacoustic tomography. To investigate whether Bragg-peak images could be captured in three dimensions and in video-rate mode, we employed (Fig. 2(a)) an ultrasonic 64 element curved array (172° half circle, center frequency 5 MHz) typically applied in optoacoustic tomography^{28,31}. The ultrasound array was moved in lateral steps of $200 \mu\text{m}$ over the particle beam, acquiring a 3D data set of generated ultrasonic waves. Image reconstruction yielded a $301 \times 301 \times 36$ volume element (voxel) image with a grid spacing of $50 \mu\text{m}$ which was used to visualize the stopped particles (see Methods). These first three dimensional reconstructions of the Bragg peak revealed the entire spatial distribution of particle beams in water (Supplementary Movie S1). The MIP along the beam axis, illustrated in Fig. 2(b) (and Supplementary Fig. S1(a)), reveals a FWHM in x and y -direction of 2.8 ± 0.3 mm and 2.0 ± 0.3 mm, in accordance with the related radiochromic film measurement (Supplementary Fig. S3(c,d)). The MIP in yz plane, shown in Fig. 2(c), visualizes the range of protons in water with the Bragg peak position at $dz = 4.3 \pm 0.2$ mm and the FWHM of the Bragg peak of $dr = 0.28 \pm 0.05$ mm. This proton range is in full agreement with earlier 1D measurements¹⁵ and Geant4 simulation results (Supplementary Fig. S2(a)). The effects of introducing a 0.5 mm thick aluminum absorber could be monitored in three dimensions (Fig. 2(d,e); Supplementary Movie S2). The increased lateral spread of stopped particles (FWHM of 6.2 ± 0.5 mm and 6.1 ± 0.5 mm in x and y axis) was confirmed by the corresponding simulations (Supplementary Fig. S2(b)) and was accompanied by a reduced Bragg peak range of $dz = 3.3 \pm 0.2$ mm, and a FWHM of the Bragg peak along the beam axis of $dr = 0.35 \pm 0.05$ mm.

Multimodal ionoacoustic, optoacoustic, and ultrasound imaging. The ability to image the Bragg peak in three dimensions comes with significant implications in terms of feedback during treatment. For accurate IAT application it would be therefore important to register the ion-beam profile onto the underlying tissue morphology. For this reason we combined IAT with ultrasound and optoacoustic imaging. Initial experiments were performed using 21 MeV proton energy for IAT and 532 nm laser illumination on an immobilized mouse leg *ex-vivo*, under identical placement conditions (Fig. 3(a)). By exchanging the IAT transducer for a co-localized linear ultrasound (US) array we also acquired pulse echo images from the same leg location. Optoacoustic images (Fig. 3(b)) revealed optical absorption morphology showing the medial marginal vein. Ultrasound imaging,

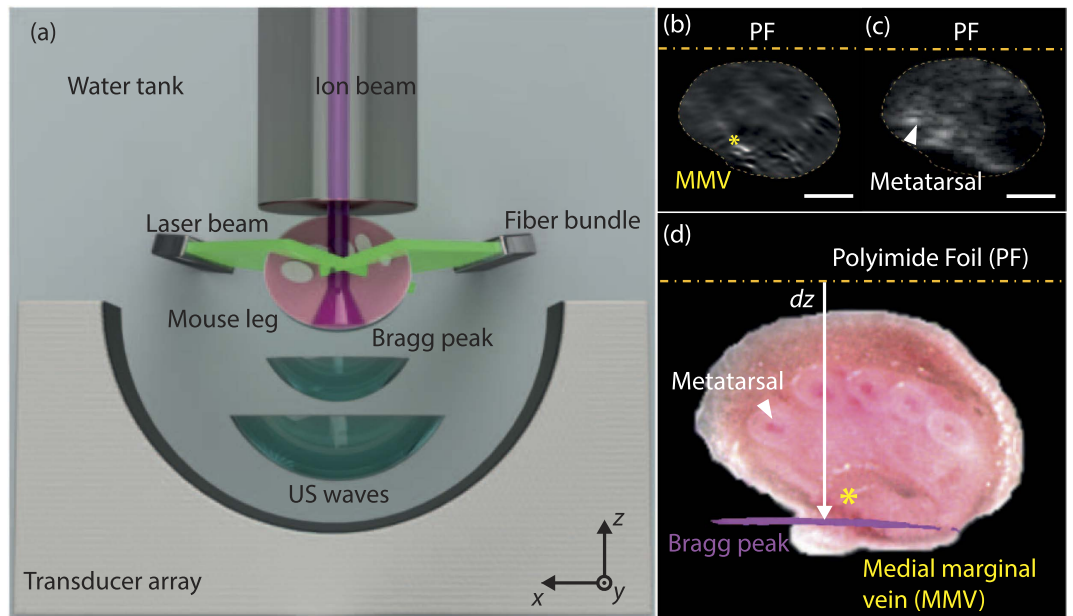


Figure 3. Triple-modality imaging of a mouse leg using optoacoustics, ionoacoustics, and ultrasonography. (a) Schematic of the opto- and ionoacoustic experiment. For ultrasonography we replaced the curved array with a linear US-array (picture not shown). (b) Optoacoustic reconstruction of a mouse leg positioned in the proton beam line (scale bar represents 2 mm, star marks the medial marginal vein). (c) Ultrasonography of the mouse leg, showing metatarsal bones (scale bar represents 2 mm). (d) Cryoslice of a mouse leg with the ionoacoustic reconstruction (magenta color) co-registered to the optical image, displaying the Bragg peak at the distal end of the leg with a proton range $dz = 4.7 \pm 0.2$ mm (star marks the medial marginal vein).

depicted in Fig. 3(c), further revealed anatomical features, such as bone structures that can be co-registered with IAT and optoacoustic images. An invasive cryo-slice image of the mouse leg, shown in Fig. 3(d), demonstrated good agreement with the optoacoustic and ultrasound image. Furthermore, Fig. 3(d) shows the co-registration of the IAT image onto the optical image, illustrating the Bragg peak position reaching the distal end of the mouse leg with a proton range of $dz = 4.7 \pm 0.2$ mm in the mouse leg tissue. We note that an increased lateral spreading of the Bragg peak as shown in Fig. 3(d) can be attributed to lower SNR compared to previous experiments due to soft tissue effects. The longer range of protons in tissue compared to water experiments (Geant4 simulation predicts $dz = 4.5$ mm at 21 MeV proton energy) can be explained by the slightly different properties of the leg tissue over water. The registration of IAT signals on other tissue images may pave the way towards monitoring of beam quality and proton therapy treatments³².

Discussion. Our results effectively establish ionoacoustic tomography as a potent tool that could be utilized in multiple applications within the proton-beam development and proton-therapy fields. We present a novel experimental arrangement to interrogate two abilities. The first feature is related to the so far unknown capacity to generate images of proton beams stopped within tissues and tissue-like media. Such capacity could be fundamental to enable on-the-fly optimization of beam delivery during proton treatment. Moreover, IAT could be uniquely suited for characterization of the very intense beam pulses of future compact laser-driven accelerators^{9,10,33} due to its large dynamic range and the temporal separation of the acoustic signal from the laser pulse induced electromagnetic pulse (EMP). The second ability is related to the development of a hybrid system that would allow the unique co-localization of a proton beam and the underlying tissue anatomy. Such system could be employed during treatment regimens to register experimentally measured proton beams onto the underlying tissue morphology so as to optimize dose delivery. The acoustic waves generated in response to the sharp distal falloff of stopped protons are spatiotemporally analyzed to produce two-dimensional and three-dimensional maps and videos of proton range and Bragg peak shape, resulting in submillimeter accuracy. In particle therapy, the combination of ultrasonography and IAT can enable accurate positioning of the ion beam on tissue morphology only or jointly with ultrasonic markers. As both methods are based on ultrasound effects, inhomogeneities occurring in soft tissue can be neglected in IAT. Moreover, optoacoustic tomography may be a valuable imaging combination for pre-clinical particle therapy research well adapted to small animal morphology thanks to its high spatial resolution or for clinical imaging of superficial diseases, in particular for depths of up to 3 cm (e.g breast cancer visualization)^{34,35}.

Methods

Proton beam parameters and radiochromic films. We used proton energies of 20 and 21 MeV with an energy resolution better than 0.1% delivered by the 12 MV electrostatic Tandem accelerator of the Maier-Leibnitz-Laboratory (LMU and TU München). To enable high image quality, we set the beam current to about

3 nA measured with a Faraday cup at the beam vacuum exit. This current corresponds to 10^6 particles per pulse being equivalent to $1 \mu\text{J}$ per proton pulse, one order of magnitude above the detection limit of 10^5 particles per pulse as previously determined by Assmann *et al.*¹⁵ in a similar ionoacoustic setup. For our 2D scan using 16 averages, this beam current resulted in a total energy of approximately 66 mJ while for the 3D scan averaging 512 events, a total energy of about 1.2 mJ was used.

The beam focus size was adjusted to be about 2 mm^2 at the entrance foil of the water phantom. The beam focus could be seen on a cesium iodide (CsI) scintillating screen during beam tuning and was measured after specific irradiations with a radiochromic film (GafChrom). Radiochromic films offer a simple and independent possibility to check the beam spot size immediately after entrance into the water phantom. A scan of the irradiated area (Fig. S3(a,c)) allows one to determine the intensity distribution in x and y (Fig. S3(b,d)) which can be directly compared to the corresponding values of ionoacoustic scans (Fig. 1(b,d)). At our beam intensity, a film exposure took about 30 sec followed by scanning with a photo scanner (Epson Perfection V700) using the full physical scan resolution of 1200 dpi³⁶. Measured dose profiles corresponding to Figs 1(b) and 2(b) are presented in Supplementary Information, Fig. S3 where different lateral resolutions (radiochromic film $\sim 50 \mu\text{m}$, ultrasound transducer $\sim 0.3 \text{ mm}$) and acquisition times (film $\sim 30 \text{ sec}$, transducer scan duration $\sim 1.5 \text{ h}$ suffering from long term beam instabilities) of the methods have to be taken into account.

IAT setup. All IAT measurements were performed by directing the proton beam from the Tandem accelerator through a vacuum exit window and an 8 cm air gap into a water tank ($33 \times 17 \times 19 \text{ cm}^3$) through a $50 \mu\text{m}$ polyimide window. The water tank contained different ultrasound sensors employed to study IAT feasibility and performance of proton beam characterization at different dimensions or for performing co-registered ultrasound and optoacoustic imaging.

Two dimensional images of the particle beam profile were enabled by raster scanning a spherically focused ultrasound sensor (V311, focal distance 25.4 mm, central frequency 10 MHz, bandwidth 100%, Olympus-Panametrics, USA) mounted on a xyz stage with $10 \mu\text{m}$ accuracy. The 10 MHz transducer had a beam width of $293 \mu\text{m}$ with a length of the focal zone of 4 mm at its central frequency. Raster scans were performed using a scanning distance of $dx = dy = 80 \mu\text{m}$ for the Bragg peak characterization illustrated in Fig. 1(b) and $dx = dy = 100 \mu\text{m}$ for the aluminum experiment shown in Fig. 1(d). A scan with 250 raster points took around 1.5h, during this time the beam intensity as well as the focus size fluctuated by $\pm 30\%$, therefore an increase of the measured focus size has to be expected. At its central frequency, the detector has a -6 dB beam diameter at focal length of about 0.3 mm, which limits the lateral resolution additionally. The water temperature was kept around 35°C and continuously monitored for US velocity calculation. We amplified ionoacoustic signals employing a low noise 63 dB amplifier (AU 1291, Miteq Inc., USA) and additionally increased SNR in Fig. 1(b,d) by averaging 16 waveforms. Signals were acquired using a digital oscilloscope set to a sampling rate of 500 MS/s.

Fast 2D and 3D imaging of the particle beam were performed using a 64 element curved US array (172° half circle, central frequency 5 MHz, bandwidth $> 50\%$, Vermon, France) employed in previous optoacoustic imaging studies^{22,28,37}. The in-plane spatial resolution of the US-array is estimated to be in the order of $150 \mu\text{m}$ while elevational resolution is approximately $800 \mu\text{m}$. To increase SNR, we used a homebuilt amplifier array consisting of 64 elements offering a gain of 52 dB. Additionally, signals were averaged 512 times for each scanning step, resulting in a frame rate of more than 1 frame per second.

Ultrasonography was performed employing a commercially available 128-element linear array (7.5 MHz, 12L5V linear array, Model Terason t2000, Terason, Burlington, MA, USA) which replaced the curved US array used for optoacoustic and ionoacoustic imaging. We note that the US images were not perfectly co-registered to the optoacoustic images and invasive cryo-slice images of the mouse leg after exchanging the iono/optoacoustic imaging array with the US array. This mismatch is attributed to the spatially limited geometry of our experimental imaging system, but can be improved in future experiments.

Image reconstruction. We used different reconstruction algorithms to generate ionoacoustic images. Maximum intensity projections of the two dimensional raster scans illustrated in Fig. 1(b,d) were generated by determining the peak-to-peak difference of the ionoacoustic signal at the Bragg peak position. Three dimensional representations of the Bragg peak were reconstructed using the modified backprojection algorithm²⁶ for Fig. 3(b) or the model based reconstruction²⁷ for Fig. 2.

Ex-vivo mouse imaging. All mouse procedures were approved by the Bavarian Animal Care and Use Committee and all experiments were performed in accordance with the guidelines and regulations approved by the Government of Bavaria, Germany. Iono- and optoacoustic imaging was performed on a CD-1 nude mouse sacrificed prior to the experiment. We imaged the mouse leg taking into account the limited range of protons at 21 MeV which relates to $dz = 4.5 \text{ mm}$ in water. The mouse was mounted on a custom built animal holder and illuminated from one side using three fiber bundles connected to a 532 nm laser. The measurement protocol comprised optoacoustic imaging of the mouse leg followed by ionoacoustic imaging to obtain the position of the Bragg peak. Finally, optoacoustic imaging of the mouse leg at a similar position was performed.

Thermal and stress confinement conditions. According to Wang³⁸, the characteristic dimension of the heated region is the axial FWHM of the Bragg peak with about $300 \mu\text{m}$. The related thermal relaxation time amounts to 570 ms, whereas the thermal stress relaxation time (using an US velocity of 1500 m/s) is 200 ns. Therefore, thermal and stress confinement conditions are fulfilled with proton pulse lengths below 200 ns at the considered energies.

Geant4 simulation. For calculating the proton dose deposition in water, we used Geant4²⁵ (version 10.0.p01) and activated the QGSP_BIC_HP 2.0 physics lists for handling of the main electromagnetic and nuclear

processes. A grid size between 10 μm and 100 μm was chosen for all three scoring dimensions. The value of the ionization potential of water was set to 78 eV, according to the latest recommendation of Andreo *et al.*³⁹. Due to the low proton beam energies used in our ionoacoustic experiments, inaccuracies related to the density and the ionization potential of water could be neglected in our Bragg peak position simulations¹⁵. We found that uncertainties of the simulation can mainly be attributed to inaccurate determination of the experimental settings in the beam path, such as the thickness of the polyimide foil or the air gap, resulting in $\sim 30 \mu\text{m}$ total error. Examples of Geant4 simulations for 20 MeV protons in water are shown in Supplementary Information, Fig. S2 (axial dose distribution, straggling without/with Al absorber).

k-Wave simulation. The k-Wave simulation engine was used to simulate the entire ionoacoustic propagation and detection model, including proton energy transfer to the medium, generation of acoustic waves, and the propagation of acoustic waves until detection²⁷. For this purpose, we supplied the k-Wave toolbox with the output of our Geant4 simulation. Correspondingly, the forward model comprised a 3D matrix with $30 \times 30 \times 10 \mu\text{m}^3$ grid size spacing (similar to the used Geant4 scoring), and a volume size of $13.2 \times 13.2 \times 32 \text{ mm}^3$ in corresponding x , y , and z direction.

References

- Paganetti, H. Range uncertainties in proton therapy and the role of Monte Carlo simulations. *Phys Med Biol* **57**, R99–R117 (2012).
- Knopf, A.-C. & Lomax, A. *In vivo* proton range verification: a review. *Phys Med Biol* **58** (2013).
- Schuemann, J., Dowdell, S., Grassberger, C., Min, C. H. & Paganetti, H. Site-specific range uncertainties caused by dose calculation algorithms for proton therapy. *Phys Med Biol* **59**, 4007–4031 (2014).
- Wilson, R. R. Radiological use of fast protons. *Radiology* **47**, 487–491 (1946).
- Parodi, K. *et al.* Patient study of *in vivo* verification of beam delivery and range, using positron emission tomography and computed tomography imaging after proton therapy. *International Journal of Radiation Oncology Biology Physics* **68**, 920–934 (2007).
- Parodi, K. Vision 20/20: Positron emission tomography in radiation therapy planning, delivery, and monitoring. *Medical physics* **42**, 7153, doi: 10.1118/1.4935869 (2015).
- Min, C.-H., Kim, C. H., Youn, M.-Y. & Kim, J.-W. Prompt gamma measurements for locating the dose falloff region in the proton therapy. *Appl Phys Lett* **89** (2006).
- Hueso-Gonzalez, F. *et al.* First test of the prompt gamma ray timing method with heterogeneous targets at a clinical proton therapy facility. *Phys Med Biol* **60**, 6247–6272, doi: 10.1088/0031-9155/60/16/6247 (2015).
- Malka, V. *et al.* Principles and applications of compact laser-plasma accelerators. *Nat Phys* **4**, 447–453 (2008).
- Hooker, S. M. Developments in laser-driven plasma accelerators. *Nat Photonics* **7**, 775–782 (2013).
- Parodi, K. & Assmann, W. Ionoacoustics: A new direct method for range verification. *Modern Physics Letters A* **30**, doi: 10.1142/s0217732315400258 (2015).
- Sulak, L. *et al.* Experimental studies of the acoustic signature of proton-beams traversing fluid media. *Nuclear Instruments & Methods* **161**, 203–217 (1979).
- Rosencwaig, A. Photoacoustic spectroscopy of biological materials. *Science* **181**, 657–658 (1973).
- Hayakawa, Y. *et al.* Acoustic pulse generated in a patient during treatment by pulsed proton radiation beam. *Radiation Oncology Investigations* **3**, 42–45 (1995).
- Assmann, W. *et al.* Ionoacoustic characterization of the proton Bragg peak with submillimeter accuracy. *Medical physics* **42**, 567–574 (2015).
- Terunuma, T. *et al.* Waveform simulation based on 3D dose distribution for acoustic wave generated by proton beam irradiation. *Medical physics* **34**, 3642–3648 (2007).
- Jones, K. C., Witztum, A., Sehgal, C. M. & Avery, S. Proton beam characterization by proton-induced acoustic emission: simulation studies. *Phys Med Biol* **59**, 6549–6563, doi: 10.1088/0031-9155/59/21/6549 (2014).
- Jones, K. C., Sehgal, C. M. & Avery, S. How proton pulse characteristics influence photoacoustic determination of proton-beam range: simulation studies. *Phys Med Biol* **61**, 2213–2242, doi: 10.1088/0031-9155/61/6/2213 (2016).
- Jones, K. C. *et al.* Experimental observation of acoustic emissions generated by a pulsed proton beam from a hospital-based clinical cyclotron. *Medical physics* **42**, 7090–7097, doi: 10.1118/1.4935865 (2015).
- Alsanea, F., Moskvina, V. & Stantz, K. M. Feasibility of RACT for 3D dose measurement and range verification in a water phantom. *Medical physics* **42**, 937–946, doi: 10.1118/1.4906241 (2015).
- Razansky, D. *et al.* Multispectral opto-acoustic tomography of deep-seated fluorescent proteins *in vivo*. *Nat Photonics* **3**, 412–417 (2009).
- Razansky, D., Buehler, A. & Ntziachristos, V. Volumetric real-time multispectral optoacoustic tomography of biomarkers. *Nat Protoc* **6**, 1121–1129 (2011).
- Wang, L. V. & Hu, S. Photoacoustic tomography: *in vivo* imaging from organelles to organs. *Science* **335**, 1458–1462 (2012).
- Wang, L. V. Multiscale photoacoustic microscopy and computed tomography. *Nat Photonics* **3**, 503–509 (2009).
- Agostinelli, S. *et al.* GEANT4—a simulation toolkit. *Nuclear Instruments & Methods in Physics Research Section a-Accelerators Spectrometers Detectors and Associated Equipment* **506**, 250–303 (2003).
- Xu, M. H. & Wang, L. V. Universal back-projection algorithm for photoacoustic computed tomography (vol 71, art no 016706, 2005). *Phys Rev E* **75** (2007).
- Rosenthal, A., Razansky, D. & Ntziachristos, V. Fast semi-analytical model-based acoustic inversion for quantitative optoacoustic tomography. *IEEE Trans Med Imaging* **29**, 1275–1285 (2010).
- Buehler, A., Herzog, E., Razansky, D. & Ntziachristos, V. Video rate optoacoustic tomography of mouse kidney perfusion. *Optics letters* **35**, 2475–2477 (2010).
- Lutzweiler, C. & Razansky, D. Optoacoustic imaging and tomography: reconstruction approaches and outstanding challenges in image performance and quantification. *Sensors* **13**, 7345–7384 (2013).
- Treeby, B. E. & Cox, B. T. k-Wave: MATLAB toolbox for the simulation and reconstruction of photoacoustic wave fields. *Journal of biomedical optics* **15**, doi: Artn 02131410.1117/1.3360308 (2010).
- Ntziachristos, V. & Razansky, D. Molecular imaging by means of multispectral optoacoustic tomography (MSOT). *Chemical reviews* **110**, 2783–2794 (2010).
- Bin, J. *et al.* A laser-driven nanosecond proton source for radiobiological studies. *Appl Phys Lett* **101** (2012).
- Bin, J. H. *et al.* Ion acceleration using relativistic pulse shaping in near-critical-density plasmas. *Phys Rev Lett* **115**, 4801–4801 (2015).
- Omar, M., Schwarz, M., Soliman, D., Symvoulidis, P. & Ntziachristos, V. Pushing the optical imaging limits of cancer with multi-frequency-band raster-scan optoacoustic mesoscopy (RSOM). *Neoplasia* **17**, 208–214, doi: 10.1016/j.neo.2014.12.010 (2015).
- Heijblom, M. *et al.* Photoacoustic image patterns of breast carcinoma and comparisons with Magnetic Resonance Imaging and vascular stained histopathology. *Sci Rep* **5**, 11778, doi: 10.1038/srep11778 (2015).

36. Reinhardt, S., Hillbrand, M., Wilkens, J. J. & Assmann, W. Comparison of Gafchromic EBT2 and EBT3 films for clinical photon and proton beams. *Medical physics* **39**, 5257–5262 (2012).
37. Herzog, E. *et al.* Optical imaging of cancer heterogeneity with multispectral optoacoustic tomography. *Radiology* **263**, 461–468 (2012).
38. Wang, L. V. Tutorial on photoacoustic microscopy and computed tomography. *Ieee J Sel Top Quant* **14**, 171–179, doi: 10.1109/Jstqe.2007.913398 (2008).
39. Andreo, P., Wulff, J., Burns, D. T. & Palmans, H. Consistency in reference radiotherapy dosimetry: resolution of an apparent conundrum when Co-60 is the reference quality for charged-particle and photon beams. *Phys Med Biol* **58**, 6593–6621 (2013).

Acknowledgements

We thank Murad Omar, Juan Sebastián Osorio Valencia, Christoph Gäbisch, Thomas Hellerer, and Marcus Moser for their experimental support, George Dedes for his help in simulations. S. K. acknowledges financial support from the Alexander von Humboldt-Stiftung through a Feodor Lynen Research Fellowship. This work was funded by the DFG Cluster of Excellence Munich Centre for Advanced Photonics (MAP) and the DFG Reinhart Koselleck award 'High resolution near-field thermoacoustic sensing and imaging' (NT 3/9-1).

Author Contributions

S.K. and W.A. conceived, designed, and carried out the experimental measurements, P.T., G.D., K.P. and V.N. provided critical support for the experimental work. S.K., W.A., S.L. and S.R. performed data analysis and image reconstruction, D.Q. carried out model based image reconstructions. S.L. performed simulation studies. G.S. participated in critical discussions and provided theoretical support for this work. S.K., W.A., G.D., K.P. and V.N. wrote the manuscript.

Additional Information

Supplementary information accompanies this paper at <http://www.nature.com/srep>

Competing financial interests: The authors declare no competing financial interests.

How to cite this article: Kellnberger, S. *et al.* Ionoacoustic tomography of the proton Bragg peak in combination with ultrasound and optoacoustic imaging. *Sci. Rep.* **6**, 29305; doi: 10.1038/srep29305 (2016).



This work is licensed under a Creative Commons Attribution 4.0 International License. The images or other third party material in this article are included in the article's Creative Commons license, unless indicated otherwise in the credit line; if the material is not included under the Creative Commons license, users will need to obtain permission from the license holder to reproduce the material. To view a copy of this license, visit <http://creativecommons.org/licenses/by/4.0/>

quantification the proper attenuation, scatter and partial volume corrections need to be applied. If organ or lesion dosimetry is performed, precise determination of organ/lesion volumes is necessary. Care has to be taken for an appropriate calibration of the imaging system.

b) *Biokinetics*

This requires the determination of a correct temporal sampling and the use of *ad hoc* procedures to integrate the activity within time to obtain the total number of decays occurring in the source organs and thus the time-integrated activity coefficients (TIACs).

c) *Absorbed dose Calculation*

If the TIACs of the relevant structures are known, a calculation of the absorbed doses can be performed by applying, in most cases, the "MIRD formalism":

$$D = \bar{A} \cdot S$$

D: the mean absorbed dose to a voxel or a target region from the cumulated activity in a source region.

\bar{A} : the cumulated activity (i.e. the integral of the time-activity curve)

S: S factor (= mean absorbed dose per unit cumulated activity in the voxel or the target region).

Different dose calculation approaches exist: These may either be based on tabulated S factors (with mass correction) of anthropomorphic phantoms, on convolution kernels or on Monte-Carlo simulations.

Results: The most successful pairs of isotopes for theranostics are I-123/I-124/I-131 [2] and Ga-68/Lu-177/Y-90 [3]. In addition, Y-90 PET/CT provides a good estimate of the absorbed doses in selective internal radiotherapy for loco-regional liver treatment [4].

Conclusion: Although many new radiopharmaceuticals are available for imaging and molecular radiotherapy it is still a challenge to establish reliable dose-response relationships.

Keywords: Molecular radiotherapy, quantitative imaging, absorbed dose calculation

References:

- [1] Bentzen SM. Lancet Oncol. 2005;6:112-7.
- [2] Luster et al. EJNMMI. 2008;35:1941-59
- [3] Bodei et al. EJNMMI. 2013;40:800-16
- [4] Lhommel et al. EJNMMI. 2009;36:1696

134

Single-cell S-value calculations for Auger-electron emitting radionuclides

B.Q. Lee¹, N. Falzone^{2,3}, J.M. Fernández-Varea⁴, K.A. Vallis², A.E. Stuchbery¹, T. Kibédi¹

¹ (Australian National University, Canberra, Australia)

² (University of Oxford, Oxford, United Kingdom)

³ (Tshwane University of Technology, Pretoria, South Africa)

⁴ (Universitat de Barcelona, Barcelona, Spain)

Purpose: Auger-electron (AE) emitting radionuclides could be exploited for therapeutic purposes due to the high local energy deposition by low-energy Auger electrons or may deliver an unintentional mean absorbed dose burden when used as medical imaging agents. The aim of this study is to provide S-values for selected 14 AE emitting radionuclides based on the latest radiation spectra.

Methods: The Monte Carlo code PENELOPE [1] was used to transport the complete radiation spectra of ⁶⁷Ga, ^{80m}Br, ⁸⁹Zr, ⁹⁰Nb, ^{99m}Tc, ¹¹¹In, ^{117m}Sn, ¹¹⁹Sb, ¹²³I, ¹²⁴I, ¹²⁵I, ¹³⁵La, ^{195m}Pt and ²⁰¹Tl using the methodology described in Ref. [2]. Radiation spectra was based on the unabridged nuclear decay data from MIRD RADTABS program [3] and the radiation spectra generated using the BrlccEmis code [4]. Taking the nucleus as the target, simulations were run assuming uniformly distributed activity in the nucleus (N←N), in the cytoplasm (N←Cy) or on the cell surface (N←CS).

Results: A comparison of calculated Auger yields for all 14 radionuclides is shown in the table below. Auger yields from MIRD are consistently higher than the values calculated using the BrlccEmis code. The methodology used to produce data in MIRD did not account for variations in binding energies

during atomic relaxation thus overestimated the intensity of low-energy electrons.

Radionuclide	BrlccEmis	MIRD	Radionuclide	BrlccEmis	MIRD
⁶⁷ Ga	4.84	4.96	¹¹⁹ Sb	14.29	23.68
^{80m} Br	8.96	9.6	¹²³ I	12.31	13.71
⁸⁹ Zr	6.88	9.45	¹²⁴ I	8.38	9.17
⁹⁰ Nb	7.2	8.77	¹²⁵ I	20.0	23.0
^{99m} Tc	4.39	4.41	¹³⁵ La	10.9	N/A
¹¹¹ In	7.17	7.43	^{195m} Pt	25.9	36.6
^{117m} Sn	5.72	14.2	²⁰¹ Tl	18.8	20.9

BrlccEmis determined S-values were generally lower compared with MIRD S-values with the greatest differences noted when the source is far from the target region, i.e. for the N←Cy and N←CS configurations.

Conclusions: Realistic modelling of atomic relaxation following nuclear decay is essential for producing the radiation spectra needed for the calculations of S-values.

Keywords: Auger-electron emitter; Monte Carlo simulation; S-values; Nuclear medicine;

References:

- [1] F Salvat, PENELOPE-2011; NEA 6416
- [2] N Falzone J Nucl Med 2015; 56(9): 1441
- [3] KF Eckerman and A Endo, MIRD Radionuclide Data and Decay Schemes 2008
- [4] B Lee et al. Comp Math Meth Med 2012; 651475

135

Range Verification with Ionoacoustics: simulations and measurements at a clinical proton synchro-cyclotron

S. Lehrack¹, W. Assmann¹, A. Maaß¹, K. Baumann¹, G. Dedes¹, S. Reinhardt¹, P. Thirolf¹, G. Dollinger², F. Vander Stappen³, J. Van de Walle³, S. Henrotin³, B. Reynders³, D. Bertrand³, D. Prieels³, K. Parodi¹

¹ Department for Medical Physics, Ludwig-Maximilians-Universität München, Am Coulombwall 1, 85748 Garching b. München, Germany

² Institute for Applied Physics and Instrumentation, Universität der Bundeswehr, Werner-Heisenberg-Weg 39, 85577 Neubiberg, Germany

³ IBA, 3 chemin du Cyclotron, 1348 Louvain-la-Neuve, Belgium

Purpose: The local temperature increase induced by ion energy deposition in tissue creates an "ionoacoustic" ultrasound signal, particularly at the dose maximum (Bragg peak)[1-3]. This signal may be used for range verification in ion beam therapy in the future, which is still an important challenge for this irradiation modality. This approach has recently been revisited by several groups in simulations [4, 5], and by our group in simulations and also in proof-of-principle experiments with pulsed 20 MeV proton beams [6]. Here we present new simulations and first measurements of the ionoacoustic signal produced in water by proton beams accelerated up to energies of 227 MeV at a clinical synchro-cyclotron.

Material and Methods: In preparation of ionoacoustic experiments at clinically relevant energies, we extended our simulations from previously 20 MeV to beam energies of 120-230 MeV. The propagation of ultrasound waves was simulated by the MATLAB toolbox k-Wave using Geant4 for calculations of the initial dose deposition. The corresponding experimental setup to measure the ionoacoustic signal consisted of a broadband hydrophone (500 Hz - 250 kHz) placed in a water phantom with protons entering through the water surface. We measured the transit time of the ionoacoustic signal from the Bragg peak to the hydrophone and varied this distance either by using different energies (227, 226 and 145 MeV) or by changing the detector position while using the maximum energy.

Result: The simulations showed a distinct frequency shift of the ionoacoustic signal spectrum from a few MHz at 20 MeV from our previous experiments to about 100 kHz and below at proton beam energies above 120 MeV. At the new IBA synchro-cyclotron, we were able to measure ionoacoustic

signals from a pulsed proton beam (about 5 pC/pulse, 6 μ s FWHM) and detector shifts down to 2 mm. The measured relative shifts of the Bragg peak position of 2.3 mm for 1 MeV energy change and 173.25 mm for 82 MeV are in perfect agreement with Geant4 predictions. However, the low signal amplitude below 1 mV required an averaging with 1024 acquisitions.

Conclusion: Measuring the ionoacoustic signal at the IBA synchro-cyclotron, the detectability of 2 mm range shifts could be demonstrated. Experimental upgrades will be discussed, from which we reasonably assume to improve the resolution to 1 mm and below. In order to determine an absolute ion range in water in future ionoacoustic experiments, a method using an additional ultrasound transducer to measure the distance of the hydrophone to the water surface was developed. Remaining challenges on signal detectability for clinical dose rates as well as perspectives of future setup improvements will be discussed.

Acknowledgment: Supported by DFG (Excellence Cluster MAP). We thank Stephan Kellnberger and Vasilis Ntziachristos for the fruitful discussion and support in previous experiments.

Keywords: Ionoacoustics, Range Verification, Ultrasound

References:

- [1] Hayakawa, Y., et al., Acoustic pulse generated in a patient during treatment by pulsed proton radiation beam. *Radiation Oncology Investigations*, 1995. 3(1): p. 42-45.
- [2] Sulak, L., et al., Experimental Studies of the Acoustic Signature of Proton-Beams Traversing Fluid Media. *Nuclear Instruments & Methods*, 1979. 161(2): p. 203-217.
- [3] Albul, V.I., et al., Acoustic field generated by a beam of protons stopping in a water medium. *Acoustical Physics*, 2005. 51(1): p. 33-37.
- [4] Alsanea, F., V. Moskvina, and K.M. Stantz, Feasibility of RACT for 3D dose measurement and range verification in a water phantom. *Med Phys*, 2015. 42(2): p. 937-46.
- [5] Jones, K.C., et al., Proton beam characterization by proton-induced acoustic emission: simulation studies. *Phys Med Biol*, 2014. 59(21): p. 6549-63.
- [6] Assmann, W., et al., Ionoacoustic characterization of the proton Bragg peak with submillimeter accuracy. *Med Phys*, 2015. 42(2): p. 567-74.

136

Monte Carlo simulation of prompt- γ emission in proton therapy using a track length estimator

J. M. Létang¹, W. El Kanawati¹, D. Dauvergne², M. Pinto^{2,3}, D. Sarrut¹, É. Testa², N. Freud¹

¹CREATIS, Université de Lyon; CNRS UMR5220; INSERM U1044; INSA-Lyon;

Université Lyon 1; Centre Léon Bérard, Lyon, France

²IPNL, Université de Lyon; CNRS/IN2P3 UMR5822; Université Lyon 1 Lyon, France

³now with Ludwig Maximilians University, Munich, Germany

Purpose: Online in vivo control of the ion range in a patient during proton therapy is a major challenge for quality assurance of treatments. After measurements showed that prompt- γ emission is correlated to the ion range (Min *et al* 2006, Testa *et al* 2008), prompt- γ imaging emerged as a promising method (Verburg *et al* 2013). Fast methods are required to compute accurate prompt- γ emission maps to design and predict the camera response from treatment plans. An analytic computation method based on the structure of the dose calculation engines in treatment planning system has recently been proposed (Sterpin *et al* 2015). An alternative technique based on variance reduction in Monte Carlo (MC) calculations is developed here for computing prompt- γ emission maps in proton therapy.

Materials/Methods: The track length estimator (TLE) method is a standard variance reduction technique in voxel-based dose computation in the kerma approximation (Williamson 1987), and similar approaches have also been developed for positron emitter distributions in proton therapy (Parodi *et al* 2007). A specific track length estimator has been developed here to design a continuous process along the proton track

that locally deposits the expected value of the prompt- γ emission (induced by proton inelastic scattering) that would have occurred if a large number of protons with the same incident energy had followed the same step (i.e. track element). First an elemental database of prompt- γ emission spectra is established in the clinical energy range of incident protons for all elements in the composition of human tissues. This database of the prompt- γ spectra is built offline with high statistics. Regarding the implementation of the prompt- γ TLE MC tally, each proton deposits along its track the expectation of the prompt- γ spectra from the database according to the proton kinetic energy and the local material density and composition. All software developments have been carried out with the Gate/Geant4 toolkit.

Results: A detailed statistical analysis is reported to characterize the dependency of the variance reduction on the geometrical (track length distribution) and physical (linear prompt- γ spectrum database) parameters. Benchmarking of the proposed technique with respect to an analogous MC technique is carried out. A large relative efficiency gain is reported, ca. 10^5 . Such an efficiency gain could reduce the MC computing time of a full treatment from some weeks to less than one hour. Implementation issues are also addressed.

Conclusions: This MC-based technique makes it possible to deal with complex situations such as heterogeneities for which proton straggling and secondary protons may have a decisive contribution. When considering translation to clinic, measurements for the prompt- γ spectrum database, or at least a sound calibration protocol of the simulated prompt- γ spectra, will have to be carried out.

Keywords: prompt- γ imaging, Monte Carlo simulation, variance reduction

References:

- [1] Min *et al* (2006) *App Phys Lett* 89 183517
- [2] Parodi *et al* (2007) *Phys Med Biol* 52 778-86
- [3] Sterpin *et al* (2015) *Phys Med Biol* 60 4915
- [4] Testa *et al* (2008) *App Phys Lett* 93 093506
- [5] Verburg *et al* (2013) *Phys Med Biol* 58 L37-49
- [6] Williamson (1987) *Med Phys* 14 567-76

137

Preclinical imaging and radiotherapy of prostate cancer using the theranostic twins (⁶⁸Ga/¹⁷⁷Lu)-radiolabeled peptides

J. C. Lim, E. H. Cho, S. Y. Lee, S. H. Dho, S. Y. Kim, S. H. Jung

Korea Atomic Energy Research Institute


Since the gastrin-releasing peptide receptor (GRPR) has been shown to be overexpressed in prostate cancer, bombesin which is the ligand of GRPR has been investigated to be a successful candidate for the peptide receptor radiotherapy (PRRT)[1]. The present study describes the imaging and therapeutic efficacy of the theranostic twins (⁶⁸Ga/¹⁷⁷Lu)-labeled bombesin derivatives for the PRRT of GRPR-overexpressing prostate tumors.

A series of DOTA-conjugated bombesin derivatives were synthesized using a solid-phase synthesis. Competitive binding studies were performed for selecting a GRPR-targeting peptide with high affinity. The selected peptide was labeled with ⁶⁸Ga using the NaCl method for imaging[2], and labeled with ¹⁷⁷Lu which was produced by the HANARO research reactor (thermal neutron flux of 1.8×10^{14} n·cm⁻²·s⁻¹) for therapy. The labeling yield was evaluated by iTLC-SG, and the PET/CT imaging and therapeutic efficacy of the radiolabeled peptides were evaluated using nude mice bearing PC-3 human prostate carcinoma xenograft.

Hydrophilic-modified bombesin derivative showed a nanomolar binding affinity for GRPR. The peptide was labeled with the both radionuclides in high incorporation yields (>98%). ⁶⁸Ga-labeled peptide was quickly cleared from the blood and clearly visualized in PC-3 tumors at 1 hr p.i. ¹⁷⁷Lu-labeled peptide were also rapidly accumulated in a PC-3 tumor, and the % ID/g of the tumor was 12.42 ± 2.15 1 hr p.i. The radio-peptide significantly inhibited the tumor growth

Letter

Submillimeter ionoacoustic range determination for protons in water at a clinical synchrocyclotron

Sebastian Lehrack¹, Walter Assmann^{1,5},
Damien Bertrand^{2,4}, Sebastien Henrotin², Joel Herault³,
Vincent Heymans², Francois Vander Stappen²,
Peter G Thierolf¹, Marie Vidal³, Jarno Van de Walle² and
Katia Parodi¹

¹ Department of Medical Physics, Ludwig-Maximilians-Universität München, 85748 Garching b. München, Germany

² Ion Beam Applications, 1348 Louvain-la-Neuve, Belgium

³ Centre Antoine Lacassagne, 06200 Nice, France

E-mail: Walter.Assmann@physik.uni-muenchen.de

Received 12 May 2017, revised 12 July 2017

Accepted for publication 25 July 2017

Published 18 August 2017



CrossMark

Abstract

Proton ranges in water between 145 MeV to 227 MeV initial energy have been measured at a clinical superconducting synchrocyclotron using the acoustic signal induced by the ion dose deposition (ionoacoustic effect). Detection of ultrasound waves was performed by a very sensitive hydrophone and signals were stored in a digital oscilloscope triggered by secondary prompt gammas. The ionoacoustic range measurements were compared to existing range data from a calibrated range detector setup on-site and agreement of better than 1 mm was found at a Bragg peak dose of about 10 Gy for 220 MeV initial proton energy, compatible with the experimental errors. Ionoacoustics has thus the potential to measure the Bragg peak position with submillimeter accuracy during proton therapy, possibly correlated with ultrasound tissue imaging.

Keywords: proton therapy, *in vivo* range measurements, synchrocyclotron, ionoacoustic

(Some figures may appear in colour only in the online journal)

⁴ The contribution of this author's work was done during the previous employment at IBA.

⁵ Author to whom any correspondence should be addressed.

1. Introduction

The main advantage of proton beams for use in radiation therapy, namely their favorable dose distribution with a pronounced maximum (Bragg peak) at their end of range, makes a precise positioning of this dose maximum in the patient mandatory. One reason is to avoid missing dose in the tumor, another reason is not to cause unnecessary damage in the surrounding normal tissue. The knowledge about the proton range *in vivo* is, however, limited by uncertainties in dose calculation and patient anatomy or tumor position. The resulting range uncertainty prevents taking full advantage of protons in present clinical practice (Paganetti 2012, Knopf and Lomax 2013, Schmid *et al* 2015). To overcome this obstacle real time range verification methods would be highly desirable. To this end, positron emission tomography (PET) imaging and prompt gamma detection have been extensively investigated, and new detector prototypes have just reached clinical maturity (Parodi 2016, Richter *et al* 2016). Both methods are based on nuclear techniques using bulky detectors and complex data evaluation to correlate the patient dose distribution with the measured radiation, which is unfortunately lowered at the end of range.

Another very different approach makes use of the thermoacoustic effect due to the localized and short-term ion energy (dose) deposition, creating an (iono)acoustic signal, which is thus directly correlated to and can be exploited for determination of the Bragg peak position (Parodi and Assmann 2015, Jones *et al* 2016a). Ionoacoustics for proton dose monitoring, although proposed already in 1991 by Tada *et al* (1991) and demonstrated in 1995 during hepatic cancer proton therapy (Hayakawa *et al* 1995), has found renewed and growing interest in the recent years due to improvements in ultrasound imaging as well as in ion irradiation techniques. It promises a cost-effective and direct way to characterize the dose distribution in ion therapy and, in particular, it presents a unique possibility to directly correlate ultrasound morphological images of the irradiated region with the ionoacoustic signal from the ion dose maximum quasi in real-time. This attractive feature, which all other range measuring techniques are lacking (Schardt *et al* 2008, Bäumer *et al* 2015), has recently been demonstrated in various phantoms and *ex vivo* targets at 20 MeV and 50 MeV proton energy (Kellnberger *et al* 2016, Patch *et al* 2016).

The ionoacoustic signal characteristics are determined first by the spatial dose distribution given by the ion mean energy, energy distribution, energy loss and straggling, and second by the temporal ion pulse length. The maximum acoustic amplitude can be reached, if the ion dose deposition time is shorter than the transition time of the sound wave across the Bragg peak width (stress confinement) (Wang and Wu 2007). This condition demands for the lowest therapeutically used proton energy of 70 MeV a proton pulse width of no more than 5 μs . At these time scales, the energy deposition is adiabatic as heat diffusion processes can be neglected. The mostly used (isochronous) cyclotron for proton therapy delivers a quasi-continuous beam with micro-pulses in the 50–100 MHz range. Therefore, to get a measurable ionoacoustic signal, the beam needs to be manipulated by an appropriate pulsing system. One possibility is a chopper-buncher setup (Rohrer *et al* 1984) in the injection line at source potential, cutting the beam by sweeping over an aperture in order to pulse, which could be further compressed by a buncher and adjusted to the cyclotron phase space. Using this technique, a pulse width of 1.8 μs has been produced with 50 MeV protons at a sector-focused cyclotron for ionoacoustic experiments, well matched to the stress confinement condition at this energy (Patch *et al* 2016). Another method for producing a pulsed ion beam has been performed at a 230 MeV isochronous cyclotron, where the source output itself was modulated by exciting the arc current power supply with a function generator (Jones *et al* 2015). According to proton pulse width measurements via prompt gamma emissions, this technique is so far limited to a

pulse duration of about 17 μs (FWHM), which does not fulfill the stress confinement condition for energies below 200 MeV. Jones and coworkers have therefore developed a deconvolution technique to subtract the pulse width effect from the acoustic signal, but the achievable accuracy was limited to some millimeters (Jones *et al* 2016b).

Here we present data from ionoacoustic range measurements in water at proton energies between 145 MeV and 227 MeV using a clinical synchrocyclotron, which by its acceleration principle delivers an intense and short-pulsed proton beam with a width below 10 μs and 1 kHz repetition rate, optimally suited for ionoacoustics. The resulting range values are compared to data measured with an established range monitor system on-site.

2. Material and methods

2.1. The superconducting synchrocyclotron S2C2

Ionoacoustic range measurements were performed at the recently commissioned superconducting synchrocyclotron (IBA S2C2, Louvain-la-Neuve, Belgium) of the Centre Antoine-Lacassagne (CAL, Nice, France) for proton therapy. This installation consists of a very compact proton therapy setup using a superconducting cyclotron with a magnetic field strength around 5 T and an optimized gantry geometry (Proteus[®]ONE) (Pearson *et al* 2013). The important difference between the S2C2 synchrocyclotron and a normal isochronous cyclotron in this context of ionoacoustics is the different acceleration process. To compensate for the relativistic mass increase of the protons, the synchrocyclotron RF is lowered between the injection and extraction orbit from 93 MHz to 63 MHz, hence, protons can be accelerated in single beam bunches only. The modulated RF frequency is produced by an innovative rotating capacitor (so-called rotco) with 1 kHz repetition frequency, which also delivers a proton pulse related trigger signal. Preliminary measurements have shown a pulse width around 8 μs (Van de Walle *et al* 2016), therefore this synchrocyclotron seems to be ideal for ionoacoustic range measurements without any further beam modification.

2.2. Experimental setup and data acquisition

The experiments were performed with mono-energetic proton beams ranging from 145 MeV to 227 MeV to get well defined ('pristine') depth-dose curves. The ultrasound detector was positioned distal to the Bragg peak on the beam axis to create optimum conditions for studying the achievable range resolution (Jones *et al* 2016a). The beam gantry was moved to vertical beam incidence into a water phantom (IBA Dosimetry Blue Phantom², Schwarzenbruck, Germany) and the water surface was aligned to the gantry isocenter. The protons passed an air gap of 560 mm between the last monitor foil in the gantry nozzle and the water surface, stopping at a depth between 15 cm and 32 cm. A typical beam spot size on the water surface, measured at 200 MeV with a radiochromic film, had an FWHM of about 7.5 mm. The proton pulse intensity was measured by a calibrated monitor detector in the gantry nozzle and was varied up to a maximum of 2 pC/pulse. According to simulations and recent measurements at these proton energies by Jones *et al* (2015), the main ultrasound frequency has to be expected well below 100 kHz. Therefore, we used a hydrophone (Cetacean Research C305X, Seattle, USA) with almost linear frequency response from 5 Hz up to 250 kHz and an effective sensitivity of -168 (dB, re 1 V μPa^{-1}). This detector was mounted on the remote controlled *xyz*-stage of the water phantom with its sensitive area perpendicular to the beam and centered along the proton beam axis, typically 5–10 cm distal to the expected Bragg peak position. The distance

between the detector and the water surface d_w is an important parameter in ionoacoustics, as in our axial measuring configuration the absolute proton range in water can be obtained by subtracting the ionoacoustically measured distance between the Bragg peak and detector from d_w . Therefore, the exact position of the detector sensitive area within the 11.3 mm thick protection casting was measured beforehand by ultrasound means. The sensitive volume was found to be not centered inside the hydrophone and the orientation had to be taken into account. With this information the effective detector position could be precisely aligned to the water surface in the experiment. The ultrasound analysis delivered, in addition, the speed of sound in the casting material of $1.89 \text{ mm } \mu\text{s}^{-1}$ and, hence, the water equivalent thickness (WET) of the hydrophone. The detector signals were amplified by 73 dB, limited in bandwidth by a band-pass filter with cutoff frequencies of 500 Hz and 240 kHz, and stored at 1 kHz repetition rate with a PicoScope 5444B digital oscilloscope at 250 MS s^{-1} sampling rate. To improve the signal-to-noise-ratio (SNR) software averaging of up to 1000 events had to be performed afterwards, by which we accumulated a Bragg peak dose of about 10 Gy or a 50% coverage dose (i.e. average dose above 50% of the dose maximum) of 8.5 Gy (for a typical pencil beam with initial beam energy of 220 MeV and 2 pC per pulse). Special care was taken in creating a precise trigger signal, which directly influences the ionoacoustic range precision. We used two different triggers, one trigger was delivered by the rotating capacitor defining the RF frequency of the synchrocyclotron, which was used to start the data acquisition. Another one was deduced from the prompt gamma rays induced by proton interactions in water measured with a fast plastic scintillator (Bicron BC400 R, 4.5 cm thickness) attached to the water phantom. The prompt gamma trigger is related to the start time of the ionoacoustic ultrasound wave emitted from the Bragg peak. The scintillator provided also information to determine the proton pulse time profile. The ionoacoustic range values were compared to existing range data measured with the range monitor on-site (Stingray, IBA Dosimetry, Schwarzenbruck, Germany), a plane-parallel ionization chamber with 6.0 cm radius active area and, according to the vendor, 4.9 mm WET.

3. Results and discussion

A typical ionoacoustic and corresponding (inverted) scintillator signal is shown in figure 1, both signals are 1000-fold averaged. A frequency analysis of the pressure signal reveals a main frequency of 13 kHz, which is similar to the results presented by Jones *et al* (2016b). Interestingly, also a clear response of the hydrophone to the incident proton pulse can be seen, most probably induced by prompt gamma rays and neutrons in the integrated preamplifier. From the simultaneously acquired three signals of the rotco trigger, the scintillation detector and the hydrophone for each individual proton pulse, the trigger precision as well as the proton pulse width have been derived. The 1 kHz rotco trigger stability has been measured by accumulating trigger signals for 60 s and evaluating the time difference between each consecutive signals. The resulting time distribution exhibits an FWHM of about 850 ns. This can be compared to the variation of the individual scintillator signals around the 1000-fold averaged mean value with an FWHM value of about 960 ns, probably due to an additional contribution from a jitter between the rotco trigger and the corresponding proton pulse.

The averaged scintillator signal gives also a direct measure of the proton pulse width, which was determined to be around $2.5 \mu\text{s}$ FWHM for a low beam intensity of about 100 fC/pulse, and increased to $3.7 \mu\text{s}$ FWHM at 2 pC/pulse as used in most of our experiments. Therefore, the proton pulse delivered by the synchrocyclotron fulfills very well the stress confinement condition for the therapeutically used energy range.

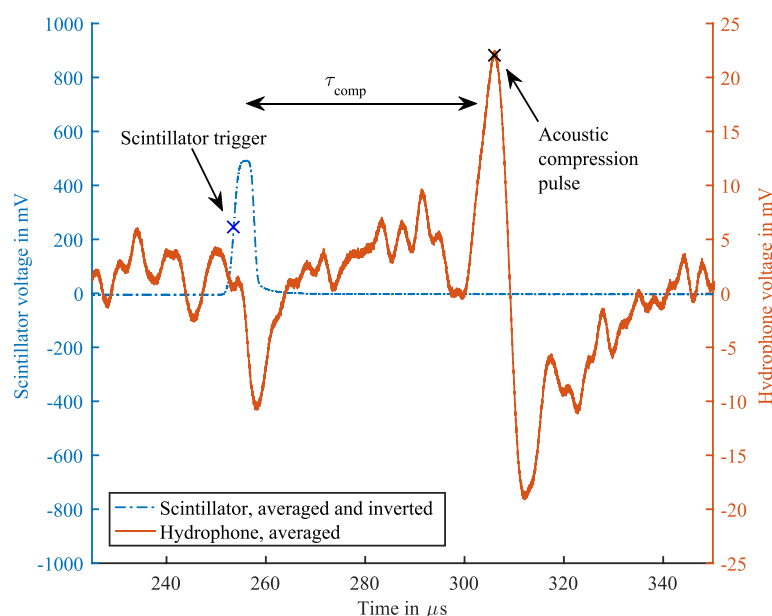


Figure 1. Example waveform of scintillator and hydrophone taken at 220 MeV proton beam energy and approximate Bragg peak dose of 10 mGy per pulse or a 50% coverage dose (i.e. average dose above 50% of the dose maximum) of 8.5 mGy per pulse (see text). Both signals are 1000-fold averaged, the scintillator signal is inverted. 33 dB internal and 40 dB external amplification and 500 Hz–240 kHz band-pass filter was used for the hydrophone. Distinct points in the signal, which were used for the data evaluation, are indicated.

The Bragg peak position (i.e. position of the dose maximum) was calculated from the time difference between the scintillator trigger and the acoustic compression pulse. According to a detailed time metrics analysis of Jones *et al* (2016a, 2016b) we used as start time the point where the trigger reaches 50% of its maximum and for the signal arrival time the maximum of the compression pulse (τ_{comp} in Jones *et al* (2016b)) (see figure 1). This time difference is independent from time delays caused by the energy degrader, as differences in the proton time of flight are compensated by the scintillator close to the water phantom. Moreover, as the ionoacoustic signal is only sensitive to the sub-macrostructure given by the few microseconds extraction, it is insensitive to momentum spread variations introduced by the energy degrader in the beam ns-microstructure (Van de Walle *et al* 2016). Furthermore, one has to take into account the known detector distance to the water surface, the sound velocity in the hydrophone casting material as well as the temperature dependent speed of sound in water. The resulting ionoacoustic Bragg peak values were compared with a power fit to earlier measured Stingray range data, from which the corresponding proton energies at the exit of the beam nozzle were calculated and indicated in the figures and tables. Here one should note that in ionoacoustics the Bragg peak position is actually measured, and therefore the Stingray Bragg curve data have been re-evaluated to obtain the comparable dose maximum position. An overview of all our measurements is presented in figure 2 together with the Stingray data power fit using an exponent of 1.74.

Variations around the mean values of 5 measurements performed at each of the proton beam energies of 200 MeV, 219 MeV and 220 MeV, respectively, can be seen in figure 3 and compared to Stingray fit values. The reproducibility of the ionoacoustic measurements has an

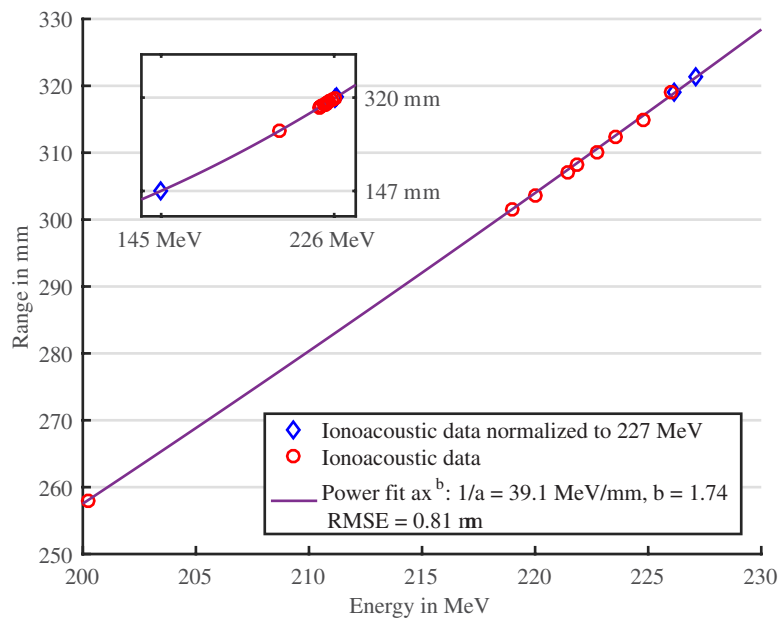


Figure 2. Compilation of all ionoacoustic measurements compared to a power fit of existing Stingray data.

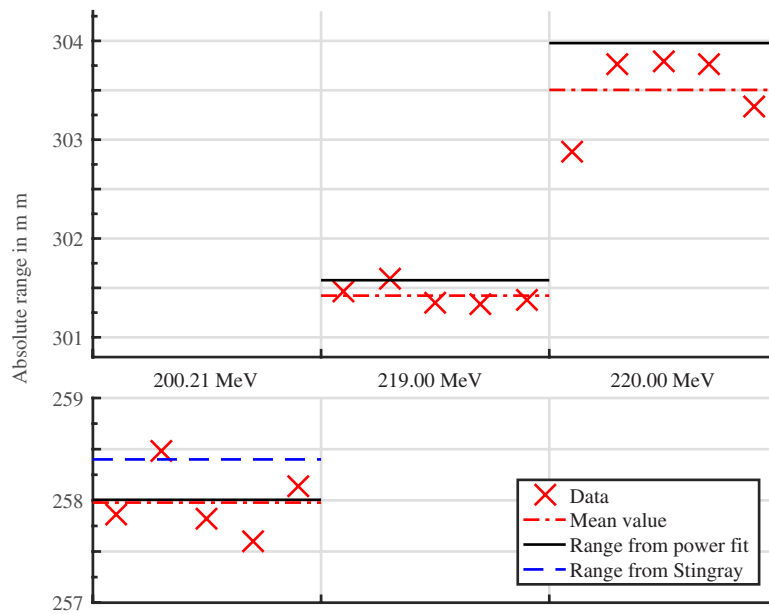


Figure 3. Variation of repeated ionoacoustic range measurements at several energies, compared to a fit of existing Stingray data. For 200.21 MeV, Stingray range value was measured consecutively to the ionoacoustic data acquisition.

Table 1. Summary of all absolute ionoacoustic range measurements using a prompt gamma trigger.

Energy in MeV	Ionoacoustic range in mm	Stingray fit in mm	Difference in μm	σ (τ_{comp}) in mm
200.21	258.0 ^a	258.0 ^a	−27	0.342
219.00	301.4	301.6	−156	0.111
220.00	303.5	304.0	−473	0.399
221.45	307.1	307.5	−367	0.394
221.87	308.3	308.5	−174	0.553
222.71	310.0	310.5	−531	—
223.55	312.4	312.6	−160	—
224.80	315.0	315.6	−646	—
226.00	319.1	318.5	564	—

^aConsecutive measurements with identical cyclotron settings (see figure 3). The difference represents the offset of the measured ionoacoustic range to the Stingray fit value at this energy. For repeated measurements the standard deviation σ is given based on the variation of τ_{comp} (see text).

uncertainty (1σ) of less than 400 μm (see table 1). For 200 MeV, the Stingray measurement was repeated during the ionoacoustic experiment without any change of the cyclotron settings, showing good agreement at this energy (see figure 3). Furthermore, a series of ionoacoustic measurements in smaller energy steps between 221 MeV and 226 MeV are summarized in table 2, including their difference to a power fit of the Stingray data, which exhibits sub-millimeter consistency.

Besides detailed measurements of the absolute beam range (as deduced from the ionoacoustic signal in combination with the above described calibration distance d_w) for selected initial proton energies, relative range shift measurements between different initial energies with unchanged experimental setup were performed by directly analyzing the ionoacoustic waveforms, acquired with the rotco trigger only. The range shift from 226 MeV and 145 MeV relative to 227 MeV was determined, and again compared in table 2 to corresponding values from the Stingray fit curve. Although the trigger jitter was much larger in this case, the mean values of the two shifts differ from the Stingray values by less than 1 mm. The reproducibility as well as the accuracy of the ionoacoustic method was tested by 5 repeated measurements, where the energy was changed according to a Stingray range shift of ± 1 mm. The resulting range data in table 1 clearly demonstrate a range accuracy better than 1 mm and a precision with a mean FWHM of 0.6 mm, corresponding to about 300 keV energy resolution. This value is in accordance with the estimated energy spread of the synchrocyclotron of about 400 keV (Henrotin *et al* 2016).

The overall good agreement of the two very different experimental techniques for range determination has to be compared with the estimated experimental errors. First, the alignment error of the hydrophone to the water surface was about 0.2 mm, the remote controlled detector positioning unit had an accuracy of better than 0.1 mm. The measured water temperature was stable within ± 1 K, the corresponding sound velocity dependence on the temperature contributes a range error of 0.4 mm. The timing error due to different cable lengths of the scintillation and ultrasound detectors can be neglected. Hence, the resulting total error of the ionoacoustic range determination can be estimated to 0.6 mm. The fit to the Stingray data had a root-mean-square-error of 0.8 mm, which covers also the Stingray alignment error, therefore, the measured range differences of the two methods are clearly within the total experimental

Table 2. Relative range shift measurements using the rotco trigger. Ionoacoustic ranges represent offsets to the Stingray value at 227.13 MeV proton energy. For the difference and σ see table 1.

Energy in MeV	Ionoacoustic Range in mm	Stingray fit in mm	Difference in μm	σ (τ_{comp}) in mm
145.00	148.0	147.2	819	5.4
226.13	319.1	318.9	224	1.3
227.13	(321.3)	321.3	—	0.7

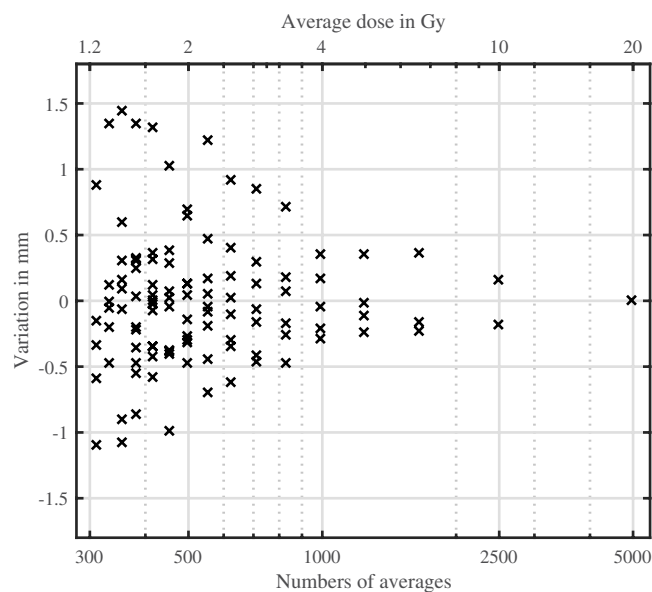


Figure 4. Range precision for various number of averages and corresponding average dose values. From a set of 5000 single pulses with 200 MeV initial proton energy, averages with different amount of pulses were made and evaluated. The variation in the range determination depending on the amount of pulses per averaged signal is shown in relation to the average with all 5000 pulses.

errors. An inter-comparison of different established range detectors has found similar uncertainties (Bäumer *et al* 2015).

In order to improve the SNR, a 1000-fold averaging of the acoustic signals was necessary. We studied at 200 MeV proton energy the dependence of the range accuracy on the number of averages, starting from 200 as the lowest reasonable number up to a maximum of 5000. In figure 4, several range values are given for each averaging number pointing to a minimum number of about 700 to get 1 mm-accuracy. The used number of averages is directly related to the applied average dose, which is also shown in figure 4 in the upper scale. Dose values are calculated for a typical beam current of 2 nA at 1 kHz pulse repetition rate, which corresponds to 2 pC/pulse or 0.4 mJ deposited energy along the proton path at 200 MeV, resulting in an average dose of roughly 4 Gy for 1000 pulses. A similar dose was reported by Jones *et al* (2015) with a comparable high sensitivity hydrophone. Hence, ionoacoustic range verification could become accessible for the most distal pencil beams of extended treatment fields, carrying the highest dose, and benefit from ongoing trends of dose escalation and hypofractionation.

Future studies will also address the influence of tissue heterogeneities, which might be examined preferentially by ultrasound imaging or by using prior information from additional patient-specific images (e.g. x-ray computed tomography), similar to work performed for speed-of-sound aberration corrections in ultrasound-guidance for radiation therapy (Fontanarosa *et al* 2013). Additionally, sophisticated spectral methods will be investigated to eliminate sources of background noise from the patient physiological activities, consistent with the findings of Hayakawa *et al* (1995). Another improvement would be a faster beam nozzle monitor for a precise trigger and determination of the proton beam arrival time (Sadrozinski *et al* 2016).

4. Conclusion

The ionoacoustic method for proton range assessment has been demonstrated for the first time at a clinical synchrocyclotron and at clinically relevant proton energies under optimized conditions such as pristine depth-dose curves, pencil beams and axial detector geometry. The measured range values have been compared to measurements with a plane-parallel ionization chamber showing sub-millimeter range accuracy and precision. Obviously, a synchrocyclotron is predestinated for this new range determination technique as it is delivering intense, microsecond-short beam bunches at the right repetition frequency without any further modifications.

The sub-millimeter range resolution, which we earlier demonstrated at 20 MeV proton energy and 2 MHz mean ultrasound frequency (Assmann *et al* 2015), points at an essential advantage of the ionoacoustic range method: the well-known trade-off between axial resolution and depth penetration in ultrasound imaging does not limit the ionoacoustic range resolution. On the contrary, besides an almost frequency independent resolution, one can take advantage of the much lower signal attenuation at 13 kHz mean signal frequency associated with 220 MeV proton energy. This feature counteracts somewhat the low SNR of ionoacoustic signals expected at clinical conditions, where the amount of pulses for an averaged waveform is limited by dose restrictions.

Apparently, the main challenge for ionoacoustics to be of clinical applicability is an improvement of the SNR with simultaneous dose reduction. This needs intense developments in detector technology and signal processing, but the unique feature of ionoacoustics offering a method to correlate the Bragg peak position with an ultrasound tumor image seems to be worth the effort. In future clinical applications with typically non-axial geometry, a set of detectors or even a detector array will be necessary for dose reconstruction (Patch *et al* 2016) but with detector elements specifically adapted to ionoacoustics and ultrasound imaging. Notwithstanding the problems to be solved for *in vivo* applications, the ionoacoustic range determination is at present a cost-effective, fast and accurate method for quality assurance in ion therapy with a state-of-the-art synchrocyclotron. For this latter application a hydrophone could be mounted inside the water phantom at a fixed position of typically 40 cm distance from the water surface and, once calibrated, presents an easy possibility to check the actual ion range and energy with sufficient resolution in a non-destructive way.

Acknowledgments

This work was funded by the DFG Cluster of Excellence Munich Centre for Advanced Photonics (MAP). We kindly acknowledge support during the experiments from Kilian Baumann and Jonathan Bortfeldt.

ORCID iDs

Sebastian Le rack  <https://orcid.org/0000-0001-8888-2631>

References

- Assmann W *et al* 2015 Ionoacoustic characterization of the proton Bragg peak with submillimeter accuracy *Med. Phys.* **42** 567–74
- Bäumer C, Koska B, Lambert J, Timmermann B, Mertens T and Takoukam Talla P 2015 Evaluation of detectors for acquisition of pristine depth-dose curves in pencil beam scanning *J. Appl. Clin. Med. Phys.* **16** 5577
- Fontanarosa D, Pesente S, Pascoli F, Ermacora D, Abu Rumeileh I and Verhaegen F 2013 A speed of sound aberration correction algorithm for curvilinear ultrasound transducers in ultrasound-based image-guided radiotherapy *Phys. Med. Biol.* **58** 1341–60
- Hayakawa Y, Tada J, Arai N, Hosono K, Sato M, Wagai T, Tsuji H and Tsujii H 1995 Acoustic pulse generated in a patient during treatment by pulsed proton radiation beam *Radiat. Oncol. Invest.* **3** 42–5
- Henrotin S, Abs M, Forton E, Jongen Y, Kleeven W, Verbruggen P and van de Walle J 2016 Commissioning and testing of the first IBA S2C2 *Proc. 21st Int. Conf. on Cyclotrons and Their Applications (Cyclotrons' 16) (Zurich, Switzerland, 11–16 September 2016)* (Geneva: JACOW) pp 178–80
- Jones K C, Sehgal C M and Avery S 2016a How proton pulse characteristics influence protoacoustic determination of proton-beam range: simulation studies *Phys. Med. Biol.* **61** 2213–42
- Jones K C, Vander Stappen F, Bawiec C R, Janssens G, Lewin P A, Prieels D, Solberg T D, Sehgal C M and Avery S 2015 Experimental observation of acoustic emissions generated by a pulsed proton beam from a hospital-based clinical cyclotron *Med. Phys.* **42** 7090–7
- Jones K C, Vander Stappen F, Sehgal C M and Avery S 2016b Acoustic time-of-flight for proton range verification in water *Med. Phys.* **43** 5213–24
- Kellnberger S, Assmann W, Le rack S, Reinhardt S, Thirof P, Queiros D, Sergiadis G, Dollinger G, Parodi K and Ntziachristos V 2016 Ionoacoustic tomography of the proton Bragg peak in combination with ultrasound and optoacoustic imaging *Sci. Rep.* **6** 29305
- Knopf A C and Lomax A 2013 *In vivo* proton range verification: a review *Phys. Med. Biol.* **58** R131–60
- Paganetti H 2012 Range uncertainties in proton therapy and the role of Monte Carlo simulations *Phys. Med. Biol.* **57** R99–117
- Parodi K 2016 On- and off-line monitoring of ion beam treatment *Nucl. Instrum. Methods Phys. Res. A* **809** 113–9
- Parodi K and Assmann W 2015 Ionoacoustics: a new direct method for range verification *Mod. Phys. Lett. A* **30** 1540025
- Patch S K *et al* 2016 Thermoacoustic range verification using a clinical ultrasound array provides perfectly co-registered overlay of the Bragg peak onto an ultrasound image *Phys. Med. Biol.* **61** 5621
- Pearson E, Abs M, Henrotin S, Kleeven W, Van de Walle J, Verbruggen P and Zaremba S 2013 The new IBA superconducting synchrocyclotron (S2C2): from modeling to reality *Proc. Int. Topical Meeting on Nuclear Applications of Accelerators (AccApp-2013) (Bruges, Belgium)* vol 11 p 348
- Richter C *et al* 2016 First clinical application of a prompt gamma based *in vivo* proton range verification system *Radiother. Oncol.* **118** 232–7
- Rohrer L, Jakob H, Rudolph K and Skorka S J 1984 The four gap double drift buncher at Munich *Nucl. Instrum. Methods Phys. Res.* **220** 161–4
- Sadrozinski H F W *et al* 2016 Ultra-fast silicon detectors (UFSD) *Nucl. Instrum. Methods A* **831** 18–23
- Schardt D, Steidl P, Krämer M, Weber U, Parodi K and Brons S 2008 Precision Bragg-curve measurements for light-ion beams in water *GSI Scientific Report 2007* ed K Große GSI, Darmstadt p 373
- Schmid S, Landry G, Thieke C, Verhaegen F, Ganswindt U, Belka C, Parodi K and Dedes G 2015 Monte Carlo study on the sensitivity of prompt gamma imaging to proton range variations due to interfractional changes in prostate cancer patients *Phys. Med. Biol.* **60** 9329–47
- Tada J, Hayakawa Y, Hosono K and Inada T 1991 Time resolved properties of acoustic pulses generated in water and in soft-tissue by pulsed proton-beam irradiation—a possibility of doses distribution monitoring in proton radiation-therapy *Med. Phys.* **18** 1100–5

Van de Walle J, Abs M, Forton E, Henrotin S, Jongen Y, Kleeven W J G M, Verbruggen P, Conjat M, Mandrillon J and Mandrillon P 2016 The S2C2: from source to extraction *Proc. Int. Conf. on Cyclotrons and Their Applications (Cyclotron2016) (Zürich)* vol 21
Wang L V and Wu H-I 2007 *Biomedical Optics: Principles and Imaging* (New York: Wiley)

Ionoacoustic monitoring of high energetic ions at SIS-18*

S. Le rack¹, W. Assmann¹, K. Parodi^{†1}, M. Bender², D. Severin², and C. Trautmann²

¹Lehrstuhl für medizinische Physik, Garching b. München, Germany; ²GSI, Darmstadt, Germany

As heavy ions are stopped in water, their energy is distributed in the form of the well-known Bragg curve. For a short pulse width, this can be considered a spatially confined, adiabatic heating, and the resulting temperature gradient results in a pressure wave containing temporal and spatial information about the beam pulse. It has been shown before, that this signal is the spatial derivative of the energy distribution. Usually studied in the context of medical physics as an in-vivo range determination [1-3], in this work the feasibility of an ionoacoustic detector for high energetic ions has been investigated with ²³⁸U, ¹²⁴Xe, and ¹²C at various energies and intensities.

A lead-zirconate-titanate crystal (PZT) ultrasound trans-

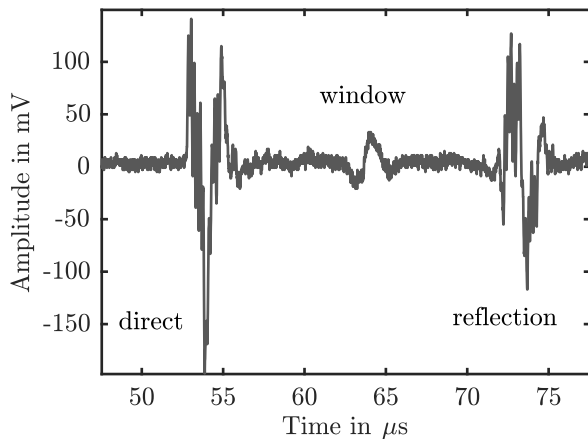


Figure 1: Example waveform measured at a uranium beam with 300 MeV/u and about 200 particles per pulse. The distinct parts of the signal are indicated (see text).

ducer (Videoscan, Olympus) was placed in a water basin axial to the beam facing a kapton entrance window. The transducer was positioned by a 3-dimensional motorized stage. After an amplification of 60 dB, the signals were acquired by a digital oscilloscope. With this rather high amplification, we were able to measure beam intensities down to 200 uranium ions, 5000 xenon ions, and 3×10^7 carbon ions per single pulse. The data acquisition was triggered by an accelerator "beam-on" signal (SIS18 extraction kicker). A typical waveform is shown in figure 1. The signal can be separated in 3 distinct parts deriving from different source locations. A *direct signal*, which is the pressure directly from the distal Bragg peak front. Also, a *reflection signal* being the reflection of the pre-distal part of the Bragg peak

at the entrance window. Between those two is a *window signal*, which is resulting from the temperature gradient at the interface between water and the entrance window. With this identification of the signal, the time differences between those signals multiplied by the speed of sound in water (1.488 mm/μs at 22 °C) is the range in water. For a correct value of the speed of sound and density of the water, its temperature was measured during every shot. As a comparison value, we calculated the expected range of the used ions in water from a GEANT4 simulation including all used parts in the beam path.

As an example, selected results of all used ion types at

Ion type	Simulated range in mm	Ionoacoustic range in mm	σ in μm
Uranium	14.28	14.43	74.5
Xenon	21.00	21.12	8.4
Carbon	70.43	71.03	7.7

Table 1: Results from ionoacoustic range measurements. The given ionoacoustic value is half of the time difference between direct and reflection signal multiplied with the proper speed of sound in water. The used energies were 300 MeV/u for uranium and xenon, and 180 MeV/u for carbon. The standard variation of the measured ranges are fitted to a normal distribution and are given as σ .

300 MeV/u for uranium and xenon and 180 MeV/u for carbon are displayed in table 1. The measured data is very stable in time as indicated by the low standard variation σ , providing a sub-millimeter-precise measurement of the range over several shots. For all used energies and ion types, we are in good agreement with the simulated ranges. The evaluation is ongoing and sophisticated methods to exploit the rich frequency content of the signals are being developed. With this further understanding, an ionoacoustic detector can be a simple, fast, and precise monitor for high energy ions even at high beam intensity, since this method is not suffering from e.g. EMP or pile-up effects as seen in standard particle detectors.

References

- [1] K. Parodi and W. Assmann, "Ionoacoustics: A new direct method for range verification," *Modern Physics Letters A*, vol. 30, no. 17, p. 1540025, 2015.
- [2] W. Assmann et al, "Ionoacoustic characterization of the proton Bragg peak with submillimeter accuracy," *Medical physics*, vol. 42, no. 2, pp. 567–574, 2015.
- [3] S. Kellnberger et al, "Ionoacoustic tomography of the proton Bragg peak in combination with ultrasound and optoacoustic imaging," *Scientific Reports*, vol. 6, p. 29305, 2016.

* Work funded by DFG Cluster of Excellence Munich Centre for Advanced Photonics (MAP). We thank the GSI beam instrumentation group.

† katia.parodi@physik.lmu.de

Bibliography

- Agostinelli, S., Allison, J., Amako, K., Apostolakis, J., Araujo, H., Arce, P., Asai, M., Axen, D., Banerjee, S., Barrand, G., *et al.* Geant4-a Simulation Toolkit. Nuclear Instruments and Methods in Physics Research Section A-Accelerators Spectrometers Detectors and Associated Equipment, volume 506(3), 2003:pp. 250–303. doi:10.1016/S0168-9002(03)01368-8.
- Albul, V. I., Bychkov, V. B., Vasil'ev, S. S., Gusev, K. E., Demidov, V. S., Demidova, E. V., Krasnov, N. K., Kurchanov, A. F., Luk'yashin, V. E., and Sokolov, A. Y. Measuring the Ultrasonic Field Generated in Water upon the Deceleration of a Proton Beam. Instruments and Experimental Techniques, volume 47(4), 2004:pp. 502–507. ISSN 1608-3180. doi:10.1023/B:INET.0000038397.71532.71.
- Albul, V. I., Bychkov, V. B., Vasil'ev, S. S., Gusev, K. E., Demidov, V. S., Demidova, E. V., Krasnov, N. K., Kurchanov, A. F., Luk'yashin, V. E., and Sokolov, A. Y. Acoustic Field Generated by a Beam of Protons Stopping in a Water Medium. Acoustical Physics, volume 51(1), 2005:pp. 33–37. ISSN 1063-7710. doi:10.1134/1.1851626.
- Alsanea, F., Moskvina, V., and Stantz, K. M. Feasibility of RACT for 3D Dose Measurement and Range Verification in a Water Phantom. Medical Physics, volume 42(2), 2015:pp. 937–946. ISSN 0094-2405. doi:10.1118/1.4906241.
- Askaryan, G. A. Hydrodynamic Radiation from the Tracks of Ionizing Particles in Stable Liquids. The Soviet Journal of Atomic Energy, volume 3(2), 1957:pp. 921–923. doi:10.1007/bf01480076.
- Askaryan, G. A., Dolgoshein, B. A., Kalinovsky, A. N., and Mokhov, N. V. Acoustic Detection of High Energy Particle Showers in Water. Nuclear Instruments and Methods, volume 164(2), 1979:pp. 267–278. ISSN 0029-554X. doi:10.1016/0029-554X(79)90244-1.
- Assmann, W., Boer, J. D., Meyer-Berkhout, U., Skorka, S., Huenges, E., Kienle, P., Morinaga, H., Nolte, E., Vonach, H., Münzer, H., *et al.* The Munich MP Tandem. Nuclear Instruments and Methods, volume 122(Supplement C), 1974:pp. 191–203. ISSN 0029-554X. doi:10.1016/0029-554X(74)90482-0.

- Assmann, W., Kellnberger, S., Reinhardt, S., Lehrack, S., Edlich, A., Thirolf, P. G., Moser, M., Dollinger, G., Omar, M., and Ntziachristos, V. Ionoacoustic Characterization of the Proton Bragg Peak with Submillimeter Accuracy. Medical Physics, volume 42(2), 2015:pp. 567–574. ISSN 0094-2405. doi:10.1118/1.4905047.
- Attix, F. H. Introduction to Radiological Physics and Radiation Dosimetry (Wiley-VCH, 1991), 1st edition. ISBN 9780471011460.
- Barendsen, G. W., Beusker, T. L. J., Vergroesen, A. J., and Budke, L. Effects of Different Ionizing Radiations on Human Cells in Tissue Culture: II. Biological Experiments. Radiation Research, volume 13(6), 1960:pp. 841–849. doi:10.2307/3570859.
- Barthel, R. and Nolle, A. A Precise Recording Ultrasonic Interferometer and Its Application to Dispersion Tests in Liquids. The Journal of the Acoustical Society of America, volume 24(1), 1952:pp. 8–15. doi:10.1121/1.1906862.
- Baumann, K. Praktikumsbericht. Dep. med. Phys. LMU Munich, 2016.
- Bäumer, C., Ackermann, B., Hillbrand, M., Kaiser, F.-J., Koska, B., Latzel, H., Lühr, A., Menkel, S., and Timmermann, B. Dosimetry Intercomparison of Four Proton Therapy Institutions in Germany Employing Spot Scanning. Zeitschrift für Medizinische Physik, volume 27(2), 2017:pp. 80–85. doi:10.1016/j.zemedi.2016.06.007.
- Bell, A. G. On the Production and Reproduction of Sound by Light. American Journal of Science, volume Series 3 Vol. 20(118), 1880:pp. 305–324. doi:10.2475/ajs.s3-20.118.305.
- Bennett, G., Goldberg, A., Levine, G., Guthy, J., Balsamo, J., and Archambeau, J. Beam Localization via ^{15}C Activation in Proton-radiation Therapy. Nuclear Instruments and Methods, volume 125(3), 1975:pp. 333–338. doi:10.1016/0029-554X(75)90246-3.
- Bennett, G. W. and Archambeau, J. O. Experimental Tests of Proton Beam Localization. Medical physics, volume 4(2), 1977:pp. 115–117. doi:10.1118/1.594389.
- Bethe, H. Zur Theorie des Durchgangs schneller Korpuskularstrahlen durch Materie. Annalen der Physik, volume 397(3), 1930:pp. 325–400. ISSN 1521-3889. doi:10.1002/andp.19303970303.

- Bortfeld, T. An Analytical Approximation of the Bragg Curve for Therapeutic Proton Beams. Medical Physics, volume 24(12), 1997:pp. 2024–2033. ISSN 2473-4209. doi:10.1118/1.598116.
- Bortfeld, T. and Schlegel, W. An Analytical Approximation of Depth - Dose Distributions for Therapeutic Proton Beams. Physics in Medicine and Biology, volume 41(8), 1996:p. 1331.
- Bowen, T., Chen, C., Liew, S., Lutz, W., and Nasoni, R. Observation of Ultrasonic Emission from Edges of Therapeutic X-ray Beams. Physics in medicine & biology, volume 36(4), 1991:p. 537. doi:10.1088/0031-9155/36/4/011.
- Bragg, W. H. and Kleeman, R. XXXIX. On the α Particles of Radium, and Their Loss of Range in Passing through Various Atoms and Molecules. Philosophical Magazine, volume 10(57), 1905:pp. 318–340. doi:10.1080/14786440509463378.
- Caballero, M. A. A., Rosenthal, A., Buehler, A., Razansky, D., and Ntziachristos, V. Optoacoustic Determination of Spatio-temporal Responses of Ultrasound Sensors. IEEE Trans. Ultrason. Ferroelectr. Freq. Control, volume 60(6), 2013:pp. 1234–1244. doi:10.1109/TUFFFC.2013.2687.
- Carstensen, E. L. Measurement of Dispersion of Velocity of Sound in Liquids. The Journal of the Acoustical Society of America, volume 26(5), 1954:pp. 858–861. doi:10.1121/1.1907429.
- Courant, R., Friedrichs, K., and Lewy, H. Über die partiellen Differenzgleichungen der mathematischen Physik. Mathematische Annalen, volume 100(1), 1928:pp. 32–74. ISSN 1432-1807. doi:10.1007/BF01448839.
- Cox, B., Laufer, J., and Beard, P. The Challenges for Quantitative Photoacoustic Imaging. In Proc. SPIE, volume 7177 (2009), p. 717713. doi:10.1117/12.806788.
- Cox, B. T., Kara, S., Arridge, S. R., and Beard, P. C. K-Space Propagation Models for Acoustically Heterogeneous Media: Application to Biomedical Photoacoustics. Journal of the Acoustical Society of America, volume 121(6), 2007:pp. 3453–3464. ISSN 0001-4966. doi:10.1121/1.2717409.
- Daido, H., Nishiuchi, M., and Pirozhkov, A. S. Review of Laser-driven Ion Sources and Their Applications. Reports on Progress in Physics, volume 75(5), 2012:p. 56401. ISSN 0034-4885. doi:10.1088/0034-4885/75/5/056401.
- De Bonis, G. Acoustic Detection of Ultra-high-energy Cosmoic Neutrinos. Ph.D. thesis, Sapienza Università di Roma, 2008.

- Deboy, D., Assmann, R. W., Aberle, O., Carra, F., Cauchi, M., Lendaro, J., Masi, A., and Redaelli, S. MOPWO029: Remote Estimation of Collimator Jaw Damages with Sound Measurements during Beam Impacts. In Proceedings of IPAC 2013 (JACoW, 2013), pp. 951–953.
- Deboy, D., Assmann, R. W., Baccigalupi, C., Burkart, F., Cauchi, M., Derrez, C. S., Lendaro, J., Masi, A., Redaelli, S., Spiezia, G., *et al.* THPZ031: Acoustic Measurements in the Collimation Region of the LHC. In Proceedings of IPAC 2011 (2011), pp. 3759–3761.
- Doyle, L. Studies on Coherent Ionoacoustics. Bachelor's thesis, Ludwig-Maximilians-Universität München.
- Draeger, E., Mackin, D., Peterson, S., Chen, H., Avery, S., Beddar, S., and Polf, J. 3D Prompt Gamma Imaging for Proton Beam Range Verification. Physics in Medicine and Biology, volume 63(3), 2018:p. 035019. doi:10.1088/1361-6560/aaa203.
- Duque, A. S. Studies on the Calibration of Ultrasonic Transducers for Ionoacoustics. Bachelor's thesis, Ludwig-Maximilians-Universität München.
- Durante, M. and Paganetti, H. Nuclear Physics in Particle Therapy: A Review. Reports on Progress in Physics, volume 79(9), 2016:p. 096702. ISSN 0034-4885. doi:10.1088/0034-4885/79/9/096702.
- Espana Palomares, S., Zhu, X., Daartz, J., El Fakhri, G., Bortfeld, T., and Paganetti, H. Study of the Reliability of the Cross Sections Used to Model the Production of PET Isotopes with Proton Beams. Physics in Medicine and Biology, volume 56, 2011:pp. 2687–98. doi:10.1088/0031-9155/56/9/003.
- Feynman, R. P., Leighton, R. B., and Sands, M. The Feynman Lectures on Physics, Vol. 1: Mainly Mechanics, Radiation, and Heat (Addison Wesley, 1977), 1st edition. ISBN 9780201021165.
- Freiwang, P. Messung der Zeitstruktur eines gepulsten 20MeV-Protonenstrahl. Bachelor's thesis, Ludwig-Maximilians-Universität München.
- Gao, Y., Bin, J., Haffa, D., Kreuzer, C., Hartmann, J., Speicher, M., Lindner, F. H., Ostermayr, T. M., Hilz, P., Rösch, T. F., *et al.* An Automated, 0.5 Hz Nano-foil Target Positioning System for Intense Laser Plasma Experiments. High Power Laser Science and Engineering, volume 5, 2017. doi:10.1017/hpl.2017.10.

- Gedanitz, H. Schallgeschwindigkeits- und Dichtemessungen in Fluiden. Ph.D. thesis, Ruhr-Universität Bochum, 2010.
- Gottschalk, B. Proton Therapy Physics (Series in Medical Physics and Biomedical Engineering), chapter Physics of Proton Interactions in Matter (CRC Press, Boca Raton, 2012). ISBN 978-1-4398-3645-3, pp. 19–59.
- Haberer, T., Becher, W., Schardt, D., and Kraft, G. Magnetic Scanning System for Heavy Ion Therapy. Nuclear Instruments and Methods in Physics Research Section A: Accelerators, Spectrometers, Detectors and Associated Equipment, volume 330(1), 1993:pp. 296–305. ISSN 0168-9002. doi:10.1016/0168-9002(93)91335-K.
- Haller, M. I. and Khuri-Yakub, B. T. A Surface Micromachined Electrostatic Ultrasonic Air Transducer. IEEE transactions on ultrasonics, ferroelectrics, and frequency control, volume 43(1), 1996:pp. 1–6. doi:10.1109/ultsym.1994.401810.
- Hayakawa, Y., Tada, J., Arai, N., Hosono, K., Sato, M., Wagai, T., Tsuji, H., and Tsujii, H. Acoustic Pulse Generated in a Patient during Treatment by Pulsed Proton Radiation Beam. Radiation Oncology Investigations, volume 3(1), 1995:pp. 42–45. ISSN 1520-6823. doi:10.1002/roi.2970030107.
- He, P. Direct Measurement of Ultrasonic Dispersion Using a Broadband Transmission Technique. Ultrasonics, volume 37(1), 1999:pp. 67–70. doi:10.1016/S0041-624X(98)00040-7.
- Henrotin, S., Abs, M., Forton, E., Jongen, Y., Kleeven, W., Verbruggen, P., and Walle, J. v. d. Commissioning and Testing of the First IBA S2C2. In Cyclotron2016 (2016). ISBN 978-3-95450-167-0.
- Hoesl, M., Deepak, S., Moteabbed, M., Jassens, G., Orban, J., Park, Y., Parodi, K., Bentefour, E., and Lu, H. Clinical Commissioning of an in Vivo Range Verification System for Prostate Cancer Treatment with Anterior and Anterior Oblique Proton Beams. Physics in Medicine and Biology, volume 61(8), 2016:p. 3049. doi:10.1088/0031-9155/61/8/3049.
- ICRU. 5. Recommended Values for Key Data. Journal of the International Commission on Radiation Units and Measurements, volume 14(1), 2014a:pp. 31–48. doi:10.1093/jicru/ndw038.
- ICRU. Appendix. Stopping Power and Range Tables for Charged Particles. Journal of the International Commission on Radiation Units and Measurements, volume 14(1), 2014b:p. 79. doi:10.1093/jicru/ndw030.

- Jacobsen, F., Barrera Figueroa, S., and Rasmussen, K. A Note on the Concept of Acoustic Center. The Journal of the Acoustical Society of America, volume 115(4), 2004:pp. 1468–1473. doi:10.1121/1.1652036.
- Jacques Curie, P. C. Développement par compression de l'électricité polaire dans les cristaux hémihédres à faces inclinées. Bulletin de la Société minérologique de France, volume 3, 1880:pp. 90–93.
- Jaros, J., Nikl, V., and Treeby, B. E. Large-scale Ultrasound Simulations Using the Hybrid OpenMP/MPI Decomposition. In Proceedings of the 3rd International Conference on Exascale Applications and Software (University of Edinburgh, 2015), pp. 115–119.
- Jaros, J., Rendell, A. P., and Treeby, B. E. Full-wave Nonlinear Ultrasound Simulation on Distributed Clusters with Applications in High-intensity Focused Ultrasound. The International Journal of High Performance Computing Applications, volume 30(2), 2016:pp. 137–155. doi:10.1177/1094342015581024.
- Jensen, J. A. Field: A Program for Simulating Ultrasound Systems. In 10th Nordicbaltic Conference on Biomedical Imaging, volume 4, Supplement 1, Part 1 (Citeseer, 1996), pp. 351–353.
- Jensen, J. A. and Svendsen, N. B. Calculation of Pressure Fields from Arbitrarily Shaped, Apodized, and Excited Ultrasound Transducers. IEEE Transactions on Ultrasonics, Ferroelectrics, and Frequency Control, volume 39(2), 1992:pp. 262–267. doi:10.1109/58.139123.
- Jones, K. C., Nie, W., Chu, J. C. H., Turian, J. V., Kassae, A., Sehgal, C. M., and Avery, S. Acoustic-based Proton Range Verification in Heterogeneous Tissue: Simulation Studies. Physics in Medicine and Biology, volume 63(2), 2017a:p. 025018. doi:10.1088/1361-6560/aa9d16.
- Jones, K. C., Nie, W., Chu, J. C. H., Turian, J. V., Kassae, A., Sehgal, C. M., and Avery, S. WE-G-605-6: Effects of Tissue Heterogeneity on Acoustic-based Proton Range Verification: Simulation Studies. In 59th Meeting of the AAPM (2017b), pp. –.
- Jones, K. C., Sehgal, C. M., and Avery, S. How Proton Pulse Characteristics Influence Protoacoustic Determination of Proton-beam Range: Simulation Studies. Physics in Medicine and Biology, volume 61(6), 2016a:pp. 2213–2242. ISSN 0031-9155. doi:10.1088/0031-9155/61/6/2213.

- Jones, K. C., Vander Stappen, F., Bawiec, C. R., Janssens, G., Lewin, P. A., Prieels, D., Solberg, T. D., Sehgal, C. M., and Avery, S. Experimental Observation of Acoustic Emissions Generated by a Pulsed Proton Beam from a Hospital-based Clinical Cyclotron. Medical Physics, volume 42(12), 2015:pp. 7090–7097. ISSN 0094-2405. doi:10.1118/1.4935865.
- Jones, K. C., Vander Stappen, F., Sehgal, C. M., and Avery, S. Acoustic Time-of-flight for Proton Range Verification in Water. Medical Physics, volume 43(9), 2016b:pp. 5213–5224. ISSN 0094-2405. doi:10.1118/1.4961120.
- Jones, K. C., Witztum, A., Sehgal, C. M., and Avery, S. Proton Beam Characterization by Proton-induced Acoustic Emission: Simulation Studies. Physics in Medicine and Biology, volume 59(21), 2014:p. 6549.
- Kaatsch, P. e. a. Krebs in Deutschland 2011/2012 (Robert Koch-Institut (Hrsg) and Gesellschaft der epidemiologischen Krebsregister in Deutschland e.V. (Hrsg), Berlin, 2015), 10th edition. ISBN 978-3-89606-228-4.
- Kell, G. S. Density, Thermal Expansivity, and Compressibility of Liquid Water from 0 °C to 150 °C: Correlations and Tables for Atmospheric Pressure and Saturation Reviewed and Expressed on 1968 Temperature Scale. Journal of Chemical and Engineering Data, volume 20(1), 1975:pp. 97–105. doi:10.1021/je60064a005.
- Kellnberger, S., Assmann, W., Lehrack, S., Reinhardt, S., Thirolf, P., Queiros, D., Sergiadis, G., Dollinger, G., Parodi, K., and Ntziachristos, V. Ionoacoustic Tomography of the Proton Bragg Peak in Combination with Ultrasound and Optoacoustic Imaging. Scientific Reports, volume 6, 2016:p. 29305. ISSN 2045-2322. doi:10.1038/Srep29305.
- Khachatryan, A., Semenovskaya, S., and Vainshtein, B. Statistical-thermodynamic Approach to Determination of Structure Amplitude Phases. Soviet Physics Crystallography, volume 24(5), 1979:pp. 519–524.
- Khachatryan, A., Semenovskaya, S., and Vainshtein, B. The Thermodynamic Approach to the Structure Analysis of Crystals. Acta Crystallographica Section A, volume 37(5), 1981:pp. 742–754. doi:10.1107/S0567739481001630.
- Khuri-Yakub, B. T., Cheng, C.-H., Degertekin, F.-L., Ergun, S., Hansen, S., Jin, X.-C., and Oralkan, O. Silicon Micromachined Ultrasonic Transducers. Japanese Journal of Applied Physics, volume 39(5S), 2000:p. 2883. doi:10.1143/JJAP.39.2883.

- King McCubbin, T., Jr. The Dispersion of the Velocity of Sound in Water between 500 and 1500 Kilocycles. The Journal of the Acoustical Society of America, volume 26(2), 1954:pp. 247–249. doi:10.1121/1.1917826.
- Knopf, A. C. and Lomax, A. In Vivo Proton Range Verification: A Review. Physics in Medicine and Biology, volume 58(15), 2013:pp. R131–R160. ISSN 0031-9155. doi:10.1088/0031-9155/58/15/R131.
- Koehler, A. Proton Radiography. Science, volume 160, 1968:pp. 303–304. doi:10.1126/science.160.3825.303.
- Kozlovsky, B., Murphy, R. J., and Ramaty, R. Nuclear Deexcitation Gamma-ray Lines from Accelerated Particle Interactions. The Astrophysical Journal Supplement Series, volume 141(2), 2002:p. 523. doi:10.1086/340545.
- Kroebel, W. and Mahrt, K.-H. Recent Results of Absolute Sound Velocity Measurements in Pure Water and Sea Water at Atmospheric Pressure. Acta Acustica united with Acustica, volume 35(3), 1976:pp. 154–164. ISSN 1610-1928.
- Lahmann, R., Anton, G., Graf, K., Höfl, J., Kappes, A., Katz, U., Mecke, K., and Schwemmer, S. Thermo-acoustic Sound Generation in the Interaction of Pulsed Proton and Laser Beams with a Water Target. Astroparticle Physics, volume 65, 2015:pp. 69–79. ISSN 0927-6505. doi:10.1016/j.astropartphys.2014.12.003.
- Lee, C. C., Lahham, M., and Martin, B. Experimental Verification of the Kramers-Kronig Relationship for Acoustic Waves. IEEE transactions on ultrasonics, ferroelectrics, and frequency control, volume 37(4), 1990:pp. 286–294. doi:10.1109/58.56489.
- Lehrack, S. An Automatic Laser Beam Delivery Alignment for LEX and CALA. Master's thesis, Ludwig-Maximilians-Universität München, 2014.
- Lehrack, S., Assmann, W., Bertrand, D., Henrotin, S., Herault, J., Heymans, V., Stappen, F. V., Thirolf, P. G., Vidal, M., de Walle, J. V., *et al.* Submillimeter Ionoacoustic Range Determination for Protons in Water at a Clinical Synchrocyclotron. Physics in Medicine and Biology, volume 62(17), 2017:p. L20. doi:10.1088/1361-6560/aa81f8.
- Lehrack, S., Assmann, W., Maaß, A., Baumann, K., Dedes, G., Reinhardt, S., Thirolf, P., Dollinger, G., Vander Stappen, F., Van de Walle, J., *et al.* Range Verification with Ionoacoustics: Simulations and Measurements at a Clinical Proton Synchro-cyclotron. Radiotherapy and Oncology, volume 118, 2016:pp. S66–S67. ISSN 0167-8140. doi:10.1016/s0167-8140(16)30135-9.

- Levin, W., Kooy, H., Loeffler, J., and DeLaney, T. Proton Beam Therapy. British Journal of Cancer, volume 93(8), 2005:p. 849. doi:10.1038/sj.bjc.6602754.
- Litzenberg, D. W., Roberts, D. A., Lee, M. Y., Pham, K., Vander Molen, A. M., Ronningen, R., and Becchetti, F. D. Online Monitoring of Radiotherapy Beams: Experimental Results with Proton Beams. Medical Physics, volume 26(6), 1999:pp. 992–1006. doi:10.1118/1.598491.
- Lühr, A., Toftegaard, J., Kantemiris, I., Hansen, D. C., and Bassler, N. Stopping Power for Particle Therapy: The Generic Library LibdEdx and Clinically Relevant Stopping-power Ratios for Light Ions. International Journal of Radiation Biology, volume 88(1-2), 2012:pp. 209–212. doi:10.3109/09553002.2011.595877.
- Macchi, A., Borghesi, M., and Passoni, M. Ion Acceleration by Superintense Laser-plasma Interaction. Reviews of Modern Physics, volume 85, 2013:pp. 751–793. doi:10.1103/RevModPhys.85.751.
- Marczak, W. Water As a Standard in the Measurements of Speed of Sound in Liquids. The Journal of the Acoustical Society of America, volume 102(5), 1997:pp. 2776–2779. doi:10.1121/1.420332.
- Mast, T. D. Empirical Relationships between Acoustic Parameters in Human Soft Tissues. Acoustics Research Letters Online, volume 1(2), 2000:pp. 37–42. doi:10.1121/1.1336896.
- Mijnheer, B., Beddar, S., Izewska, J., and Reft, C. In Vivo Dosimetry in External Beam Radiotherapy. Medical Physics, volume 40(7), 2013:p. 070903. ISSN 0094-2405. doi:10.1118/1.4811216.
- Min, C.-H., Kim, C. H., Youn, M.-Y., and Kim, J.-W. Prompt Gamma Measurements for Locating the Dose Falloff Region in the Proton Therapy. Applied Physics Letters, volume 89(18), 2006:p. 183517. doi:10.1063/1.2378561.
- Montanari, C. C. and Dimitriou, P. The IAEA Stopping Power Database, Following the Trends in Stopping Power of Ions in Matter. Nuclear Instruments and Methods in Physics Research Section B: Beam Interactions with Materials and Atoms, volume 408, 2017:pp. 50–55. doi:10.1016/j.nimb.2017.03.138.
- Moteabbed, M., Espana, S., and Paganetti, H. Monte Carlo Patient Study on the Comparison of Prompt Gamma and PET Imaging for Range Verification in Proton Therapy. Physics in Medicine and Biology, volume 56(4), 2011:p. 1063. doi:10.1088/0031-9155/56/4/012.

- Newhauser, W. D. and Zhang, R. The Physics of Proton Therapy. Physics in Medicine and Biology, volume 60(8), 2015:p. R155. ISSN 0031-9155. doi:10.1088/0031-9155/60/8/R155.
- Nie, W., Jones, K. C., Petro, S., Kassae, A., Sehgal, C. M., and Avery, S. Proton Range Verification in Homogeneous Materials through Acoustic Measurements. Physics in Medicine and Biology, volume 63(2), 2017:p. 025036. doi:10.1088/1361-6560/aa9c1f.
- O'Donnell, M., Jaynes, E., and Miller, J. Kramers–Kronig Relationship between Ultrasonic Attenuation and Phase Velocity. The Journal of the Acoustical Society of America, volume 69(3), 1981:pp. 696–701. doi:10.1121/1.385566.
- Olympus NDT INC. Ultrasonic Transducers Technical Notes. Technical report, Olympus, 2001.
- Paganetti, H. Range Uncertainties in Proton Therapy and the Role of Monte Carlo Simulations. Physics in Medicine and Biology, volume 57(11), 2012:pp. R99–R117. ISSN 0031-9155. doi:10.1088/0031-9155/57/11/R99.
- Parodi, K. On- and Off-line Monitoring of Ion Beam Treatment. Nuclear Instruments and Methods in Physics Research Section A: Accelerators, Spectrometers, Detectors and Associated Equipment, volume 809, 2016:pp. 113–119. ISSN 0168-9002. doi:10.1016/j.nima.2015.06.056. Advances in detectors and applications for medicine.
- Parodi, K. and Assmann, W. Ionoacoustics: A New Direct Method for Range Verification. Modern Physics Letters A, volume 30(17), 2015:p. 1540025. ISSN 0217-7323. doi:10.1142/S0217732315400258.
- Parodi, K., Paganetti, H., Shih, H. A., Michaud, S., Loeffler, J. S., DeLaney, T. F., Liebsch, N. J., Munzenrider, J. E., Fischman, A. J., Knopf, A., *et al.* Patient Study of in Vivo Verification of Beam Delivery and Range, Using Positron Emission Tomography and Computed Tomography Imaging After Proton Therapy. International Journal of Radiation Oncology, Biology, Physics, volume 68(3), 2007:pp. 920–934. doi:10.1016/j.ijrobp.2007.01.063.
- Patch, S. K., Covo, M. K., Jackson, A., Qadadha, Y. M., Campbell, K. S., Albright, R. A., Bloemhard, P., Donoghue, A. P., Siero, C. R., Gimpel, T. L., *et al.* Thermoacoustic Range Verification Using a Clinical Ultrasound Array Provides Perfectly Co-registered Overlay of the Bragg Peak onto an Ultrasound Image. Physics in Medicine and Biology, volume 61(15), 2016:p. 5621. ISSN 0031-9155. doi:10.1088/0031-9155/61/15/5621.

- Patch, S. K., Hoff, D. E., Webb, T. B., Sobotka, L. G., and Zhao, T. Two-stage Ionoacoustic Range Verification Leveraging Monte Carlo and Acoustic Simulations to Stably Account for Tissue Inhomogeneity and Accelerator-specific Time Structure - a Simulation Study. Medical Physics, volume 45(2), 2017:pp. 783–793. ISSN 2473-4209. doi:10.1002/mp.12681.
- Peiffer, A. Ein Beitrag zur Anwendung der ionenakustischen Dosisbestimmung in der Tumorthherapie mit Schwerionen. Ph.D. thesis, Technische Universität Dresden, 1998.
- Peiffer, A. and Köhler, B. Acoustic Detection of Therapeutical Radiation for Modern Cancer Therapy with Heavy Ions. In World congress on Ultrasonics, volume 2 (1997), pp. –.
- Peiffer, A., Köhler, B., Hasch, B., and Enghardt, W. Sound Radiation Caused by Heavy Ions Stopping in Water and Its Possibilities for Dose Distribution Monitoring in Modern Cancer Therapy. In World congress on Ultrasonics, volume 1 (1995), pp. 1095–1098.
- Peucelle, C., Nauraye, C., Patriarca, A., Hierso, E., Fournier-Bidoz, N., Martínez-Rovira, I., and Prezado, Y. Proton Minibeam Radiation Therapy: Experimental Dosimetry Evaluation. Medical Physics, volume 42(12), 2015:pp. 7108–7113. doi:10.1118/1.4935868.
- Pinkerton, J. The Absorption of Ultrasonic Waves in Liquids and Its Relation to Molecular Constitution. Proceedings of the Physical Society. Section B, volume 62(2), 1949:p. 129. doi:10.1088/0370-1301/62/2/307.
- Polf, J., Peterson, S., Ciangaru, G., Gillin, M., and Beddar, S. Prompt Gamma-ray Emission from Biological Tissues during Proton Irradiation: A Preliminary Study. Physics in Medicine and Biology, volume 54(3), 2009a:p. 731. doi:10.1088/0031-9155/54/3/017.
- Polf, J., Peterson, S., McCleskey, M., Roeder, B., Spiridon, A., Beddar, S., and Trache, L. Measurement and Calculation of Characteristic Prompt Gamma Ray Spectra Emitted during Proton Irradiation. Physics in Medicine and Biology, volume 54(22), 2009b:p. N519. doi:10.1088/0031-9155/54/22/N02.
- Prezado, Y. and Fois, G. R. Proton-minibeam Radiation Therapy: A Proof of Concept. Medical Physics, volume 40(3), 2013:p. 031712. ISSN 2473-4209. doi:10.1118/1.4791648. 031712.
- Prezado, Y., Sarun, S., Gil, S., Deman, P., Bouchet, A., and Le Duc, G. Increase of Lifespan for Glioma-bearing Rats by Using Minibeam Radiation Therapy.

- Journal of Synchrotron Radiation, volume 19(1), 2012:pp. 60–65. doi:10.1107/S0909049511047042.
- Redaelli, S., Aberle, O., Assmann, R. W., Masi, A., and Spiezia, G. Detecting impacts of proton beams on the LHC collimators with vibration and sound measurements. In Particle Accelerator Conference, 2005. PAC 2005. Proceedings of the (IEEE, 2005), pp. 1018–1020.
- Reinhardt, S., Hillbrand, M., Wilkens, J., and Assmann, W. Comparison of Gafchromic EBT2 and EBT3 Films for Clinical Photon and Proton Beams. Medical physics, volume 39(8), 2012:pp. 5257–5262. doi:10.1118/1.4737890.
- Richter, C., Pausch, G., Barczyk, S., Marlen, P., Keitz, I., Thiele, J., Smeets, J., Vander Stappen, F., Bombelli, L., Fiorini, C., *et al.* First Clinical Application of a Prompt Gamma Based in Vivo Proton Range Verification System. Radiotherapy and Oncology, volume 118(2), 2017:pp. 232–237. ISSN 0167-8140. doi:10.1016/j.radonc.2016.01.004. Doi: 10.1016/j.radonc.2016.01.004.
- Robinson, S. Technical Guides - Speed of Sound in Pure Water. Technical report, Technical Guides - Speed of Sound in Pure Water, National Physical Laboratory, Teddington, Middlesex, UK, TW11 0LW, 2000.
- Roellinghoff, F., Richard, M.-H., Chevallier, M., Constanzo, J., Dauvergne, D., Freud, N., Henriquet, P., Foulher, F. L., Létang, J., Montarou, G., *et al.* Design of a Compton Camera for 3D Prompt- γ Imaging during Ion Beam Therapy. Nuclear Instruments and Methods in Physics Research Section A: Accelerators, Spectrometers, Detectors and Associated Equipment, volume 648(Supplement 1), 2011:pp. S20–S23. ISSN 0168-9002. doi:10.1016/j.nima.2011.01.069. NIMA 4th International Conference on Imaging techniques in Subatomic Physics, Astrophysics, Medicine, Biology and Industry.
- Rohrer, L., Jakob, H., Rudolph, K., and Skorcka, S. J. The Four Gap Double Drift Buncher at Munich. Nuclear Instruments and Methods in Physics Research, volume 220(1), 1984:pp. 161–164. ISSN 0167-5087. doi:10.1016/0167-5087(84)90429-0.
- Rösch, F. T., Hilz, P., Bin, J., Englbrecht, F., Gao, Y., Haffa, D., Hartmann, J., Herr, S., Lindner, H. F., Speicher, M., *et al.* Considerations on Employing a PMQ-doublet for Narrow and Broad Proton Energy Distributions. In O. Dössel (editor), Current Directions in Biomedical Engineering, volume 3 (Joint Journal of the German Society for Biomedical Engineering in VDE and the Austrian and Swiss Societies for Biomedical Engineering, 2017), p. 339. doi:10.1515/cdbme-2017-0069.

- Rösch, T. F. A Permanent Magnet Focusing Structure for Laser-accelerated Ions. Master's thesis, Ludwig-Maximilians-Universität München, 2015.
- Sammer, M., Greubel, C., Girst, S., and Dollinger, G. Optimization of Beam Arrangements in Proton Minibeam Radiotherapy by Cell Survival Simulations. Medical physics, volume 44(11), 2017:pp. 6096–6104. doi:10.1002/mp.12566.
- Schardt, D., Steidl, P., Krämer, M., Weber, U., Parodi, K., and Brons, S. RADIATIONBIOPHYSICS-19: Precision Bragg-curve Measurements for Lightion Beams in Water, chapter Research programme biophysics and cancer therapy. Number 2008-1 in GSI Scientific Report (GSI Helmholtzzentrum für Schwerionenforschung, 2008), p. 373.
- Schneider, U. and Pedroni, E. Proton Radiography As a Tool for Quality Control in Proton Therapy. Medical Physics, volume 22(4), 1995:pp. 353–363. doi:10.1118/1.597470.
- Schneider, U., Pedroni, E., and Lomax, A. The Calibration of CT Hounsfield Units for Radiotherapy Treatment Planning. Physics in Medicine and Biology, volume 41(1), 1996:p. 111. doi:10.1088/0031-9155/41/1/009.
- Sihver, L., Schardt, D., and Kanai, T. Depth-Dose Distributions of High-Energy Carbon, Oxygen and Neon Beams in Water. Japanese Journal of Medical Physics, volume 18(1), 1998:pp. 1–21. doi:10.11323/jjimp1992.18.1_1.
- Smeets, J., Roellinghoff, F., Prieels, D., Stichelbaut, F., Benilov, A., Busca, P., Fiorini, C., Peloso, R., Basilavecchia, M., Frizzi, T., *et al.* Prompt Gamma Imaging with a Slit Camera for Real-time Range Control in Proton Therapy. Physics in Medicine and Biology, volume 57(11), 2012:p. 3371.
- Sommer, L. Ionoacoustic Simulations on Prostate Cancer Patients - K-Wave Simulations on CT-data. Master's thesis, Ludwig-Maximilians-Universität München, 2017.
- Stewart, B. W. and Wild, C. P. (editors). World Cancer Report 2014 (International Agency for Research on Cancer, Lyon, 2014). ISBN 978-92-832-0429-9.
- Sulak, L., Armstrong, T., Baranger, H., Bregman, M., Levi, M., Mael, D., Strait, J., Bowen, T., Pifer, A. E., Polakos, P. A., *et al.* Experimental Studies of the Acoustic Signature of Proton-beams Traversing Fluid Media. Nuclear Instruments and Methods, volume 161(2), 1979:pp. 203–217. ISSN 0029-554X. doi:10.1016/0029-554x(79)90386-0.

- Tada, J., Hayakawa, Y., Hosono, K., and Inada, T. Time Resolved Properties of Acoustic Pulses Generated in Water and in Soft-tissue by Pulsed Proton-beam Irradiation - a Possibility of Doses Distribution Monitoring in Proton Radiation-therapy. Medical Physics, volume 18(6), 1991:pp. 1100–1105. ISSN 0094-2405. doi:10.1118/1.596618.
- Tang, S., Both, S., Bentefour, H., Paly, J. J., Tochner, Z., Efstathiou, J., and Lu, H.-M. Improvement of Prostate Treatment by Anterior Proton Fields. International Journal of Radiation Oncology, Biology, Physics, volume 83(1), 2012:pp. 408–418. ISSN 0360-3016. doi:10.1016/j.ijrobp.2011.06.1974.
- Tashima, H., Yamaya, T., Yoshida, E., Kinouchi, S., Watanabe, M., and Tanaka, E. A Single-ring OpenPET Enabling PET Imaging during Radiotherapy. Physics in Medicine and Biology, volume 57(14), 2012:p. 4705.
- Terunuma, T., Sakae, T., Hayakawa, Y., Nohtomi, A., Takada, Y., Yasuoka, K., and Maruhashi, A. Waveform Simulation Based on 3D Dose Distribution for Acoustic Wave Generated by Proton Beam Irradiation. Medical Physics, volume 34(9), 2007:pp. 3642–3648. ISSN 2473-4209. doi:10.1118/1.2767985.
- Tessonier, T., Mairani, A., Brons, S., Haberer, T., Debus, J., and Parodi, K. Experimental Dosimetric Comparison of ^1H , ^4He , ^{12}C and ^{16}O Scanned Ion Beams. Physics in Medicine & Biology, volume 62(10), 2017:p. 3958. doi:10.1088/1361-6560/aa6516.
- Thirolf, P. G., Lang, C., Aldawood, S., van der Kolff, H. G., Maier, L., Schaart, D., and Parodi, K. Development of a Compton Camera for Online Range Monitoring of Laser-accelerated Proton Beams Via Prompt-gamma Detection. In EPJ Web of Conferences, volume 66 (EDP Sciences, 2014), p. 11036. doi:10.1051/epjconf/20146611036.
- Trbojevic, D., Alessi, J., Blaskiewicz, M., Cullen, C., Hahn, H., Lowenstein, D., Marneris, I., Meng, W., Mi, J.-L., Pai, C., *et al.* Lattice Design of a Rapid Cycling Medical Synchrotron for Carbon/Proton Therapy. Proceedings of IPAC, 2011.
- Treeby, B. E. and Cox, B. T. K-Wave: Matlab Toolbox for the Simulation and Reconstruction of Photoacoustic Wave Fields. Journal of Biomedical Optics, volume 15(2), 2010:p. 021314. ISSN 1083-3668. doi:10.1117/1.3360308.
- Treeby, B. E., Jaros, J., Rendell, A. P., and Cox, B. Modeling Nonlinear Ultrasound Propagation in Heterogeneous Media with Power Law Absorption Using a k-Space Pseudospectral Method. The Journal of the Acoustical Society of America, volume 131(6), 2012:pp. 4324–4336. doi:10.1121/1.4712021.

- Verburg, J. M., Shih, H. A., and Seco, J. Simulation of Prompt Gamma-ray Emission during Proton Radiotherapy. Physics in Medicine and Biology, volume 57(17), 2012:p. 5459. doi:10.1088/0031-9155/57/17/5459.
- Wagner, W. and Pruß, A. The IAPWS Formulation 1995 for the Thermodynamic Properties of Ordinary Water Substance for General and Scientific Use. Journal of physical and chemical reference data, volume 31(2), 2002:pp. 387–535. doi:10.1063/1.1461829.
- Wang, L. V. and Wu, H.-i. Biomedical Optics : Principles and Imaging (Wiley-Interscience, Hoboken, N.J., 2007). ISBN 9780471743040 (cloth) 0471743046 (cloth).
- Wiener, N. Generalized Harmonic Analysis. Acta Math., volume 55, 1930:pp. 117–258. doi:10.1007/BF02546511.
- Wilson, R. R. Radiological Use of Fast Protons. Radiology, volume 47(5), 1946:pp. 487–491. ISSN 0033-8419. doi:10.1148/47.5.487.
- Würl, M., Englbrecht, F., Lehrack, S., Gianoli, C., Olivari, F., Rösch, T., Lindner, F. H., Haffa, D., Assmann, W., Tran, L., *et al.* Development of Two Prototype Spectrometers for Laser-accelerated Proton Bunches. In 17th International Symposium on Microdosimetry (MICROS) (2017).
- Xiang, L., Han, B., Carpenter, C., Prax, G., Kuang, Y., and Xing, L. X-ray Acoustic Computed Tomography with Pulsed X-ray Beam from a Medical Linear Accelerator. Medical physics, volume 40(1), 2013. doi:10.1118/1.4771935.
- Xie, Y., Bentefour, E. H., Janssens, G., Smeets, J., Vander Stappen, F., Hotoiu, L., Yin, L., Dolney, D., Avery, S., O’Grady, F., *et al.* Prompt Gamma Imaging for in Vivo Range Verification of Pencil Beam Scanning Proton Therapy. International Journal of Radiation Oncology, Biology, Physics, volume 99(1), 2017:pp. 210–218. doi:10.1016/j.ijrobp.2017.04.027.
- Yamaya, T., Yoshida, E., Inaniwa, T., Sato, S., Nakajima, Y., Wakizaka, H., Kokuryo, D., Tsuji, A., Mitsunashi, T., Kawai, H., *et al.* Development of a Small Prototype for a Proof-of-concept of OpenPET Imaging. Physics in Medicine and Biology, volume 56(4), 2011:p. 1123.
- Yang, R. Ion Bunch Energy Acoustic Tracing (I-BEAT). Master’s thesis, Ludwig-Maximilians-Universität München, 2017.
- Yao, D.-K., Zhang, C., Maslov, K., and Wang, L. V. Photoacoustic Measurement of the Grüneisen Parameter of Tissue. Journal of Biomedical Optics, volume 19(1), 2014:pp. 017007–017007. doi:10.1117/1.jbo.19.1.017007.

Zhang, R. and Newhauser, W. D. Calculation of Water Equivalent Thickness of Materials of Arbitrary Density, Elemental Composition and Thickness in Proton Beam Irradiation. Physics in Medicine and Biology, volume 54(6), 2009:p. 1383.

Ziegler, J. F., Biersack, J., and Littmark, U. The Stopping and Range of Ions in Solids, volume 1 of Stopping and Range of Ions in Matter (Pergamon Pr, New York, 1985). ISBN 008021603X.

Ziegler, J. F., Ziegler, M., and Biersack, J. SRIM - the Stopping and Range of Ions in Matter (2010). Nuclear Instruments and Methods in Physics Research Section B: Beam Interactions with Materials and Atoms, volume 268(11), 2010:pp. 1818–1823. ISSN 0168-583X. doi:10.1016/j.nimb.2010.02.091. 19th International Conference on Ion Beam Analysis.

Danksagung

Ich danke meiner Doktormutter Prof. Dr. Katia Parodi und meinem Gruppenleiter PD Dr. Walter Assmann für die Betreuung dieser Arbeit in allen Aspekten und Facetten.

Außerdem Prof. Dr. Jörg Schreiber, Prof. Dr. Paul Balton und PD Dr. Peter Thirolf für ihre offenen Ohren zu allen Themen, egal ob Physik oder Eishockey. Ich habe die Gespräche sehr geschätzt.

Ich danke dem gesamten Lehrstuhl für medizinische Physik, mehr als eine Arbeitsstelle über die letzten 3 Jahre. Insbesondere sind hier die Senior Scientist zu nennen: Dr. Sabine Reinhardt, Dr. Chiara Gianoli, Dr. Stella Veloza, Dr. George Dedes, Dr. Marco Pinto, und Dr. Guillaume Landry. Danke für eure Bereitschaft, Fachwissen zu teilen. Aber auch meine Doktorandenkollegen: Silvia, Juliana, Matthias, Franz, Daniel, die vermutlich beste Riege an Doktoranden ever.

Ich hatte auch das Vergnügen, mit jüngeren Talenten zu arbeiten. Die Arbeit mit euch hat mir immer Freude bereitet, weil ich auch nur selten enttäuscht wurde. Danke an Anna-Sophie, Alexandra, Ricarda, Rong, Killian, Lenny, Johannes, Lukas, Julian, Alexander und Andreas.

During my studies, I had the opportunity to work abroad. I would like to thank Dr. Bradley Treeby, Dr. Ben Cox and Dr. Elly Martins from the Ultrasoundgroup in London for their hospitality and advice during the last 3 years.

Also: Dr. Kevin Jones, Dr. Stephen Avery and Jamie Merwin who took care of me during two beam times in Philadelphia, it had been a great pleasure.

Ich danke meiner Familie für ihre Unterstützung.

Außerdem allen Freunden, die das Leben in meine Work-Life-Balance gesteckt haben. Dazu gehören unter anderem: Die Kommilitonen Christian “Hübi” Huber, Max “Cpt. Obvious” Mehlhorn, Peter “Es gibt nur ein Vollgas” Zeidler und Robin “); DROP TABLE Students;–” Schlenga, die Storcheneltern Anja und Tom sowie die Storchenmaler Yvonne und Julia, die Berchtesgadener Gretchen und Bene, und Krzystof mit dem Rest der Brettspielgruppe. Ihr alle habt, vielleicht ohne Bewusstsein, viel verändert und bewegt in mir, und dafür danke ich euch.

Whoever is missing, the rest of this page is left blank intentionally for you.

